PREDICTION OF DYNAMIC FORCE CHARACTERISTICS OF RADIAL TIRES USING FINITE ELEMENT AND EXPERIMENTAL TECHNIQUES

by

Veysel Alkan

B.S., M.E., Pamukkale University, 1996

M.S., M.E., Pamukkale University, 1999

Submitted to the Institute for Graduate Studies in
Science and Engineering in partial fulfillment of
the requirements for the degree of
Doctor of Philosophy

Graduate Program in Mechanical Engineering

Boğaziçi University

2008

PREDICTION OF DYNAMIC FORCE CHARACTERISTICS OF RADIAL TIRES USING FINITE ELEMENT AND EXPERIMENTAL TECHNIQUES

APPROVED BY:

Prof. Günay Anlaş (Thesis Supervisor)	.....
Assoc. Prof. Orhan Alankuş	.....
Prof. Ali Rana Atılgan	.....
Assist. Prof. Nuri Ersoy	.....
Assoc. Prof. Fazıl Önder Sönmez	.....

DATE OF APPROVAL: 23.01.2008

ACKNOWLEDGEMENTS

First of all, I would like to express my sincere gratitude to my thesis supervisor, Professor Günay Anlaş. He provided me many helpful suggestions, important advice and encouragement during the course of this work. It was a pleasure to work with him.

I wish to express my appreciation to my thesis committee members, Dr. Orhan Alankuş, Dr. Ali Rana Atılgan, Dr. Nuri Ersoy, and Dr. Fazıl Önder Sönmez for their valuable suggestions and constructive advices.

I acknowledge financial support of this research by the Scientific and Technological Research Council of Turkey (TÜBİTAK) during the experimental studies conducted at the University of Michigan Transportation Research Institute (UMTRI) in Ann Arbor, Michigan, USA. I also wish to acknowledge the contributions of Professor Tim Gordon, Professor Paul Fancher, Mr. Steven M. Karamihas , Mr. Mike Campbell, Mr. John Koch, Mr. Stewart Simonett and all staff of the University of Michigan Transportation Research Institute. Special thanks go to Mr. Aydın Kuntay and Mr. Ender Koç of BIAS for their help in the finite element analysis part of this work. I lived in Ann Arbor, Michigan during 11 months and I met many Turkish people. I would like to thank to Dr. Ali Rıza Yıldız, Mrs. Arzucan Özgür, Mrs. Hacer Karataş and Professor İrfan Civcir and his wife Professor Pervin Civcir, for their encouragement and support.

I would like to thank Dr. Yasin Yılmaz, Mr. Ahmet Hanifi Ertaş, Mr. Alpay Oral and all other assistants, staff and graduate students in my department and Dr. Mehmet Orhan and Dr. Erkan Yüce of Pamukkale University for their support and encouragement.

I would like to give my special thanks to my parents and my wife Pınar whose patient love, moral support, and collaboration enabled me to complete this work. I would also like to say that this thesis is dedicated to my parent and my wife Pınar.

ABSTRACT

PREDICTION OF DYNAMIC FORCE CHARACTERISTICS OF RADIAL TIRES USING FINITE ELEMENT AND EXPERIMENTAL TECHNIQUES

A tire is one of the most important components of a vehicle. To predict its dynamic force characteristics, a detailed finite element model is constructed. In the finite element analysis of the tire, nonlinear stress-strain relationship of rubber, the reinforcements of the tire and contact between the tire and ground are modeled. First, a static tire model is constructed. Its vertical force-deflection characteristics on a surface with and without cleat and the pressure distribution over the cross section are obtained. Then, dynamic force characteristics of the tire are predicted. In the dynamic analysis of the tire, lateral and vertical force characteristics are examined, tire enveloping characteristics at low speed are investigated.

Experimental studies are performed to validate finite element model results. All experiments are conducted using the Flat-bed Tire Test Machine at the University of Michigan Transportation Research Institute (UMTRI). Model and experimental results are compared to each other and it is concluded that to some extent, there is a good correlation between them. Error tables are also given to show the accuracy range of the proposed model.

ÖZET

RADYAL LASTİKLERİN SONLU ELEMANLAR VE DENEYSEL TEKNİKLER KULLANILARAK KUVVET KARAKTERİSTİĞİNİN BELİRLENMESİ

Lastik, aracın en önemli parçalarından biridir. Bu çalışmada lastiğin dinamik kuvvet karekteristiğini belirlemek için, detaylı sonlu elemanlar modeli oluşturuldu. Sonlu elemanlar analizinde kauçuğun lineer olmayan gerilim-birim uzama ilişkisi, lastiğin katmanları ve lastik ile yer arasındaki kontak modellendi. Öncelikle, statik lastik modeli oluşturulup, engelli ve engelsiz yüzey üzerinde lastiğin düşey kuvvet-çökme karekteristiği ve kesitteki iç basınç dağılımı elde edildi. Daha sonra, lastiğin dinamik kuvvet karekteristiği belirlendi. Lastiğin dinamik kuvvet analizinde yanal ve düşey kuvvet karekteristiği ile lastiğin düşük hızlarda engelleri aşma özelliği (enveloping) araştırıldı.

Sonlu elemanlar metodu ile elde edilen sonuçları kıyaslamak ve geçerlilik alanını belirlemek için, deneysel çalışmalar yapıldı. Bütün deneylerde Michigan Üniversitesi Taşımacılık Araştırma Enstitüsü'nde mevcut düz yüzeyli lastik test makinası kullanıldı. Model ve deneysel sonuçlar birbirleri ile kıyaslanıp bir dereceye kadar her iki sonuç arasında yeterli uyum olduğu sonucuna varıldı. Önerilen modelin doğruluk derecesini göstermek için hata tabloları verildi.

TABLE OF CONTENTS

LIST OF FIGURES

LIST OF TABLES

LIST OF SYMBOLS/ABBREVIATIONS

c_z	Vertical unit rate
C_s	Longitudinal stiffness
f	The force per unit distance
F	Lateral force
F_x	Longitudinal (Tractive) force
F_y	Lateral force
F_z	Vertical force
F_C	Cornering force
F_D	Drag force
F_Z	Normal load
k	Lateral stiffness per unit width
k	Empirical deformation coefficient
K_x	Longitudinal spring constant
K_y	Lateral spring constant
l	Contact patch length
l_0	Contact patch length
l_a	Length of the adhesion region from the front extremity to the breakaway point
l_1	Length of the effective area of application of lateral force
l_n	Normalized contact patch length
L	Normal load
M	Self-aligning moment
M_x	Overturning moment
M_y	Rolling resistance moment
M_z	Self-aligning moment
p	Pressure distribution
P	Normal pressure (Contact pressure)
P_{max}	Maximum normal pressure
P_r	Residual pneumatic scrub

$P_{s,m}$	Pneumatic scrub by direct measurement
$P_{s,s}$	Pneumatic scrub by simple model
P_H	Horizontal contact patch force
P_V	Vertical contact patch force
$q(\phi, t)$	Radial tread force component
Q	Camber force
r	Tire static radius
r_1	Tread radius
R_e	Rolling tire radius
R_L	Tire static radius
s	Contact patch width
$s(\phi, t)$	Tangential tread force component
S_s	Absolute value of slip ratio
S_{sc}	Critical slip ratio
S_α	Absolute value of lateral slip ratio due to slip angle
S_γ	Absolute value of lateral slip ratio due to camber angle
$S_{\alpha\gamma}$	Combined slip ratio due to both slip and camber angle
$S_{s\alpha\gamma}$	Resultant slip ratio
t	Time
v	Traveling velocity of a wheel
V	Circumferential velocity of a wheel
V_c	Circumferential velocity of the tire tread base
V_x	Road velocity in longitudinal direction
V_y	Road velocity in lateral direction
V_R	Road velocity
w	Contact patch width
z_{max}	Maximum vertical deflection
α	Slip angle
β	The angle of slip velocity with respect to the longitudinal axis
β	Elastic trail angle
γ	Camber angle

θ	Slip angle
ϕ	Angular measure in tire plane
ΔV	Slip velocity
σ	Stress
μ	Coefficient of friction
ν_x	Coefficient of friction in longitudinal direction
ν_y	Coefficient of friction in lateral direction
Ω	Wheel spin velocity
ζ_{zz}	Vertical stiffness coefficient
ϵ	Elastic trail coefficient

ADAMS	Automated Dynamics Analysis of Mechanical Systems
ASTM	American Society for Testing & Materials
BFC	Braking Force Coefficient
CPU	Central Processing Units
DOF	Degree of Freedom
FEM	Finite Element Method
FFT	Fast Fourier Transform
fps	Foot per second
HVE	Humans, Vehicles & Environments
ISO	International Standards Organization
MATLAB	Matrix Laboratory
MSS	Multibody System Dynamics
MTTM	Mobile Tire Testing Machine
N/A	Not applicable
NHTSA	National Highway Traffic Safety Administration
OD	Outer diameter
OTM	Overturning Moment
PSD	Power Spectral Density
REBAR	Reinforcement bars
SAE	Society of Automotive Engineers

SFC	Sideway force coefficient
TIRF	Tire Research Facility
TÜBİTAK	Scientific and Technological Research Council of Turkey
UMTRI	University of Michigan Transportation Research Institute

1. INTRODUCTION

1.1. Pneumatic Tire

A tire is the connecting link between the vehicle and the ground. A through understanding of the tire behavior is an important part of the vehicle dynamic analysis.

In this chapter, components of a tire, its functions, tire designations and tire materials are discussed briefly. Also, tire models available in literature are presented with their basic concepts, formulations and results.

1.1.1. Tire Materials and Their Requirements

Pneumatic tires are made of cord-rubber materials in which the low-modulus, high-elongation rubber contains air and provide abrasion resistance and road grip and the high-modulus, low-elongation cords provide reinforcement for rubber and carry most of the load acting on a tire. There are many different rubber compositions to fulfill requirements of tire in service. Nylon, polyester, steel, fiberglass and Kevlar are, on the other hand, the most commonly used cord materials. In the past, cotton and rayon were used as well. Requirements for rubber compounds are given following [1]. Rubber in the tread compound requires the abrasion resistance, wet and dry skid resistance and crack growth resistance and also showing low hysteresis. Undertread rubber material requires bonding well to the cord-rubber composite making up the carcass or body of the tire and showing low hysteresis. Requirements of the sidewall part of the tire are good fatigue life, resistance to oxygen and ozone attack and good molding properties. Carcass coat stock rubber material requires good flow, adhesion and fatigue properties and showing low hysteresis. Bead filler and rubber compound in the bead area, on the other hand, requires high modulus and good adhesion properties. Rubber compound in innerliner part of the tubeless tires requires good flex resistance, molding with no imperfections and also having low air permeability.

1.1.2. Tire Components and Construction Types

All modern tires have a number of elements in common regardless of their constructions. As shown in Figure 1.1, a typical radial pneumatic tire consists of several different components.

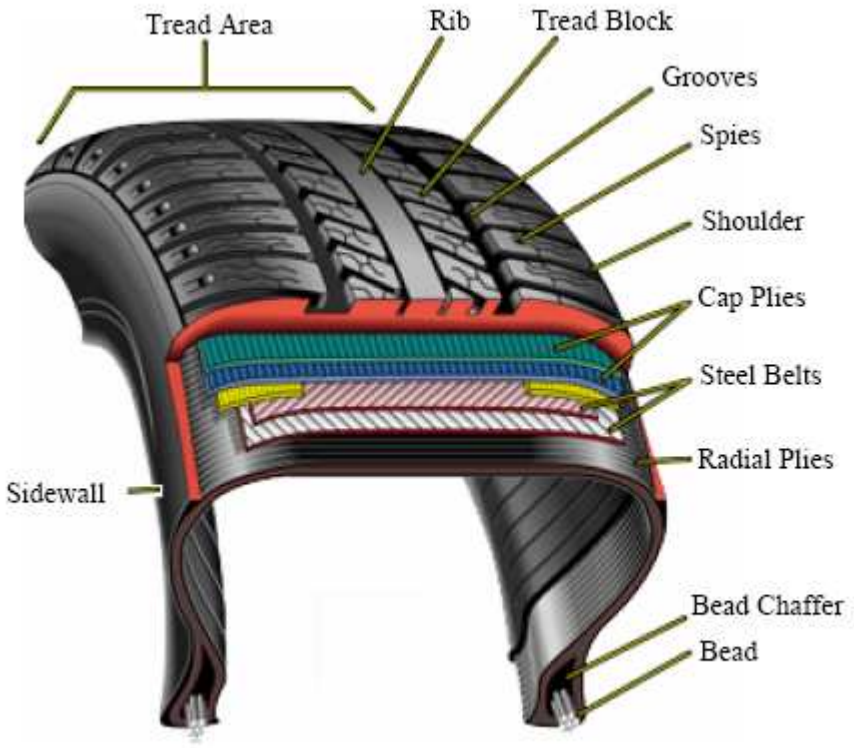

Figure 1.1. Components of a tire [2]

The tread is the outermost part of the tire. While tread designs vary greatly, there are common components in all tread patterns. The tread block grips at its leading and trailing edge. Within each block, there are sipes to provide additional traction. The grooves built into the tread pattern are designed to channel away water. Ribs are the parts of a tire tread pattern created by grooves that run circumferentially around the tire. The sidewall is the portion of the tire between beads and the tread. It is a protective rubber coating on the outer side of the tire and designed to resist cutting, scuffing and cracking. The shoulder is the upper portion of the sidewall below the tread edge and affects tire's thermal behavior and cornering characteristics. Cap plies are optional parts of a tire and placed under the tread. They are included to enhance

cornering and stability at high speeds, and at the same time, to reduce heat. Body plies running from bead to bead are the components restricting the pressure which carry the load and they transmit forces and moments from belts to rim. The belts are layers of steel cords placed between tread and body plies. They increase the rigidity of the tread and provide directional control and stability. They are also protective layers against impacts and punctures. The bead consists of high tensile strength steel wire strands formed into hoops. The wires are wrapped around the bead and they keep the tire assembly on the rim of the wheel. The Chafer consists of narrow strips of material around the outside of the bead that protect the cord against wear and cutting by the rim, distributes flex above the rim, and prevents dirt and moisture from getting into the tire [2].

There are two basic types of tire constructions: Cross-ply and Radial tires. Today, nearly all tires are radial tires. In the cross-ply construction, cords run diagonally across the tire at an angle of 30 to 40 degree with the tread centerline and there are no tread plies. In addition to body plies, bias-belted tire has two or more belt plies. Radial construction is characterized by parallel plies (referred to as carcass) running directly across the tire from bead to bead at a 90-degree angle to the circumference. This construction makes for an extremely flexible sidewall and a soft ride but provides little directional stability. This deficiency is eliminated by adding steel belt plies. The ply rating is usually 2-4 for passenger cars. In this construction, the tread and sidewall function independently from each other. The benefits of radial tire technology can be listed as follows: Longer tire life, resistance to cuts, punctures and tears, better traction, improved handling and fuel economy and smooth ride and operator comfort.

Regardless of tire construction, all tires must satisfy a basic set of functions [3];

- Provide load-carrying capacity
- Provide cushioning and dampening
- Transmit driving and braking torque
- Provide cornering force
- Provide dimensional stability

- Resist abrasion
- Generate steering response
- Have low rolling resistance
- Provide minimum noise and minimum vibration
- Be durable throughout the expected life span

1.1.3. Tire Forces and Moments

All forces and corresponding moments acting on the vehicle, with the exception of aerodynamic and gravitational forces, result from tire-ground interaction. To construct reliable and accurate vehicle models, tire forces and moments should be well modeled and understood.

There are three force and three moment components: Longitudinal, lateral and normal forces are the resultant force components; overturning, self-aligning and rolling resistance moments are the moment components acting on the tire. To describe tire forces and moments Society of Automotive Engineers (SAE) has defined the axis system as shown in Figure 1.2. Wheel plane is the central plane of the tire normal to the axis of rotation (spin axis). Wheel center is the intersection of the spin axis and the wheel plane. Center of tire contact is defined as the intersection of the wheel plane and projection of the spin axis onto the road plane. On the other hand, longitudinal force is the component of the force acting on the tire by the road in the plane of the road and parallel to the intersection of the wheel plane with the road plane. Lateral force is the component of force acting on the tire by the road and normal to the intersection of the wheel plane with the road plane. Normal force is the component of the force acting on the tire by road which is normal to the plane of the road. Vertical load is defined as the negative of the normal force, and is positive in magnitude. Overturning moment is the moment acting on the tire by the road in the plane of the road and parallel to the intersection of the wheel plane with the road plane. Rolling resistance moment,or rolling moment, is the moment acting on the tire by the road in the plane of the road and normal to the intersection of the wheel plane with the road plane. Aligning torque or self aligning moment is the moment acting on the tire by the road which is normal

to the plane of the road. In addition to these, there are two important angles of the tire terminology: slip and camber angle. Slip angle is the angle between the direction of wheel heading and the direction of travel. Positive slip angle corresponds to a tire moving to the right as it rolls in the forwards direction. Camber angle is the angle between the wheel plane and the vertical axis. Positive camber angle occurs when top of wheel leans outward from vehicle [4].

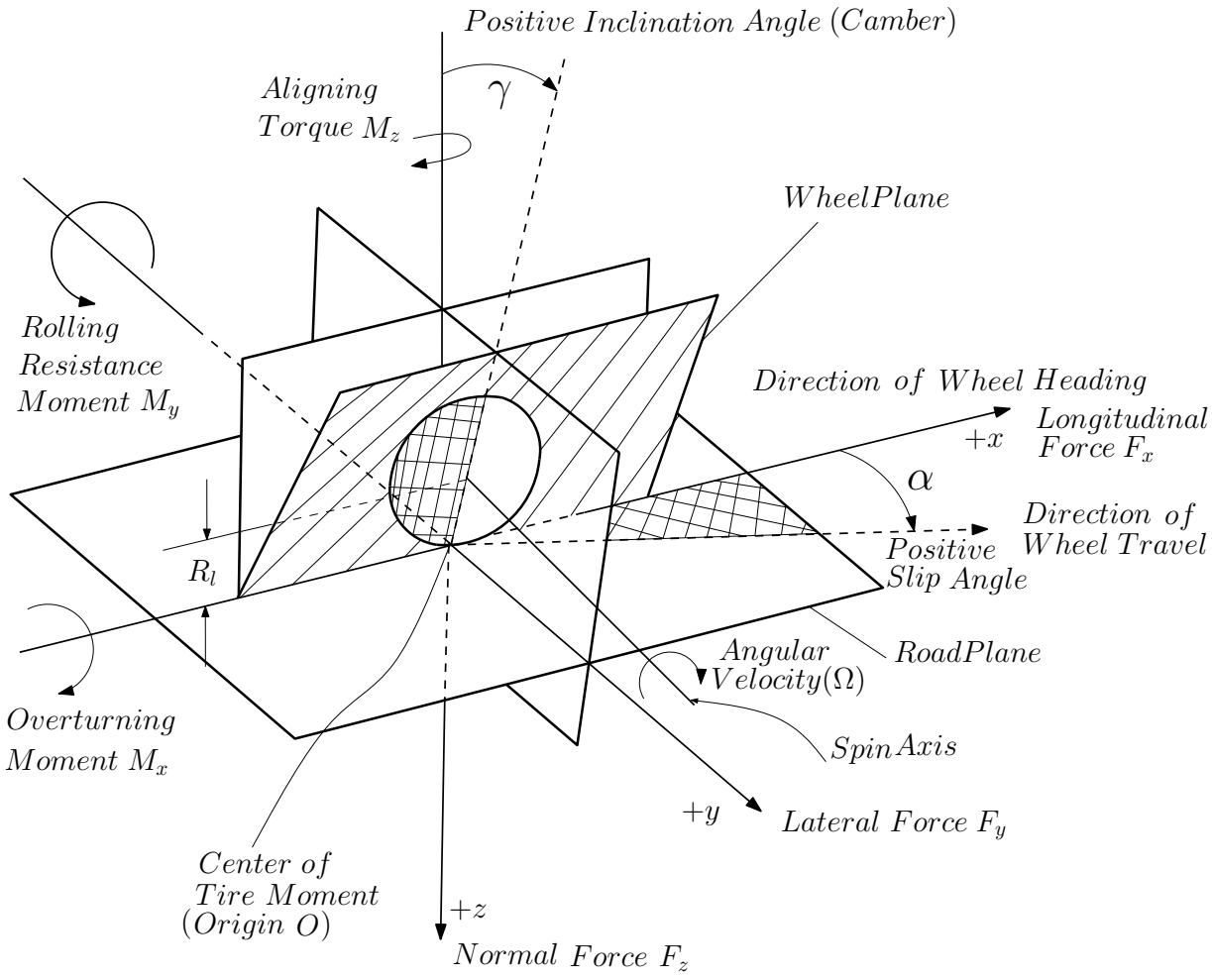

Figure 1.2. SAE tire axis system

On the other hand, tire dynamics can be classified into three groups: Ride, handling and performance. Ride quality is related to vertical force or normal force. Handling behavior of the vehicle, which is related to directional control and stability, refers to lateral force characteristics of the tire. Vehicle performance is, on the other hand, related to longitudinal characteristics of the tire i.e., tractive or braking force variations.

1.1.4. Tire Designations

Main geometric tire and rim properties such as tread width, section height, rim diameter and outer rim diameter are shown in Figure 1.3. In addition, the following definitions are given: Free radius is defined as the radius of the tire/wheel assembly that is not deflected under load and loaded radius is defined as the distance from wheel axis of rotation to supporting surface at a given load and stated inflation pressure. Deflection is defined as the free radius minus loaded radius. Loaded section height is defined as the loaded radius minus half of the nominal rim diameter or the distance from rim seat to outer tread surface of a loaded tire. Nominal rim diameter is the diameter of rim seat supporting the tire bead and overall diameter is the diameter of the inflated tire without any load. Overall width is, on the other hand, the maximum width in cross section of unloaded tire and rim width is the linear distance between rim flanges in contact with the tire. Section height is the distance from rim seat to outer tread surface, section width is the distance between the outside sidewalls of an inflated tire (both measured when the tire is unloaded). Tread width is the portion of the tread design which comes in contact with the road [5].

Tire designation gives information such as tire size, maximum speed rating and the load capacity. There are different types of tire designations. International Standards Organization (ISO) has defined the automobile tire designation that is shown in Figure 1.4. In this figure, aspect ratio is given in percent which is the ratio of section height to section width times 100. Load rating refers to load and inflation limits of specified tire and load symbol indicates load capacity of the tire. The speed rating is the maximum service speed of a passenger car tires. Both load and speed rating represent the tire's service description and their descriptions are specified in tables by tire manufacturers. Tire company name, production date, maximum inflation pressure and loads for safe driving are some information given on sidewall of tires.

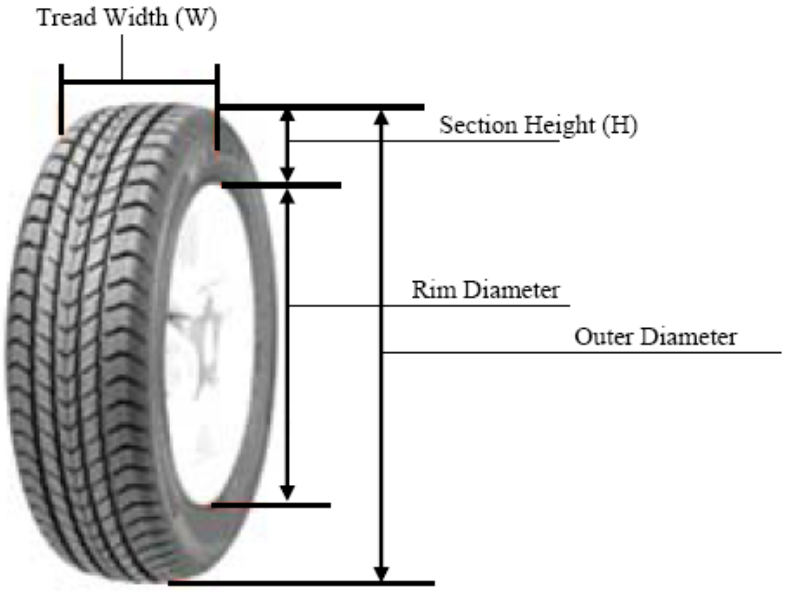

Figure 1.3. Tire geometry [5]

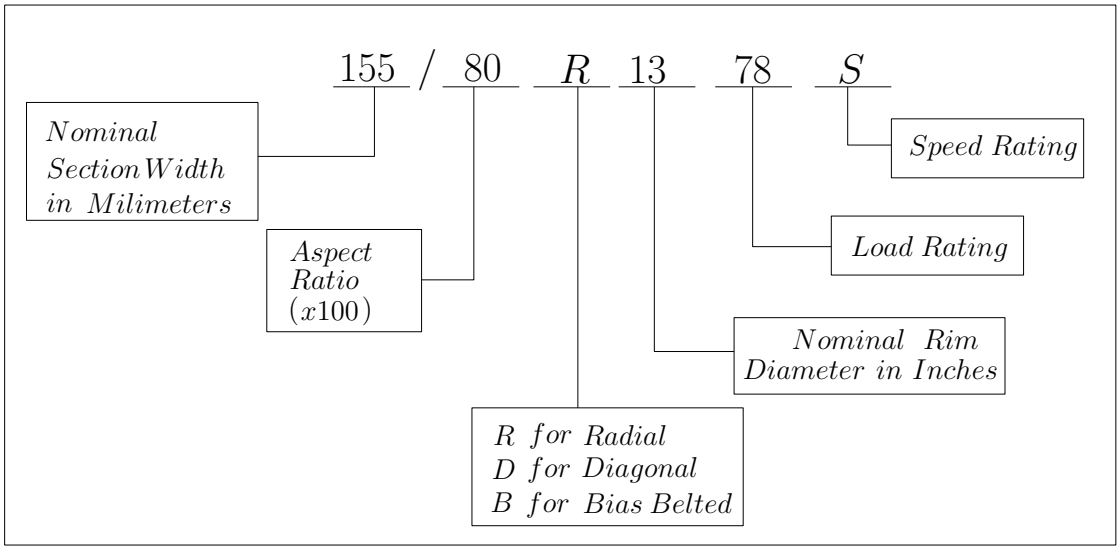

Figure 1.4. Automobile tire designation for radial tires

1.2. Tire Models

Tire models in literature can mainly be classified in two groups: static and dynamic tire studies. Pressure distribution, vertical stiffness and stresses are calculated in static tire analysis. Dynamic analysis of a tire consists of steady-state and transient parts. In dynamic analysis, there exist mainly three groups: Ride, handling and performance. Analysis of noise and vibration of a tire and durability are other research areas of dynamic analysis. Impact analysis can also be added as another interesting area of tire dynamic analysis.

To model tires, there exist three approaches: Analytical models, experimental models and finite element models. The tire, under service conditions, encounters large rotations and displacements. Its thick carcass structure allows significant shear deformations. Rubber shows geometrically and materially nonlinear behavior. All these factors make accurate analytical tire modeling extremely difficult. To get closed form solutions, there is need to make simplifications (i.e., simplifications in contact shape and its dimensions, pressure distribution on the contact patch, etc). As a result of simplifications, one can not handle tire behavior in detail. Experiments are carried out on either real road conditions or in-door test laboratories. Empirical models are obtained using experimental results and they represent tire behavior very well. However, some parameters are not obvious and extensive experiments are required. Both empirical and experimental techniques are expensive and require long time. To investigate effects of parameters such as inflation pressure on tire response, additional experiments are needed, which in turn lead to higher cost and analysis time. Finite element methods are, on the other hand, efficient numerical techniques to deal with tire analysis. A tire can be represented by using appropriate material and physical laws, boundary conditions and physical laws which result in nonlinear equations.

In this section, analytical models, empirical models, experimental studies and finite element models available in literature are examined in detail. Solution techniques, assumptions, and finite element programs used are mentioned. Results of the studies are reported.

1.2.1. Analytical Models

Both radial and bias-ply tires are examined analytically. The main aim of these studies is to investigate the force and moment characteristics of the tires with less efforts and within the shortest time. Since they are in closed form, analytical models can be used directly in vehicle dynamics equations. However, as mentioned before, to get closed form solution, there is a need to make some simplifications. All tire forces and corresponding moments phenomena take place in the small area between tire and road surface, namely, contact patch. For example, contact patch area and normal pressure distribution over footprint are important parameters for the generation of shear force in this zone. In literature, there are different assumptions for contact patch geometries and normal pressure distributions. General review of the literature in terms of these parameters are given in Table 1.1. It is noted that in general, normal pressure distributions in lateral (among the contact patch width) direction is taken to be uniform. However, there are different models for the pressure distribution in the longitudinal direction.

Table 1.1. Contact patch area shape and normal pressure distribution assumptions in literature

Year	Authors	Contact patch area	Normal pressure distribution
1954	Fiala [6]	Rectangular	Cubic parabola
1961	Bergman [7]	Rectangular	Parabolic
1969	Livingston & Brown [8]	Rectangular	Rectangular, parabolic and elliptical
1970	Dugoff et al. [9]	Rectangular	Rectangular
1977	Bernard et al. [10]	Rectangular	Symmetrical trapezoidal
1981	Sakai [11]	Rectangular	Parabolic
1983	Singh et al. [12]	Rectangular	Rectangular
1990	Gim & Nikravesh [13]	Rectangular	Parabolic
1993	Sjahdanulirwan [14]	Rectangular	Unsymmetrical trapezoidal
1995	Sjahdanulirwan & Yang [15]	Rectangular	Unsymmetrical inverted boat shaped
1997	Gupta & Goel [16]	Elliptical	Symmetrical trapezoidal
2004	Ramji et al. [17]	Combination of rectangular and part of circles at the edges	Symmetrical trapezoidal
2006	Shifrin [18]	Rectangular	Parabolic

It is important to note that, in reality, contact patch dimensions or shapes are mostly dependent on tire operation conditions. Contact patch geometry is related to some factors such as vertical load, inflation pressure and tire structure. Zegelear [19] proposed an elliptical shape for the contact patch area varying from oval to rectangular. He further defined an effective contact area as a rectangle with area and width proportion determined by measurements. He tabulated both actual and effective contact patch areas for different vertical loads on both drum and flat surface. Friction plays a more important role controlling the force characteristics of the tires. Friction between tire and road is very complex. Therefore, the "friction coupling" term is used in literature instead of using friction coefficient. It depends on many factors such as normal load, tire size, tire tread pattern, tire tread material, road surface conditions, slip and slip velocity. In general, the friction coupling is taken to be a function of slip or slip velocity, vertical load, and the friction coefficients at zero slip or slip velocity.

Livingston and Brown [8] investigated lateral force and self-aligning moment properties of tires considering pure slip angle and three different pressure distributions; Uniform, elliptical and parabolic. Wheel slip occurs if its traveling velocity is different form its longitudinal velocity. Slip is a result of deformation of the tire in the footprint area. Longitudinal slip is associated with the development of the tractive or braking force while lateral or side slip is associated with cornering force. The schematic diagram of a wheel (tire) in a right turn is shown in Figure 1.5. In this figure, v is the traveling velocity tangent to the path at a slip angle θ to the circumferential velocity V, ΔV is the slip velocity, F is the lateral force, with cornering component F_C and drag component F_D. Drag force can be called as the negative tractive force in traveling direction. While cornering force is perpendicular to traveling direction, drag force is parallel to traveling direction.

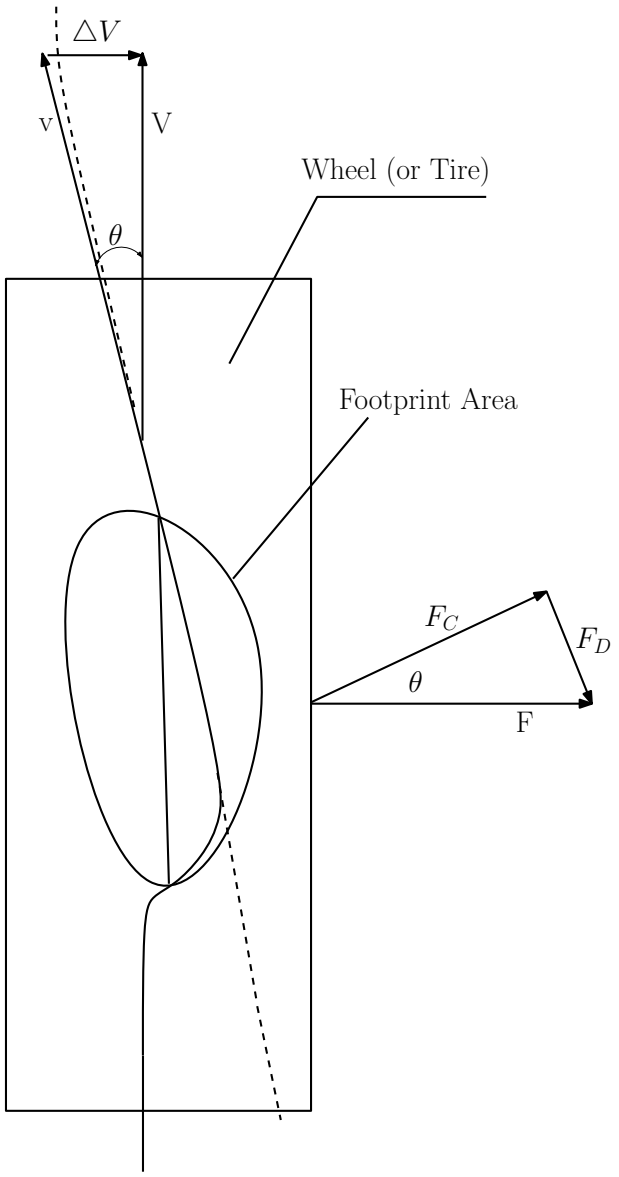

Figure 1.5. Schematic diagram of a wheel (or tire) in a right turn [8]

The path of an element in the contact region is shown in Figure 1.6 in which element deflection is shown against its distance x through contact, l is the contact length and a is the point at which the linear adhesion region of slip ends, and the region of sliding relative to ground begins. As the element slips to the side, away from centerline, the restoring force due to the lateral rigidity of the wheel increases until a point is reached in which the side deflection can no longer be sustained by the friction force. Then, sliding begins and the element returns back to midplane in consistence with maximum frictional force, and finally joins the midplane.

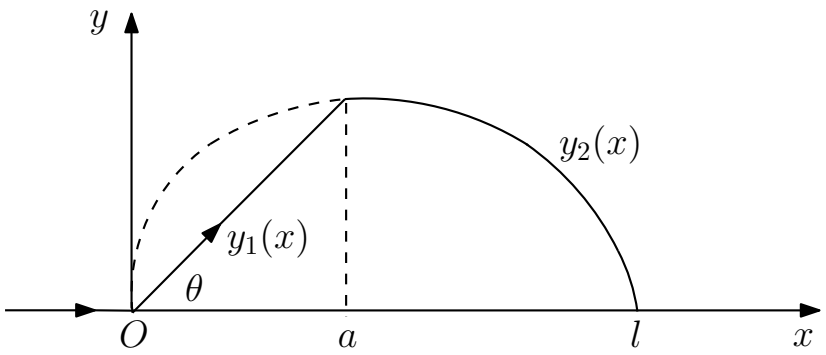

Figure 1.6. Enlarged diagram of the deflection path of an element in the contact region, placed on a coordinate system. The pressure distribution is elliptical [8]

The lateral force F can be calculated by summing the forces on all deflected elements in the contact area.

$$F = \int_0^l f(x)dx \tag{1.1}$$

in which $f(x)$ is the force per unit distance along x on a section of the circumference taken through the contact width w, perpendicular to x. If the wheel is assumed to be a thin disk and each element considered independent of the others, then the deflection across any section at x can be considered as uniform. So, for the small deflections, the force density can be calculated by a simple law as,

$$f(x) = wky(x) \tag{1.2}$$

where k is the lateral stiffness per unit width and unit distance along x with the dimensions of force divided by distance cubed. The path in the adhesion region is straight line at the angle θ and deflection is

$$y_1(x) = (tan\theta)x. \qquad 0 \leq x \leq a \tag{1.3}$$

Then, Equation 1.2 becomes,

$$f(x) = (wktan\theta)x \qquad 0 \leq x \leq a \tag{1.4}$$

In the sliding region, the force is determined by the pressure distribution, $p(x)$ averaged across the width, and the coefficient of friction μ,

$$f(x) = w\mu p(x) \qquad a \leq x \leq l \tag{1.5}$$

using Equation 1.2, deflection in the sliding region can be calculated as,

$$y_2(x) = (\mu/k)p(x). \qquad a \leq x \leq l \tag{1.6}$$

At point a, the force satisfies Equations 1.4 and 1.5 and a can be obtained using them as follows:

$$(ktan\theta)a = \mu p(a). \tag{1.7}$$

Substituting Equations 1.4 and 1.5 into Equation 1.1 and assuming constant contact width, the following general lateral force equation is obtained:

$$F = (\frac{1}{2}wktan\theta)a^2 + \mu w \int_a^l p(x)dx. \tag{1.8}$$

The corresponding moment about the vertical axis (self-aligning torque) at the center of contact is obtained from the following equation:

$$M = \int_0^l (x - \frac{l}{2})f(x)dx. \tag{1.9}$$

Evaluating the integral considering two separate regions: adhesion and sliding

region, and gives the general moment equations as follows:

$$M = (\frac{1}{3}wktan\theta)a^3 + \mu w \int_a^l xp(x)dx - \frac{1}{2}lF. \tag{1.10}$$

After deriving general lateral force and aligning moment equations given by Equations 1.8 and 1.10, respectively, Livingston and Brown calculated lateral force and self-aligning torque for three different pressure distributions, namely uniform, elliptical and parabolic.

In the first case, pressure is constant over the contact length as follows:

$$p(x) = \frac{L}{wl} \tag{1.11}$$

and using Equation 1.6, deflection in the sliding region becomes

$$y_2(x) = \frac{\mu L}{wkl} \tag{1.12}$$

in which L is the normal load. As seen from this equation, deflection in the sliding region is constant and deflections over the contact patch are illustrated in the Figure 1.7.

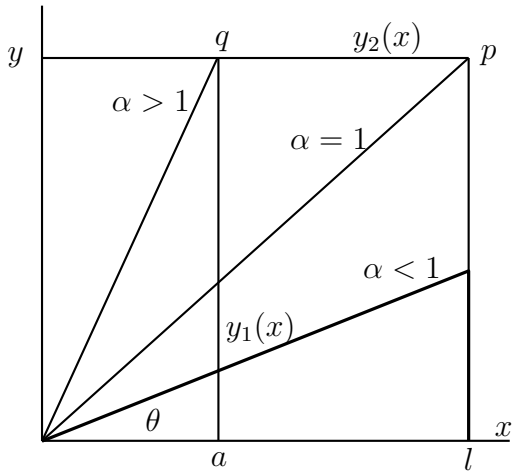

Figure 1.7. Deflection diagram for the uniform pressure distribution at small, critical, and large angles [8]

As seen in Figure 1.7, for small θ values there is no sliding region and $a = l$ until θ is larger than $arctan(\mu L/wkl^2)$. For this case, F and M values can be obtained using Equations 1.8 and 1.9 and setting $a = l$. Then, one gets the following equations for constant pressure

$$F = \frac{1}{2} wkl^2 tan\theta \tag{1.13}$$

and

$$M = \frac{1}{12} wkl^3 tan\theta. \tag{1.14}$$

The reduced variable α is defined as

$$\alpha \equiv \frac{wkl^2 tan\theta}{\mu L} \tag{1.15}$$

and its physical limits correspond to θ values at which the pressure drops to *zero*, $\theta = 0, \frac{\pi}{2}$, so that α varies from 0 to ∞. At the critical value of $\theta = \mu L/wkl^2$, α is unity. Therefore, Equations 1.13 and 1.14 can be rewritten as

$$\frac{F}{\mu L} = \frac{1}{2\alpha} \qquad 0 \leq \alpha \leq 1 \tag{1.16}$$

and

$$\frac{M}{l\mu L} = \frac{1}{12\alpha} \qquad 0 \leq \alpha \leq 1 \tag{1.17}$$

Beyond α = unity, a rectangular region (apql) is added. Substituting Equation 1.11 into 1.8 and 1.9 and using Equation 1.7 for a, one gets the following equations:

$$\frac{F}{\mu L} = 1 - \frac{1}{2\alpha} \qquad 1 \leq \alpha \leq \infty \tag{1.18}$$

and

$$\frac{M}{l\mu L} = \frac{1}{4\alpha} - \frac{1}{6\alpha^2} \qquad 1 \leq \alpha \leq \infty \tag{1.19}$$

Using Equations 1.16 - 1.19, reduced lateral force and aligning moment versus slip variable α are replotted and given in Figures 1.8.

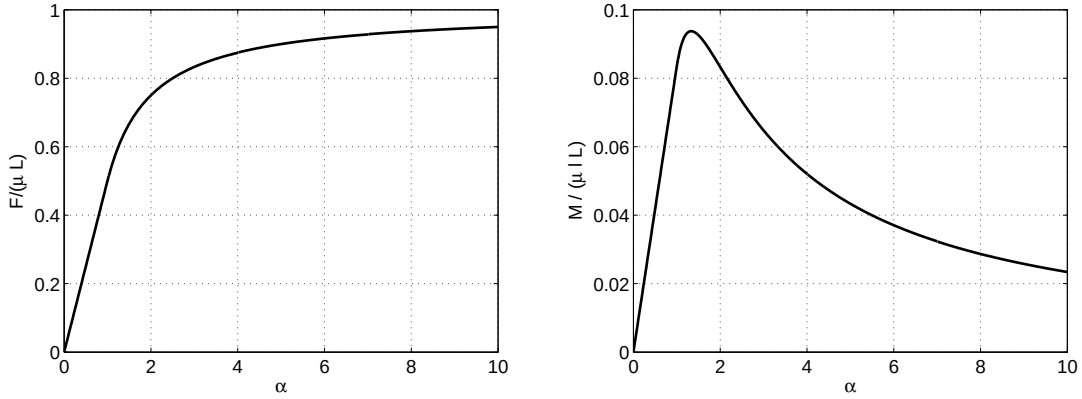

Figure 1.8. Reduced lateral force and aligning torque for uniform pressure distribution

For the second case, Livingston and Brown assumed an elliptical pressure distribution as given below.

$$p(x) = \frac{8L}{\pi w l^2}\sqrt{lx - x^2} \tag{1.20}$$

and from Equation 1.6, one gets y_2 as shown below:

$$y_2(x) = \frac{8\mu L}{\pi w k l^2}\sqrt{lx - x^2}. \tag{1.21}$$

Inserting $p(a)$ into Equation 1.7 yields

$$\alpha = \frac{1}{\beta^2 + 1} \tag{1.22}$$

where

$$\beta = \frac{\pi w k l^2 tan\theta}{8\mu L}. \tag{1.23}$$

Substituting Equation 1.22 into 1.20 yields

$$p(a) = \frac{8L}{\pi w l}[\frac{\beta}{\beta^2 + 1}] \tag{1.24}$$

where a is a function of θ and takes values between 0 and l while θ takes values between 0 and $\frac{\pi}{2}$. The pressure must be zero at these points and the physical limit of β is $0 \leq \beta \leq \infty$.

Finally, substituting Equation 1.20 into Equations 1.8 and 1.9 and using Equations 1.22 and 1.23, one gets the following equations:

$$\frac{F}{\mu L} = (\frac{1}{\pi})\{[\frac{2\beta}{(1+\beta^2)}] + arcsin[\frac{2\beta}{(1+\beta^2)}]\} \qquad 0 \leq \beta \leq \infty \tag{1.25}$$

and

$$\frac{M}{l\mu L} = \frac{(\frac{2}{3\pi})\beta}{(1+\beta^2)^2} \qquad 0 \leq \beta \leq \infty \tag{1.26}$$

Using Equations 1.25 and 1.26, reduced lateral force and aligning moment versus slip variable β are replotted and given in Figures 1.9.

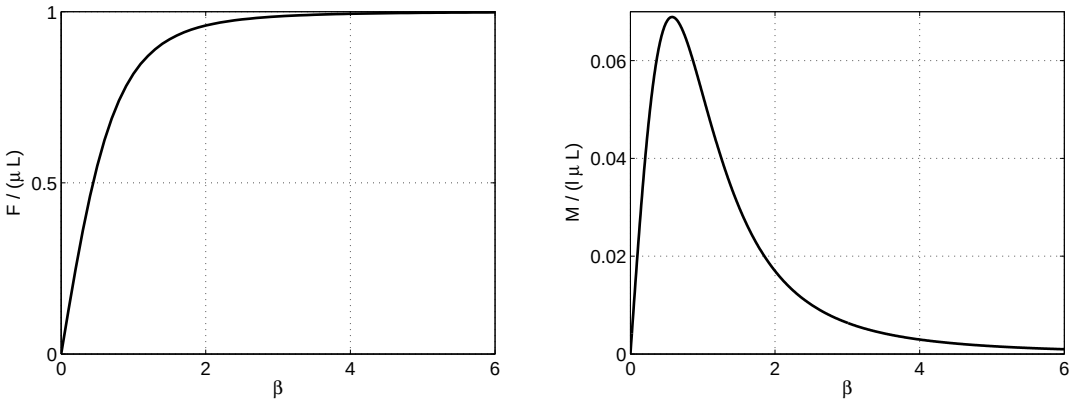

Figure 1.9. Reduced lateral force and aligning torque for elliptical pressure distribution

For the final case, Livingston and Brown assumed a parabolic pressure distribution as shown below and in Figure 1.10.

$$p(x) = (\frac{6L}{wl^3})(lx - x^2) \tag{1.27}$$

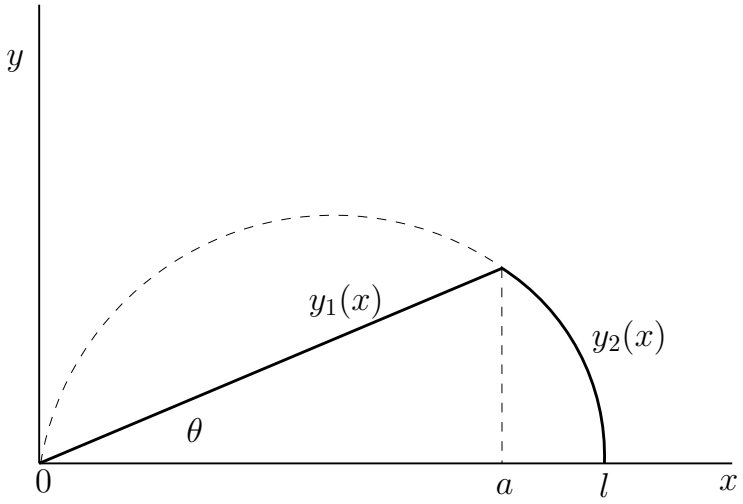

Figure 1.10. Deflection diagram for the parabolic distribution [8]

From Equations 1.27 and 1.7, a is obtained as

$$a = l(1 - \gamma) \tag{1.28}$$

where

$$\gamma = \frac{wkl^2 tan\theta}{6\mu L} \tag{1.29}$$

Then, using Equation 1.27 gives

$$p(a) = (\frac{6L}{wl})\gamma(1-\gamma) \tag{1.30}$$

The physical limits of γ are $0 \leq \gamma \leq 1$, corresponding to $0 \leq \theta \leq arctan(6\mu L/wkl^2)$. At the upper limit, no further force is obtained with increasing θ. Substituting Equations 1.28 and 1.29 into 1.8 and 1.9 give the following reduced lateral force and aligning torque equations

$$\frac{F}{\mu L} = 1 - (1-\gamma)^3 \qquad 0 \leq \gamma \leq \ 1 \tag{1.31}$$

and

$$\frac{M}{l\mu L} = \frac{1}{2}\gamma(1-\gamma)^3 \qquad 0 \leq \gamma \leq \ 1 \tag{1.32}$$

Using Equations 1.31 and 1.32, reduced lateral force and aligning moment versus slip variable γ are plotted in Figure 1.11. In addition, theoretical results are compared with experimental results [8]. Elliptical and parabolic pressure distributions fit well with the experimental data obtained from vehicle tests. Parabolic pressure distribution gives better results when compared to experimental data obtained from a laboratory cornering drum.

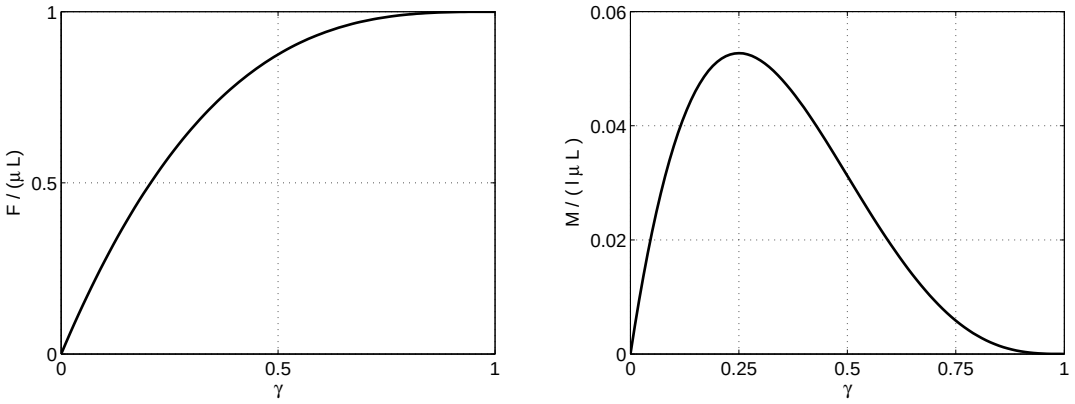

Figure 1.11. Reduced lateral force and aligning torque for parabolic pressure distribution

In a similar fashion, Gim and Nikravesh presented a series of an analytical study consisting of three subsequent papers. In the first study [13], they examined tire forces and moments for pure slip conditions. The term "pure slip" refers to either pure slip ratio, pure slip angle or pure camber angle due to nonzero value the slip ratio, slip angle or camber angle, respectively. In the second study [20], they considered combined slip with nonzero value of the slip ratio, slip angle and camber angle. Finally, they verified their theoretical tire model with experimental studies [21]. In the analytical model, they considered the tire as a series of three-dimensional deformable elements transmitting forces in radial, longitudinal and lateral directions. Each tire element is modeled by three elementary springs whose axes of symmetry are perpendicular to each other.

In the first study, the contact patch is assumed to be rectangular as shown in Figure 1.12a. l is the contact patch length, w is the contact patch width, δ and ρ_1 are the radial deformation and tire radius, respectively. They also assumed that the radial deformation of a tire is small relative to the undeflected radius. That is, $\delta << \rho_1$.

To express the elastic deformation and stress of a tire during braking or traction, the road coordinate system or the carcass coordinate system is used, namely, ξ and η, respectively. The former is along the longitudinal and the latter is along the lateral direction of the wheel. The origin of the these axes is located at the front extremity

of the contact patch length and at the center of contact patch width, so they provide the absolute values of the tire force and moment which can be transformed into the $xyz-$ coordinate system fixed to the wheel center. In the derivation, it is assumed that the tire center does not travel, instead the road moves with respect to the wheel center. The contact pressure P is shown in Figure 1.12a, it is assumed that its average value over the contact patch width has a parabolic distribution in the circumferential direction and is given in Equation 1.33

$$P = \frac{4P_{max}}{l}\xi(1 - \frac{\xi}{l}) \tag{1.33}$$

in which the $\xi-$ axis represents the longitudinal displacement of the tire and P_{max} the maximum value of the contact pressure distribution at $\xi = \frac{l}{2}$.

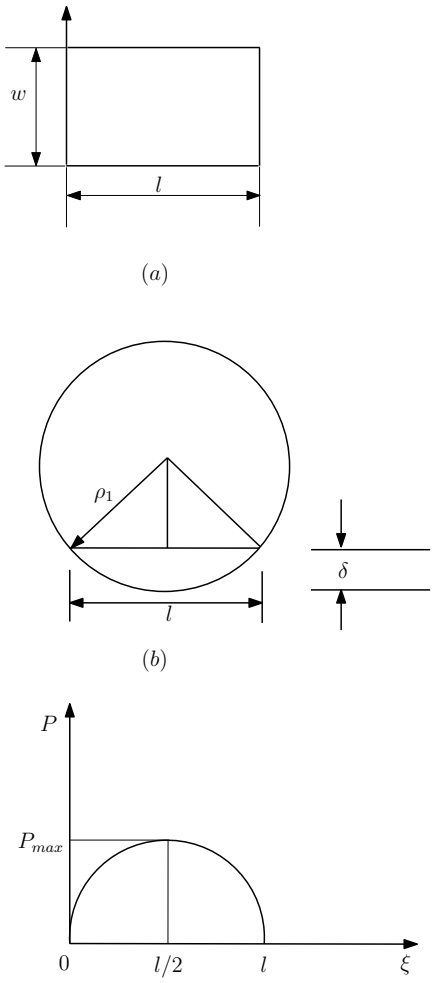

Figure 1.12. (a) Contact patch, (b) Radial deformation, (c) Parabolic distribution of contact pressure [13]

The road velocity (V_R) has two components V_x and V_y as shown below.

$$V_x = V_R \, cos\alpha, \tag{1.34}$$

$$V_y = V_R \, sin\alpha, \tag{1.35}$$

in which α (slip angle) is

$$\alpha = arctan(\frac{V_y}{V_x}). \tag{1.36}$$

The slip velocity between the tire and the road is expressed as

$$V_s = [(V_x - V_C)^2 + V_y^2]^{\frac{1}{2}} \tag{1.37}$$

where V_C is the circumferential velocity of the tire tread base. The directional angle of slip velocity with respect to the tire longitudinal axis (wheel plane axis) is defined as

$$\beta = arcsin(\frac{V_y}{V_x}) \tag{1.38}$$

The longitudinal slip ratio s, the absolute value of slip ratio (S_s), the absolute value of the lateral slip ratio (S_α) due to the slip angle, the absolute value of the lateral slip ratio due to the camber angle (S_γ), the absolute value of combined slip ratio and camber angle and resultant slip ratio due to the slip ratio, slip angle and camber angle are defined in the following equations.

$$s \equiv \begin{cases} \frac{V_x - V_C}{V_x} > 0 & \text{for braking} \\ \frac{V_x - V_C}{V_x} < 0 & \text{for traction,} \end{cases} \tag{1.39}$$

$$S_s \equiv \mid s \mid, \tag{1.40}$$

$$S_\alpha \equiv \begin{cases} \mid tan\alpha \mid & \text{for braking} \\ (1 - S_s) \mid tan\alpha \mid & \text{for traction,} \end{cases} \tag{1.41}$$

$$S_\gamma \equiv \mid sin\gamma \mid, \tag{1.42}$$

$$S_{\alpha\gamma} \equiv \begin{cases} \mid tan\alpha + \frac{lsin\gamma}{2\rho_1} \mid & \text{for braking} \\ \mid (1 - S_s)tan\alpha + \frac{lsin\gamma}{2\rho_1} \mid & \text{for traction,} \end{cases} \tag{1.43}$$

$$S_{s\alpha\gamma} = (S_s^2 + S_{\alpha\gamma}^2)^{\frac{1}{2}}. \tag{1.44}$$

In addition, non-dimensional contact patch length l_n is defined as

$$l_n = \frac{l_a}{l} \tag{1.45}$$

in which l_a is the length of the adhesion region from the front extremity to the break-away point for the sliding region of the contact patch. Another non-dimensional parameter S_n is defined as

$$S_n = 1 - l_n \tag{1.46}$$

and since $0 \leq l_a \leq l$, then, $0 \leq S_n \leq 1$. The limits of S_n provide the boundary of the slip ratio, slip angle and camber angle for elastic deformation.

On the other hand, the resultant friction coefficient may be assumed to be a function of sliding velocity of the tire tread and a friction parameter $\mu 0$ at zero sliding

velocity. Gim and Nikravesh calculated friction coefficient in terms of resultant slip ratio $S_{s\alpha\gamma}$. Since $V_s = V_\xi S_{s\alpha\gamma}$ and $V_\xi = V_x$ during braking and $V_\xi = V_C$ during traction, for quadratic formulation,

$$\mu = \mu_0(1 - A_s^* S_{s\alpha\gamma} - B_s^* S_{s\alpha\gamma}^2) \tag{1.47}$$

in which

$$A_s^* = \frac{(1-\frac{\mu_1}{\mu_0})S_2^2-(1-\frac{\mu_2}{\mu_0})S_1^2}{S_1S_2(S_2-S_1)} \quad \text{and} \quad B_s^* = \frac{(1-\frac{\mu_1}{\mu_0})S_2-(1-\frac{\mu_2}{\mu_0})S_1}{S_1S_2(S_2-S_1)}$$

where μ_0 is the friction parameter at zero sliding velocity, μ_1 and μ_2 are the friction parameters at S_1 and S_2, respectively. For linear formulation,

$$\mu = \mu_0(1 - A_s^* S_{s\alpha\gamma}) \tag{1.48}$$

where $A_s^* = \frac{(1-\frac{\mu_1}{\mu_0})}{S_1}$ and both formulations are plotted in Figure 1.13.

Using considerations above and a procedure similar to those mentioned before, Gim and Nikravesh derived the longitudinal force F_ξ as follows:

$$F_\xi = C_s S_s(1 - S_n + \frac{1}{3}S_n^2) \quad ; \quad S_s \le S_{sc} \tag{1.49}$$

and

$$F_\xi = \mu_x F_z \quad ; \quad S_s \ge S_{sc} \tag{1.50}$$

in which C_s is the longitudinal stiffness and $C_s = \frac{k_x w l^2}{2}$, k_x is the longitudinal stiffness rate per unit area, F_z normal load, $\mu_x = \mu$ at $S_{s\alpha\gamma} = S_s$, S_{sc} the critical (or maximum)

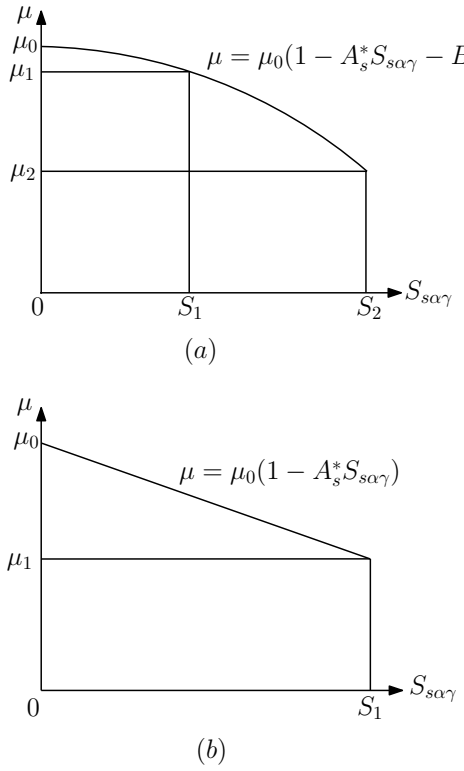

Figure 1.13. Friction coefficient models: (a) Quadratic, (b) Linear [13]

slip ratio allowing longitudinal elastic deformation and given as

$$S_{sc} = \frac{3\mu_x F_z}{C_s} \tag{1.51}$$

and

$$S_n = \frac{C_s S_s}{3\mu_x F_z} \tag{1.52}$$

In the case of pure slip angle conditions, the lateral force ($F_{\eta\alpha}$) and self-aligning torque ($M_{z\alpha}$) can be calculated by using the following equations:

$$F_\xi = C_\alpha S_\alpha (1 - S_n + \frac{1}{3} S_n^2) \quad ; \quad S_\alpha \leq S_{\alpha c} \tag{1.53}$$

$$M_{z\alpha} = \frac{C_\alpha S_\alpha}{6} (1 - S_n)^3 \quad ; \quad S_\alpha \leq S_{\alpha c} \tag{1.54}$$

and

$$F_\xi = \mu_y F_z \quad ; \quad S_\alpha > S_{\alpha c} \tag{1.55}$$

and

$$M_{z\alpha} = 0 \quad ; \quad S_\alpha > S_{\alpha c} \tag{1.56}$$

where C_α is the cornering stiffness and $C_\alpha = \frac{k_y w l^2}{2}$, k_y is the lateral stiffness rate per unit area, $\mu_y = \mu$ at $S_{s\alpha\gamma} = S_\alpha$, $S_{\alpha c}$ the critical (or maximum) lateral slip ratio that allows lateral elastic deformation and is given as follows:

$$S_{\alpha c} = \frac{3\mu_y F_z}{C_\alpha} \tag{1.57}$$

and

$$S_n = \frac{C_\alpha S_\alpha}{3\mu_y F_z} \tag{1.58}$$

The self-aligning torque is zero for $S_\alpha > S_{\alpha c}$ because the friction force is zero symmetric with respect to centerline of the wheel in lateral direction.

For pure camber angle conditions, Gim and Nikravesh stated that the path of the center of a tire when a camber angle is present is elliptical as discussed before. Lateral force as a result of pure camber angle is derived as follows:

$$F_{\eta\gamma} = C_\gamma S_\gamma \quad ; \quad S_\gamma \leq S_{\gamma c} \tag{1.59}$$

and

$$F_{\eta\gamma} = \mu_y F_z \quad ; \quad S_\gamma > S_{\gamma c} \tag{1.60}$$

where $C_\gamma = \frac{k_y w l^3}{12\rho_1}$ and C_γ is the camber stiffness, $\mu_y = \mu$ at $S_{s\alpha\gamma} = S_\gamma$ and $S_{\gamma c} = \frac{\mu_y F_z}{C_\gamma}$.

In this case, at a critical value of the camber angle the adhesion region shifts to sliding region without breakaway point. That is to say, the elastic stress changes to a frictional stress at the critical camber angle γ_c, i. e., $l_a = l$ for adhesion region and $l_a = 0$ for the sliding region. These may be attributed to the fact that because the lateral displacement, and the elastic stress resulting from pure camber angle are approximately parabolic, similar to the distribution of the contact pressure, the adhesion region extends to the full length l of the contact patch.

In the following Figures 1.14 - 1.17, for pure slip conditions and various normal loads, longitudinal force versus slip ratio, lateral force versus both slip angle and camber angle and self-aligning moment versus slip angle are plotted.

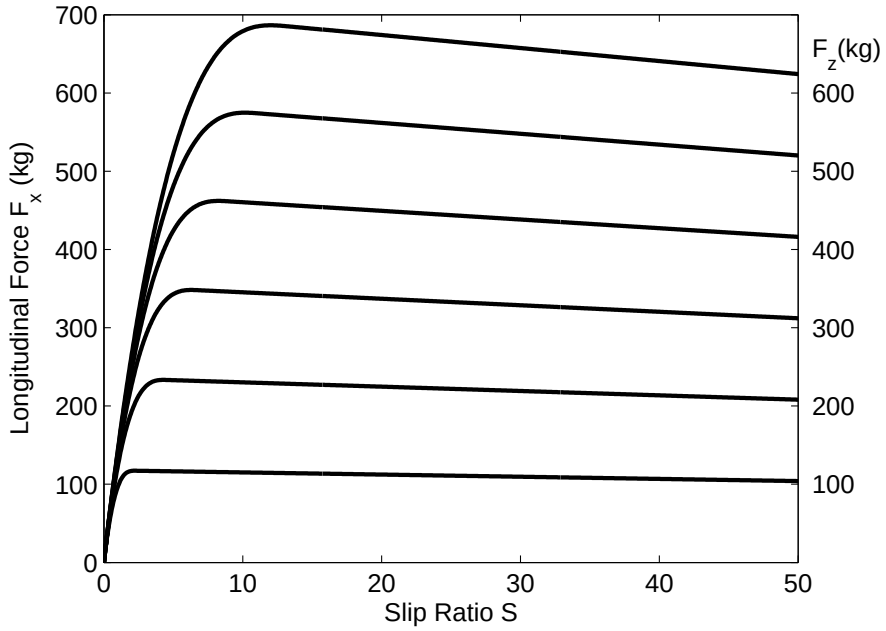

Figure 1.14. Longitudinal force vs slip ratio s for different normal loads

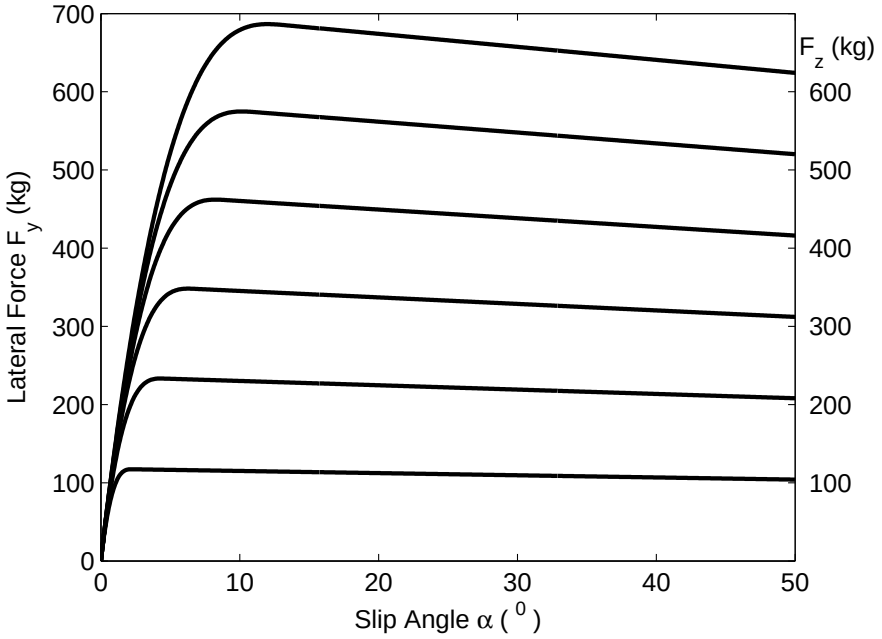

Figure 1.15. Lateral force vs slip angle,α,($\gamma = 0$) for different normal loads

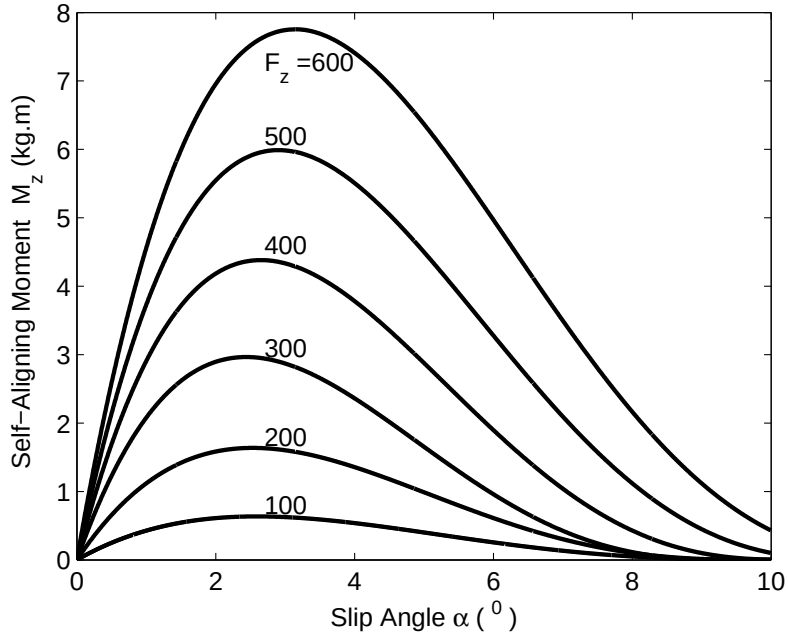

Figure 1.16. Self-aligning moment vs slip angle,α, for different normal loads

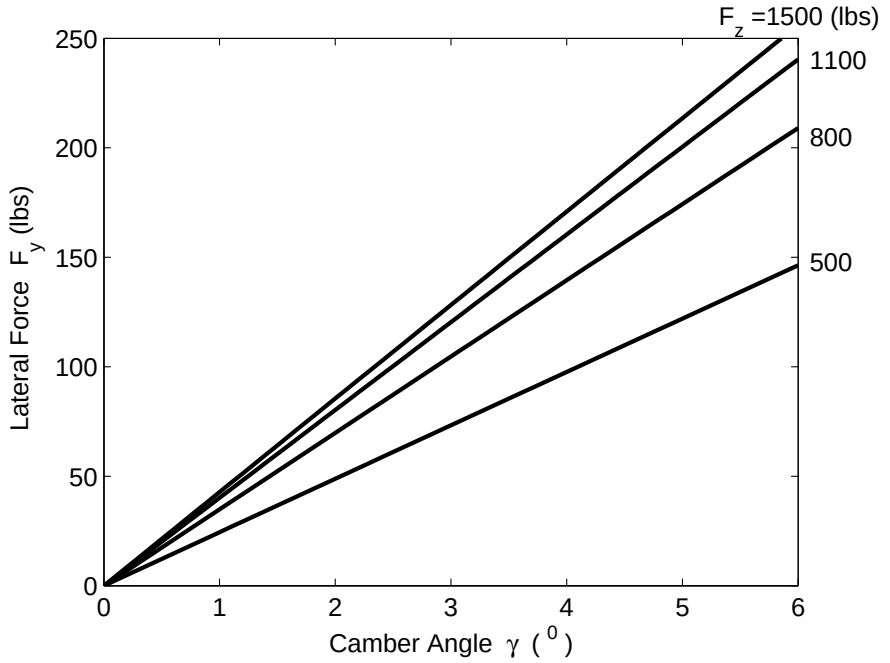

Figure 1.17. Lateral force vs camber angle, γ, for different normal loads

Sjahdanulirwan [14] constructed an analytical model for prediction of tire-road interaction under braking and cornering. The geometry of tire-road contact region is shown in Figure 1.18.

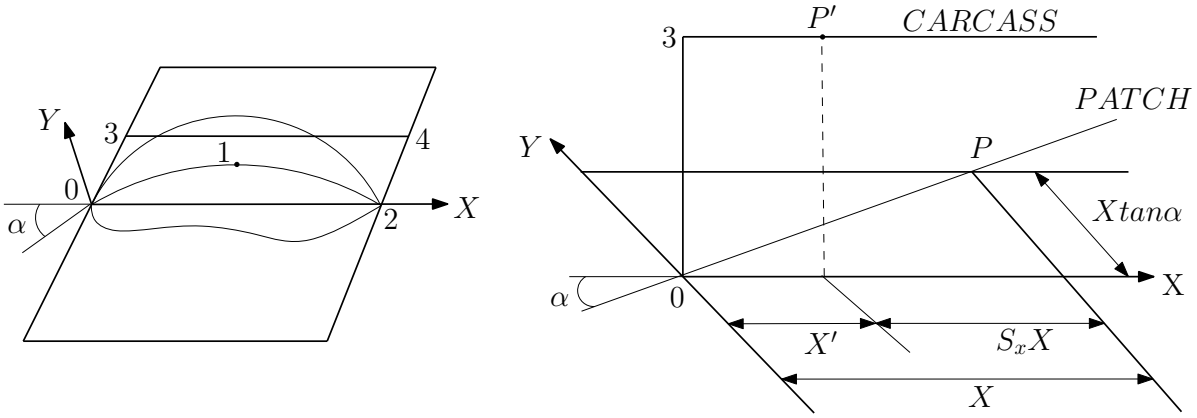

Figure 1.18. Tire-road contact geometry and deformation in nonsliding portion of contact patch [14]

In Figure 1.18, the $X - Y$ coordinate system is placed on the ground plane. The point 0 is the origin and the tread contact point. This coordinate system passes through point 2 which is the tread liftoff point. The line $3 - 4$ is the longitudinal centerline of the tire carcass. It is assumed that each point on the carcass centerline is elastically connected to tread $(0 - 1 - 2)$ through orthogonal springs which produce

independent forces in $X-Y$ directions. The carcass centerline deformation (lateral) is approximated by a constant. So, line $3-4$ lies in the vertical plane passing through the $X-$axis. Point 1 represents the sliding boundary. The deformations at a typical point $P(X,Y)$ on the nonsliding segment $(0-1)$ of patch centerline is shown in Figure 1.18. The longitudinal coordinate of point P can be calculated as

$$X = V_x \Delta t \tag{1.61}$$

where V_x is the tire's longitudinal velocity and Δt is the time elapsed to $P\ from\ O$.

During the same time interval, point P' moves a distance X' given by

$$X' = \Omega R_e \Delta t \tag{1.62}$$

in which Ω is wheel spin velocity and R_e is tire's rolling radius. The longitudinal deformation of point P relative to point P' is given as

$$X - X' = S_x X \tag{1.63}$$

where $S_x = (1 - \frac{\Omega R_e}{V_x})$.

Then, the longitudinal component of stress at point P can be calculated as

$$\sigma_x = K_x S_x X \tag{1.64}$$

in which K_x is the longitudinal spring constant (unit: weight per unit length, per unit width, per unit longitudinal deflection). The lateral deformation of point P is

$$Y = X\ \tan\alpha = X S_y \tag{1.65}$$

So, the lateral component of stress at point P is calculated as

$$\sigma_y = K_y S_y X \tag{1.66}$$

where K_y is the lateral spring constant (unit: weight per unit length, per unit width, per unit longitudinal deflection).

On the other hand, different from above analytical studies, Sjahdanulirwan assumed different pressure distribution over the contact patch as shown in Figure 1.19.

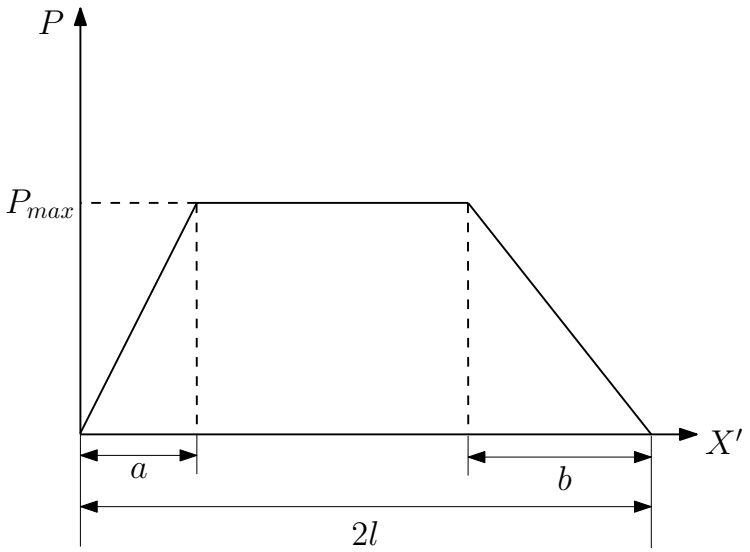

Figure 1.19. Idealized pressure distribution within the contact patch [14]

The maximum normal pressure over contact patch is given by

$$P_{max} = \frac{F_z}{\{2l - 0.5(a+b)\}w} \tag{1.67}$$

where F_z is the normal (wheel) load, w is the width of the contact patch, $2l$ is the length of the contact patch, a is the length of increasing pressure zone and b is the length of decreasing pressure zone. In lateral direction, the pressure distribution is assumed to be uniform. The normal pressure in each of three regions of the contact

region is

$$P = \begin{cases} \frac{P_{max}(2l-X')}{b} & 2l-b \leq X' \leq 2l \\ P_{max} & a \leq X' \leq 2l-b \\ \frac{P_{max}X'}{a} & 0 \leq X' \leq a \end{cases} \tag{1.68}$$

Sjahdanulirwan introduced two types of coefficient of friction: nominal (or available) friction coefficients (μ_s, μ_α) and frictional force coefficients (μ_x, μ_y). Former is assumed to be a linear function of sliding speed or slip, while latter is defined as the ratio of frictional forces to normal load. These are given as follows;

$$\mu_s = \mu_{s0} - (\mu_{s0} - \mu_d)S_x \tag{1.69}$$

$$\mu_\alpha = \mu_{\alpha 0} - (\mu_{\alpha 0} - \mu_d)\frac{2\alpha}{\pi} \qquad \tan\alpha = S_y \tag{1.70}$$

$$\mu = \mu_s - (\mu_\alpha - \mu_s)\frac{2\theta}{\pi} \qquad \tan\theta = \frac{S_y}{S_x} \tag{1.71}$$

in which μ is the coefficient of friction, μ_s and μ_α are the longitudinal and lateral components of the coefficient of friction, respectively, and μ_d is the locked-wheel coefficient and the plots of these coefficients are given in Figures 1.20. It is also noted that in the case of complete sliding without any elastic deformation, frictional force coefficient equals to the nominal friction coefficient.

As noted in the previous studies, there is a need to locate the sliding boundary. At point 1, the resultant elastic deformation stress is equal to tire-road shear stress limit, that is,

$$(\sigma_x^2 + \sigma_y^2)^{0.5} = \sigma_{max} = \mu P \tag{1.72}$$

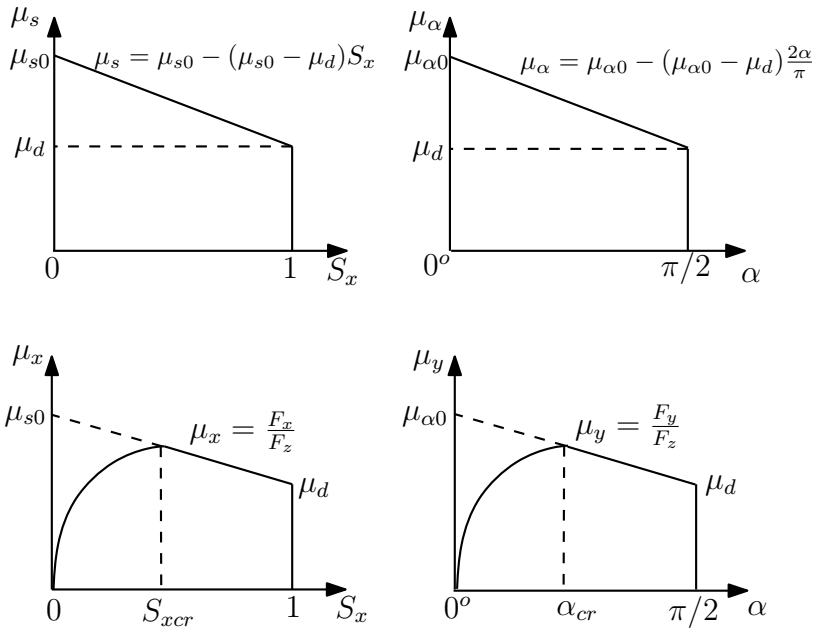

Figure 1.20. (a) Longitudinal and lateral components of available friction coefficient (b) Longitudinal and lateral components of frictional force coefficient [14]

Let X_s refer to longitudinal coordinate of the point where sliding starts. Substituting Equations 1.64 and 1.66 into 1.72 gives X_s as follows:

$$X_s = \mu P\{(K_x S_x)^2 + (K_y S_y)^2\}^{-0.5} \tag{1.73}$$

Using Equations 1.63 and 1.73 results in the following equation for the corresponding point X_s' on tire carcass.

$$X_s{}' = \mu P(1 - S_x)\{(K_x S_x)^2 + (K_y S_y)^2\}^{-0.5} \tag{1.74}$$

Due to trapezoidal pressure distribution, there exist three separate regions in which $X_s{}'$ may be located. In the first region, that is $2l - b \leq X_s$,

$$2l - b \leq \mu P_{max}(1 - S_x)/b\{(K_x S_x)^2 + (K_y S_y)^2\}^{0.5} \tag{1.75}$$

and using Equations 1.68 and 1.75 and inserting the limit value of X' gives the following

inequality,

$$\frac{S_x}{1-Sx} \leq \frac{\mu F_z S_x \{(C_x S_x)^2 + (C_y S_y)^2\}^{-0.5}}{\{2 - 3(\frac{b}{2l}) - (\frac{a}{2l}) + (\frac{a}{2l})(\frac{b}{2l}) + (\frac{b}{2l})^2\}} \tag{1.76}$$

where C_x is the longitudinal stiffness given by $C_x = 2l^2 w K_x$, C_y is the lateral stiffness given by $C_y = 2l^2 w K_y$ and $a/2l$ and $b/2l$ are the shape of the pressure distribution.

Similarly, for the second region ($a \leq X_s{'} \leq 2l - b$), following inequality can be get,

$$\frac{\mu F_z S_x \{(C_x S_x)^2 + (C_y S_y)^2\}^{-0.5}}{\{2 - 3(\frac{b}{2l}) - (\frac{a}{2l}) + (\frac{a}{2l})(\frac{b}{2l}) + (\frac{b}{2l})^2\}} \leq \frac{S_x}{1-S_x} \leq \frac{\mu F_z S_x \{(C_x S_x)^2 + (C_y S_y)^2\}^{-0.5}}{2(\frac{a}{2l}) - (\frac{a}{2l})^2 - (\frac{a}{2l})(\frac{b}{2l})} \tag{1.77}$$

and for the last region, it is found that

$$\frac{S_x}{1-S_x} \geq \frac{\mu F_z S_x \{(C_x S_x)^2 + (C_y S_y)^2\}^{-0.5}}{2(\frac{a}{2l}) - (\frac{a}{2l})^2 - (\frac{a}{2l})(\frac{b}{2l})} \tag{1.78}$$

Above three inequalities determine the sliding region and Equation 1.74 yields $X_s{'}$. After that the longitudinal (braking) force F_x and lateral (sideway) force F_y can be calculated performing the following integrations.

$$F_x = w \int_0^{X_s{'}} \sigma_x(X{'}) dX{'} + cos\theta \int_{X_s{'}}^{2l} \sigma_{max}(X{'}) dX{'} \tag{1.79}$$

$$F_y = w \int_0^{X_s{'}} \sigma_y(X{'}) dX{'} + sin\theta \int_{X_s{'}}^{2l} \sigma_{max}(X{'}) dX{'} \tag{1.80}$$

Now, the integrations given above are evaluated for the three cases and given

below. For the first case ($2l - b \leq X_s'$), using Equations 1.68 and 1.74 yields

$$\frac{X_s'}{2l} = \frac{1}{1 + \frac{\{2(b/2l) - (a/2l)(b/2l) - (b/2l)^2\}\{(C_x S_x)^2 + (C_y S_y)^2\}^{0.5}}{\mu F_z (1 - S_x)}} \tag{1.81}$$

and using Equations 1.79 and 1.80 results in

$$F_x = \frac{C_x S_x}{(1 - S_x)}(\frac{X_s'}{2l})^2 + \frac{\mu F_z cos\theta\{1 - 2(X_s'/2l) + (X_s'/2l)^2\}}{2(b/2l) - (a/2l)(b/2l) - (b/2l)^2} \tag{1.82}$$

$$F_y = \frac{C_y S_y}{(1 - S_x)}(\frac{X_s'}{2l})^2 + \frac{\mu F_z sin\theta\{1 - 2(X_s'/2l) + (X_s'/2l)^2\}}{2(b/2l) - (a/2l)(b/2l) - (b/2l)^2} \tag{1.83}$$

In a similar manner, for the second case $a \leq X_s' \leq 2l - b$,

$$\frac{X_s'}{2l} = \frac{\mu F_z (1 - S_x)}{\{2 - (a/2l) - (b/2l)\}\{(C_x S_x)^2 + (C_y S_y)^2\}^{0.5}} \tag{1.84}$$

$$F_x = \frac{C_x S_x}{(1 - S_x)}(\frac{X_s'}{2l})^2 + \frac{\mu F_z cos\theta\{1 - 0.5(b/2l) + (X_s'/2l)\}}{1 - 0.5(a/2l) - 0.5(b/2l)} \tag{1.85}$$

$$F_y = \frac{C_y S_y}{(1 - S_x)}(\frac{X_s'}{2l})^2 + \frac{\mu F_z sin\theta\{1 - 0.5(b/2l) + (X_s'/2l)\}}{1 - 0.5(a/2l) - 0.5(b/2l)} \tag{1.86}$$

For the last case ($a \geq X_s'$), sliding will occur at all points since both pressure and stress are linear functions of X_s'. Then, Equations 1.79 and 1.80 reduce to

$$F_x = cos\theta \int_0^{2l} w\sigma_{max}(X')dX' \tag{1.87}$$

$$F_y = sin\theta \int_0^{2l} w\sigma_{max}(X')dX' \tag{1.88}$$

and evaluating these integrations yields

$$F_x = \mu F_z cos\theta \tag{1.89}$$

$$F_y = \mu F_z sin\theta \tag{1.90}$$

It is seen from above equations that there is a need to calculate friction parameters. To do this, there are two methods Sjahdanulirwan offered. One of them is the locked-wheel braking force coefficient (BFC) and the other is the sideway coefficient (SFC). Detailed information for both methods are given in this paper, but not mentioned here. Also, a BASIC program is given to calculate the frictional forces. However, the following figures are plotted using a computer program using MATLAB.

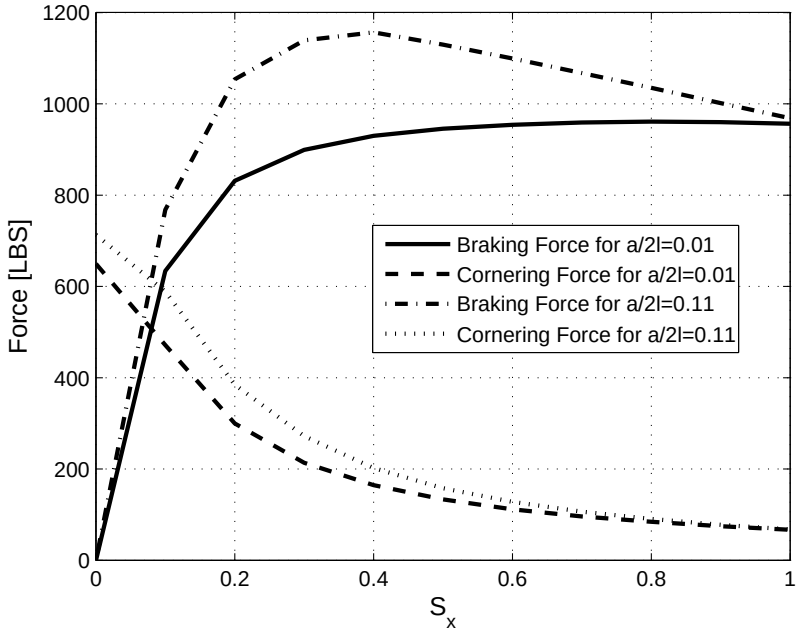

Figure 1.21. Analytical model results of H78-14 tire with b/2l=0.2 and different a/2l values (F_x and F_y versus S_x at $\alpha = 4$)

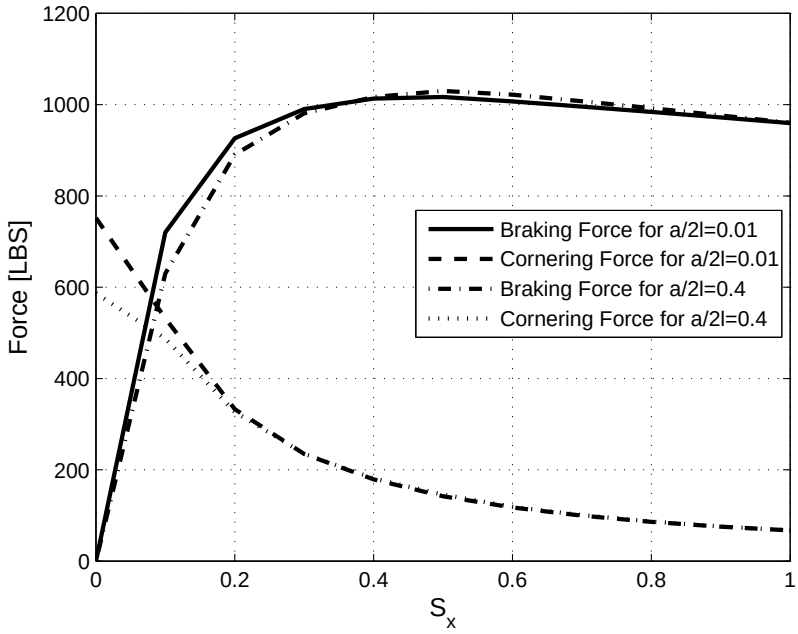

Figure 1.22. Analytical model results of H78-14 tire with a/2l = 0.06 and different b/2l values (F_x and F_y versus S_x at $\alpha = 4$)

In addition to considerations above, it should also be noted that there is a maximum tractive force a tire can support as shown in Figure 1.23 . In the absence of lateral force, the maximum force is the thrust (positive or negative). If there is no thrust (or braking force) and there is lateral force only, the maximum force is the maximum lateral force. If lateral and braking (or tractive) force exist at the same time, the maximum tractive force is the vectorial sum of the thrust and maximum lateral force. So, the maximum thrust is reduced and vice versa. The friction ellipse below relates the maximum lateral force and maximum thrust to the maximum tractive force as shown in Figure 1.23. It is a friction circle if there is no bias longitudinally or laterally, otherwise it will be a friction ellipse and governed by the following equation:

$$(\frac{F_y}{F_{y,max}})^2 + (\frac{F_x}{F_{x,max}})^2 = 1 \tag{1.91}$$

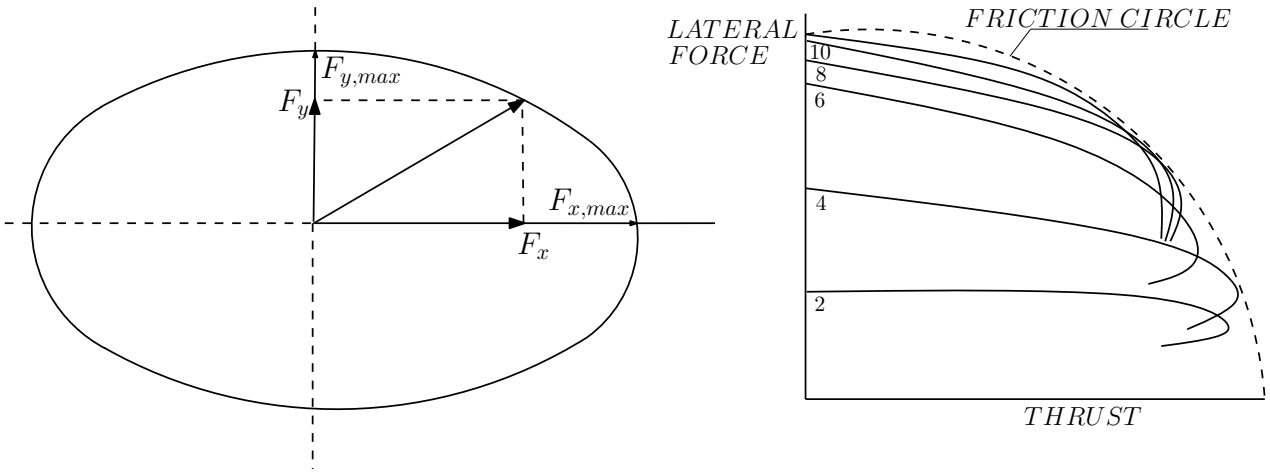

Figure 1.23. The concept of friction ellipse

In Figure 1.24, typical pure lateral ($\kappa = 0$) and longitudinal ($\alpha = 0$) slip characteristics are shown together with a number of combined slip curves. κ stands for the slip ratio and camber angle is kept equal to zero. It is defined that pure slip is the situation when either longitudinal or lateral slip occurs in isolation. This figure shows that a drop in force arises when the other component is added. The resulting situation is designated as combined slip. The decrease in force can be explained by releasing that the total horizontal frictional force can not exceed the maximum value (radius of friction circle) which is calculated multiplying the friction coefficient and the normal load.

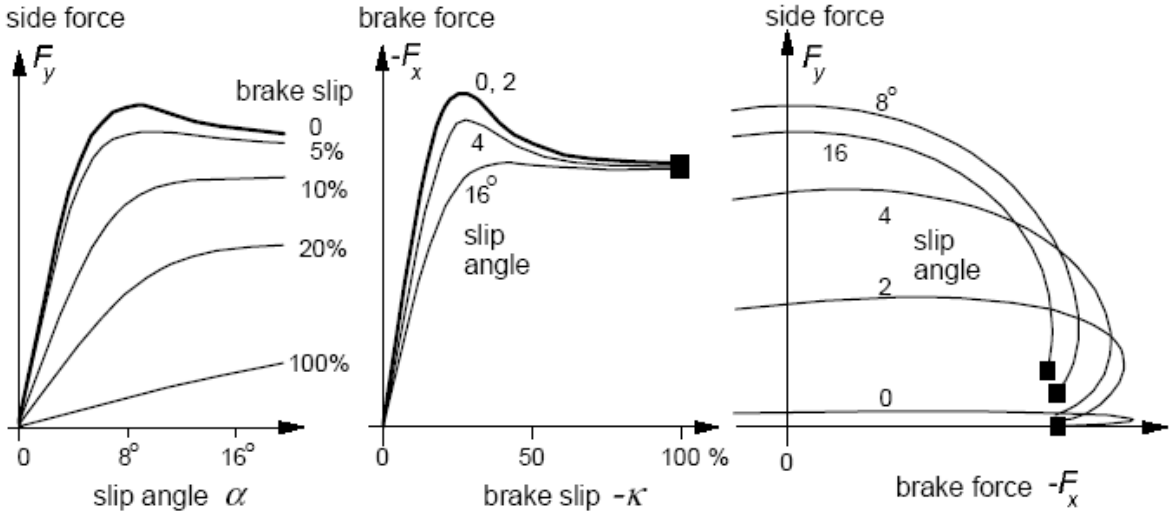

Figure 1.24. The concept of friction ellipse [22]

1.2.2. Experimental Models

Experimental studies are conducted either on road conditions or in laboratories. In-door testing measurements are carried out using testing machines that have flat or cylindrical surfaces (drum). The validation of a proposed tire model is one of the main aims of experimental studies. Testing conditions are constructed based on proposed studies and vice versa. There are also purely experimental studies in which tire behavior is directly investigated.

Tönük and Ünlüsoy [23, 24] constructed a simple drum-type tire testing setup to show accuracy and validity of their proposed finite element model to predict cornering force characteristics of a 155R13 radial tire. The drum has a width of 258 mm and a diameter of 979 mm. The test speed is variable between 0.05 and 150 km/h. There are T-slots on testing machine to adjust slip angle of the tire. Slip angle is adjusted optically by a laser beam. The vertical load is applied through an air spring.

Burke and Olatunbosun [25] conducted experiments on tire testing setup with a flat surface to verify their tire model.They measured vertical stiffness of a 195/65R15 tire. They constructed force-displacement equipment setup and carried out static tire analysis. The force is applied in a controlled manner by an electro-hydraulic actuator and displacement is monitored using an actuator controller and an externally mounted dial test indicator for greater accuracy.

Calspan Tire Research Facility machine uses an indoor test machine with a flat surface. Yap [26] made experiments on this machine to investigate cornering characteristics of radial truck tire with rib and lug tread designs and construct a tire empirical model. This machine has a 71 cm wide stainless belt roadway running over two 0.7 m diameter drums. The advantage of this testing machine is that it simulates somewhat real road conditions and it has a wide range of speed. The flat belt is covered with a grit surface. The roadway under the tire contact patch is supported by an air-bearing pad.

Vertical, longitudinal and lateral behaviors of vehicles are largely influenced by the dynamic characteristics of tires. In vehicle modeling stages, vertical, longitudinal and also torsional stiffness of tires are needed. From this fact, Ramji et al. [17] conducted experiments to determine stiffness properties of small-sized pneumatic tires. A vertical column in the test setup slides in guides and gives the tire vertical load. A base support moves in horizontal plane, in longitudinal, lateral and twist directions and its motion is guided on ball bearings. Two pneumatic cylinders, which are mounted in different orientation, apply longitudinal, lateral forces and twist moment on base support. Tire deflection is measured by dial gauges in static condition. Measurements of the contact patch are obtained from the print of the contact patch using a paper placed between the horizontal plate and the tire. Inflation pressure and normal loads are the experimental parameters. There is a variation in load while the vehicle is moving. This effect is also taken into account to decide range of loads on tires.

Hollaway et al. [27] investigated passenger car tire properties at high slip and camber angles. To do this, they used Mobile Tire Testing Machine (MTTM). In testing stages, they used six different passenger tires; namely, P215/70R14, 155SR13, P215/70R14, P205/70R15, P185/80R13 and P195/75R14. These tires are tested on 13, 14 and 15 *in.* wheels. Instead of using rated load and maximum inflation pressure, they tested tires at approximately 50% , 100% and 150% of curb weight loading at recommended inflation pressure. Slip angle, camber angle, longitudinal slip ratio (braking) are parameters of measurements. They concluded that camber stiffness decreases with the increasing slip angle when slip and camber angles are both positive. At limit conditions in slip angle, camber angle has a little effect on lateral force value. When slip angle is negative, and camber angle is positive, greater lateral force is produced when compared to conditions in slip angle alone.

On the other hand, empirical tire models use experimental data in their formulation. There are mainly two methods to represent measured data: special functions and series or polynomial representations.

The “ Magic Formula” model [28] is one good example of special function repre-

sentations. In this model, mathematical functions are used to write lateral force and aligning torque as a function of slip angle, and longitudinal force as a function of longitudinal slip. At the beginning, a *sine* function is used. For larger slip angles, *sine* alone does not give a good representation of measured data. Then, *arctan* function is included into the formulation. When *sine* is used all curves pass through origin. This is not the case in reality. Due to ply steer, conicity and rolling resistance, curves can be shifted on horizontal and vertical axes. That is to say, for 0^0 slip angle, there are nonzero lateral force values. To eliminate this problem, these shifts are included. In addition, to reduce total number of coefficients and to be able to calculate force and moment at vertical loads which are different from values used in measurements, there is a need to include vertical load explicitly into formulas. On the other hand, camber effect, combining cornering and braking conditions are taken into consideration as well.

Steps of "Magic Formula" are given in following equations [28]:

$$y = D\ Sin(B\ x) \tag{1.92}$$

where y represents either side force, aligning torque or brake force. x refers to slip angle (α) or longitudinal slip (κ). D is the peak value and product DB is equal to the slip stiffness at zero slip. The effects of constants D and B on y are shown in Figures 1.25. Cornering force vs. slip angle plot of 155R13 tire is give to illustrate the starting point of Magic Formula. As seen in Figures 1.25, there are similarities between sine function and cornering force characteristics of 155R13. However, there is a need to make some modifications to get satisfactory results. Especially for higher values of x, Equation 1.92 does not yield satisfactory results. In a similar manner, the final form of the formula was obtained. The same conclusions can be drawn for the another force and moment characteristics.

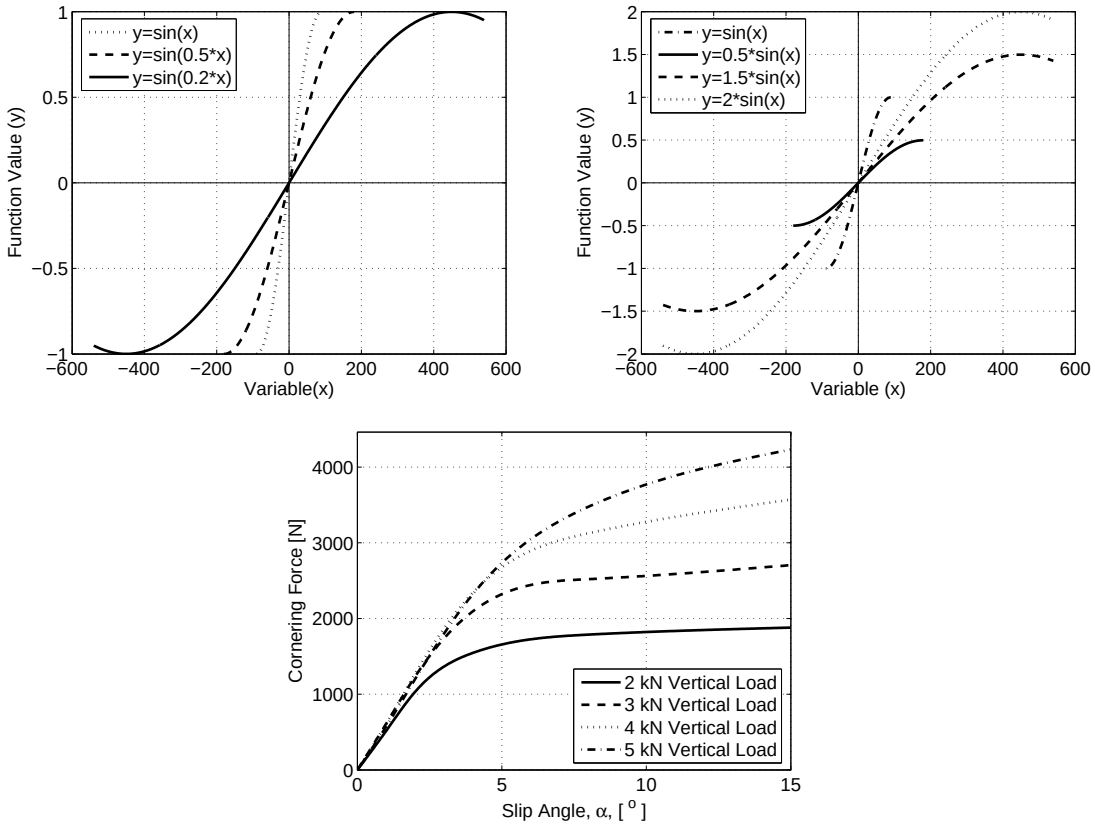

Figure 1.25. Representation of the starting point of the "Magic Formula"

The form proposed for tire formula that takes care of consideration above is given in Equations 1.93, 1.94 and 1.95 for side force, self aligning torque and braking force. For side force:

$$F_y = D\ Sin(C\ arctan(B\Phi)) + \Delta S \tag{1.93}$$

where $C = 1.30$, and

$$\Phi = (1 - E)(\alpha + \Delta S_h) + (\tfrac{E}{B})\ \arctan(B(\alpha + \Delta S_h)),$$

$$D = a_1 F_z^2 + a_2 F_z,$$

$$B = (\frac{a_3 sin(a_4 arctan(a_5 F_z}{CD})\ (1 - a_{12}|\gamma|),$$

$$E = a_6 F_z^2 + a_7 F_z + a_8,$$

$$\Delta S_h = a_9 \gamma,$$

$$\Delta S_v = (a_{10} F_z^2 + a_{11} F_z)\ \gamma.$$

For self aligning torque:

$$M_z = D\ Sin(C\ arctan(B\Phi)) + \Delta S_v \tag{1.94}$$

where $C = 2.40$, and

$$\Phi = (1 - E)(\alpha + \Delta S_h) + (\frac{E}{B})\ \arctan(B(\alpha + \Delta S_h)),$$

$$D = a_1 F_z^2 + a_2 F_z,$$

$$B = (\frac{a_3 F_z^2 + a_4 F_z}{C\ D\ e^{a_5 F_z}})(1 - a_{12}\ |\ \gamma\ |),$$

$$E = (\frac{a_6 F_z^2 + a_7 F_z + a_8}{(1 - a_{13}|\gamma|)}),$$

$$\Delta S_h = a_9 \gamma,$$

$$\Delta S_v = (a_{10}F_z^2 + a_{11}F_z)\ \gamma.$$

For braking force:

$$F_x = D\ Sin(C\ arctan(B\Phi)) \tag{1.95}$$

where $C = 2.40$, and

$$\Phi = (1 - E)\kappa + (\tfrac{E}{B})\ \arctan(B\kappa),$$

$$D = a_1F_z^2 + a_2F_z,$$

$$B = (\tfrac{a_3F_z^2 + a_4F_z}{C\ D\ e^{a_5F_z}}),$$

$$E = (\tfrac{a_6F_z^2 + a_7F_z + a_8}{(1 - a_{13}|\gamma|)}),$$

and in formulas above, C determines the shape of the curve. B is the stiffness factor, E is the curvature factor, F_z is the vertical load, S_h is the horizontal and S_v is the vertical shift. a_i's are coefficients for tire formula determined experimentally and are given in Table 1.2 and 1.3.

Table 1.2. Coefficients for tire formula (with load influence) [28]

	a_1	a_2	a_3	a_4	a_5	a_6	a_7	a_8
F_y	-22.1	1011	1078	1.82	0.208	0.0000	-0.354	0.707
M_z	-2.72	-2.28	-1.86	-2.73	0.110	-0.070	0.643	-4.04
F_x	-21.3	1144	49.6	226	0.069	-0.006	0.056	0.486

Table 1.3. Coefficients for tire formula connected camber influence [28]

	a_9	a_{10}	a_{11}	a_{12}	a_3
F_y	-22.1	1011	1078	1.82	0.208
M_z	-2.72	-2.28	-1.86	-2.73	0.110

On the other hand, authors carried out tire measurements on dry asphalt road by using a specially built test trailer under steady state conditions to get data for curve fitting. Pure cornering, pure braking and combined cornering and braking conditions are considered. During cornering, the speed is 70 km/h and for braking tests, 60 km/h. The tests include variations of slip angles between -10^o and 14^o and vertical loads are taken as 2, 4, 6 and 8 kN. Camber angle are, on the other hand, taken as -5^o and 5^o. Side force, aligning moment and brake force characteristics obtained using magic tire formula are replotted and given in Figures 1.26, 1.27 and 1.28, respectively.

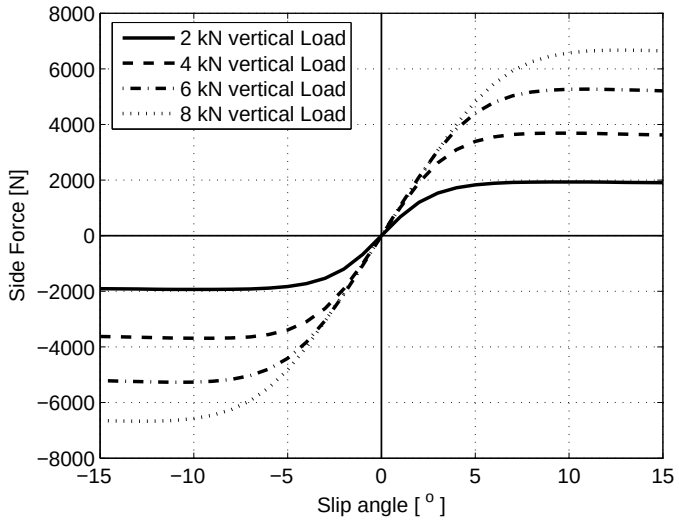

Figure 1.26. Side force vs slip angle obtained using Magic Formula for different vertical loads

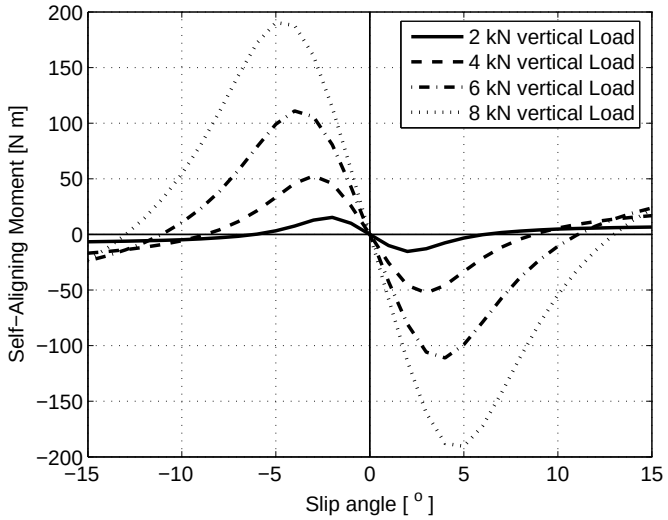

Figure 1.27. Self-aligning moment vs slip angle obtained using Magic Formula for different vertical loads

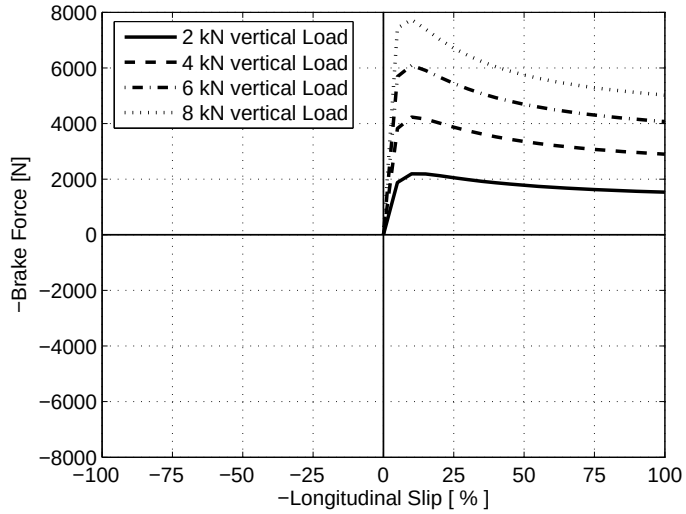

Figure 1.28. Brake force vs longitudinal slip obtained using Magic Formula for different vertical loads

Another mathematical representation of experimental results is done using polynomials. One of the outstanding polynomial representations of tire behavior is the study conducted by Maalej et al [29]. They used third order polynomial to represent the lateral force as shown below:

$$F_y = C_0 + C_1\alpha + C_2\alpha|\alpha| + C_3\alpha^3 \tag{1.96}$$

where C_0, C_1, C_2 and C_3 are constants to be determined experimentally. They defined

these constants using a second-order polynomial as a function of normal force F_z as

$$C_i = A_{i0} + A_{i1}F_z + A_{i2}F_z^2 \qquad i = 0, 1, 2, 3 \tag{1.97}$$

in which A's are the constants to be determined experimentally. C_0 is attributed to lateral force value at zero slip angle due to the tire construction distortion.

The coefficients can be determined using least square method. As an example, they considered P195/70R14 and data supplied from the Firestone Tire and Rubber Company (Akron, Ohio). Typical values for the constants obtained for a test tire at zero camber angle are given in Table 1.4. To compare their proposed polynomial model with Magic Tire formula, corresponding coefficients are tabulated in Table 1.4.

Table 1.4. Coefficients for tire formula (with load influence) [29]

	F_z	A_y	B_y	C_y	E_y	S_h	S_v
Pacejka	462	−1009.72	0.36	0.31	−1.51	0	0
	995	−2946	0.22	0.33	−0.5	0	0
	1065	−3348	0.27	0.25	−1.23	0	0
	F_z	C_0	C_1	C_2	C_3		
Polynomial	462	15.6	−138.12	12.01	−0.38		
	995	22.8	−248.67	22.88	−0.67		
	1455	28.8	−256.3	17.5	−0.48		

The two methods' results, proposed by Pacejka [28] and Maalej et al. [29] are compared and given in Figure 1.29. The peak value of the lateral force is not well presented in third-order polynomial representation. The results can be improved by considering a fourth-order equation of the the form given in Equation 1.98. When examining Figure 1.29, it can be concluded that the there is a good agreement between the results obtained from [28] and [29].

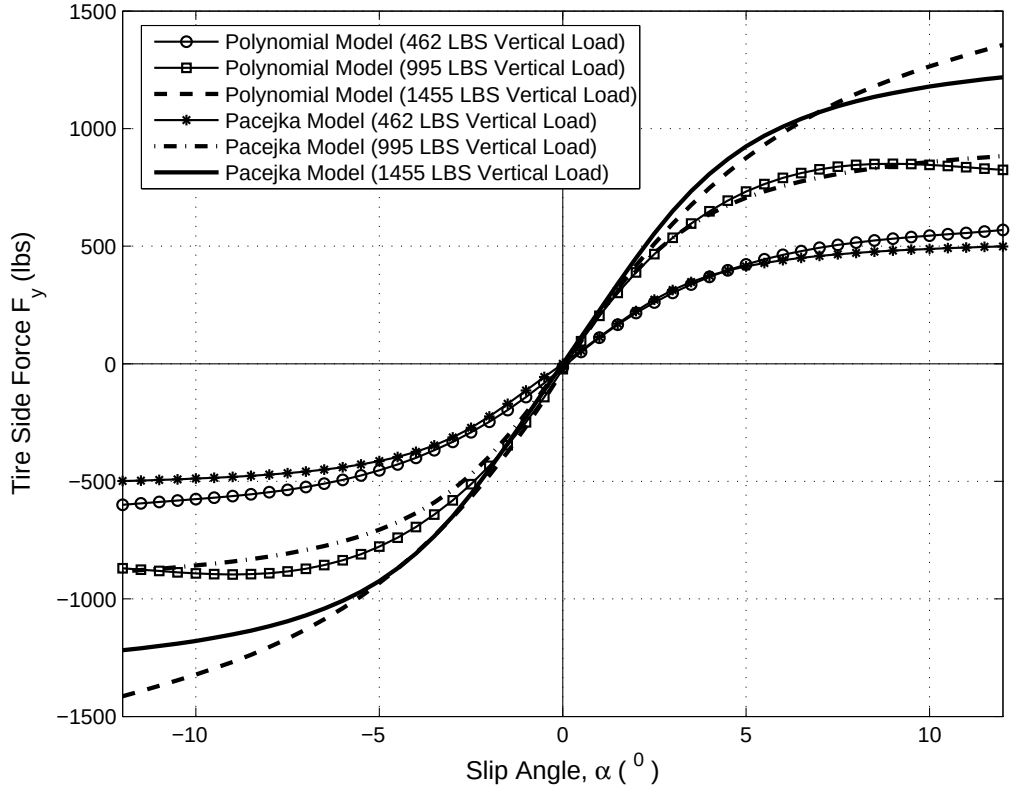

Figure 1.29. Comparison of Pacejka [28] and Polynomial model's [29] results

$$F_y = C_0 + C_1 S + C_2 S|S| + C_3 \S^3 + C_4 S^3|S| \tag{1.98}$$

Takahashi and Hada [30] proposed an empirical tire model based on Magic Formula for predicting overturning moment (OTM) characteristics and its effects on vehicle rollover behavior. For latter, they conducted full vehicle simulations in ADAMS. In the model, pneumatic scrub, which is the lateral shift of action of the vertical load from contact patch center, is the parameter causing the generation of OTM. First, it is calculated using Equation 1.99 from measured OTM, and then using Equation 1.100 from the simple model. In the simple model, they assumed that the tire contacts the road at a point, the cross section of the tire tread is circular and the tire contact point

moves laterally under the side force and the lateral stiffness.

$$P_{s,m} = \frac{M_x}{F_z} \tag{1.99}$$

$$P_{s,s} = 1/K_L.F_y - R_L tan\gamma \tag{1.100}$$

in which F_y is side force, F_z is the vertical load, K_L is the lateral stiffness, M_z is the overturning moment, $P_{s,m}$ is the pneumatic scrub by direct measurement, $P_{s,s}$ is the pneumatic scrub by simple model, R_L is the tire static radius, and γ is the camber angle.

They calculated a difference between measurement and simple model results and they introduced "residual pneumatic scrub, (P_r)" concept. They added P_r to Equation 1.100 and redefined P_s. Due to the similarity in shape, the same expression used for the side force in "Magic Formula" is taken for the residual pneumatic scrub definition. They constructed an empirical model, namely new OTM model. The formulations are given below:

$$P_{s,s} = 1/K_L.F_y - R_L tan\gamma - P_r, \tag{1.101}$$

$$P_r = D\ sin[C\ arctan\{Bx - (E_0 + \Delta E\ sgn(x))(Bx - arctanBx)\}] + S_v, \tag{1.102}$$

$$x = \alpha + S_h, \tag{1.103}$$

$$K_L = m_{18}, \tag{1.104}$$

$$R_L = m_{19}, \tag{1.105}$$

$$C = m_{20}, \tag{1.106}$$

$$D = (m_1 F_z^2 + m_2 F_z)(1 - m_{15}\gamma^2), \tag{1.107}$$

$$BCD = m_3 \ sin[\ 2 \ arctan(\frac{F_z}{m_4})](1 - m_5 \mid \gamma \mid), \tag{1.108}$$

$$B = \frac{BCD}{CD}, \tag{1.109}$$

$$E_0 = m_6 F_z^2 + m_7 F_z, \tag{1.110}$$

$$dE_0 = -(m_6 F_z^2 + m_7 F_z)(m_{16}\gamma + m_{17}) \ sgn(\alpha + S_h), \tag{1.111}$$

$$S_h = m_8 F_z^2 + m_9 F_z + m_{10} F_z \gamma, \tag{1.112}$$

$$S_v = m_{11} F_z^2 + m_{12} F_z + (m_{13} F_z^2 + m_{14} F_z)\gamma, \tag{1.113}$$

where α is the slip angle, and parameters B to S_v in Equations 1.102 and 1.103 are called the Magic Formula coefficients, which are functions of vertical load and camber angle and m's are called Magic Formula parameters.

In their model, Takahashi and Hada [30], firstly, identified and optimized Magic

Formula coefficients and then calculated P_r. Finally, by using the coefficients and parameters obtained as initial values, all coefficients and parameters are again simultaneously optimized by using experimental data. They compared calculated and measured results and showed that new OTM model yields better results than the simple model.

In addition, they studied the influence of tire OTM on vehicle rollover behavior by using results obtained from simple model, new model and the model without OTM. They compared lateral accelerations calculated for rollover with values obtained from experiments. They concluded that the effect of OTM on the tire reduces lateral acceleration for rollover, and among the models checked, the new OTM model agrees better results than the simple model and the model without OTM.

Kageyama and Kuwahara [31] examined camber angle effects on tire characteristics in detail. The 185/60R14 (Smooth type) automobile radial tire is selected. They proposed a tire model for camber thrust and camber torque on an irregular road surface and conducted experiments using a flat-surface tire-testing machine. They reported the results of characteristic measurements in terms of contact patch and shape, contact patch area, largest contact width, contact length, changing in inside and outside diameters, lateral displacement, camber force and camber torque. They confirmed from measurements that the variation in contact pressure in lateral direction can be estimated based on the dependence of contact length on camber angle to the ground. They also estimated lateral stiffness (C_y). Based on the experiment results and Brush Model, lateral stiffness including the sidewall and tread is calculated by Equation 1.114.

$$C_y = \frac{2F_y}{l^2 W tan\alpha} \tag{1.114}$$

in which W is the contact width, l contact length and F_y lateral force and α is the slip angle.

From the above considerations, they constructed an empirical tire model. The Brush Model is taken as a basic structure, camber angle and change in contact patch shape by load are considered in the modeling stages. Contact pressure, load, lateral

and longitudinal stiffness for each block of the contact patch which is divided widthwise as shown in Figure 1.30 are determined by considering load and camber angle. The lateral force generated in each block is referred to as camber thrust and movement around the center of the contact patch, calculated from longitudinal force generated due to a difference in the equivalent change in the radius in the width direction is referred to as camber torque.

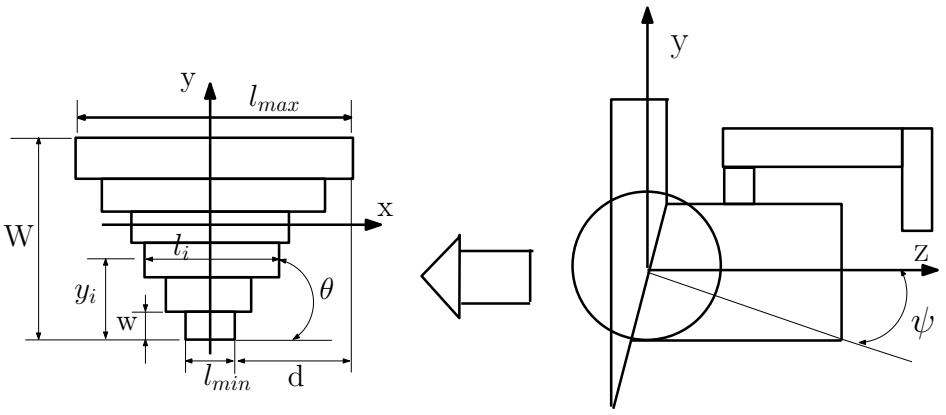

Figure 1.30. Modeling of contact shape [31]

On the other hand, Kageyama and Kuwahara [31] made following assumptions in the model: The shape of the contact patch is similar to a trapezoid at some camber angles. The contact patch area and width are dependent on load but not camber angle. The ground length is dependent on both load and on camber angle. They formulated contact patch area, A; maximum contact width, W, and maximum ground length, l_{max} are derived using multiple regression analysis and given as,

$$A = 3.55 \times 10^{-6} F_z + 1.65 \times 10^{-3}, \tag{1.115}$$

$$W = (-9.79 + 2.80\ ln(F_z)) \times 10^{-3}, \tag{1.116}$$

$$l_{max} = 2.14 \times 10^{-5} F_z - (1.35 \times 10^{-3} F_z + 4.59) \times 10^{-3} \psi + 3.55 \times 10^{-2}. \tag{1.117}$$

Using Equations 1.115- 1.117, l_{min}, y_i and l_i for each block are determined as,

$$l_{min} = \frac{2\ A}{W} - l_{max}, \tag{1.118}$$

$$y_i = \frac{W}{N}(i - \frac{1}{2}), \tag{1.119}$$

$$l_i = l_{min} + \frac{y_i}{tan\theta} \tag{1.120}$$

where, l_i are contact length and i is the block number ($i = 1 - N$).

Contact pressure, p_i is estimated by using contact length as,

$$p_i = 2.69 \times 10^5\ (1 - exp\ (-27.0\ l_i)) \tag{1.121}$$

Lateral stiffness (C_{yi}) and longitudinal stiffness (C_{xi}) for each block are estimated as follows:

$$C_{yi} = 2.77 \times 10^8\ [1 - exp\ \{-1.72 \times 10^5 \times (2.65 \times 10^5 - p_i)\}]\ a_1, \tag{1.122}$$

$$C_{xi} = C_{yi}\ a_2 \tag{1.123}$$

in which a_1 and a_2 are the correction factors used for camber thrust and camber torque, respectively. The outside diameter of the tire crown is determined from the following equation:

$$r_u = -5.11 \times 10^{-6} F_z + (5.40 \times 10^{-9} F_z + 9.07 \times 10^{-4})\ \psi + 2.87 \times 10^{-1} \tag{1.124}$$

Finally, Kageyama and Kuwahara constructed a camber thrust model based on the above consideration and Fiala Model [6] . Camber thrust is taken as the product of the displacement of tread and lateral stiffness. The sum of lateral forces generated in each block is defined as camber thrust, F_{ct}. However, bending deflection of the tread base is not considered.

$$y_c = \frac{l_i^2 sin\psi}{2r_i} \frac{x}{l_i}(1 - \frac{x}{l_i}), \tag{1.125}$$

$$F_{cti} = -C_{yi}\ w \int_0^{l_i} y_c\ dx, \tag{1.126}$$

$$F_{ct} = \sum_{i=1}^{N} F_{cti} \tag{1.127}$$

where, w is width of the one block.

Camber torque model, on the other hand, is derived based on differences in rolling radius of the tire. The longitudinal force for each block is obtained from the slip ratio generated from changes in outside diameter and is given as follows:

$$F_{xi} = \frac{C_{xi} s w l_{hi}^2}{2} + p_i \mu_d w (l_i - l_{hi}) \tag{1.128}$$

in which $l_{hi} = \frac{p_i\ \mu_s}{C_{xi}\ s}$ and s is the slip ratio, μ_s and μ_d are static and dynamic friction coefficients, respectively. By summation of F_{xi} multiplied by the arm length, y_i, from the ground tire center is defined as camber torque:

$$M_z = \sum_{i=1}^{N} F_{xi}\ y_i. \tag{1.129}$$

In addition, the model results (Model 1 constructed above) are compared with

a simple model (Model 2). In the Model 2, they assumed that the contact patch shape is rectangular and the contact pressure and stiffness remain unchanged. They concluded that Model 1 indicates that camber thrust and torque are load dependent and Model 2 indicates that the effects of the change in contact patch shape, contact pressure widthwise, and the change in various stiffness should be considered. Also, they mentioned that there is a great differences between Model 2 and experimental results.

Fuller et al. [32] conducted an experimental study on effects of testing conditions on rolling resistance of radial and bias-ply tires, designated as P195/75R14 and P195/75D14. Load, speed and inflation pressure were the experimental parameters. They also examined the running time to warm-up, which is an important parameter to reduce the total time required for rolling resistance tests. To carry out measurements, they used Spindle force Apparatus designed for testing automobile and light truck tires. It has a wheel having 170.8cm diameter and fulfills SAEJ1269 standards developed by the SAE Subcommittee on rolling resistance of tires. In the measurements, rolling resistance is defined as the force requiring running a tire forward and reverse on the test wheel.

In the test design stage, the ten a-coefficients in the second order response equations are calculated. The response equation is,

$$Y = a_0+a_1x_1+a_2x_2+a_3x_3+a_{11}x_1x_1^2+a_{22}x_2^2+a_{33}x_3^2+a_{12}x_1x_2+a_{13}x_1x_3+a_{23}x_2x_3 \quad (1.130)$$

in which Y is the rolling resistance; x_1 is inflation pressure in experimental units (e.u.); x_2 is speed in e.u.; x_3 is the load in e.u.; a_0 is rolling resistance at the center of the design ($x_1 = x_2 = x_3 = 0$); a_1, a_2, and a_3 are the main effects of pressure, speed and load, respectively; a_{11}, a_{22}, and a_{33} are the curvature effects of pressure, speed and load, respectively; a_{12}, a_{13}, and a_{23} are the interaction effects of pressure-speed, pressure-load, and speed-load, respectively. They determined 10 coefficients from the 27 trials for each tire type.

Finally, they concluded that among the experiment parameters, load is found to be most critical. Quadratic response equation is enough to model interaction of these parameters. Also, they mentioned that rolling resistance should not be measured at speeds above that at which it starts to increase rapidly.

After completed experiments on each surface mentioned above, rolling resistance forces are consistently higher on Safety Walk than on bare steel and these forces are found to be higher at higher speed on either surface. Another conclusion they stated is that warm-up time required for automobile tires to reach equilibrium need not exceed 20 minutes. In the case of maintaining air pressure at the desired level, this time can be reduced to 15 minutes.

In the 1970s, the U.S. Department of Transportation sponsored tire studies. In these studies, tires were examined in detail, especially for vehicle dynamic simulations. One important study is the work done by the Calspan Corporation for the National Highway Traffic Safety Administration (NHTSA)[33]. The main aim of the program was to generate comprehensive force and moment characteristics of passenger car and light truck tires and to present them in a suitable form for vehicle dynamic computer simulations. They prepared an empirical tire model and equations were available for

- Cornering stiffness as function of load (constants A_0, A_1, A_2),
- Camber stiffness as function of load (constants A_3, A_4),
- Peak lateral force coefficient as function of load (constants B_1, B_2, B_3),
- Peak braking coefficient as function of load (constants P_0, P_1, P_2),
- Slide braking coefficient as function of load (constants S_0, S_1, S_2),
- Longitudinal slip at peak braking force as function of load (constants R_0, R_1),
- Overturning moment as function of vertical load, lateral force, and inclination angle (constants C_1, C_2, C_3),
- Aligning torque as function of vertical load, lateral force, and inclination angle (constants K_1, K_2, K_3).

The equation developed for cornering stiffness as a function of vertical load was

$$C_\alpha = (-\partial F_y/\partial\alpha)_{\alpha=0} = [A_0 + A_1F_z - (A_1/A_2)F_z^2]\pi/180. \qquad Ib/deg \qquad (1.131)$$

Camber stiffness as function of vertical load was modeled

$$C_\gamma = (-\partial F_y/\partial\gamma)_{\gamma=0} = [A_3F_z - (A_3/A_4)F_z^2]\pi/180, \qquad Ib/deg \qquad (1.132)$$

and for peak lateral force coefficient as function of vertical load, the model equation was

$$\mu_{yp} = F_{yMax}/F_z = B_3 + B_1F_z + B_4F_z^2. \qquad Ib/Ib \qquad (1.133)$$

The equation developed for peak braking coefficient as function of vertical load was

$$\mu_{xp} = F_{xPeak}/F_z = P_0 + P_1F_z + P_2F_z^2, \qquad Ib/Ib \qquad (1.134)$$

for slide braking coefficient as function of vertical load,

$$\mu_{xs} = F_{xSlide}/F_z = S_0 + S_1F_z + S_2F_z^2, \qquad Ib/Ib \qquad (1.135)$$

and for longitudinal slip at peak braking force as function of vertical load was given as

$$S_{LP} = R_0 + R_1F_z \qquad (1.136)$$

On the other hand, the equation developed for overturning moment as function

of vertical force, lateral force and inclination angle (in radian) was

$$M_x = (C_1 + C_2\ |\gamma|)\ F_y\ F_z + C_3\ \gamma\ F_z, \qquad ftIb \qquad (1.137)$$

and for the aligning torque as function of vertical force, lateral force and inclination angle (in radian), the equation was given as

$$M_z = (K_1 + K_2\ |F_y|)\ F_y + K_3\ F_z\ \gamma/\sqrt{|\gamma|}. \qquad ftIb \qquad (1.138)$$

These eight equations contain 22 coefficients. A data reduction computer program was developed permitting computation of all coefficients from raw data recorded on Tire Research Facility (TIRF). Finally, test results for each tire were presented in the following form [33]:

- A list of tire identification data, such as size, brand name, and cord material; and a list of run identification data such as run number, road speed, and design load,
- A tire footprint,
- Tire uniformity data,
- A list of cornering computer model constants and tire coefficients, such as cornering stiffness, camber stiffness and pneumatic trail,
- A list of braking computer model constants and tire coefficients, such as peak braking coefficient, and braking stiffness,
- A plot of lateral force versus slip angle at various loads,
- A plot of lateral force versus slip angle at various camber angles,
- A plot of braking force coefficient versus slip ratio at various loads.

1.2.3. Finite Element Models

Parallel to developing computer technology, finite element modeling has become a popular tool to tackle more complex problems like tire structure. There are many different finite element tire models available in literature. Each uses different modeling

techniques, assumptions and finite element codes. Also, different aspects of tire analysis are examined. Cornering analysis, lateral force characteristics, vibration analysis and durability analysis are some areas of tire analysis. In addition, there are many different methods for modeling cord-rubber reinforced structures. Some investigators use classical laminate theory and Halpin-Tsai equations, some others use rebar elements embedded into continuum elements to model reinforcing parts of the tire. Layered continuum and shell elements are used to model tire structure as well.

In this section, each modeling technique, finite element codes, assumptions, scope of the studies and also results are given in detail.

Noor and Tanner [1] presented a review of computational models available in literature and pointed out the deficiencies of them. They mainly focused on a number of aspects of tire modeling: tire materials and their characterizations; evaluation of tire models; characteristics of effective finite element models for tire analysis; analysis needs for tires and impact of the advances made in finite element technology, computational algorithms and new computing systems on tire modeling and analysis.

Danielson et al. [34] presented computational strategies for tire-ground contact analysis. First, they introduced a digital scanning image procedure to determine the cross-section of the tire, geometric detail and the location of reinforcements. They pointed out three new strategies for reducing the computational effort. Reduction strategies use the idea supported by St Venant's Principle that the footprint loads do not significantly stimulate a response in the top portion of the tire. In the first strategy, namely,"omission of elements with little significance", the top portion is omitted and its generalized displacements are specified from inflation analysis. In the second strategy, namely, "partitioning solution scheme", the nonlinear finite element equations are partitioned to get a more efficient solution. In this strategy, tire model is divided into two separate regions. The first region includes elements that are expected to experience a significant response from ground. The other is the remaining part of the tire. The last strategy, namely, "exploitation of the tire coordinate system" uses tire coordinate system to reduce the number of elements in regions of the tire experiencing

small circumferential variations in response. They also presented numerical results to show the accuracy and efficiency of the reduction techniques.

Kabe and Koishi [35] constructed a finite element model of 235/45 ZR 17 radial tire by using ABAQUS. They conducted tire cornering analysis with implicit ABAQUS/Standard and explicit ABAQUS/Explicit. The former describes the steady-state and the latter refers to transient cornering simulations. In rubber parts, Mooney-Rivlin material model is used and reinforcements are modeled by using REBAR elements with linear elastic material properties embedded into continuous elements. They modeled pavement with rigid elements. They presented cornering and self-aligning moment results and compared them with experimental results obtained from MTS Flat-Test Tire Test System. Their model results agree well with the experimental results. In addition, in terms of CPU (Central Processing Units) time, they showed that CPU time for implicit analysis is about 30 times shorter than that of explicit analysis.

Burke and Olatunbosun [25] conducted semi-analytical study using MSC.Nastran V67 finite element solver. They introduced a gap element formulation, which is purely theoretical, to model static tire/road interaction. In this method, gap element status changes when load is applied and corresponding internal forces are computed based on the gap status. So, analyst has a chance to change some parameters to see their effects on tire behavior such as inflation pressure, hub load and material properties. One of the outstanding advantages of this formulation is that one can model contact without prior knowledge of the exact contact area. In the tire model, 780 MSC/NASTRAN CQUAD4 quadrilateral composite shell elements are used to model composite material nature of the tire cross-section. In addition, they constructed Force/displacement equipment setup to show model verification as mentioned before. By making several trial and error runs, they reached. In terms of load-displacement results, for a range of inflation pressure and hub load, proposed formulation is found to be viable and accurate.

Hall and Moreland [36] investigated the quasi-static behavior of 195/65 R 15 tire loaded against a rigid surface. They used Dunlop Tires LTD's technical data in modeling stages. There are 56400 linear solid and membrane elements, which model the

matrix and reinforcements of the tire structure, respectively. Mooney-Rivlin constants modeling rubber parts of the tire are calculated from estimated stress-strain curves using a curve fitting program based on least squares method. The reinforcements are represented by orthotropic elastic material model and their constants are calculated using volume fractions and estimated elastic constant data for the constituents using Halphin-Tsai micromechanical equations. On the other hand, the wheel and the surface are modeled using 1400 quadrilateral shell elements. Both of them are assumed to be rigid. Contact modeling is carried out by using surface-to-surface interfaces defined penalty formulation available in LS-DYNA3D program. Friction coefficient of tire-wheel interface is 0.1 and dynamic friction coefficient of tire-surface region is taken as 0.7. In addition, they compared model results with experimental results taken from Dunlop Tyres LTD and they got excellent agreement between the results. However, in terms of contact dimensions, they pointed out that there exists a discrepancy between model and experimental results. They explained reasons as the density of the mesh or capability of the contact algorithms used in LS-DYNA3D.

Pelc [37] constructed a finite element tire model using MSC. Marc to calculate displacements, radial stiffness, delimitation stresses, shape of contact patch and pressure distributions occurring in the contact patch. They modeled the cord-rubber composite by using rebar elements. A 9-node incompressible rubber element is used for the mechanical properties of single-ply rubber and 8-node orthotropic element is used for a single-ply steel cord. The elastic constants for orthotropic elements are predicted using Halphin-Tsai equations with negligibly small Young's Modulus of rubber ($0.01MPa$ is taken). Rubber materials are described using third order strain energy function. Pelc [37] used Coulomb friction model with a coefficient of friction of 0.3 between contacting bodies. He showed delamination stress and strain energy density at the centroid of rubber located between the second and third belts, in the belt edge zone. In addition to these, he compared his model results with experimental results and found excellent agreement between them.

Huh and Kwak [38] developed an updated Lagrangian finite element contact formulation for stress analysis of the reinforced tires under inflation pressure and contact

with rigid flat surface. Different from well known equations for composite structures such as Halpin-Tsai, Gough-Tangorra and Akasaka-Hirano equations, they considered bending effects of reinforced cords. To demonstrate validity of proposed formulation, they compared model results with experimental data and also with well known equations' results in terms of contact deformation of the section height and width. When comparing experimental results, their results are found to be more accurate than the results of Halphin-Tsai, Gough-Tangorra and Alaska-Hirono equations. In addition, they obtained stress distributions for different belt angles. Maximum equivalent stress is found to be at minimum when the belt angle is taken as 20^o in comparison with 30^o and 45^o belt angles. They plotted contact pressure for various belt angles and load. The contact pressure at the edge of the contact surface decreases smoothly to zero when the belt angles are 20 or 30, but increases suddenly when the belt angle is 45^o. Moreover, it is found that the contact surface decreases as the belt angle increases. They finally stated that the belt angles of $20^o - 30^o$ are the optimum for tire design. They concluded that the deformation mode under a heavy load leads to severe wear around the corner of the crown. This is also attributed to the increasing contact surface as the load increases.

Yan [39] developed a nonlinear 3-D finite element model of 900 R20 radial truck tire. They simulated rubber compounds as incompressible elements. Their material characteristics are modeled using Mooney-Rivlin model. Belts, carcass and bead are modeled by equivalent orthotropic material model based on Halphin-Tsai equations. The contact condition is treated using variable constrained method presented in [40]. Yan [39] used Lagrangian method to include large deformation effects of the tire. On the other hand, for numerical illustration of the model, he developed an in-house finite element code in which there are two kinds of 3-D element, namely an 8-node brick isoparametric and 6-node isoparametric elements. Also he used three different mesh densities of quarter tire model for footprint loading analysis. He took five different loading conditions which are inflation, 10, 20, 32 and $40mm$ deflections. He presented the maximum sectional width, resultant reaction force and the contact area of tire-foundation. He also gave the variation of pressure distribution, size and shape of contact area for different footprint deflections. He compared model results with results

of Clark in [41] and found consistency between them. In addition, he gave normal and shear stress distributions in belt plies. Finally he stated that his numerical results showed that the model proposed is reliable and convergence is fairly good.

Patel and Kennedy [42] formulated a geometrically nonlinear finite element model for axisymmetric structures under axisymmetric loading with general orthotropic material properties in plane of fibers. They used pseudo-three dimensional approaches in which geometry and displacements are specified as axisymmetric but displacements in all three coordinate directions (circumferential, axial and radial direction). To do so, they used 6-node linear strain axisymmetric triangular elements having three displacement components at each node. They also constructed in-house program to solve the finite element equations. They considered two problems: thin shallow spherical shell made of isoparametric materials loaded by a vertical load at the apex, and a radial truck tire under inflation pressure. In the second problem, they took Poisson's ratio as 0.47 to model nearly incompressible rubber and they did not consider viscoelastic effects. Only half of the tire is modeled in which there are 18 material groups, 520 elements and 1131 nodes. The predicted shapes of the tire cross section at the final state are consistent with experimental results. They also plotted the shape of tire under inflation pressure using linear analysis. As expected, nonlinear analysis gave more accurate representation of the tire under inflation pressure. They also presented maximum interlaminar shear strain distribution across the belt width. This distributions matched well with experimental results. Although there was a convergence problem in the model, their results agreed well with experimental data.

Wallerstein and Dilley [43] proposed a finite element model to predict load-deflection characteristics of a tire and determined the response of it to lateral movement of the tread-ground interface by using linear elastic materials and layered composite plate element in MSC.Nastran. They constructed a partial 3-D model consisting of 616 physical grid points with 2094 degrees of freedom. In this model, QUAD4 isotropic plate elements are used to represent the basic tire structure including the individual component plies, BAR elements to model the tire bead, GAP elements to model tire-ground contact and TORSION SPRING element to represent the torsional stiffness of

the rubber in the bead region. In terms of load-deflection result, the axle loads are predicted within 15 % of the loads obtained experimental study. They also pointed out that mesh size changes may cause numerical inaccuracy in the calculation of pressure loading which in turn, cause a circumferential load to be produced at the boundary between the meshes having different size. So, this results in rigid body motion. Moreover, they concluded that the tire can be modeled by using thick walled anisotropic shell structure. However, more exhaustive experiments need to be done to substantiate the use of shell elements.

Watanabe and Kaldjian [44] developed a finite element model for a bias-ply motorcycle tire using a finite number of cords and rubber slabs. They omitted the tread part of the tire for simplicity. In the model, 3-D solid elements of linear, low modulus, isotropic, nearly incompressible material are used to represent rubber matrix in the sidewall or tread. The cords in the sidewall or tread are modeled by truss element. The bead area is modeled by using elements which are linear, anisotropic, elastic and 3-D solid. However, they mentioned that there are two disadvantages of this tire representation. One of them is that in the real cord-rubber lamina, the bonding between cords and surrounding rubber is probably at least more than 60 % whereas the cords are bonded only at their ends to solid elements at the diagonal corners in this model. Other deficiency of this model is the coarseness of element size and limited number of cord layers. In actual tires, the number of plies is generally more than two and the end count of cords is usually near $25/inc$, while in the present model, there are cord angle arrangements between inner and outer surface of rubber slab. Although this problem affects the stress distributions over the tire negatively, the model gives better results in terms of load-displacement behavior. On the other hand, a couple of merits can be drawn for this model. An advantage is that unlike shell model, there is no need to recalculate the anisotropic material properties. They used Goodyear M/C 130/90-17 motorcycle tire and computed all forces and moments acting on the tire. Also, for a contact patch load on tire model, deformations in the cross section at various locations along the tire are plotted. As mentioned, they are looking forward to comparing model results with experimental work currently in progress at the University of Michigan.

Cho et al. [45] introduced an effective 3-D meshing technique with detailed tread blocks of variable depth in an asymmetric pattern. They developed a mesh generation program using I-DEAS and ABAQUS. Initially, tire body and tread mesh are separately generated and then both are assembled and tied. They used CONTACT/PAIR/TIED function in ABAQUS. For numerical applications, they used P205/60R14 automobile tire. To validate the proposed technique, they conducted experimental tests in the research center of Kumho Industrial Company in Korea. In static tire contact analysis, their meshing technique does not cause any error. When compared with traditional simplified tire meshes, detailed tire meshing gives realistic and accurate prediction of footprint and contact pressure.

Helnwein et al. [46] proposed an alternative computational approach for finite element modeling of cord-rubber composites. They introduced "rebar elements" concept, which has been successfully applied in concrete structures. In this approach, they modeled rubber matrix as an hyperelastic material and formulated reinforced cords using rebar elements. For rubber materials, Mooney-Rivlin material model is used. The plies are assumed to be Neo-Hookean. Another advantage of rebar element formulation is that it does not increase the degrees of freedom because matrix and reinforcement elements share the same nodes. To demonstrate the capacity of the proposed modeling technique, they constructed the finite element model of a 195/65R15 tire with smooth tread using MSC. Marc. They calculated radial stiffness and obtained pressure distribution in the contact patch under different loading conditions on a rigid pavement. They used eight different types of rubber materials in the model, which is rare in literature. They compared their results to experimental results provided by Semperit Reifen AG, Austria, and they have obtained very good agreement.

Liu et al. [47] developed a direct tying algorithm for linking of two geometrically incompatible finite element meshes with different degrees of refinement. The main idea is to enforce geometric compatibility between them through modification of the coordinates located on their common boundary and to specify displacement constraint to get geometric compatibility. To demonstrate reliability and applicability of proposed algorithm, they constructed two models. One of them is the model with simplified tread

profile in which only circumferential grooves are taken into consideration. The other model consists of more realistic tread patterns. Due to the lack of computer with powerful capacity, they didn't realize the second model. They plotted the load-vertical displacement diagram of the tire with a simplified tread pattern. They presented the distribution of contact pressure obtained from first model. They found a good agreement between numerical and experimental results.

Tönuk and Ünlüsoy [23] proposed a finite element model for a 155R13 radial tire to predict cornering force characteristics of the tire by using MSC. Marc. They constructed a drum-type tire testing machine to verify their results. For rubber parts in the model, both Mooney-Rivlin and linear elastic material properties are used and large displacement effects are considered. Their initial static tire model tests have revealed that because of the stiff reinforcements of the tire structure, strains in the rubber matrix of the tire rarely exceed 20% and linear elastic approximation with large displacements showed similar tire behavior with the one obtained using Mooney-Rivlin material model. They used continuum elements to model rubber matrix and rebar elements to model textile and steel reinforcements. They modeled the drum as a deformable body with relatively stiffer material properties. In the model, contact of the tire and rim is simplified with "total contact" of the tire to a rigid rim at the bead, and they ignored bead bundle contact. In tire rolling model, the tire is fixed and the drum rotates around the tire, which is called the kinematic inversion method. They concluded that their model is capable of predicting cornering force characteristics of radial tires to an acceptable accuracy. However, for larger vertical tire loads, the cornering force can be calculated only for small slip angles.

Erşahin [48] developed a tire model using finite element method to predict cornering force characteristics of the tire using MSC. Marc. The tire is the one used in [23] and its finite element model is prepared by LS-DYNA. For rubber parts, he used two different sets of material properties. Linear elastic material properties are used for initial model setup and program parameter adjustments. In the cornering simulation stage, he used Mooney-Rivlin material model. Material properties for steel and textile reinforcements are analytically derived. First, he represented reinforcement layers by

using continuum elements with orthotropic material properties and then, he used truss elements to model textile body plies. In addition, he modeled drum and rim as rigid bodies. Rim is glued to the tire and then bead bundle is ignored. He compared his results with layered shell and continuum element results. Layered shell representation of the tire model resulted in bigger vertical stiffness than that of layered continuum representation. He attributed this result to bending stiffness of shell elements. He presented cornering force and self-aligning torque plots for different normal loads and slip angles. He examined the tire behavior on both flat and cylindrical surfaces. Comparison of his results with experimental results taken from Tönuk's thesis [24] yielded satisfactory agreement.

On the other hand, it is a well known fact that when a vehicle runs on roads, the tire frequently rolls over various kinds of road roughnesses. A major source of disturbance on a vehicle is the force transmitted to the axle. These interactions affect the tire performance, ride and handling negatively. During tire-cleat impact process, most of the dynamic impact forces are absorbed by the tire and some remaining are transmitted to vehicle. In tire design, for improving vehicle dynamic stability and ride-comfort of passengers, an accurate understanding of tire-cleat interaction is of great importance. In the following parts of this section, tire enveloping characteristics which is another important topic in tire study will be presented. The word enveloping is a traditional description of tire properties that enable the pneumatic tire to partially swallow the obstacle while slowly rolling over it. Its current meaning has been extended to include tire's responses on uneven roads [49]. One of the earliest experimental studies of tire enveloping characteristics is the one conducted by Julien and Paulsen [50]. They conducted an experimental study for measuring and defining the absorbing capacity of a pneumatic tire. They stated that the absorbing capacity increases when pressure decreases and vice-versa. In addition, for a given inflation pressure, the cleat absorbing capacity of a tire decreases quickly as deflection diminishes, for similar obstacles, it is higher with smaller obstacles. At equal obstacle heights, the absorbing capacity is greater for short obstacles than for long, but, for equal obstacle sections, it is less for short obstacles.

Gough [51] considered bias-ply and radial truck tires and noted that the forces generated when tire rolls at constant axle height over a 1x1 inch bar that extends full width of the tire are little different. He also stated that if the forces developed by a tire rolling over an asymmetrically placed obstacle are studied there are substantial differences in lateral forces developed by two types of tires. He suggested that suspensions are designed to be soft in the vertical direction but very stiff in other two directions and therefore provide good transmission paths for force fluctuations.

Chiesa et al. [52] conducted an experimental study on high frequency tread and sidewall vibration of both radial and bias-ply tires. They used a drum with large diameter, a road wheel. There were two types of disturbances considered: a small cleat fastened to the road wheel, and percussion of the tire with a rod. The accelerations associated with the oscillations transmitted from the tire to hub were recorded. Medium and high frequency cases were observed. They stated that the former is dependent on tire dynamic stiffness and inertia of the oscillation system. Using a similar test setup, Mills and Dunn [53] carried out an experimental study to explore the vertical response and resonance frequencies of the tire. Different speeds and radial and bias-ply tires were considered. They concluded that higher frequencies appeared at higher speeds as expected. They used different types of cleats. Among velocities they considered, the vertical resonance is intense in the 15-25 mph speed range and the longitudinal force is intense in the 25-30 mph speed range. They stated that although the same frequency for two different cleats were observed, the magnitude is somewhat different. In addition, they concluded that damping must be considered as well.

Böhm [54] presented a study of radial tire using a ring on elastic foundation model. He compared resonant frequencies obtained to experimental results. Based on Böhm's analysis, Majcher [55] conducted a similar study considering damping and rotational effects of the tire. He calculated resonant frequencies of the tire with wheel locked and free to rotate. He presented time plots of tire forces and moments while tire impacting the obstacle. Both experimental and simulation results showed that vertical forces oscillated at nearly 58 Hz and longitudinal forces at 28 Hz. He found out that simulated and experimental axle forces and moments show similar trends but

are not identical. Gough et al. [56] defined the transmission ratio of a rolling tire as the square root ratio of power densities of surface and the axle. They mentioned that care must be taken as the value for a particular surface at given test speeds. Takayama and Yamagishi [57] defined the transmissibility of a tire as the ratio of its output force (going to axle) to its input force (coming from its ground contact). They constructed a mass-spring tire model having five degrees of freedom to investigate tire enveloping forces. 2-D in-plane forces and displacements are assumed to occur when the tire rolls on road. However, out of plane forces and displacements are not considered. Cleat forces determined experimentally are taken as input forces for the dynamic modeling. They defined an enveloping index as a function of position of cleat along contact patch. In the case of very low speeds, the radial force curve along the tire footprint has two peaks. They concluded that while transmissibility is the dominant factor at low speeds, input from cleat and contact pressure dominate at higher speeds. He studied two cases: Tire vibrations at 40 km/h and at 80 km/h. He found out that damping is more effective at 40 km/h.

Lippmann and Nanny [58] used linearity and superposition principle to explore tire enveloping characteristics at low speeds. A linear model for tire-road system was developed and its validity was checked using experimental results. They used different deflection and inflation pressure values to examine effects of operational conditions on tire enveloping forces. They stated that a greater part of forces resulted from inflation pressure, and they focused on the pneumatic mechanism and discussed volume changes of tires on both smooth and irregular road surfaces. They constructed a test stand for measuring inflation pressure changes during enveloping of cleats. They mentioned that volume changes due to irregularities do not explain the vertical enveloping components completely, size of surface irregularity and axle height should be considered as well. For the tire to develop vertical pneumatic enveloping components, volume changes on enveloping irregular surfaces must occur.

Bandel and Monguzzi [59] constructed a mathematical model to investigate vertical and horizontal force variations at the hub by considering the tire encountering obstacles at both low and high speeds. Starting from experimentally obtained force-

deflection diagram, they defined a “basic curve” and offset law to fit a curve to experimental data. By dividing forces by vertical stiffness of the tire, the curve obtained represents a characteristic of the tire which is independent of its inflation pressure and displacements. After this transformation, the curve can be regarded as the shape of obstacle transformed or filtered by the tire. The shape of the curve depends on the shape of the obstacle. Before investigating high speed cases, they examined the low-speed case. The low-speed forces are taken as input for 1 degree of freedom high speed modeling to get high speed forces. An experimental study was also conducted to determine vehicle model parameters like vertical stiffness and vertical damping coefficient. To check the validity of the proposed model, they compared calculated vertical and longitudinal enveloping forces with experimental results. They compared calculated and measured maximum peaks of forces as a function of speed and determined the accuracy of their model.

Nakajima and Padovan [60, 61] conducted a finite element analysis using ADINA 77 to examine sliding contact on an arbitrarily shaped surface and then, on triangular holes and bumps. The response of a tire over a bump is related to passing time over the bump and to resonant frequency of the tire. Therefore changing the velocity magnitude leads to change in passing time and impact forces. So, overall tire response changes by velocity change. They showed that the tire bounces off the ground after sliding over the bump. They considered different velocity cases. For the low sliding velocity, a ”camel-back” response curve is seen. This behavior is highly distorted at high velocities.

Bereś [62] carried out static tire tests, and using load-deflection curves, he found an empirical formula for vertical load response of 165-SR-14 tire depending on inflation pressure and displacement. To describe the enveloping effect of a tire rolling along a random surface profile, he assumed the tire to be a linear low-pass filter in a spatial frequency domain. He assumed a linear surface contact between the tire and surface instead a point contact. A simulated surface roughness of 15 mm height was used. His results and experimental results agreed well. For proper measurement of tire enveloping properties, various tires, inflation pressures and surface roughness should be considered.

Wei et al. [63] constructed a tire model based on ring on the elastic and viscoelastic foundation (REF) to investigate tire-road contact problem on both flat and uneven road conditions. They mentioned that both damping and velocity have strong effects on tire enveloping characteristics and they showed that the frequency of dynamic load is mainly controlled by the first tire mode.

Dihua and Chengjian [49] proposed a tire model using experimental modal parameters to calculate static vertical tire stiffness on both drum and road surfaces. They used their model to investigate tire enveloping properties. They examined obstacle's effects on tire vertical properties, the axial load responses under rectangle obstacles with a fixed axle height and the effects of tire pressure on enveloping properties. A qualitative explanation for typical operating conditions of enveloping properties was given in regard to shear forces and moments they cause in contact patch. The distribution and magnitude of shear forces influence tire vertical stiffness. Slowly rolling tire has less stiffness than static one. The vertical stiffness of the rolling tire was found to be smaller than that of the static one by about 5-10 % . These facts showed that different tire stiffnesses result from different contact conditions, depending on contact patch length, distribution of contact pressure and shear forces under the same vertical load. These phenomena can be used to explain tire static enveloping properties. Their results showed that under low deflection, the vertical axle load curve has two maxima; between them a minimum occurs when the axle is located directly above the center of the obstacle. Under large deflection, the minimum occurs even lower than the vertical load on a flat surface. In the second case, the center height was constant but the height of the obstacle changed. When the height of the obstacle is small enough (5 mm) the minimum vertical axle load becomes even lower than that on a flat surface.

Based on [49], Dihua et al. [64] constructed a tire model in which tire sidewall nonlinear characteristic is included. They did experimental studies using a flat tire test rig. They determined that the vertical force at the patch center is even lower than that on a flat surface. This is a typical enveloping characteristic of a tire. They pointed that the calculated results for force amplitude agreed well with experimental data, but the contact time of the tire with the obstacle is shorter than that measured in the

experiment especially for higher loads.

In addition to above two studies, Chengjian and Dihua [65] conducted a quantitative tire analysis based on [49]. Their model was developed considering the influence of the modal order numbers and tire sidewall nonlinear stiffness, which improved their results. When calculating static enveloping properties, cleat location varies on the flat surface used. It can be seen for a certain height (10 mm) of the obstacle, although the tire vertical deflection is big, the vertical force at the position of the contact patch center is lower than the vertical force on a flat surface.

Kamoulakos and Kao [66] proposed a transient dynamics study of tire rolling over small obstacles using experimental and numerical techniques. For numerical calculations, they used PAM-SHOCK. They presented static and transient tire-cleat impact results obtained using PAM-SHOCK and experiments. Although predicted spindle forces were higher than those measured experimentally, the frequency contents and overall characteristics of numerical results showed good correlation with the experimental results.

Chang and El-Gindy [67] constructed a nonlinear finite element model of a passenger tire. Their virtual tire/drum finite element model was tested using nonlinear finite element software, PAM-SHOCK. Reaction forces at the tire axle in vertical and longitudinal directions were recorded when the tire rolled over a cleat on the drum and they used FFT (Fast Fourier Transform) algorithms to examine the response information in frequency domain. They got satisfactory results when they compared model results with those of ten previous theoretical and experimental studies available in literature. They concluded that the tire has peaks of 84 and 45 Hz transmissibility in vertical and longitudinal directions and that tire size, construction, inflation pressure and operating conditions like loads and temperature affect the resonance frequency of the tire free vibration modes. They ignored displacement and forces out of vertical plane. They also concluded that only the first free vibration resonance in the vertical direction can be transmitted to the vehicle; all of the second-and- higher order modes' vibration will be absorbed without transmitting forces to the axle since they

are completely symmetric.

Zegelear and Pacejka [68] investigated in-plane dynamics of tires on uneven roads. They considered two situations of tire rolling over unevenness: quasi-static rolling at very low velocity and dynamic rolling at high velocity. For the quasi-static rolling simulations, a flexible ring model was used. The responses of the tire measured and simulated at quasi-static conditions were transformed into effective inputs. These effective inputs were used in a simpler model, rigid ring model. This model was used to simulate the dynamic behavior of the tire rolling over the road unevenness, also at higher velocities. Detailed information is given in [69]. Although forces generated by the model are slightly larger than the measured ones, their variation is quite similar. They stated that the response of tire at higher velocities showed that the relative damping of the in-phase mode increases with velocity while the relative damping in out-of phase modes is almost constant.

Mousseau and Clark [70] proposed a tire model based on ring on elastic foundation (REF) model that uses finite elements to analyze a tire rolling over a stepped cleat at low speed. To implement the model, they used ABAQUS. The experiments were conducted using the flatbed tire test machine at the University of Michigan Transportation Research Institute (UMTRI). The results showed that inflation pressure and foundation axial stiffness have the greatest influence on tire forces. Other parameters such as surface friction, tread axial stiffness, bending and shear stiffness do not significantly affect the hub force magnitude and shape. Another important issue they considered was the computational efficiency of the simulation. They mentioned that the model is suitable for vehicle dynamic simulations.

Mousseau and Hulbert [71] constructed a tire model which is an extension of the work of Mousseau and Clark [70]. The model uses an extensible, circular membrane to approximate the shape to account for forces that result from elastic deformation of the sidewall. They showed that their model is efficient and produce more accurate results than those of traditional simple tire models. Mousseau and Hulbert also investigated dynamic response of spindle forces resulting from a tire impacting large obstacle in a

plane [72]. They concluded that the first tire modes of vibration and damping play an important role in the tire response. They have also noted that although experiments and simulations were conducted on drum and flat surfaces, respectively, the results showed good agreement. Detailed information on both slow and high speed tests can be found in the work by Mousseau [73].

Darnell et al. [74] constructed an efficient 3-D tire model to predict spindle loads produced from durability road events, such as curb or chuckhole impact and off-road scenarios and account for lateral, vertical and longitudinal behaviour of the tire. They conducted quasi-static experiments and considered four different cases; namely, vertical load, lateral load, normal step rollover and oblique step rollover (20^o angle). They compared calculated and measured results to show the accuracy of the model.

Although considering a tire as a one body gives very important information, tire-vehicle modeling should be considered [1]. Mousseau et al. [75] presented a comprehensive vehicle dynamic model to simulate the dynamic response of the ground vehicles on rough surfaces. They used ADAMS to simulate the vehicle and a nonlinear finite element model to model tires. Parallel processing of the tire model improved the efficiency of overall simulations. They concluded that for the case of vehicle driving on an obstacle, the combined tire and vehicle simulation was able to predict the vertical spindle forces accurately. However, the spindle longitudinal force predictions were less accurate.

Schemeitz et al. [76] conducted a detailed tire enveloping studies and proposed a semi-empirical dynamic tire model to investigate tire enveloping properties on various types of road irregularities. First, they examined different enveloping models and they decided to use the tandem model with elliptical cams mounted in a quarter vehicle system. They conducted different experiments. The quasi-static experiments carried out at Vehicle Research Laboratory of Delft University of Technology were used to validate the enveloping model. Experiments carried on 2.5 m drum were used to validate dynamic model. In addition, they carried out some tests using instrumented vehicle. They calculated and measured the power spectral density (PSD) of different road pro-

files. Time domain responses were compared for triangular bump and the pothole. When compared to experimental results, their proposed tire model gave satisfactory results.

Day [77] proposed a new tire-terrain model showing the capability of simulating tire interaction with irregular terrain. The model not only simulates non-homogeneous pressure distribution at the footprint, but also simulates forces and moments produced by the tire sidewall interaction with pavement edges, curbs and soft soil.

Mousseau and Sayer [78] examined how changes in the tire and suspension impact the dynamic spindle force response of automobile tire rolling over an obstacle on a roadway. The tire model uses an inexentensible, circular membrane to approximate the shape and an empirical, nonlinear term to account for forces that result from the elastic deformation of the sidewall. To illustrate the method, a simple 2 DOF quarter-car model generated with AUTOSIM, namely radial spring model, was used. Both radial spring and tire FE models were used to generate spindle response for test cases. The radial spring model was tuned to match the FE model over a narrow deformation range in the vicinity of initial static load. The results of tire FE and radial spring models show that the most notable differences between two models are high frequency oscillations which are present in FE results and not present in results of radial spring model. Because the radial spring tire model is a purely static model, it misses high frequency oscillations that involve tread bending. Mousseau and Sayer examined the following parameters: inflation pressure, mass of the tread and suspension stiffness. The inflation pressure affects both static tire stiffness and the frequency mode. In this example, the inflation pressure affected the horizontal force more than the vertical load. As expected, the frequency of oscillations changed with inflation pressure. The mass of the tread affected the magnitude of longitudinal force more than the vertical load. There is a little difference in magnitude of vertical force between the two responses. However, the frequency of oscillations is significantly different between base tire and base tire with 150 % tread mass. Change in suspension stiffness results in very small change in the spindle force.

Lugner et al. [79] conducted a detailed review of tire models and testing procedures. They discussed some tire models, with their basic concepts and gave plots to clarify the idea behind the models. The necessities of the cleat tests were mentioned. In addition, Zoeppritz [80] tabulated some parameters affecting the tire behavior and presented their requirements and design measures. He mentioned that accurate representation of vehicle suspension behavior required the testing of tire compliance.

Cho et al. [81] extended the work published of Cho et al. [45] on generation of 3-D tire model to the transient dynamic analysis of tire impacting a cleat. To reduce CPU time, two belt layers embedded in rubber matrix and carcass layer in innerliner are represented using shell elements. Steel cords and underlying rubber matrix in bead region are modeled as homogenized solid elements. Rubber parts except for fiber reinforced rubbers are modeled using Mooney-Rivlin material model with three constants determined from experiments. Frictional dynamic contact problem is formulated by using total Lagrangian scheme and penalty method. The dynamic viscoelastic effect is included by imposing mass-proportional damping to tire parts showing significant lateral deformations. As an example, they gave numerical illustration of P205/60R15 tire rolling over a rigid cleat with 50.8 mm width and 12.7 mm height protruding from a rotating rigid drum having with 1.7 m diameter. The drum and cleat were modeled as rigid elements. They presented deformed configurations of the tire and normal and tangential stress contours at the start and at the end of impact. Due to the relatively higher stiffness of the shoulder part, the normal stress shows higher stress concentration at the tire shoulder. They also examined time-history and frequency response of the dynamic forces and compared them to experimental results. Inflation pressure and rolling speed effects are investigated. They concluded that the rolling speed has a significant effect on dynamic response of both vertical and horizontal forces. Inflation pressure does not produces remarkable variation in the transient dynamic response of horizontal forces.

Nonlinear nature of tires and large deflections occurring in misuse situations make tire modeling difficult. Relatively simple models, that use rings and springs to represent belts and sidewall respectively, do not represent nonlinear aspect of the

problem adequately. Finite element models are alternative techniques, but they are computationally expensive. Developments in computer technology make the Multi Body System representation of vehicles together with tire finite element models of tires to be an alternative tool to tackle this problem. Hanley et al. [82] investigated what is required in tire models applied to misuse and vehicle dynamic simulations. Misuse refers to a tire encountering large deflections resulting from impact of a tire with large obstacles such as curbs and potholes. To model tire under these conditions adequately, the model should fulfill some requirements. The model should predict dynamic tri-axial forces at hub, should be applicable to a range of tire size and tire data. They pointed out that in terms of element selections, instead of using brick or solid elements, shell elements adequately model in-plane bending stiffness of tire carcass. Also, they mentioned that modeling of the air inside the tire-rim assembly is also needed. As an example, they constructed a tire model with PAMCRASH and used a 195/65R15 tire. In the model, rubber parts were modeled by Mooney-Rivlin material model and reinforcements were modeled using linearly orthotropic materials. Layered shell elements were used to represent the composite structure of the tire. Individual bi-phase cord-matrix plies are defined in terms of moduli and volume fraction of the two phases, which combined to yield the appropriate ply modulus. Behavior of the air inside the tire-rim assembly is represented by using an airbag function relating the internal pressure and the volume that uses ideal gas law. Finally, they analyzed dynamic behavior of the tire with 30 km/h velocity and traversing a 20 mm step. They plotted predicted spindle force during loading, acceleration and step traversal stages. They stated that computational efficiency of the proposed model still remains to be a problem.

In Table 1.5, a general review of tire enveloping studies available in literature is summarized with respect to operational conditions, tires used, tester and roughness types.

Table 1.5. General review of tire enveloping studies

Authors	Tire Designation	Tester Type	Cleat Type and Dimensions	Inflation Pressure [kPa]	Vertical Load or Deflection	Tire Velocity [km/h]
Julien and Paulsen [50]	$5.0x15$	Flat Surface	20x20, 30x30,40x40, 60x60,20x80 and 30x120 and Trapezoidal obstacles	68, 98, 127, 157,186 and 216	0, 4, 8, 12, 16, 20 and 24 mm	Slow speed
Takayama and Yamagishi [57]	165 SR 13	Flat Surface	9 mm height	N/A (Not applicable)	3776 N	Taken as a parameter
Lippmann and Nanny [58]	$8.00-14/2$ $8.15-15/2$	Drum	Steps with different heights and different sized composite rectangular cleats	206.8	25.4 mm	4
Bandel and Monguzzi [59]	N/A	Drum	25 mm height and 60 mm width	N/A	0, 17 and 33.4 mm	Taken as a parameter
Bereś [62]	165 SR 14	Special stand	15 mmheight	$90-340$	1370 N	Static
Cho and et al. [81]	205/60R15	Drum	50.8 mm width and 12.7 mm height	137.9, 179.3 and 220.6	4670 N	40, 60, and 80
Dihua and et all [64]	195/60R14	Flat test rig	20 mm width and 10 mm height	250	1962, 4905 and 8829 N	Static
	205/55R16	Flat test rig	20 mm width and 10 and 20 mm heights	250	2940, 4704 and 6468 N	2, 30 and 60
Chengjian and Dihua [65]	195/60R14	Flat test rig	20 mm width and 10 and 5 mmheights	200 and 250	1962, 4905 and 8829 N	Static (cleat position is adjusted)
Kamoulakos and Kao [66]	205/60R15	Drum	Circle with 10 mm radius	262	4316 N	48
Zegelaar and Pacejka [68]	205/60R15	Drum	Trapezoid cleat of 10 mm height, positive and negative steps of 15mmheight	220	2000, 4000 and 6000 N	$0.2-3$, 20, 40, 60
Mousseau and Clark [70]	Radial	Flat bed	50 mm step	208	25 mm	Slow speed
Mousseau and Hulbert [71]	195R15 and R16	Flat bed	50 mm step	208	25 mm	Slow speed
Mousseau and Hulbert [72]	P145SR12	Drum	25 mm high and 660 mmlong step	208	3800 N	51.3
Darnell and et al. [74]	P185/70R13	Flat bed	25 mm step	208	3558 N	Slow speed
Mousseau and et al. [75]	P145SR12	Instrumented Vehicle	760 mm long and 100 mmdeep	243	N/A	48
Schmeitz and et al. [76]	205/55 R15 205/55 R16	Flat plank, drum and instrumented vehicle	Different steps, triangular bump and pothole and from trapezoid to arbitrary shapes of obstacles	N/A	2000, 4000 and 6000 N	32, 40 and 88
Mousseau and Sayers [78]	195/65R15	Flat surface	50 mm step	208	25 and 50 mm	Slow speed
	145SR12	Drum	25 mm high and 660 mmlongstep	139, 208, and 242	3800 N	51.3

1.3. Scope of the Thesis

There are many tire studies available in literature that consider different aspects of tire analysis and investigate different tires under different operational conditions using analytical, experimental and numerical techniques. As shown in Table 1.5, there is a lack of full tire enveloping study which includes the effect of inflation pressure, vertical load, obstacle shape and tire type. This study is conducted to fill the gap in literature and to provide information on fundamental enveloping characteristics of tires. Different inflation pressures and different vertical loads, different cleat types are considered. Four different tire types are tested. In-plane and out of plane forces and moments are measured and calculated.

In this study, first, a static analysis, then a dynamic analysis is carried out using experimental and numerical techniques. In the experimental tire analysis, the tire tester at the University of Michigan Transportation Research Institute (UMTRI) is used. A 155/80R13 78 S tire and three different types of cleats are used and different inflation pressures and vertical loads are considered. The tire is modeled using MSC. Marc. Stress distribution over the cross section of the tire and the vertical stiffness of the tire on surfaces with and without cleat are calculated. Lateral and vertical force characteristics and enveloping characteristics of the tires are studied. Experimental and computational results are compared.

2. EXPERIMENTAL MEASUREMENTS OF STATIC AND DYNAMIC CHARACTERISTICS OF RADIAL TIRES

In order to validate the proposed model and to see the validity range of the results, experimental studies are conducted at the University of Michigan Transportation Research Institute.

In this section, experimental setup is introduced and experimental results are presented. First, for different inflation pressures, vertical stiffnesses of all tires on surfaces with and without cleat are calculated. Then, lateral and vertical force characteristics of 155R13 tire are examined and its enveloping characteristics at low speed are studied. In-plane and out-of plane forces and moments are measured.

2.1. Experimental Setup

The Flat-bed tire tester consists of a rigid test frame and a long steel bed that moves slowly in longitudinal forward and rearward directions. The tire tester is shown in Figure 2.1. The tire tester is an updated version of the flat-surface machine built by B.F. Goodrich, which derives an earlier General Motors device and evolves from the original "flat-plank" tire tester designed and built by Dunlop [83, 84]. The major modification over the previous version of the tester is that the new version of the tester is characterized by a substantially stronger loading frame structure and table support foundation, both designed to reduce deformation under heavy loads applied during truck tire testing. Another modification involves the use of ball-spline bearing to support the dynamometer frame with a minimum of vertical friction restraint. The specifications and performance characteristics of the Flat-bed tire tester are given in Table 2.1 where "OD" stands for the outer diameter and "fps" is abbreviation for foot per second (ft/s or ft/sec).

Figure 2.1. Flat-bed tire tester

Table 2.1. Performance characteristics of Flat-bed tire tester [83]

Velocity:	2 fps (0.61 m/s), (constant)	**Minimum tire size:**	24 in (0.61 m) OD
Length:	18 ft (5.49 m)	**Minimum rim size:**	13 in (0.33 m)
End stop:	1.5 ft (0.46 m)(each end)	**Maximum vertical load:**	10,000 Ib (44482.22 N)
Acceleration length:	3.6 ft (1.10 m)	**Maximum camber angle:**	20 deg
Tire run:	11.4 ft (3.47 m)	**Maximum steer angle:**	35 deg (1 deg inc.); 90 deg.
Drive system:	25 hp (18.64 kW), 1800 rpm	**Torque cell capacity:**	2500 $ft - Ib$ (3390 Nm)
Pinion:	5.5 in (0.14 m) diameter and 83 rpm	**Drag motor torque at** 2000 psi **(**13789.51 kPa**):**	1600 $in - Ib$ (180.80 Nm) (2 used)
Gear ratio:	21 : 1	**Drag motor speed:**	1500 rpm (25.05 rps)
Table weight:	5800 Ib (2631 kg)with concrete	**Gear ratio:**	50 : 1
Acceleration:	0.57 fps^2 (0.17 m/s^2)	**Maximum tire speed:**	30 rpm (0.5 rps)
Maximum tire size:	44 in (1.12m)OD		

The tire resides within the test frame that is positioned with a servo hydraulic mechanism in the vertical direction. The forces and moments that act on the tire hub are measured with load cells located between the test frame and machine structure. Data from analog transducers are converted to digital format on-line. Automated data processing is used later to produce traditional "carpet plots" as well as data sets compatible with UMTRI's vehicle simulation models.

2.2. Tire Tests

Experiments conducted can be grouped into two categories: static and dynamic tests. In static tests, first, the vertical stiffness of the tire is calculated on a flat surface without any obstacle. Then, cleats are placed on different locations of the surface and static enveloping properties of the tire are calculated. At dynamic tests, first, lateral and vertical force characteristics of the tire are investigated. A constant table speed of 2.3 km/h is used and adjusted using control panel of the tire tester. Then, tire enveloping characteristics are investigated at low speeds lower than 1 km/h. In this case, after a tire is pressed onto the surface of the flatbed to obtain a predefined vertical load, table is put to motion slowly with a hand crank so that the tire rolls on the table. Temperature remains almost the same in all experiments. The tires tested are : special purpose pavement test tire, G78-15 ASTM (American Society for Testing & Materials) 524, with smooth tread and maximum vertical load of 6671 N and a maximum inflation pressure of 221 kPa; 225/60R16 with regular tread, maximum vertical load of 7158 N and maximum inflation pressure of 240 kPa; 205/70R15 ASTM 1136 with regular tread, maximum vertical load of 6668 N, and maximum inflation pressure of 300 kPa: and a worn tire 155/80R13 78 S with regular tread and maximum vertical load of 4220 N and maximum inflation pressure of 220 kPa. There are three different cleats used in the tests. Three different cleats are used in the tests: Rectangular cleat with 12.7 mm (0.50 in) height and 50.8 mm (2 in) width, circular cleat with 25.4 mm (1 in) diameter, and a triangular cleat with an apex angle of 90 degrees and a height of 18 mm (0.71 in). The obstacle dimensions are chosen in such a way that their widths (or wave lengths) are smaller than that of the contact patch. This condition gives rise to notable effect on the force and moment characteristics of the tire while traversing

the obstacle when comparing cleats with longer wave length than contact patch. As mentioned in [59, 85], forces acting on axle are not only dependent on road profile but also local deformations. In addition, due to slow rolling, forces dependent on velocity and accelerations are insignificant. In other words, the influence of tire dynamics is suppressed.

The mark for centering the cleats is shown in Figure 2.2a. The cleat position is set and adjusted using this mark as a reference line. Longitudinal position and vertical height sensors shown in Figures 2.2b and 2.2c are used to control and measure the wheel height, longitudinal table position and table speed.

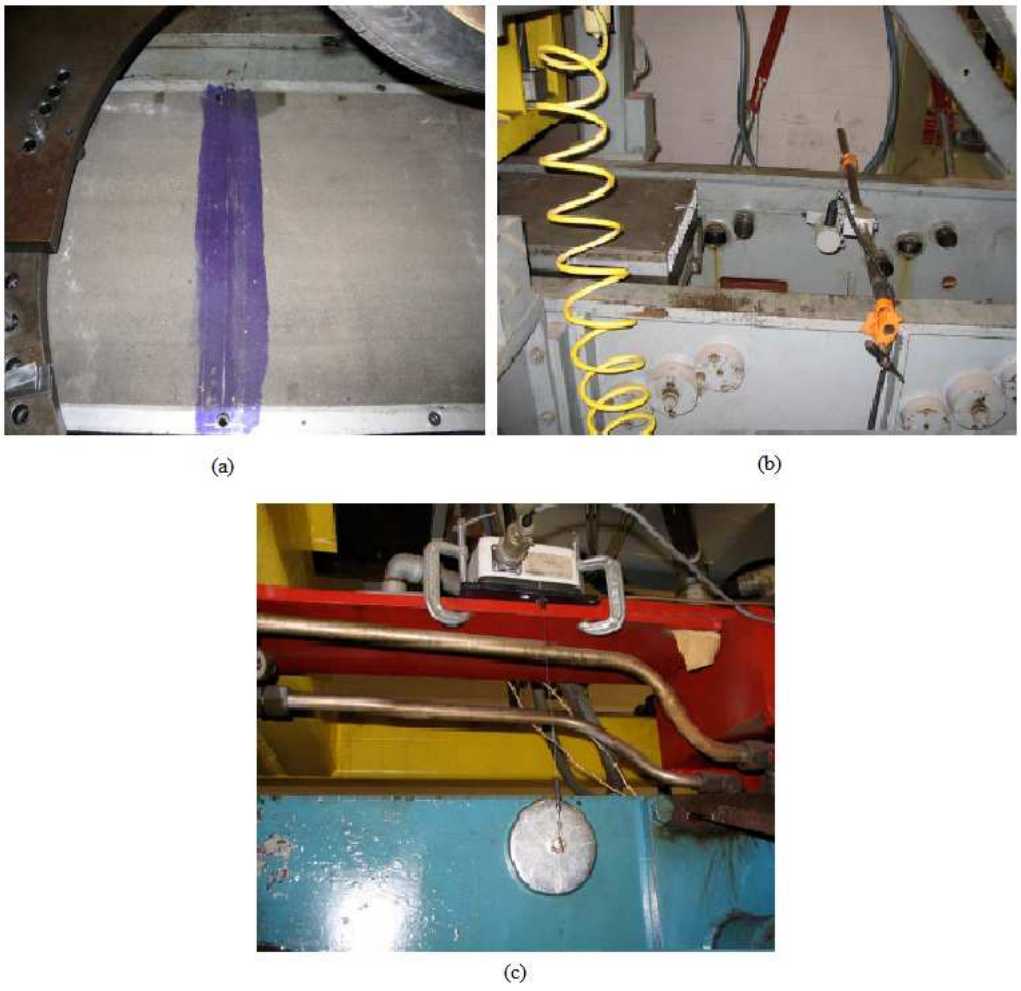

Figure 2.2. (a) Mark for centering cleats (b) Longitudinal position sensor (c) Vertical height sensor

2.2.1. Static Tire Tests

One of the simplest loading cases is static loading of a tire on a flat surface. The vertical stiffness is an important parameter of a tire. In this section, tire static enveloping characteristics are examined. The tire is inflated up to a predefined value and its vertical stiffness on a flat surface without any obstacle is measured. After the measurement of vertical stiffness, static enveloping characteristics of the tire are studied by placing different cleats under the tire. The procedure is repeated changing locations of cleats with respect to the hub center. As shown in Figure 2.2c, vertical rim/tire assembly movement is controlled using a vertical height sensor which gives the height of the wheel with respect to the flat surface. Displacements are the differences between free rolling radius and rim center height measured from sensor. In Figures 2.3- 2.9 it is seen that when the vertical displacement is zero, the vertical force takes a value different than zero depending on the height of the obstacle because the reference point is taken to be the surface of the table. It should also be noted that in literature, to investigate tire enveloping characteristics, a right-handed Cartesian coordinate system (x,y,z) oriented according to ISO 8855 is used. The x-axis is oriented along the intersection line of the wheel plane and the road plane with the positive direction forwards referring to Figure 1.2. The z-axis is perpendicular to the road plane with the positive direction upwards. The y-axis is perpendicular to the wheel plane and its direction is chosen to make the axis system orthogonal and right-handed. This convention produces a positive vertical force. As the tire first encounters the obstacle, the wheel hub feels a negative force (against the direction of travel), then a positive force (promoting travel), as it leaves the obstacle. In this study, a right-handed Cartesian coordinate system is used to investigate tire enveloping characteristics and SAE tire axis system is used for the lateral and vertical force characteristics while a tire rolls on a flat surface.

The vertical stiffness of the tire is measured on a flat surface. In Figures 2.3, for different tire inflation pressures, the effect of pressure on vertical stiffness of 155/80R13, 225/60R16 and 205/70R15 tires is plotted. As expected, higher pressure values make the tire stiffer.

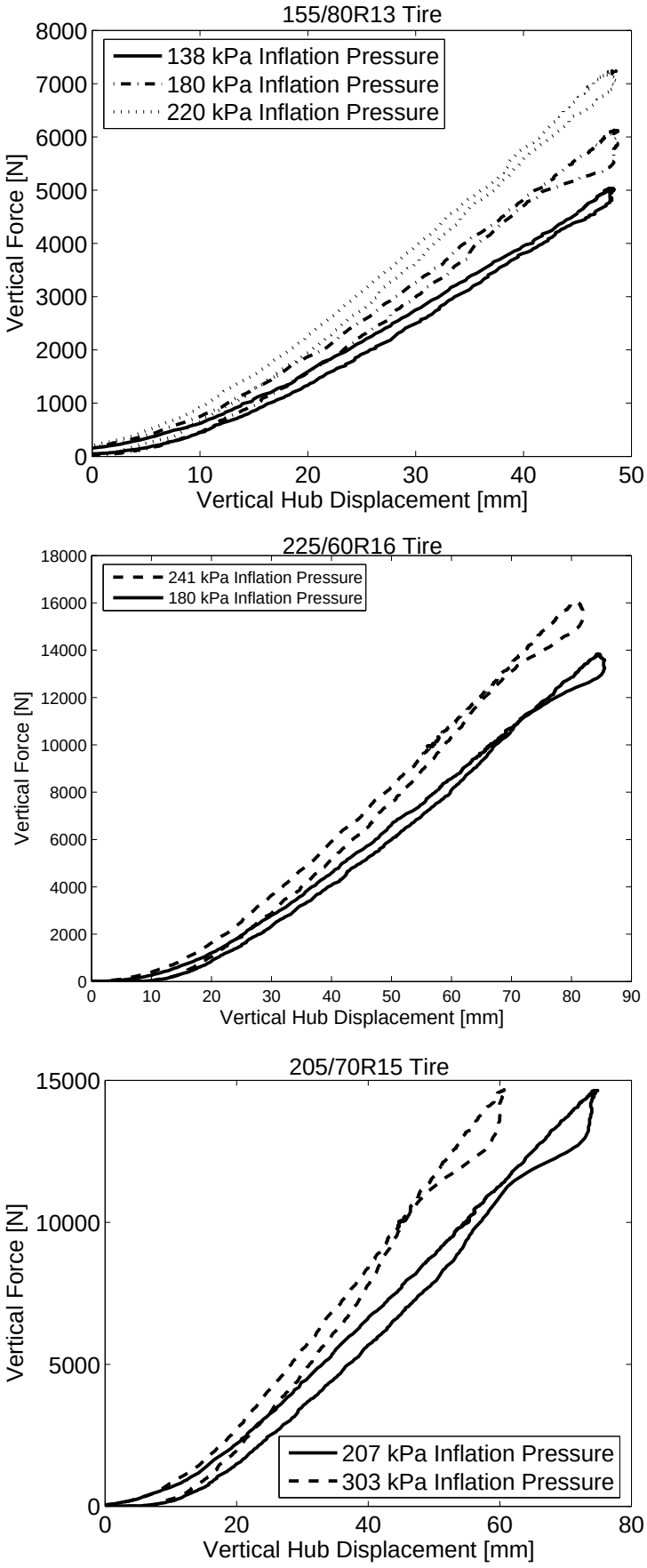

Figure 2.3. Effect of inflation pressure on vertical stiffness of 155/80R13, 225/60R16 and 205/70R15

In the study of cleats, first, the obstacles are centered under the hub center and the vertical stiffness is calculated. Vertical force versus vertical hub displacement plots are given in Figures 2.4 - 2.7. As shown in these figures, after a certain deflection, depending on tire inflation pressure, all curves in force-deflection diagrams intersect. This phenomenon is the typical tire enveloping regardless of the tire construction and size when the obstacle is centered under the hub center. The tire swallows the cleat completely, and it behaves as if there were no cleat at all.

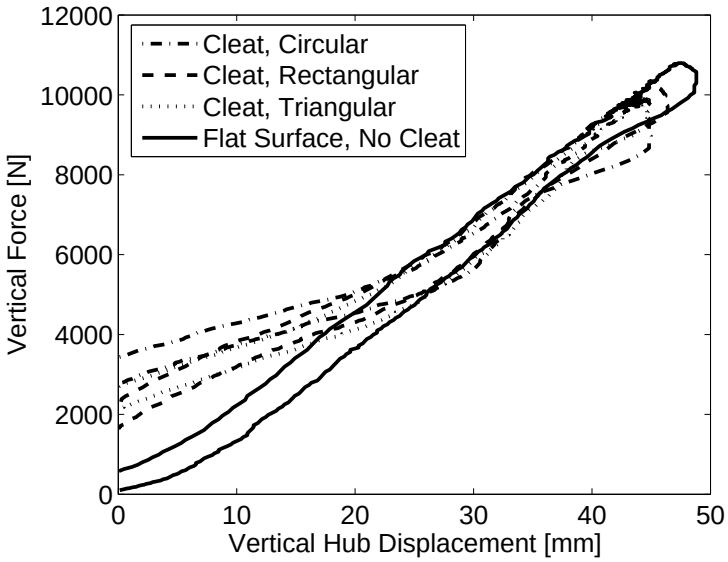

Figure 2.4. Vertical stiffness characteristics of G78-15 for an inflation pressure of 165 kPa

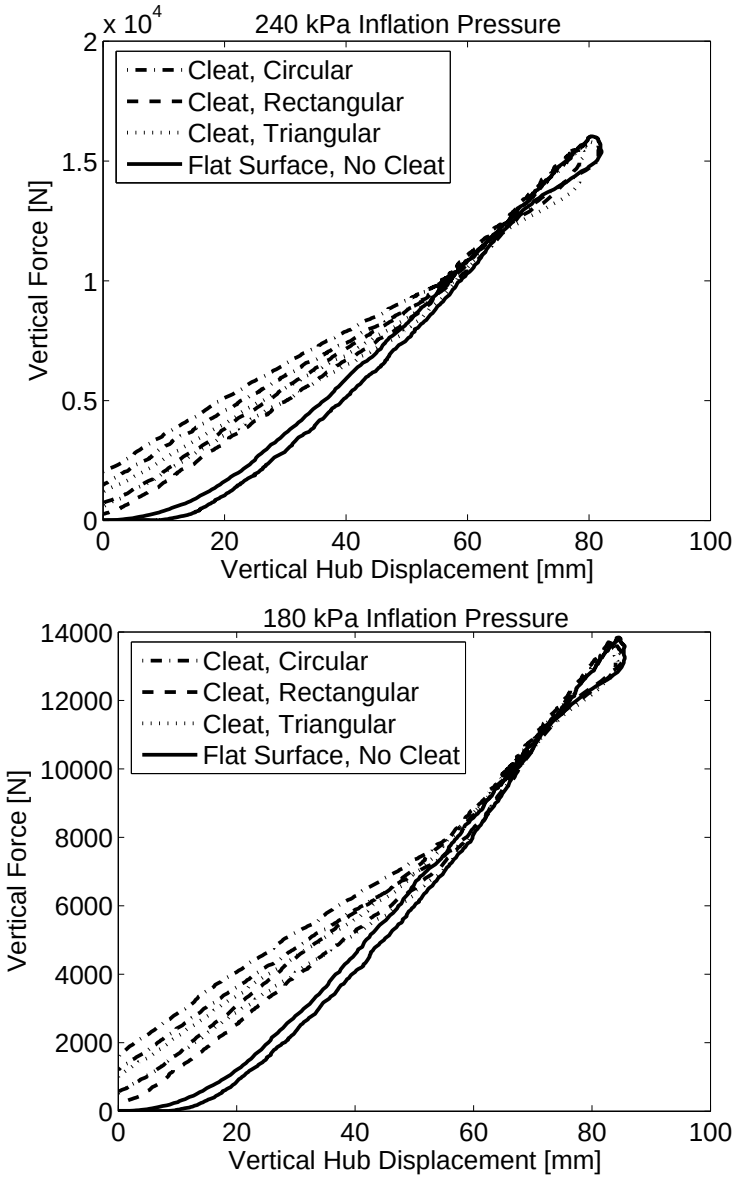

Figure 2.5. Vertical stiffness characteristics of 225/60R16 for inflation pressures of 240 kPa and 180 kPa

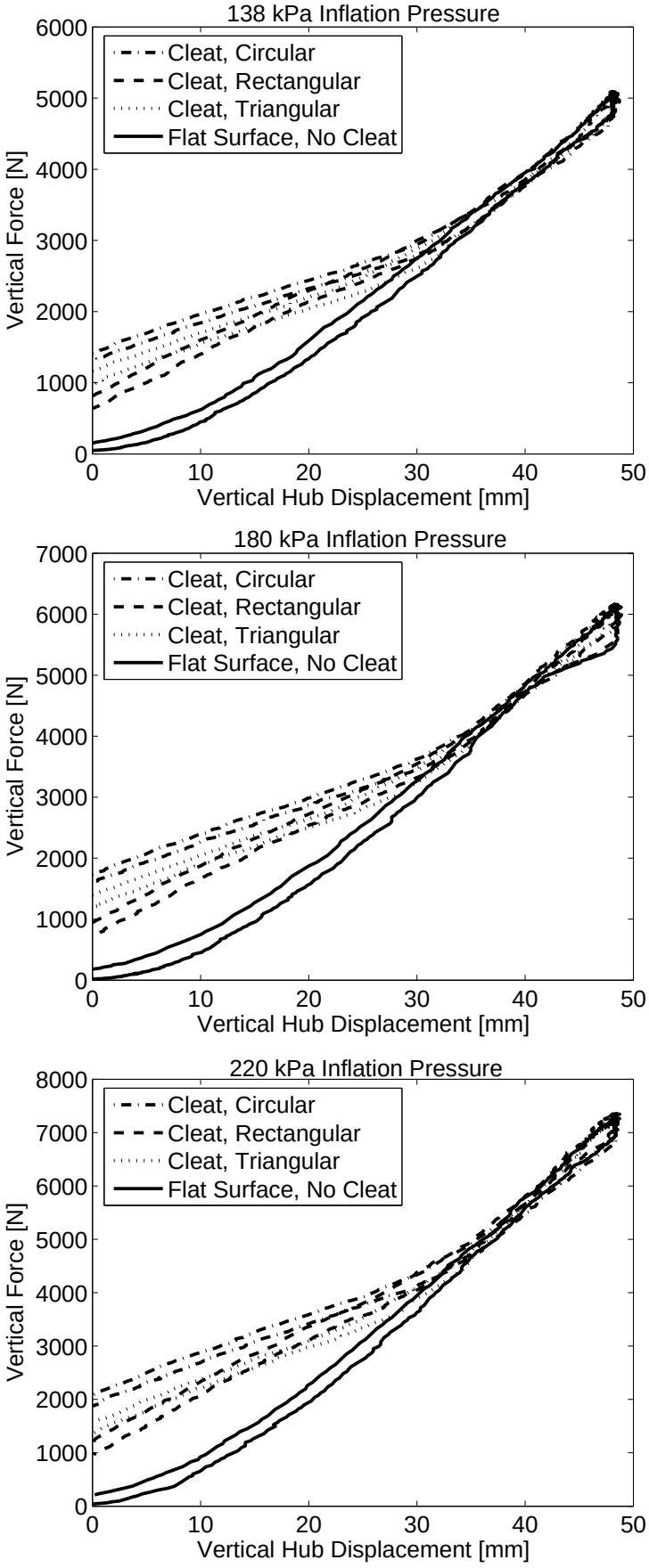

Figure 2.6. Vertical stiffness characteristics of 155R13 for inflation pressures of 138 kPa, 180 kPa and 220 kPa

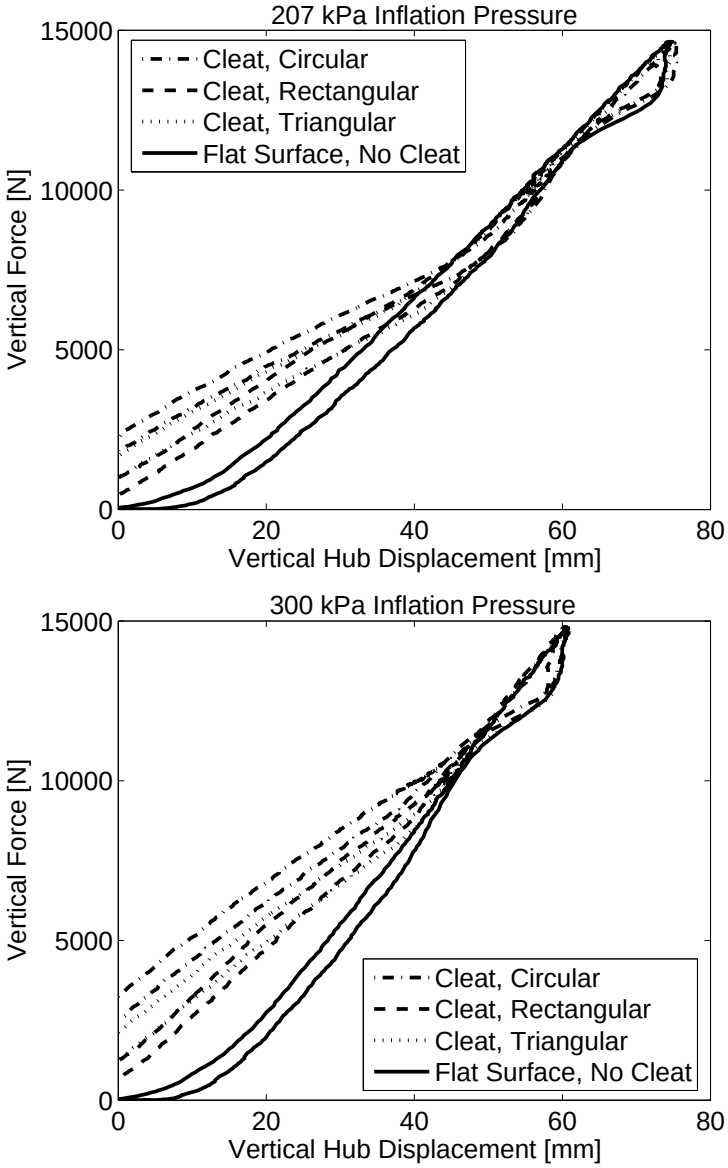

Figure 2.7. Vertical stiffness characteristics of 205/70R15 for inflation pressures of 207 kPa and 300 kPa

When the obstacle is placed off the center line, 63.50 mm (2.50 in) and then 127mm (5 in) off the center line, the curves don't intersect each other as shown in Figure 2.8. When the distance of the obstacle from the centreline increases, distinction between curves in the force-deflection diagram increases. It is also noted that the behavior does not change when the cleats place on left and right sides of the centreline as shown in Figure 2.9. In all measurements, there are hysteresis loops as shown in Figures 2.3 - 2.9. As discussed in [70], the energy dissipation within the structure leads to force variation during up and down motions of the tire.

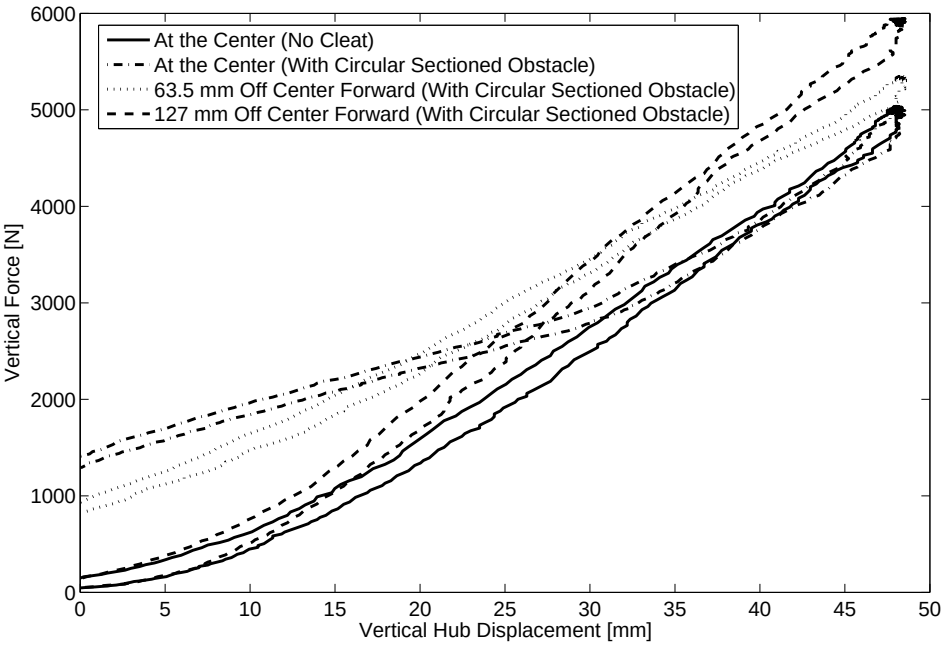

Figure 2.8. Effect of cleat location on vertical stiffness of 155R13 tire for 138 kPa inflation pressure

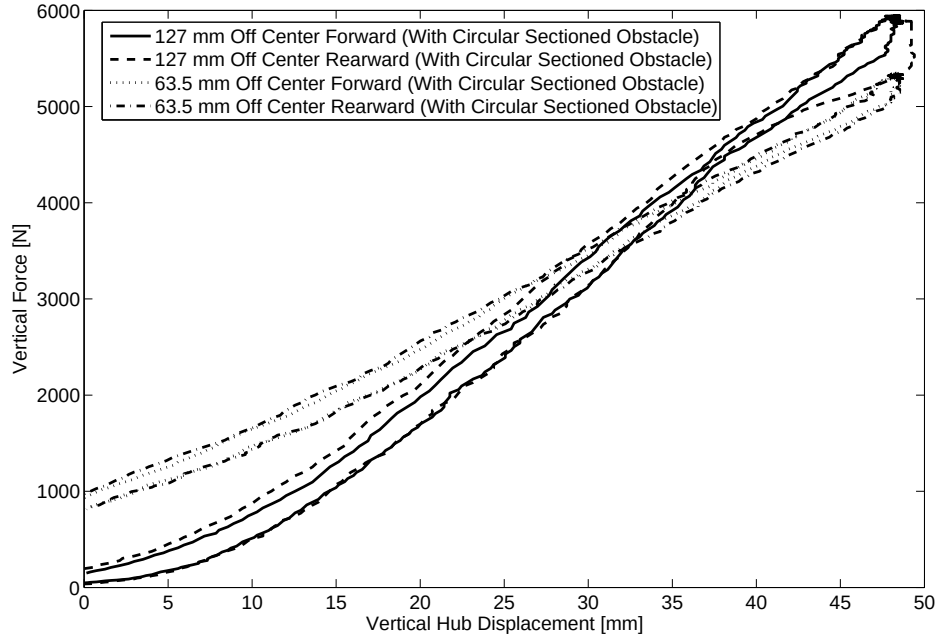

Figure 2.9. Effect of cleat location on vertical stiffness of 155R13 tire for 138 kPa inflation pressure

2.2.2. Dynamic Tire Tests

In this section, lateral and vertical force characteristics of 155R13 tire are investigated on a flat surface. A constant table speed of 2.3 km/h is used. For different vertical loads and slip angles, cornering force, self-aligning moment, overturning moment and rolling resistance moment variations are measured. Also, the same plots of 155R13 tire are given in the form of a carpet plot. Then, tire enveloping characteristics are investigated at a speed lower than 1 km/h. The table is put to motion slowly with a hand crank. In this case, G78-15, 225/60R16, 205/70R15 and 155R13 tires are tested. Force and moment variations of all tires during tires traverse different obstacles are measured. After testing of all four tires, experimental results showed that there are only small differences in general behavior of tires; as a result, the effect of inflation pressure and vertical load on force and moment responses of 155/80R13 78 S are only presented in this section.

2.2.2.1. Experimental Analysis of Lateral and Vertical Force Characteristics of the Tire.

Investigating lateral and vertical force characteristics of the tires is one of the most important aspects of vehicle dynamics. Handling behavior of the vehicle is related to lateral force characteristics of the tire and ride quality of the vehicle is mostly determined by the vertical force or normal force characteristics of the tire. In all experiments performed camber angle is zero. In this section, cornering force, self-aligning moment, overturning moment and rolling resistance moment variations of the 155R13 tire running on a surface at a constant speed of 2.3 km/h for different vertical loads (2,3,4 and 5 kN) and slip angles (0^0,1^0,2^0,4^0,8^0 and 15^0) are presented. In these figures, for five slip angle values, there are five experimental data points and between them curve fitting procedure is applied.

When tire is cornering there is a sideways force on it. Camber and slip angle are the important parameters governing the lateral force generation. In the case of zero camber angle, cornering force term is used instead of lateral force. The distribution of lateral forces in the contact patch produces a shift in position in direction of the resul-

tant lateral force from the geometrical contact center and it determines the generation of the self-aligning moment. In Figure 2.10, for 180 kPa rated inflation pressure and different vertical force values, cornering force characteristics of 155R13 tire is examined. It can be seen that up to a certain slip angle value (between 2^o and 4^o), the cornering force is approximately proportional to the slip angle. After this value, the cornering force increases with an increase of the slip angle at a lower rate and it reaches the maximum value (road adhesion limit). Beyond the maximum value, tire begins sliding laterally. Another important factor affecting the cornering force characteristics of the tires is vertical load. The vertical load strongly influences the cornering force characteristics of the tires. It can be observed that for a given slip angle, the cornering force increases with the increase in vertical load. However, there is a nonlinear relationship between vertical load and the cornering force as seen in Figure 2.10.

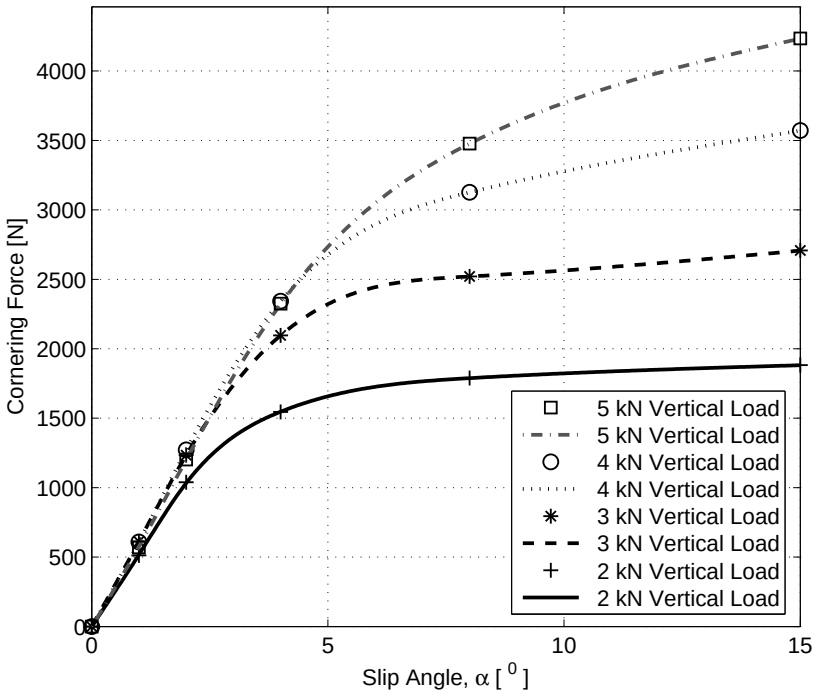

Figure 2.10. For rated 180 kPa inflation pressure and different vertical loads, cornering force characteristics of 155R13 tire at 2.3 km/h table speed

The cornering force usually don't pass through the contact patch center and there is a moment arm called pneumatic trail. The resultant moment is the self-aligning moment. In Figure 2.11, for 180 kPa rated inflation pressure and different vertical

force values, self-aligning moment versus slip angle plots is given. For a given vertical load, the self-aligning moment first increases with an increase of the slip angle and it reaches a maximum at a particular slip angle (4^o). Then it decreases with a further increase of the slip angle. It can also be noted that self-aligning moment increases with an increase in the vertical load for a given slip angle.

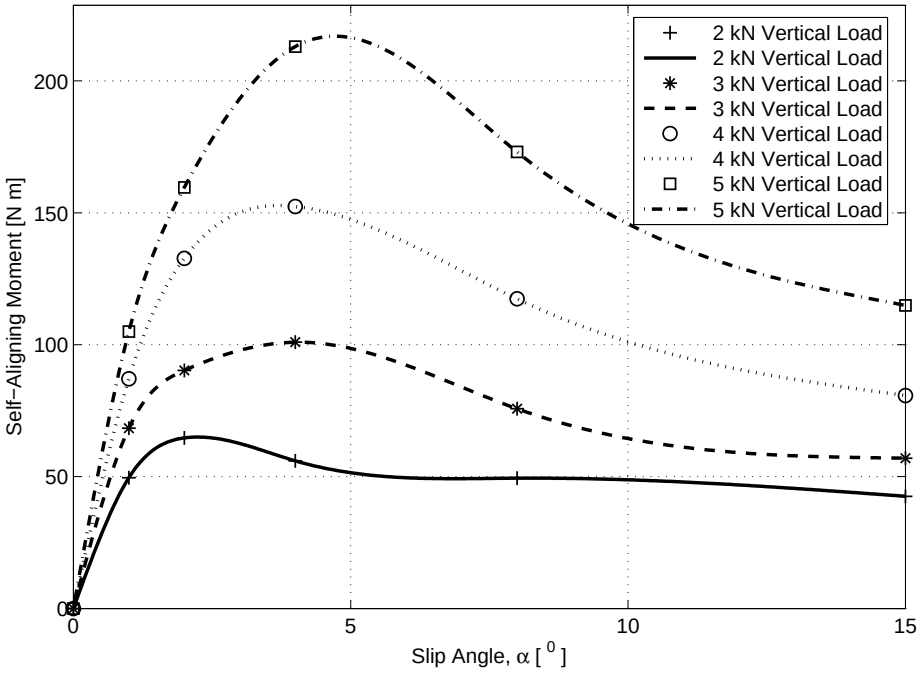

Figure 2.11. For rated 180 kPa inflation pressure and different vertical loads, self-aligning moment characteristics of 155R13 tire at 2.3 km/h table speed

When a tire is rolling, tire carcass and tread are deflected, which ,in turn, the normal pressure in the leading edge of the contact patch is higher than that of trailing edge. So, normal pressure center is shifted in the direction of rolling. This shift produces the moment called as rolling resistance moment. Among the factors affecting rolling resistance moment like tire structure and operating conditions (Inflation pressure, temperature, speed and road surface texture) requiring extensive experiments, vertical load effects on the rolling resistance moment shown in Figure 2.12 are examined. Rolling resistance moment increases with an increase in vertical load value and there is a nonlinear relationship between vertical load and the rolling resistance moment as seen in Figure 2.12.

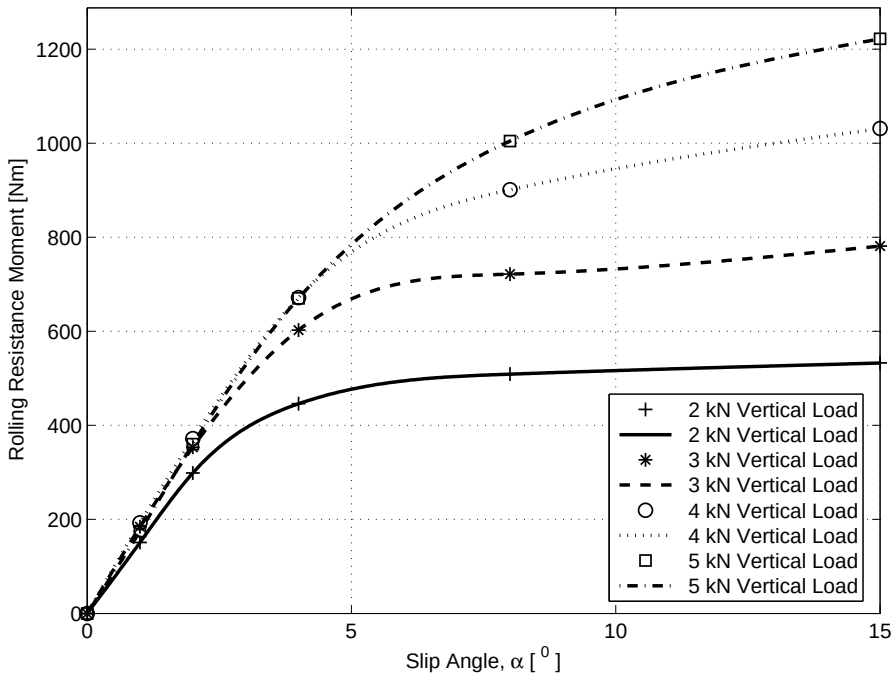

Figure 2.12. For rated 180 kPa inflation pressure and different vertical loads, rolling resistance moment characteristics of 155R13 tire at 2.3 km/h table speed

Overturning moment, on the other hand, results from an offset between contact patch center and resultant vertical tire contact forces. It determines mostly vehicle rollover phenomena. In Figure 2.13, for 180 kPa rated inflation pressure and different vertical force values, Overturning Moment vs slip angle plot is presented. The vertical force has a greater influence on the overturning moment. Similar conclusion can be made for the overturning moment variation. In addition to the above considerations, it is interesting to note that there is a similarity between the lateral force and rolling resistance and overturning moment in shape. From this point, Takahashi and Hada [30] carried out studies considering this similarity.

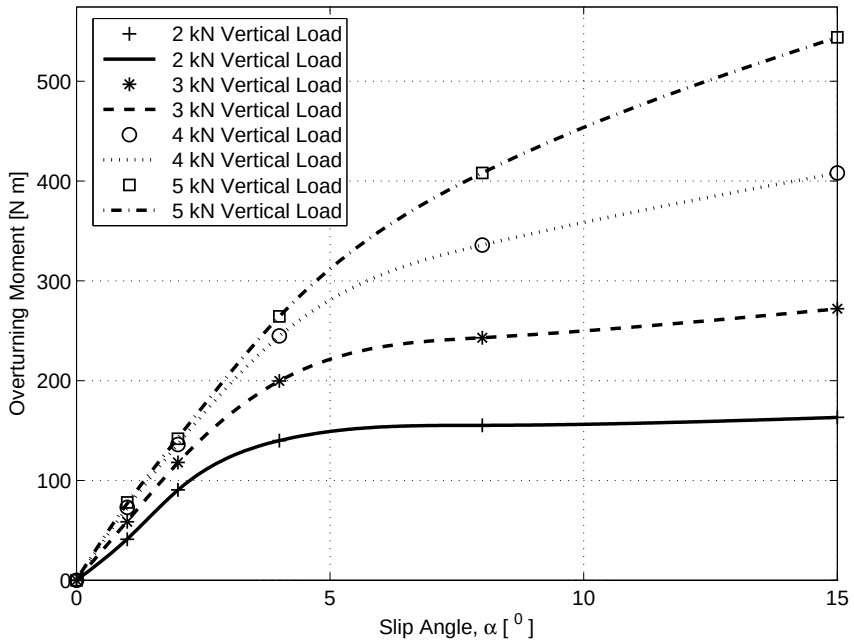

Figure 2.13. For rated 180 kPa inflation pressure and different vertical loads, overturning moment characteristics of 155R13 tire at 2.3 km/h table speed

On the other hand, in addition to the above figures, carpet plots are given in Figures 2.14 - 2.17. Especially, tire manufacturers want to get tire force and moment characteristics in a carpet plot format. In this type of figure, vertical load and slip angle effects can be understood easily.

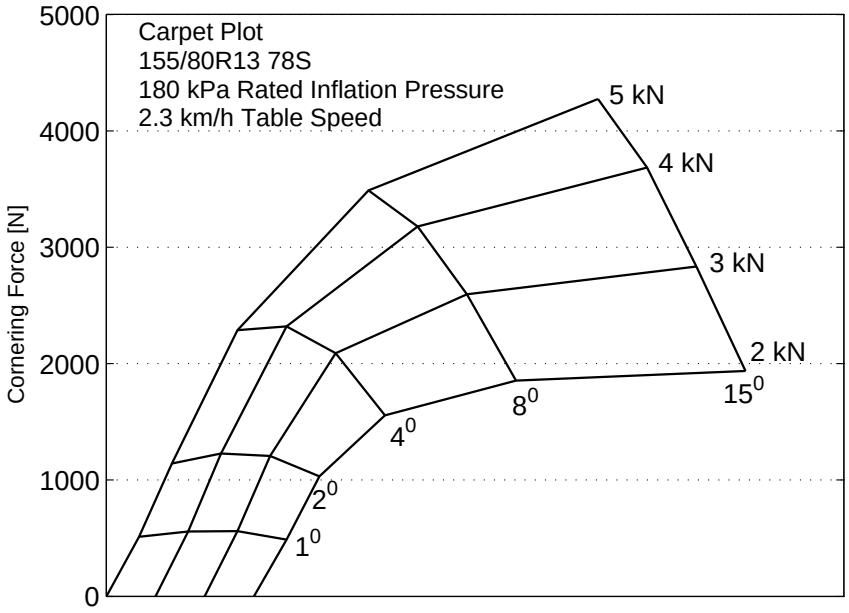

Figure 2.14. For rated 180 kPa inflation pressure and different vertical loads, cornering force characteristics of 155R13 tire at 2.3 km/h table speed

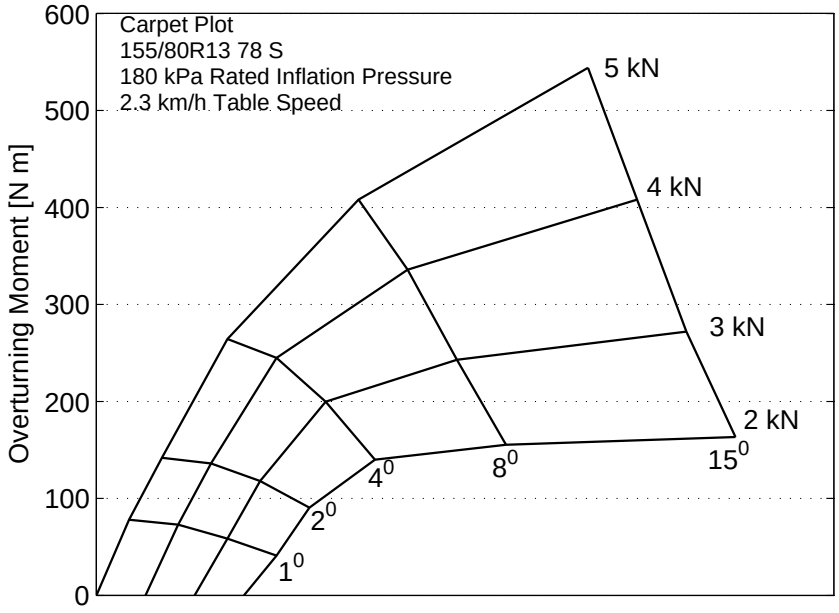

Figure 2.15. For rated 180 kPa inflation pressure and different vertical loads, overturning moment characteristics of 155R13 tire at 2.3 km/h table speed

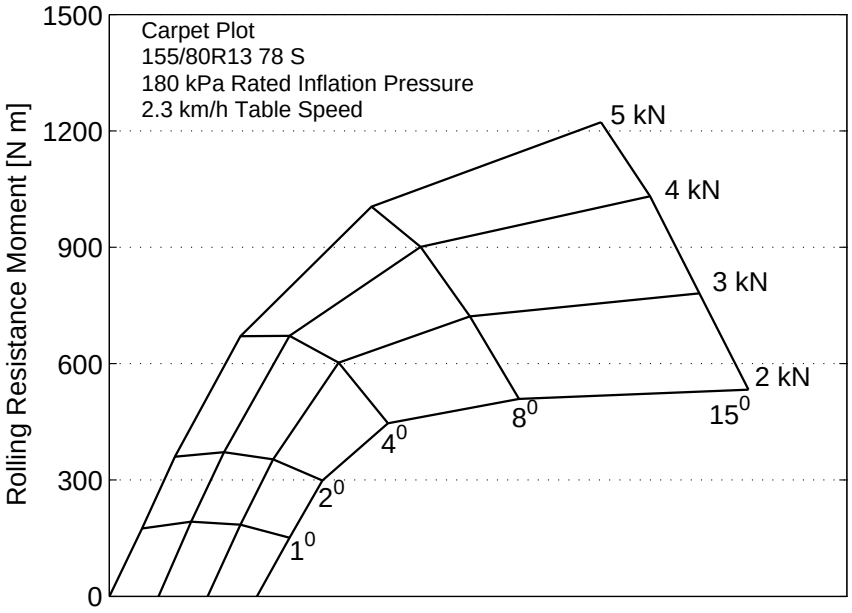

Figure 2.16. For rated 180 kPa inflation pressure and different vertical loads, rolling resistance moment characteristics of 155R13 tire at 2.3 km/h table speed

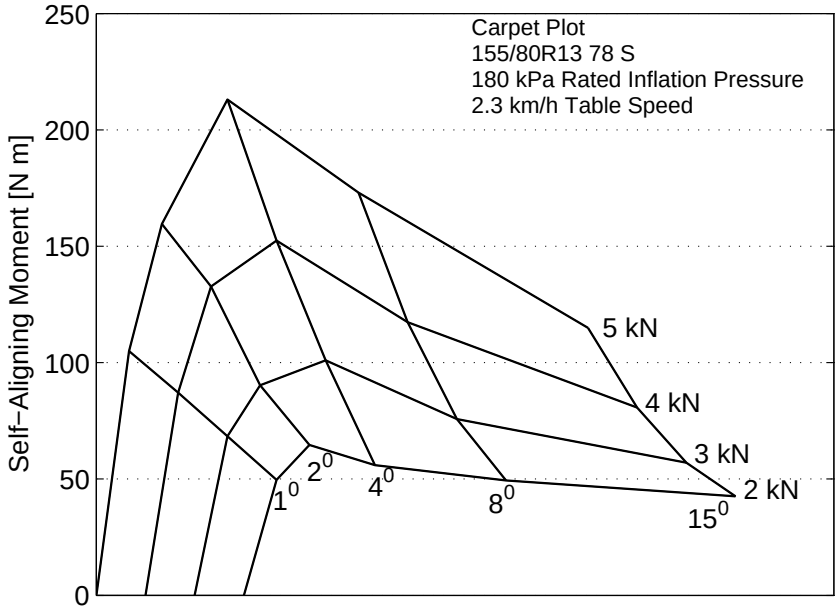

Figure 2.17. For rated 180 kPa inflation pressure and different vertical loads, self-aligning moment characteristics of 155R13 tire at 2.3 km/h table speed

2.2.2.2. Experimental Analysis of Tire Enveloping Characteristics at Low Speeds. In this section, experimental analysis of tire enveloping characteristics was investigated at low speeds. For different vertical loads and inflation pressures, force and moment characteristics of the all tires are investigated while the tires traverse the different obstacles at a table speed low speed lower than 1 km/h. The longitudinal table position is measured from the point where the tire starts to rotate to the point where it stops using a linear potentiometer. Zero longitudinal table position corresponds to a point under the wheel hub center. The tire was, firstly, pressed onto the flat surface to get predefined vertical load value. Then, the plank was moved slowly with a hand crank. As mentioned before, the influence of the tire dynamics is suppressed.

In the following figures, for different vertical loads and inflation pressures, force and moment characteristics of the all tires are shown. The vertical force variation can be grouped into three categories for low, medium and large deflections of the tire. In the low deflection case, vertical force curves are similar to a parabola. With increasing deflection, in the medium deflection case, there are two maxima and between them a minimum occurs. Nakajima and Padovan [61] called this trend as "camel back (double-hump)" response of tires. In the last case, the minimum becomes lower than the force on a flat surface which is a typical enveloping characteristic. Julien and Paulsen [50] attributed this tire property to the deformation imposed on the carcass while tires traverse cleats. Local buckling of the sidewalls introduces a negative flexibility which decreases the total elastic vertical reaction of the tire. However, a cleat with a rectangular cross section is an exception where this phenomenon is less observed. When the vertical load is increased, minimum force seems to be lower than the force on a flat surface as mentioned in [49]. When the longitudinal response of the tire is concerned, there exist two separate regions: a maximum in negative table position and a maximum in positive table position. All curves intersect at the origin, which coincide with the vertical plane of the hub center and there is no symmetry with respect to zero longitudinal table position. Longitudinal forces while leaving the obstacle (first quadrant) are always less than the forces at entry (third quadrant) as shown in the longitudinal force versus longitudinal table position plots. As mentioned in [58], this may be attributed to the translational energy lost in surmounting the obstacle. It can

also be noted that more longitudinal force is required to swallow the cleat while exiting. When considering lateral force response of the tires, there is no general behavior of the tires. In all experiments, the side slip angle is zero and cleats are placed perpendicular to the rolling direction of the tire. So, the magnitude of the lateral force response is lower than those of non-zero slip angle case and the cleats placed diagonally with respect to the rolling direction of the tire. For the moment responses of the tires, it can be seen from the following figures that there exist two separate regions as seen in longitudinal force response of the tires. Except aligning moment, there is no symmetric behavior of the tires between entering and leaving the obstacle. It can also be noted that before hitting the cleat and after leaving the cleats, the tire has non-zero force and moment values. This can be attributed to the plysteer and conicity effects of the tires [86].

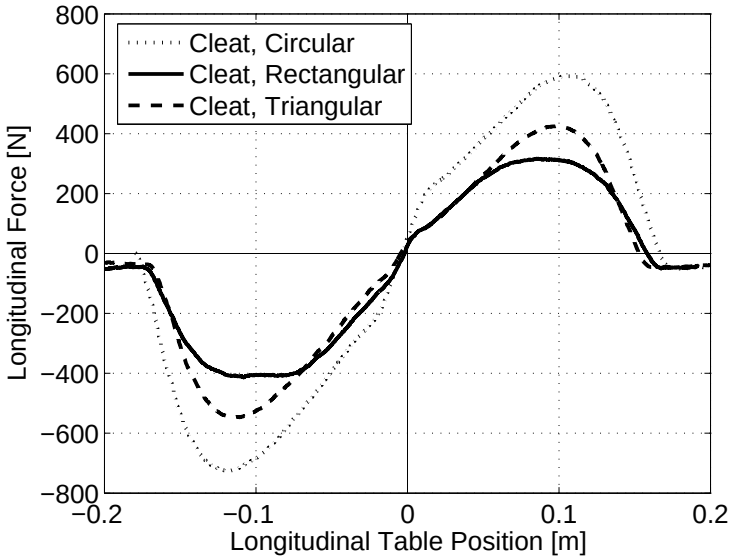

Figure 2.18. Longitudinal force vs. longitudinal table position of G78-15 for 165 kPa inflation pressure and 4800 N vertical load on different cleats

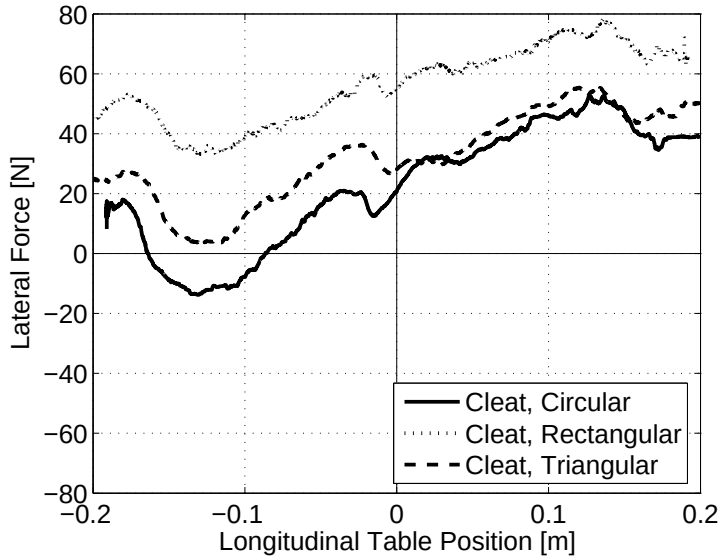

Figure 2.19. Lateral force vs. longitudinal table position of G78-15 for 165 kPa inflation pressure and 4800 N vertical load on different cleats

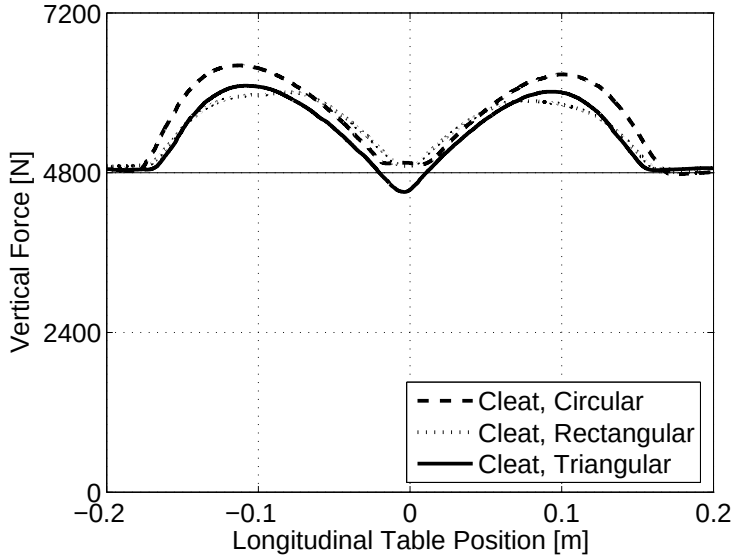

Figure 2.20. Vertical force vs. longitudinal table position of G78-15 for 165 kPa inflation pressure and 4800 N vertical load on different of cleats

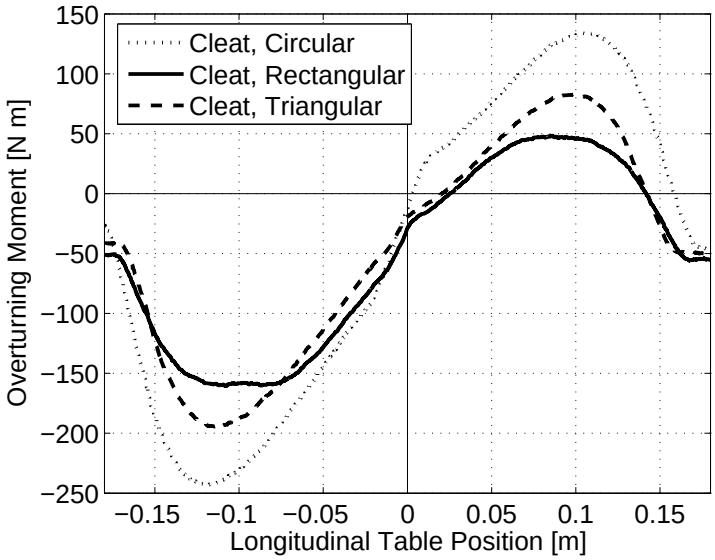

Figure 2.21. Overturning moment vs. longitudinal table position of G78-15 for 165 kPa inflation pressure and 4800 N vertical load on different cleats

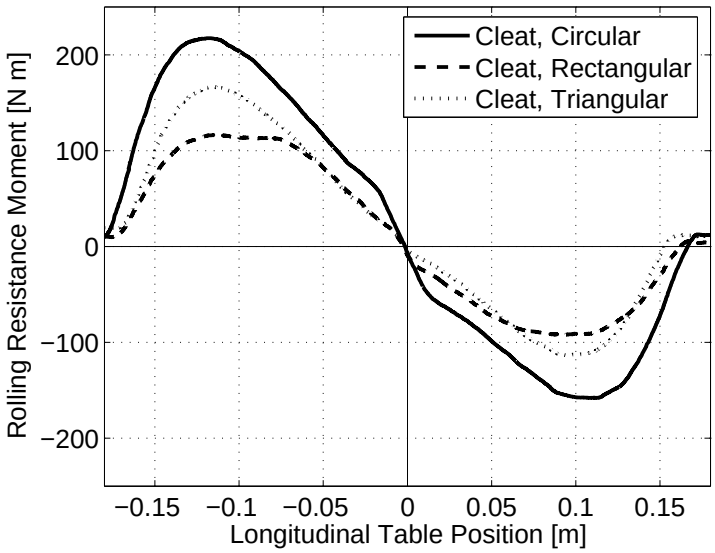

Figure 2.22. Rolling resistance moment vs. longitudinal table position of G78-15 for 165 kPa inflation pressure and 4800 N vertical load on different cleats

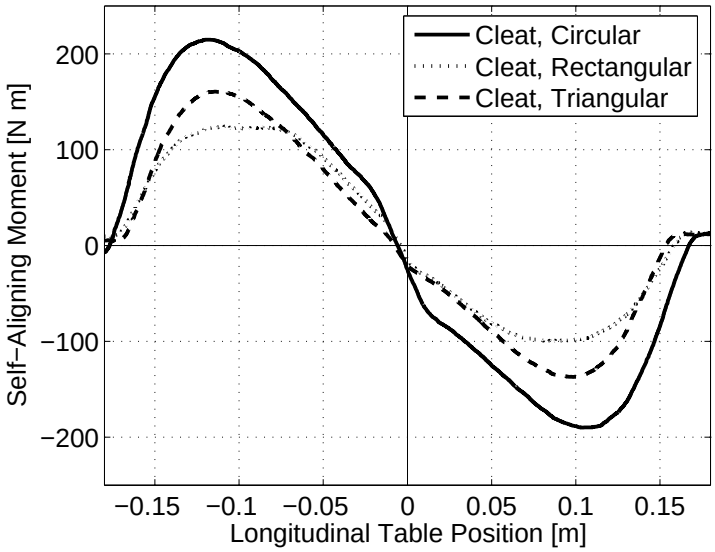

Figure 2.23. Self-aligning moment vs. longitudinal table position of G78-15 for 165 kPa inflation pressure and 4800 N vertical load on different cleats

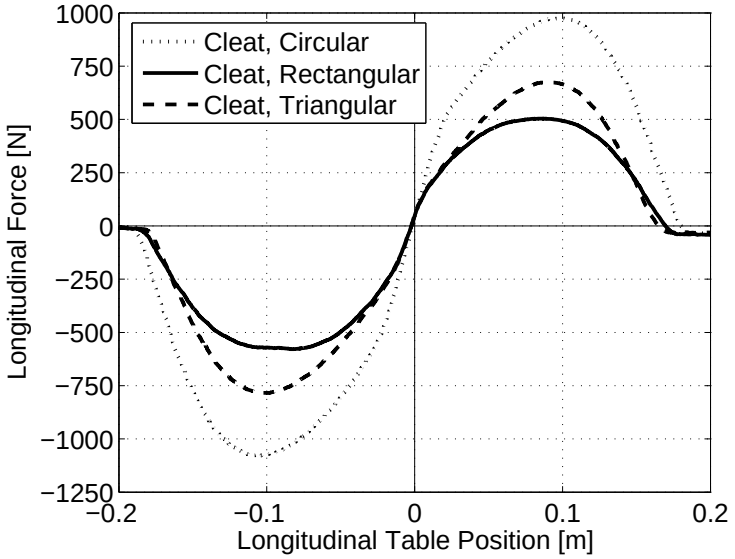

Figure 2.24. Longitudinal force vs. longitudinal table position of 225/60R16 for 240 kPa inflation pressure and 7200 N vertical load on different cleats

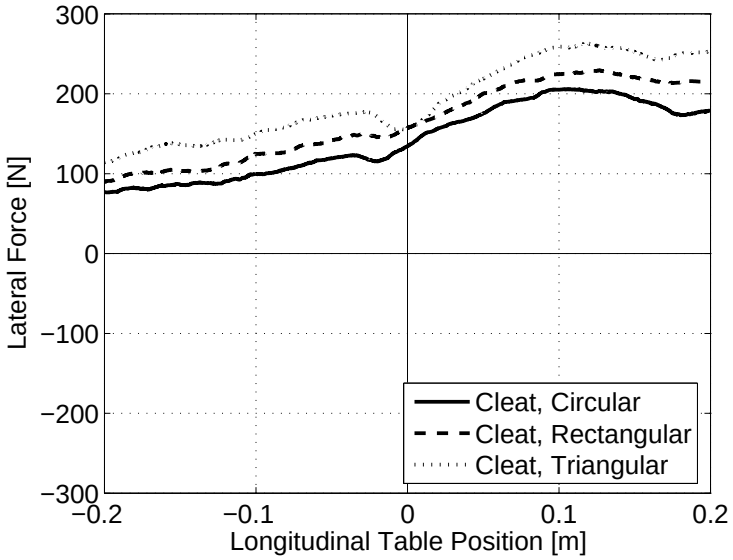

Figure 2.25. Lateral force vs. longitudinal table position of 225/60R16 for 240 kPa inflation pressure and 7200 N vertical load on different cleats

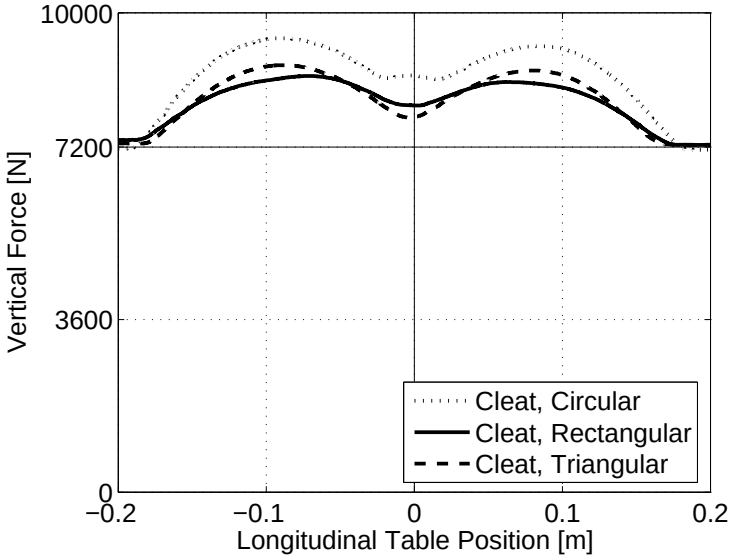

Figure 2.26. Vertical force vs. longitudinal table position of 225/60R16 for 240 kPa inflation pressure and 7200 N vertical load on different cleats

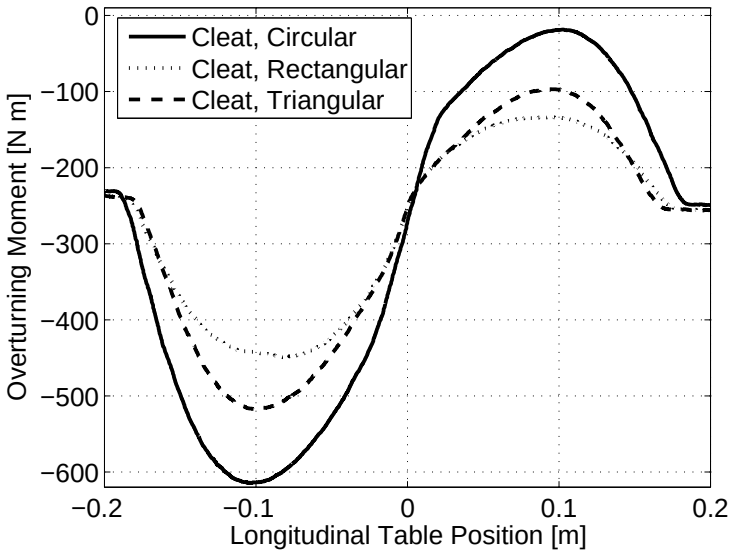

Figure 2.27. Overturning moment vs. longitudinal table position of 225/60R16 for 240 kPa inflation pressure and 7200 N vertical load on different cleats

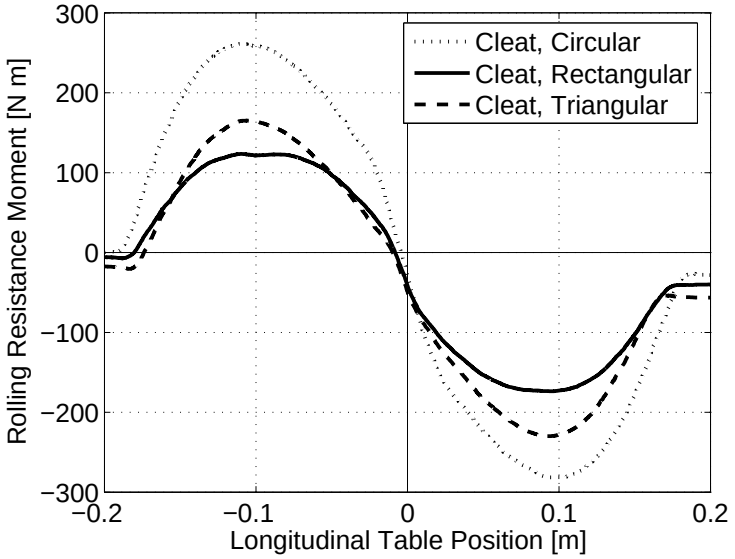

Figure 2.28. Rolling resistance moment vs. longitudinal table position of 225/60R16 for 240 kPa inflation pressure and 7200 N vertical load on different cleats

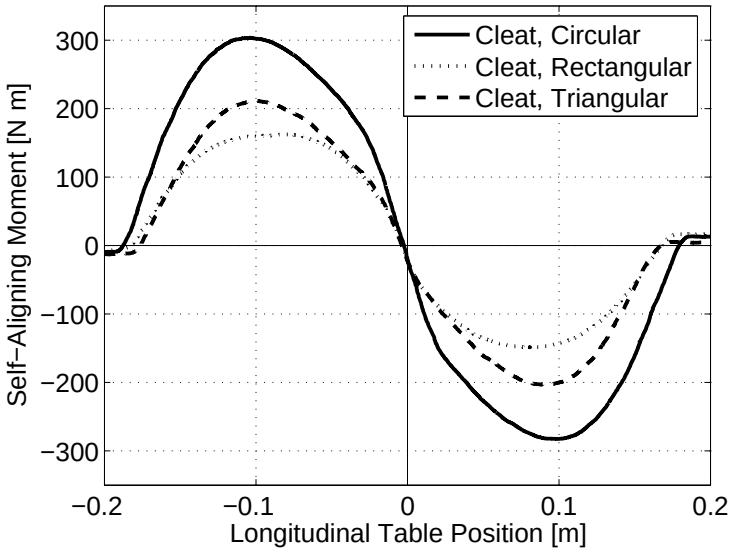

Figure 2.29. Self-aligning moment vs. longitudinal table position of 225/60R16 for 240 kPa inflation pressure and 7200 N vertical load on different cleats

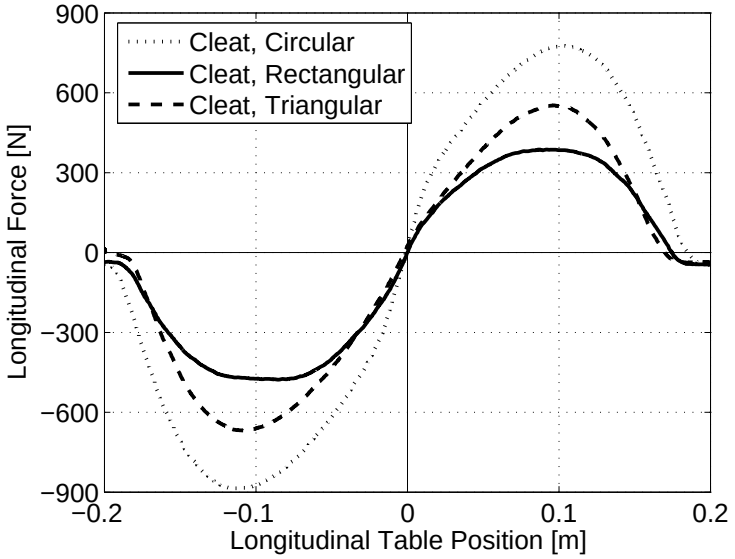

Figure 2.30. Longitudinal force vs. longitudinal table position of 225/60R16 for 180 kPa inflation pressure and 6200 N vertical load on different cleats

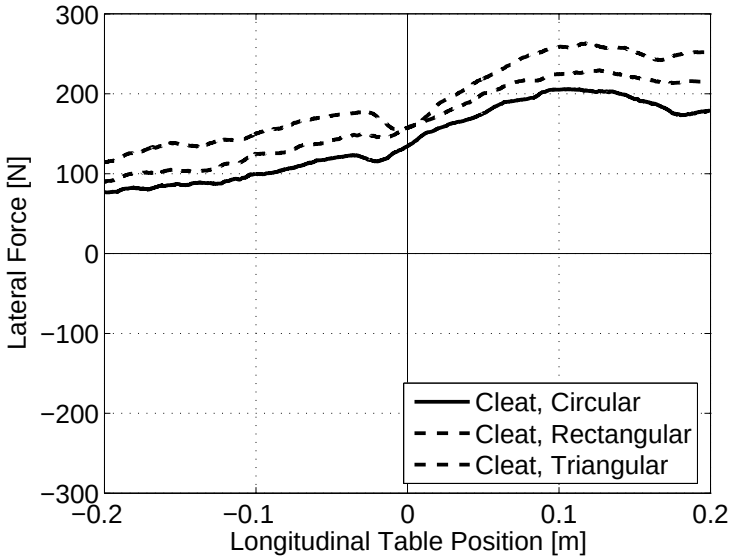

Figure 2.31. Lateral force vs. longitudinal table position of 225/60R16 for 180 kPa inflation pressure and 6200 N vertical load on different cleats

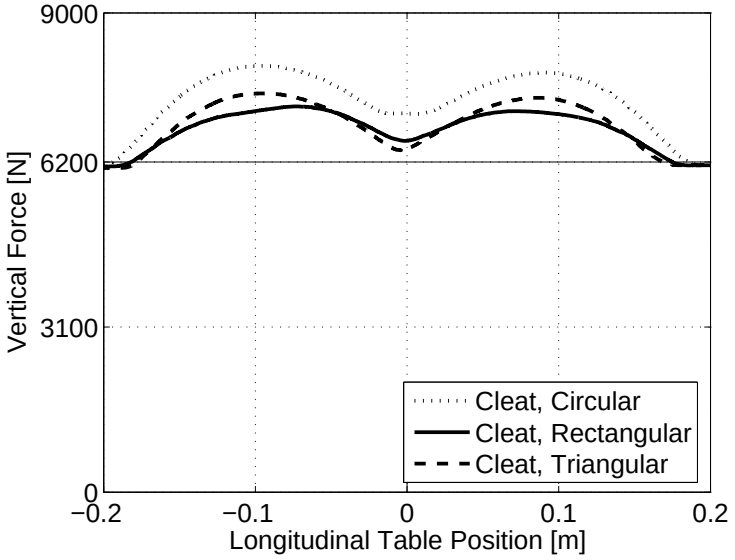

Figure 2.32. Vertical force vs. longitudinal table position of 225/60R16 for 180 kPa inflation pressure and 6200 N vertical load on different cleats

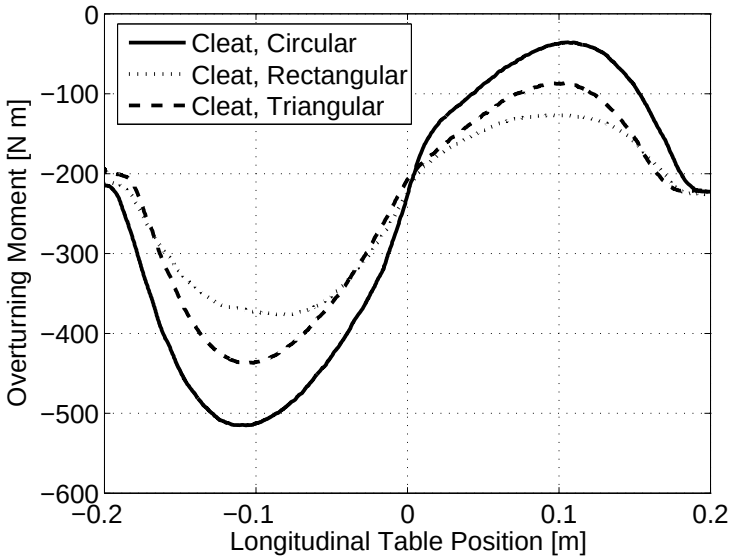

Figure 2.33. Overturning moment vs. longitudinal table position of 225/60R16 for 180 kPa inflation pressure and 6200 N vertical load on different cleats

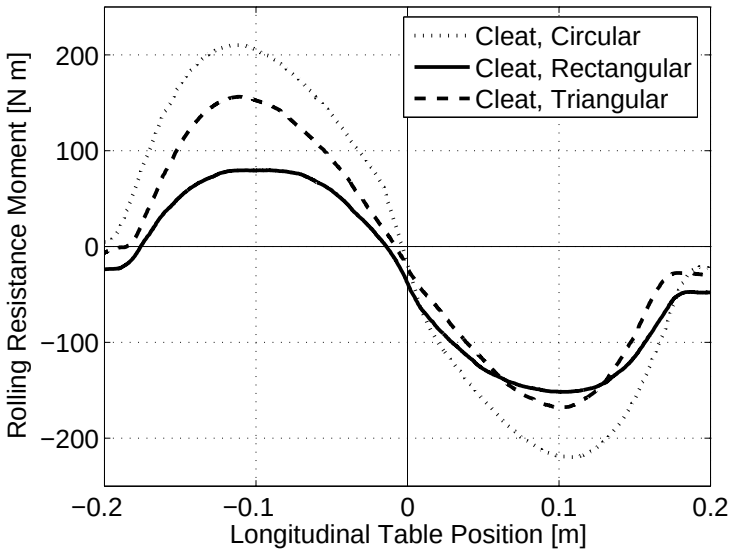

Figure 2.34. Rolling resistance moment vs. longitudinal table position of 225/60R16 for 180 kPa inflation pressure and 6200 N vertical load on different cleats

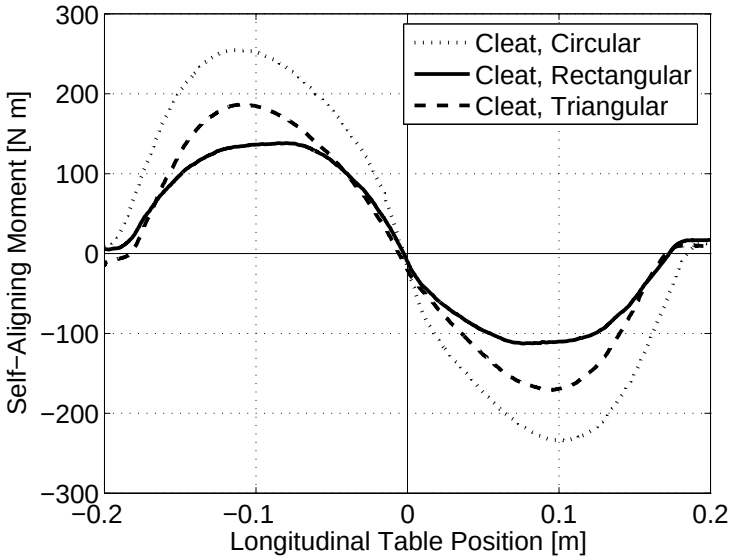

Figure 2.35. Self-aligning moment vs. longitudinal table position of 225/60R16 for 180 kPa inflation pressure and 6200 N vertical load on different cleats

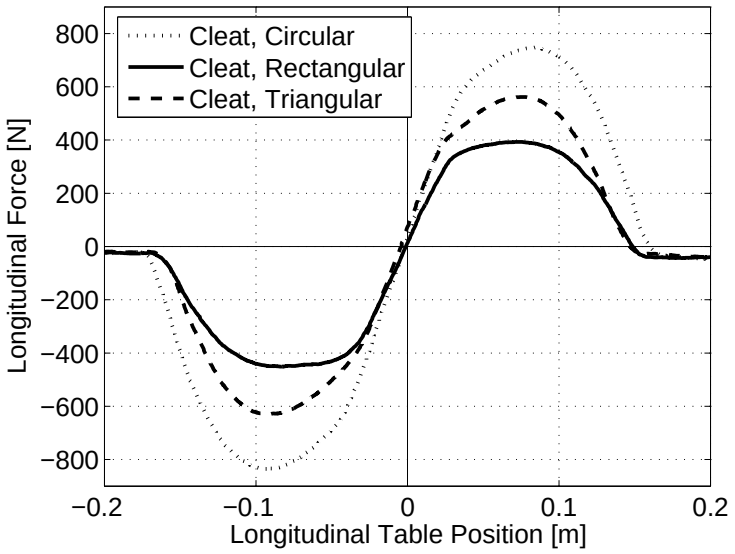

Figure 2.36. Longitudinal force vs. longitudinal table position of 205/70R15 for 207 kPa inflation pressure and 4000 N vertical load on different cleats

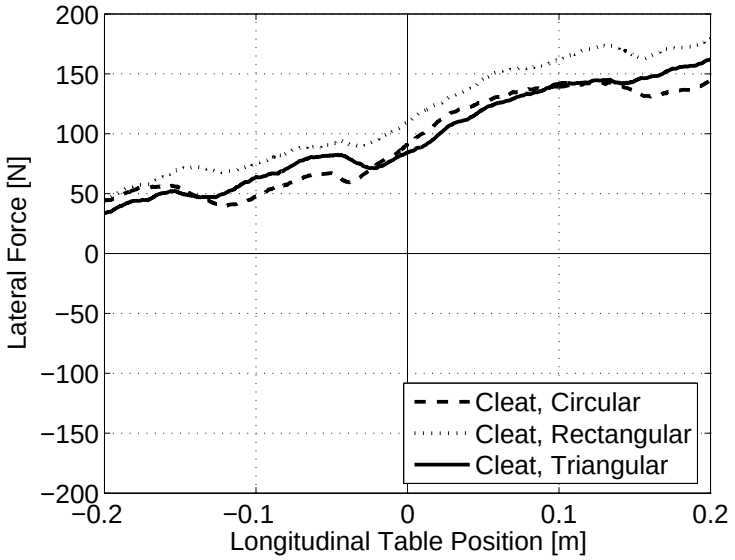

Figure 2.37. Lateral force vs. longitudinal table position of 205/70R15 for 207 kPa inflation pressure and 4000 N vertical load on different cleats

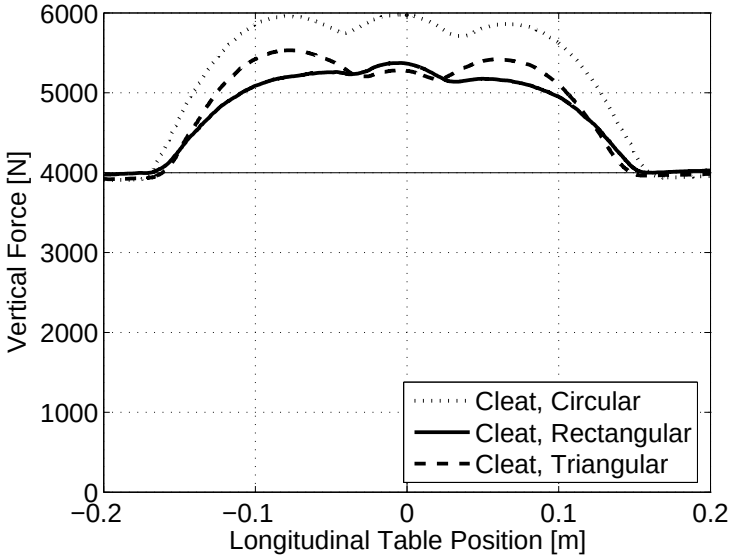

Figure 2.38. Vertical force vs. longitudinal table position of 205/70R15 for 207 kPa inflation pressure and 4000 N vertical load on different cleats

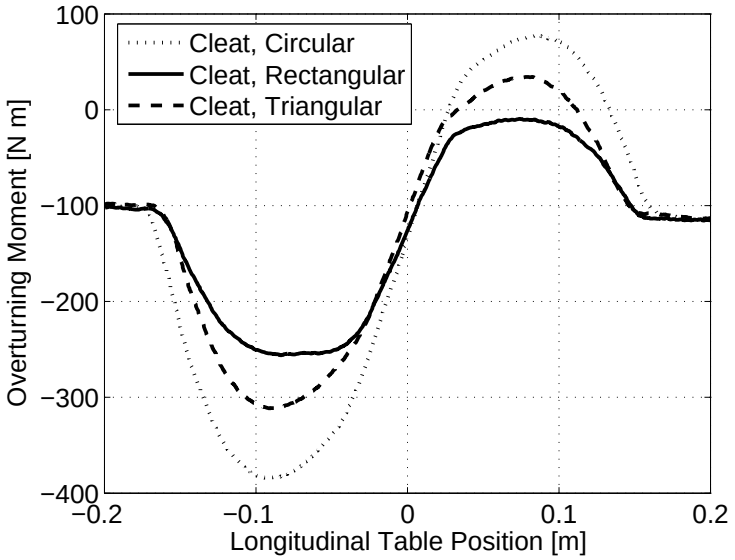

Figure 2.39. Overturning moment vs. longitudinal table position of 205/70R15 for 207 kPa inflation pressure and 4000 N vertical load on different cleats

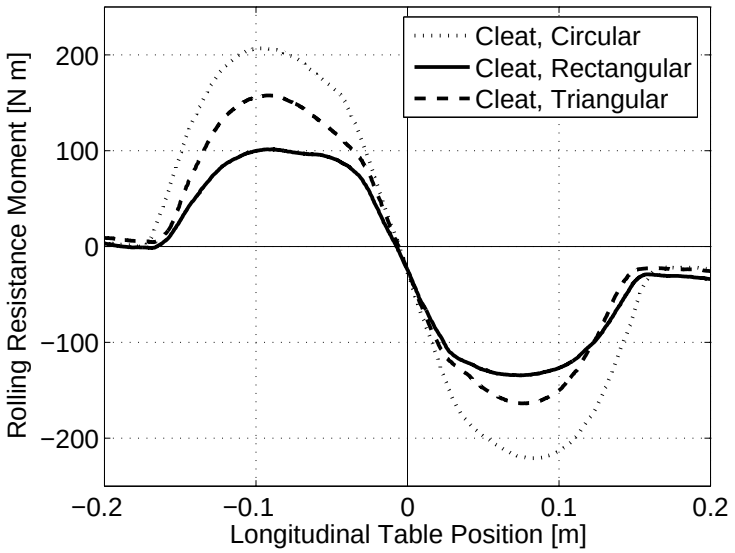

Figure 2.40. Rolling resistance moment vs. longitudinal table position of 205/70R15 for 207 kPa inflation pressure and 4000 N vertical load on different cleats

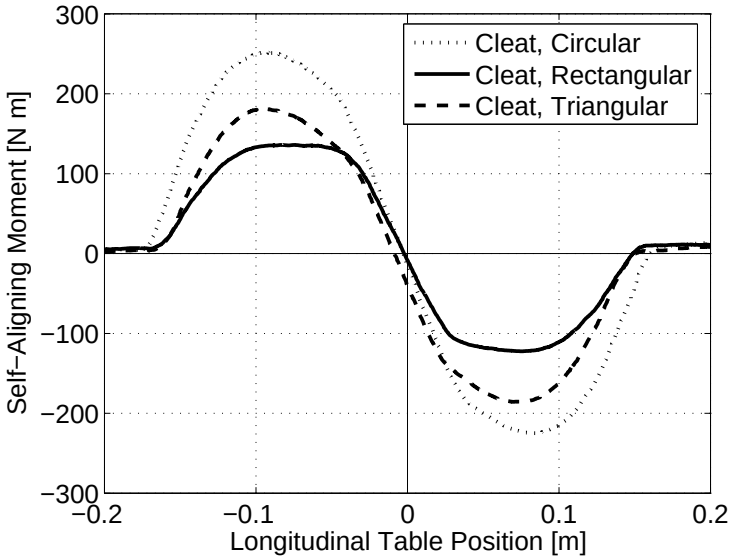

Figure 2.41. Self-aligning moment vs. longitudinal table position of 205/70R15 for 207 kPa inflation pressure and 4000 N vertical load on different cleats

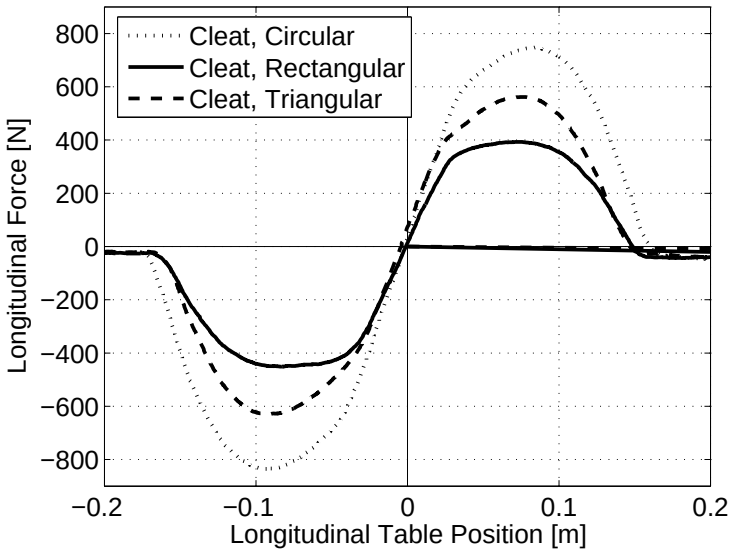

Figure 2.42. Longitudinal force vs. longitudinal table position of 205/70R15 for 207 kPa inflation pressure and 6228 N vertical load on different cleats

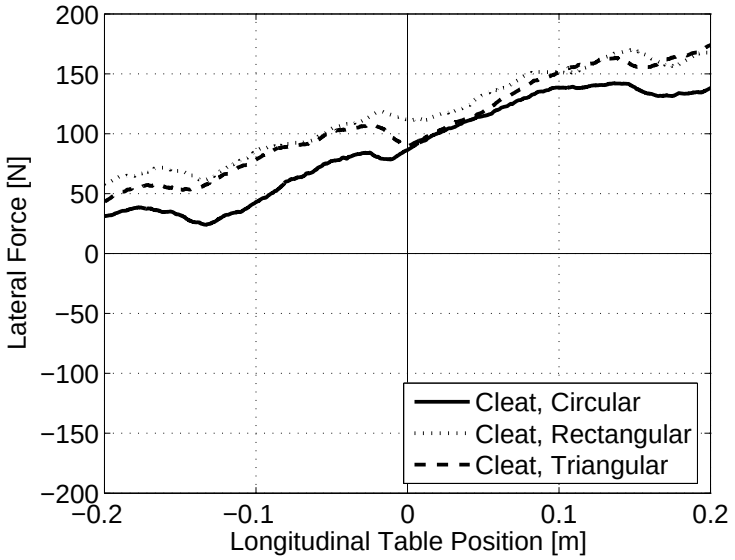

Figure 2.43. Lateral force vs. longitudinal table position of 205/70R15 for 207 kPa inflation pressure and 6228 N vertical load on different cleats

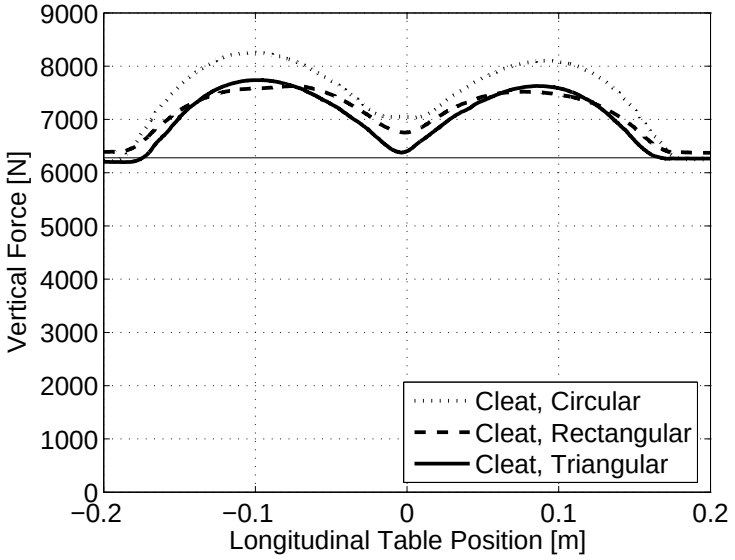

Figure 2.44. Vertical force vs. longitudinal table position of 205/70R15 for 207 kPa inflation pressure and 6228 N vertical load on different cleats

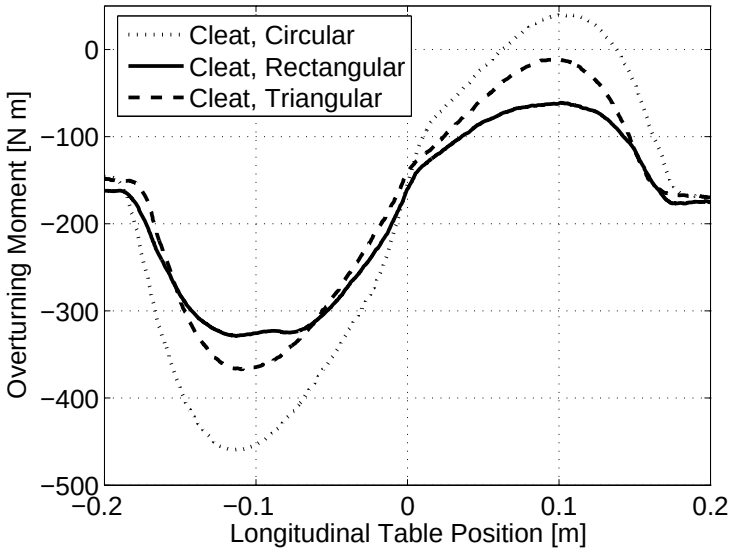

Figure 2.45. Overturning moment vs. longitudinal table position of 205/70R15 for 207 kPa inflation pressure and 6228 N vertical load on different cleats

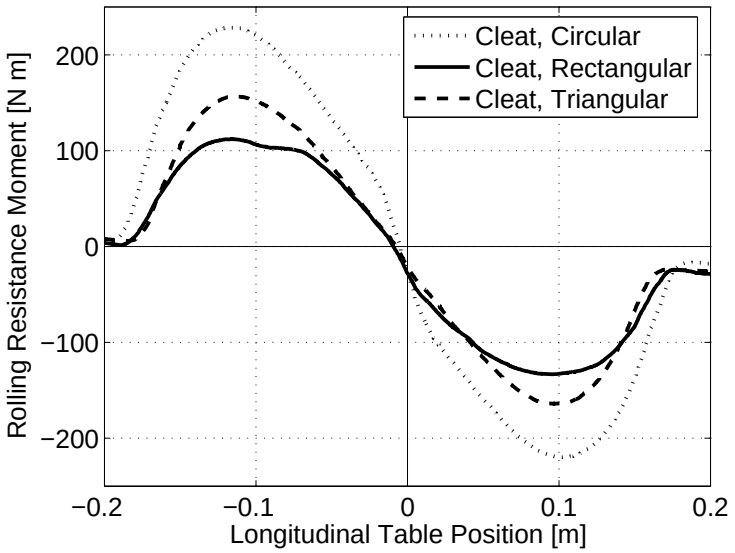

Figure 2.46. Rolling resistance moment vs. longitudinal table position of 205/70R15 for 207 kPa inflation pressure and 6228 N vertical load on different cleats

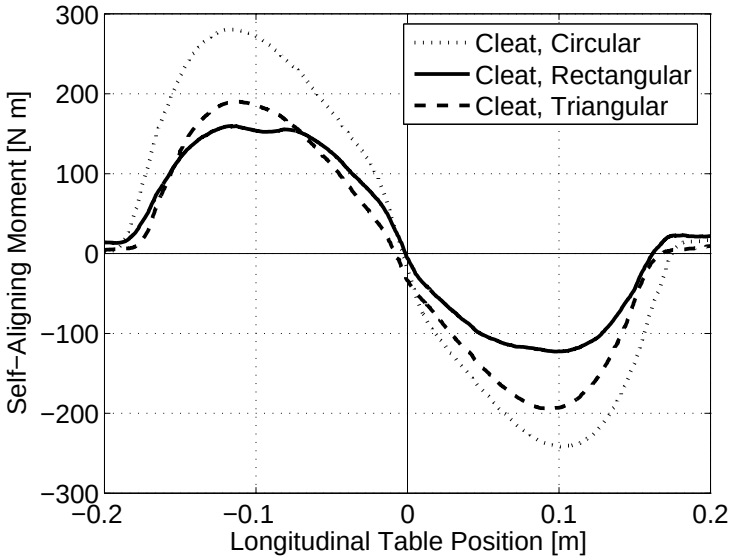

Figure 2.47. Self-aligning moment vs. longitudinal table position of 205/70R15 for 207 kPa inflation pressure and 6228 N vertical load on different cleats

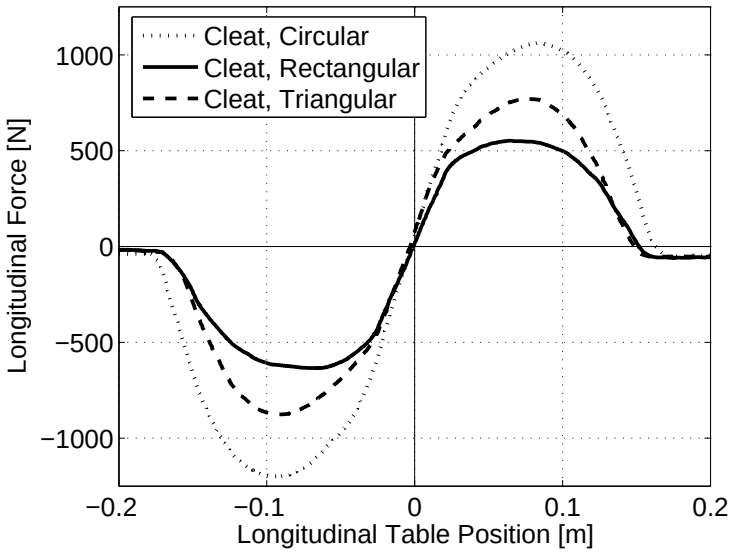

Figure 2.48. Longitudinal force vs. longitudinal table position of 205/70R15 for 303 kPa inflation pressure and 6228 N vertical load on different cleats

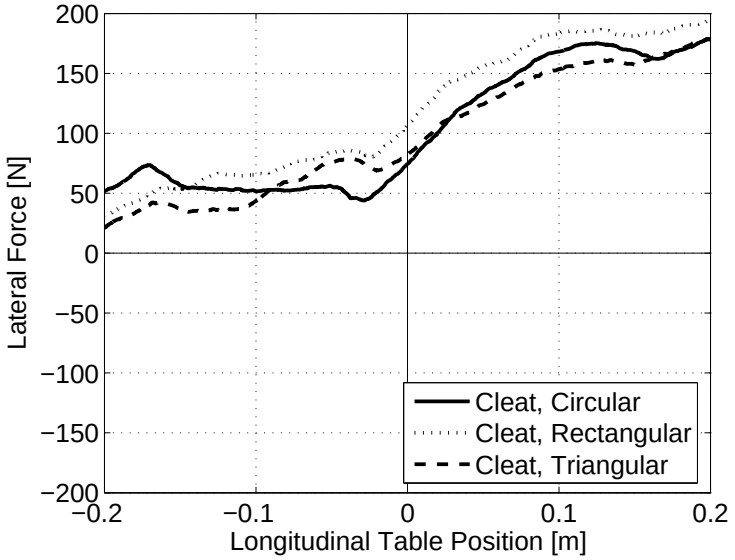

Figure 2.49. Lateral force vs. longitudinal table position of 205/70R15 for 303 kPa inflation pressure and 6228 N vertical load on different cleats

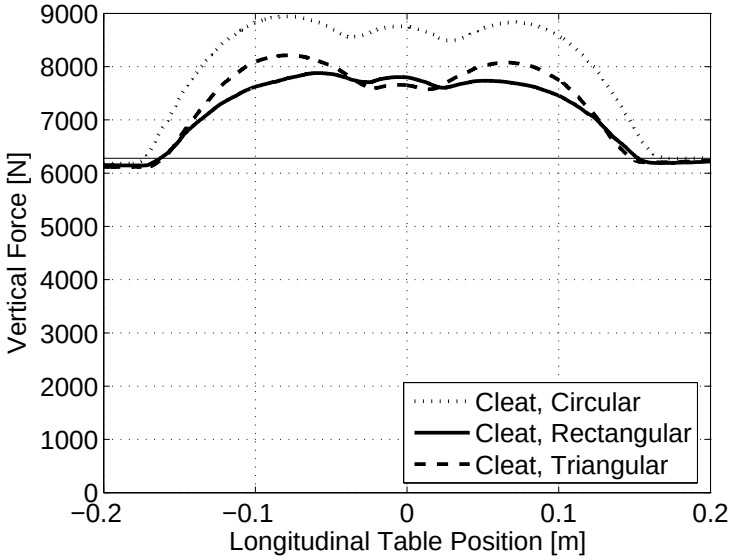

Figure 2.50. Vertical force vs. longitudinal table position of 205/70R15 for 303 kPa Inflation Pressure and 6228 N Vertical Load on different cleats

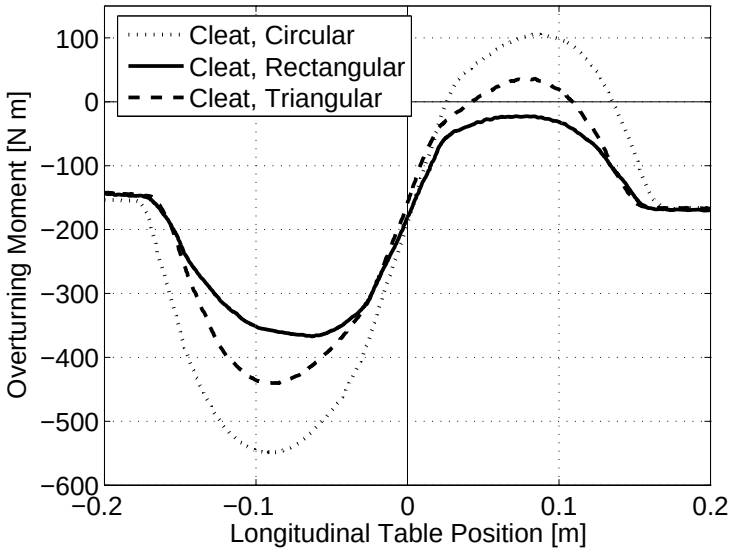

Figure 2.51. Overturning moment vs. longitudinal table position of 205/70R15 for 303 kPa inflation pressure and 6228 N vertical load on different cleats

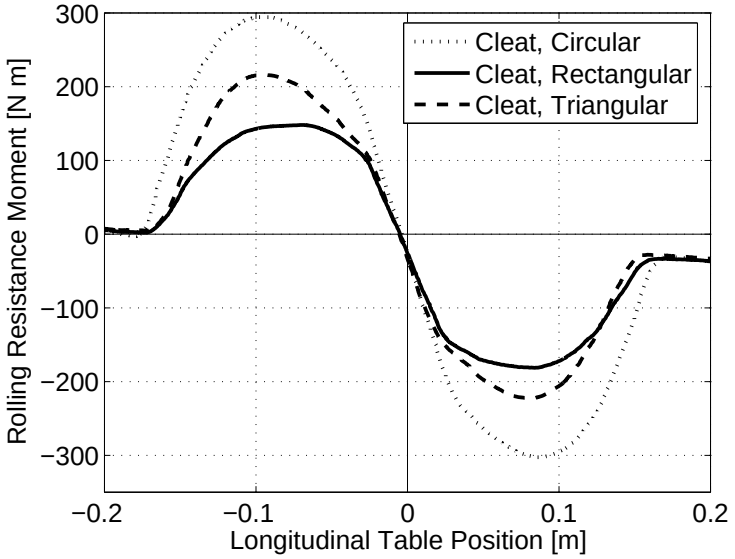

Figure 2.52. Rolling resistance moment vs. longitudinal table position of 205/70R15 for 303 kPa inflation pressure and 6228 N vertical load on different cleats

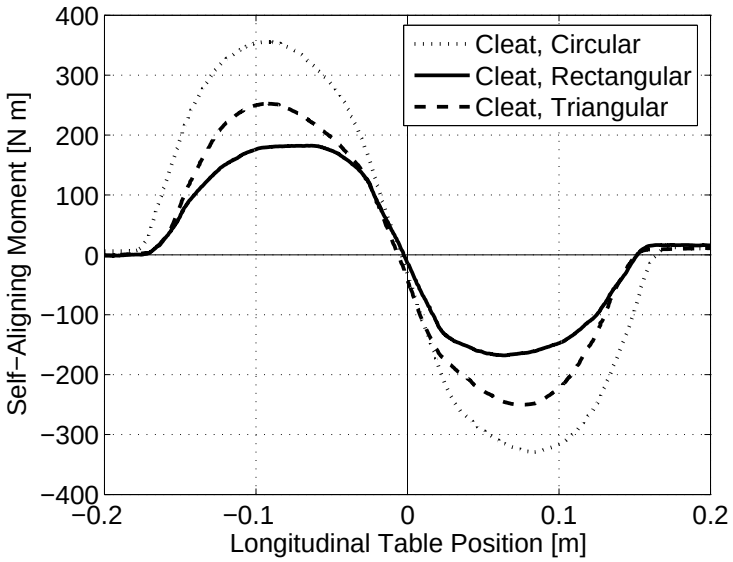

Figure 2.53. Self-aligning moment vs. longitudinal table position of 205/70R15 for 303 kPa inflation pressure and 6228 N vertical load on different cleats

So far, for different inflation pressures and vertical loads, force and moment variations of tires traversing over different cleats have been investigated. In following figures, first, the effect of vertical load on force and moment responses for 155/80R13 78 S traversing different type of cleats for 180 kPa rated inflation pressure are investigated. Then, for 3 kN vertical load, the effects of inflation pressure on force and moment responses for the tire traversing different types of cleats are shown. From Figures 2.54 - 2.89, it can be concluded that for all three types of obstacles, there is a considerable influence of the vertical load on vertical and lateral force responses of the tire. In all experiments, the side slip angle is zero and cleats are placed perpendicular to the rolling direction of the tire. The magnitude of the lateral force value is lower than those of non-zero slip angle and oblique cleat conditions. For longitudinal force and all moment values, the effect of vertical load is less pronounced when compared to vertical and lateral reaction forces. On the other hand, the change of the tire inflation pressure does not produce remarkable variation in force and moment responses of the tire. There are small changes with the inflation pressure variation. On the other hand, Cho et al. [45] mentioned that the variations in the transient dynamic response of the vertical force are completely opposite to increasing inflation pressure values. This is not the case under low speed conditions.

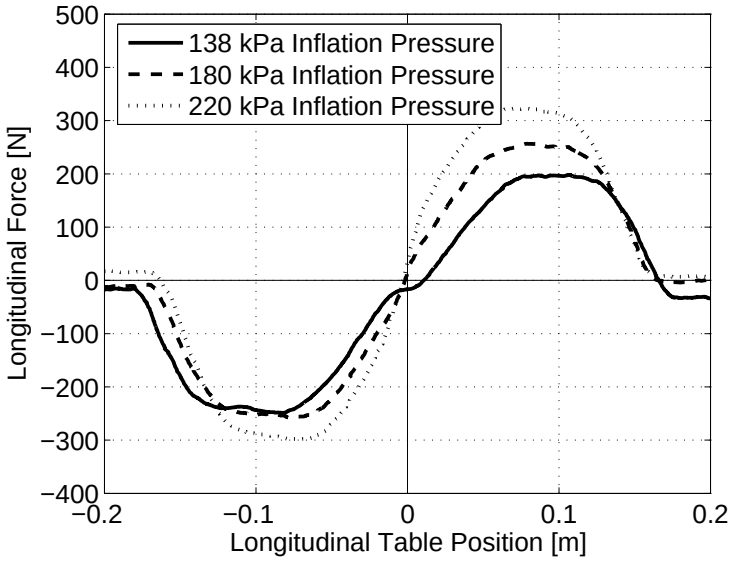

Figure 2.54. The effect of inflation pressure on longitudinal force responses for 155/80R13 78 S traversing a rectangular cleat at low speed for 3 kN rated vertical load

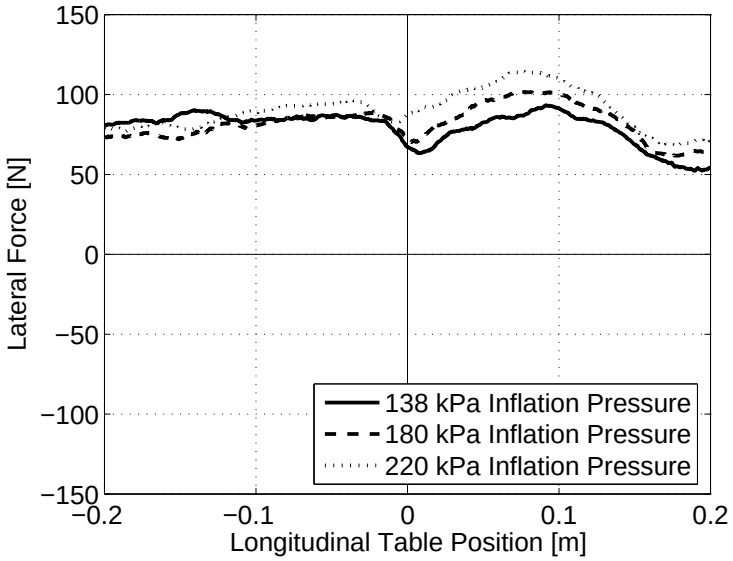

Figure 2.55. The effect of inflation pressure on lateral force responses for 155/80R13 78 S traversing a rectangular cleat at low speed for 3 kN rated vertical load

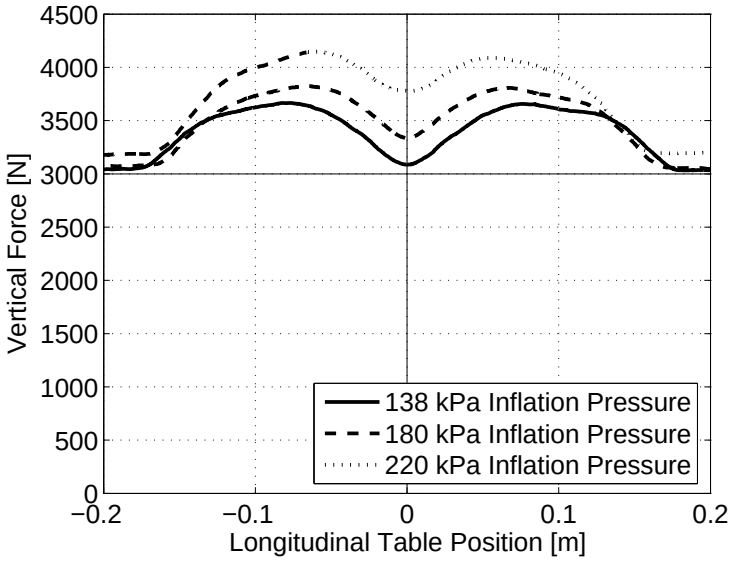

Figure 2.56. The effect of inflation pressure on vertical force responses for 155/80R13 78 S traversing a rectangular cleat at low speed for 3 kN rated vertical load

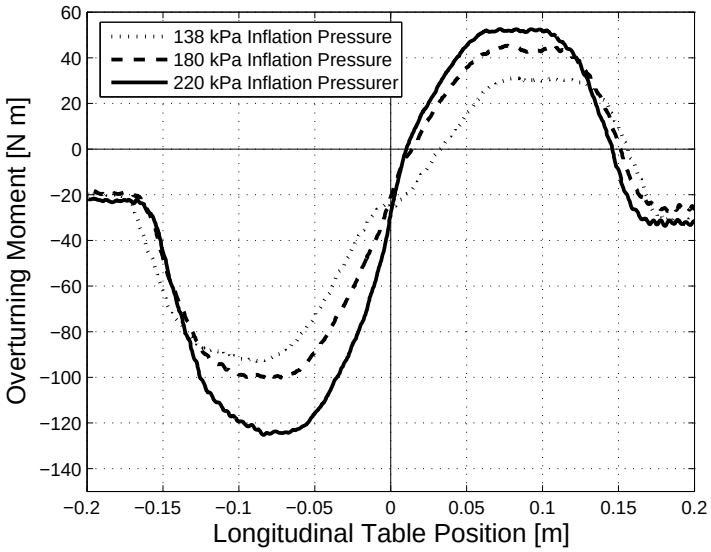

Figure 2.57. The effect of inflation pressure on overturning moment responses for 155/80R13 78 S traversing a rectangular cleat at low speed for 3 kN rated vertical load

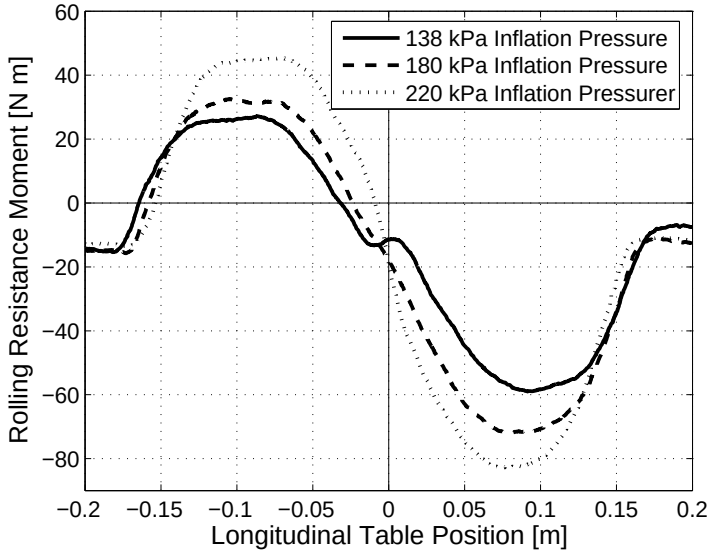

Figure 2.58. The effect of inflation pressure on rolling resistance moment responses for 155/80R13 78 S traversing a rectangular cleat at low speed for 3 kN rated vertical load

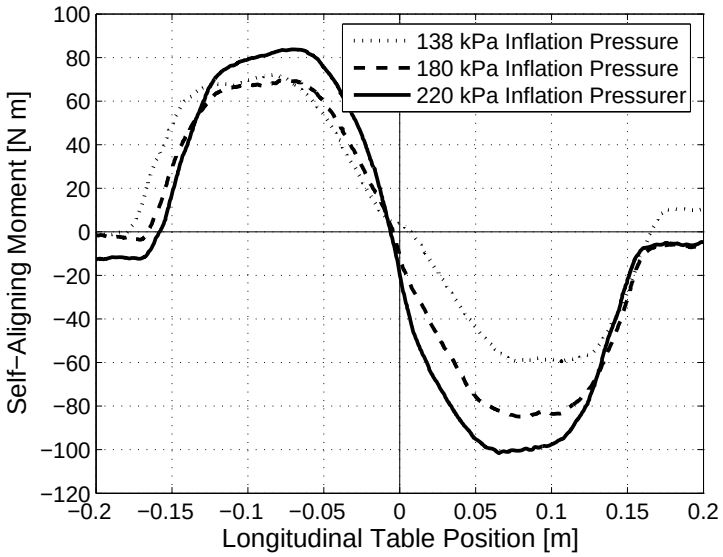

Figure 2.59. The effect of inflation pressure on self-aligning moment responses for 155/80R13 78 S traversing a rectangular cleat at low speed for 3 kN rated vertical load

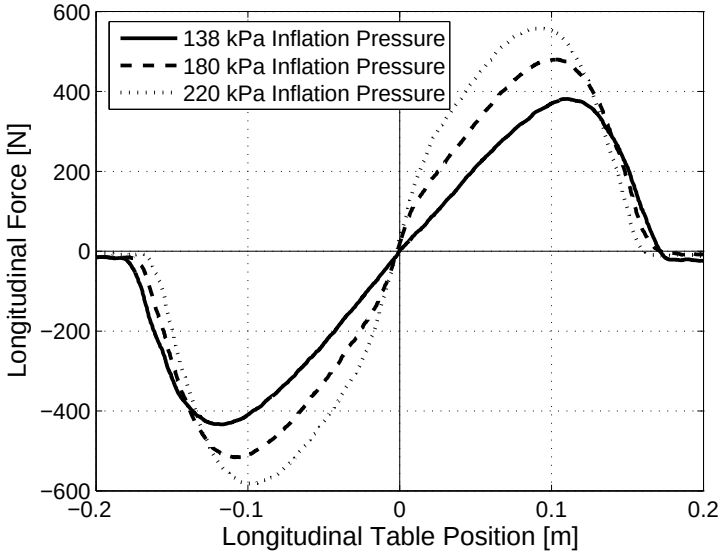

Figure 2.60. The effect of inflation pressure on longitudinal force responses for 155/80R13 78 S traversing a circular cleat at low speed for 3 kN rated vertical load

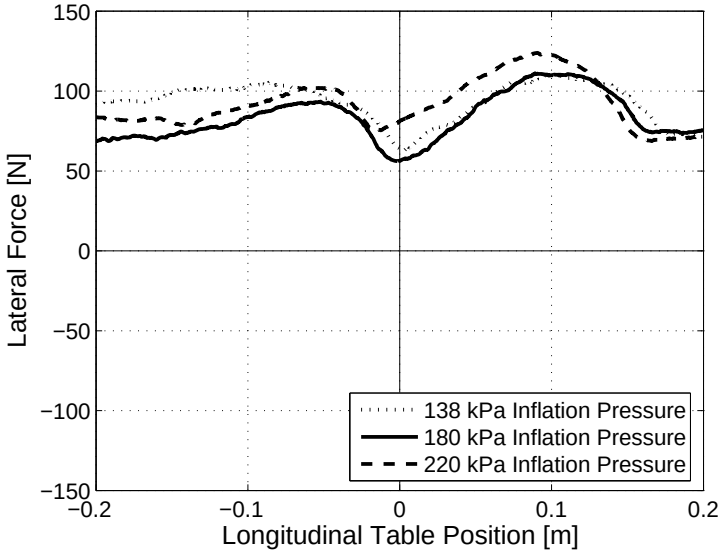

Figure 2.61. The effect of inflation pressure on lateral force responses for 155/80R13 78 S traversing a circular cleat at low speed for 3 kN rated vertical load

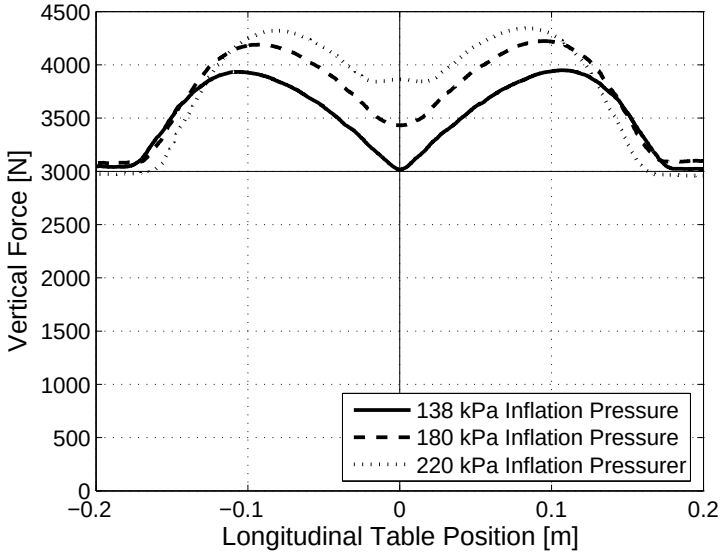

Figure 2.62. The effect of inflation pressure on vertical force responses for 155/80R13 78 S traversing a circular cleat at low speed for 3 kN rated vertical load

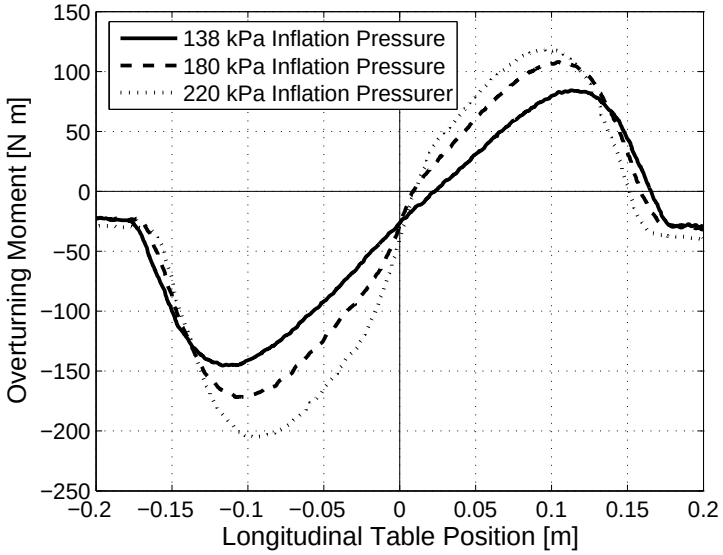

Figure 2.63. The effect of inflation pressure on overturning moment responses for 155/80R13 78 S traversing a circular cleat at low speed for 3 kN rated vertical load

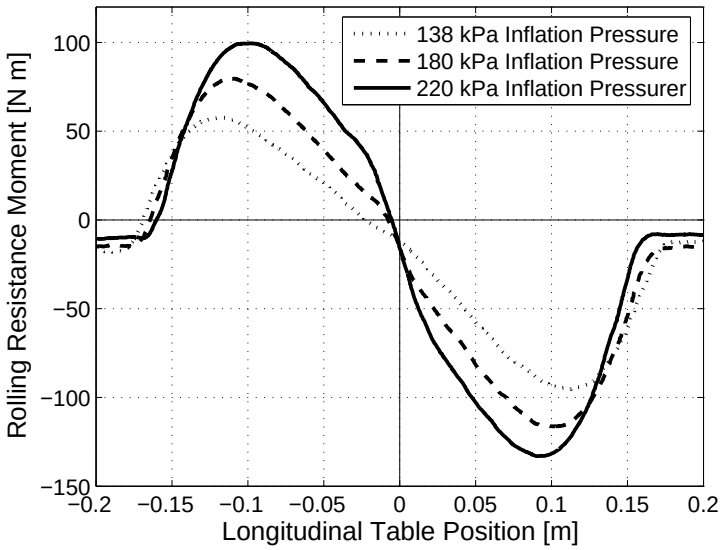

Figure 2.64. The effect of inflation pressure on rolling resistance moment responses for 155/80R13 78 S traversing a circular cleat at low speed for 3 kN rated vertical load

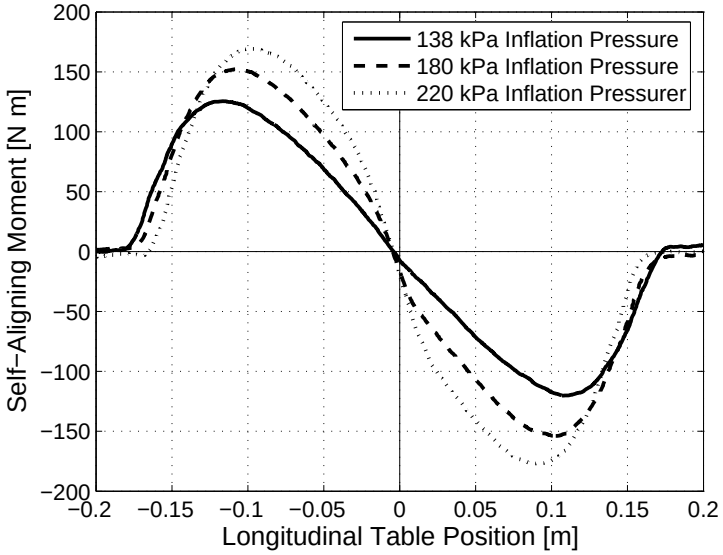

Figure 2.65. The effect of inflation pressure on self-aligning moment responses for 155/80R13 78 S traversing a circular cleat at low speed for 3 kN rated vertical load

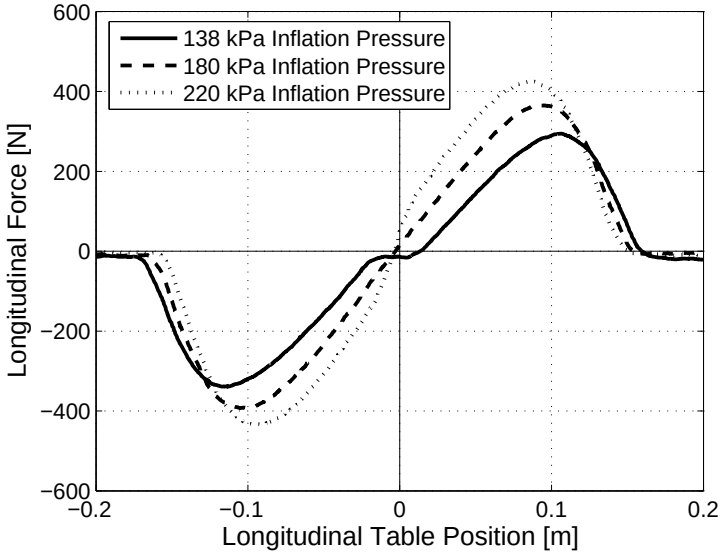

Figure 2.66. The effect of inflation pressure on longitudinal force responses for 155/80R13 78 S traversing a triangular cleat at low speed for 3 kN rated vertical load

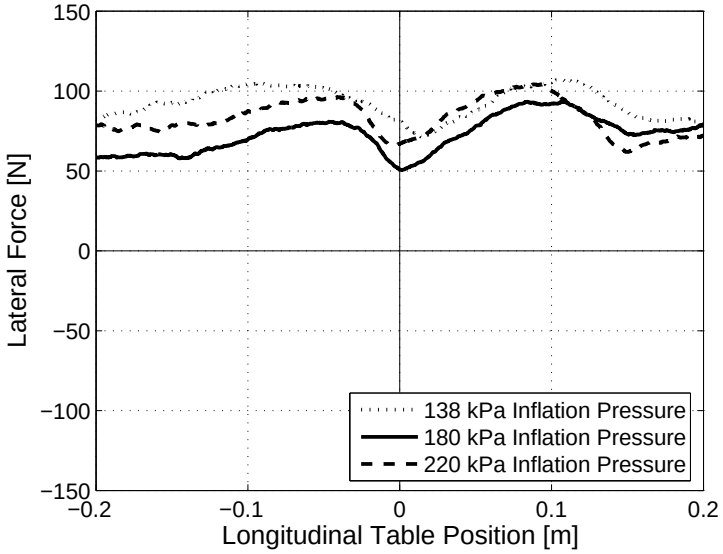

Figure 2.67. The effect of inflation pressure on lateral force responses for 155/80R13 78 S traversing a triangular cleat at low speed for 3 kN rated vertical load

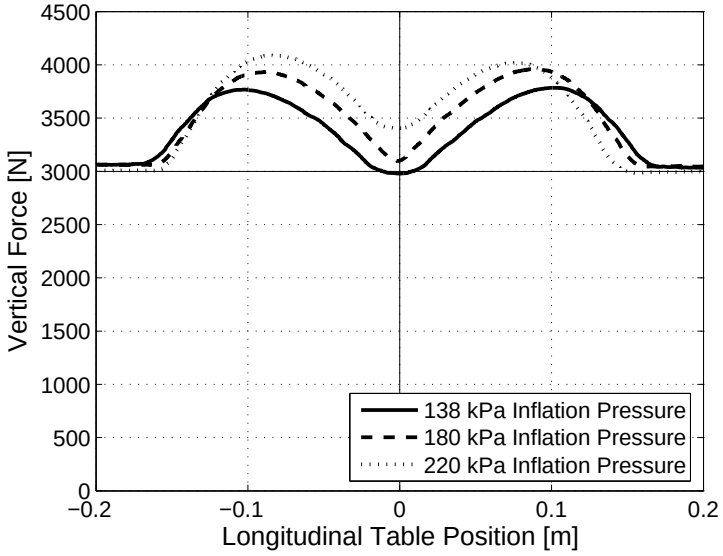

Figure 2.68. The effect of inflation pressure on vertical force responses for 155/80R13 78 S traversing a triangular cleat at low speed for 3 kN rated vertical load

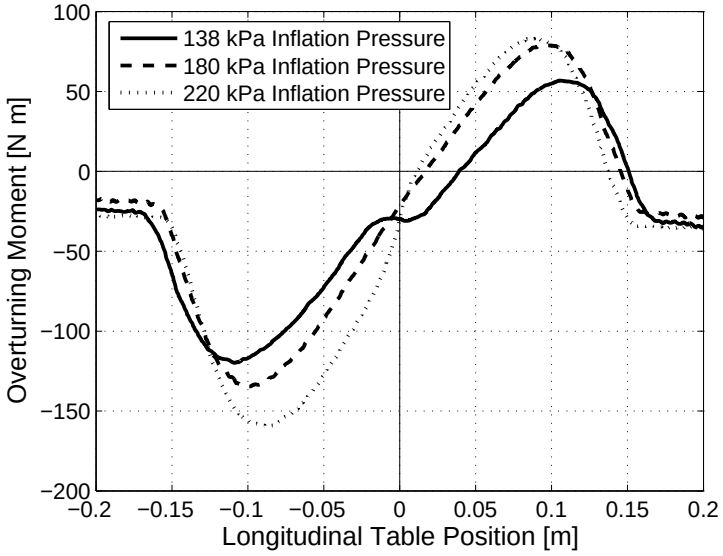

Figure 2.69. The effect of inflation pressure on overturning moment responses for 155/80R13 78 S traversing a triangular cleat at low speed for 3 kN rated vertical load

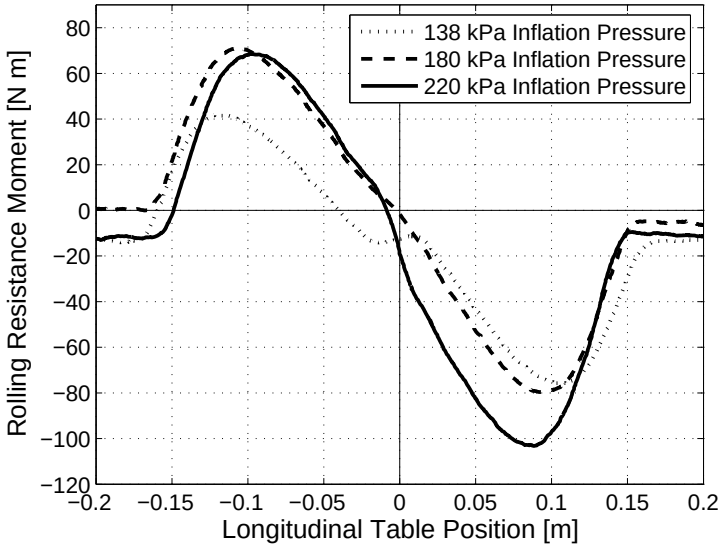

Figure 2.70. The effect of inflation pressure on rolling resistance moment responses for 155/80R13 78 S traversing a triangular cleat at low speed for 3 kN rated vertical load

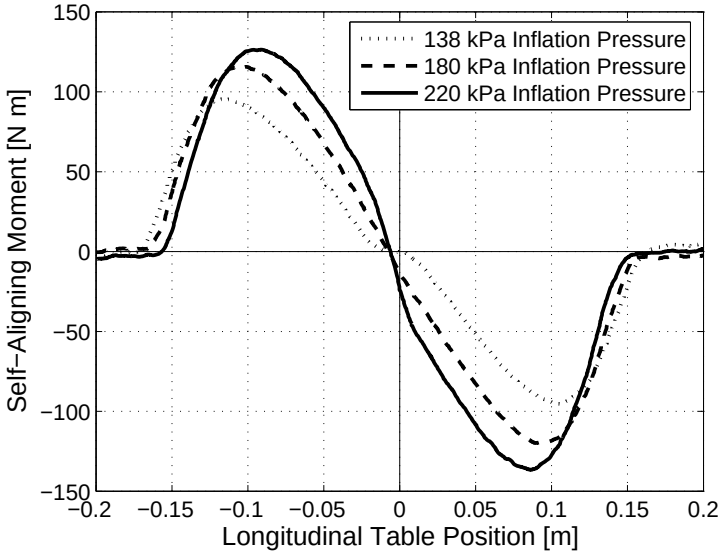

Figure 2.71. The effect of inflation pressure on self-aligning moment responses for 155/80R13 78 S traversing a triangular cleat at low speed for 3 kN rated vertical load

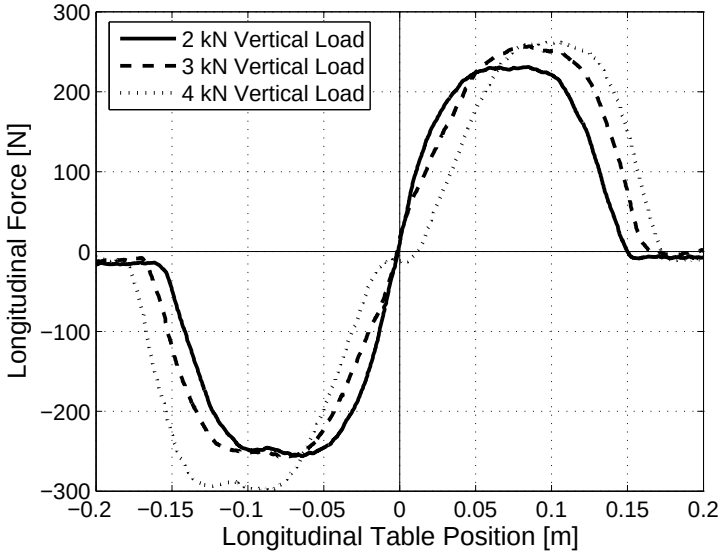

Figure 2.72. The effect of vertical load on longitudinal force responses for 155/80R13 78 S traversing a rectangular cleat at low speed for 180 kPa rated inflation pressure

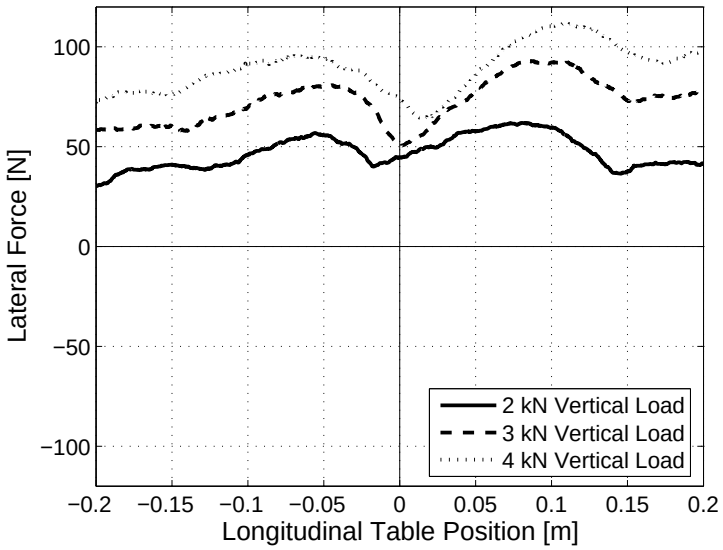

Figure 2.73. The effect of vertical load on lateral force responses for 155/80R13 78 S traversing a rectangular cleat at low speed for 180 kPa rated inflation pressure

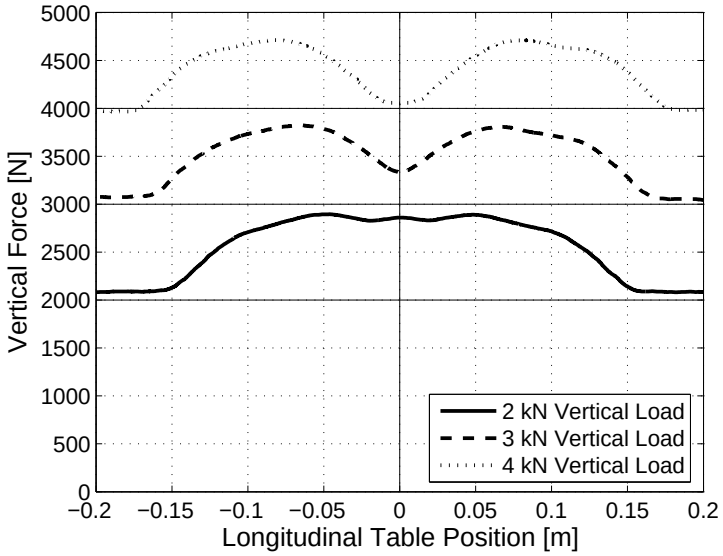

Figure 2.74. The effect of vertical load on vertical force responses for 155/80R13 78 S traversing a rectangular cleat at low speed for 180 kPa rated inflation pressure

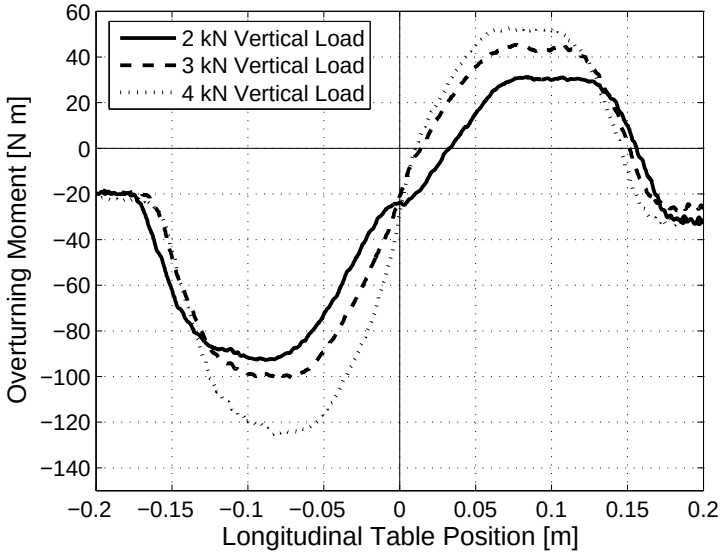

Figure 2.75. The effect of vertical load on overturning moment responses for 155/80R13 78 S traversing a rectangular cleat at low speed for 180 kPa rated inflation pressure

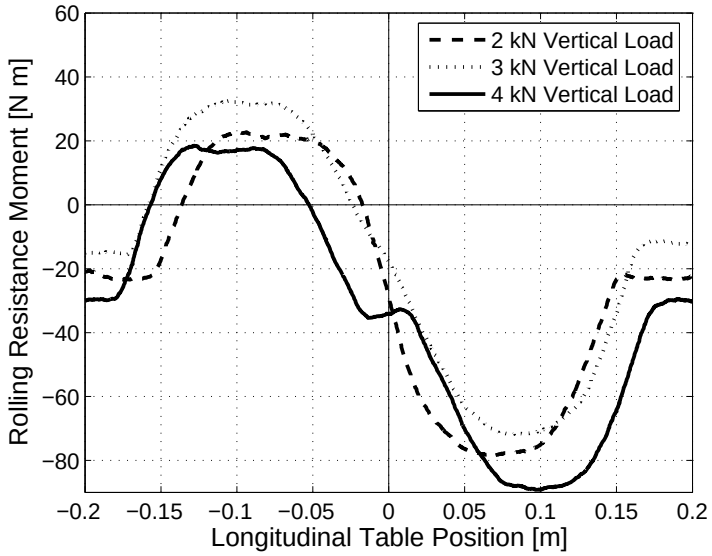

Figure 2.76. The effect of vertical load on rolling resistance moment responses for 155/80R13 78 S traversing a rectangular cleat at low speed for 180 kPa rated inflation pressure

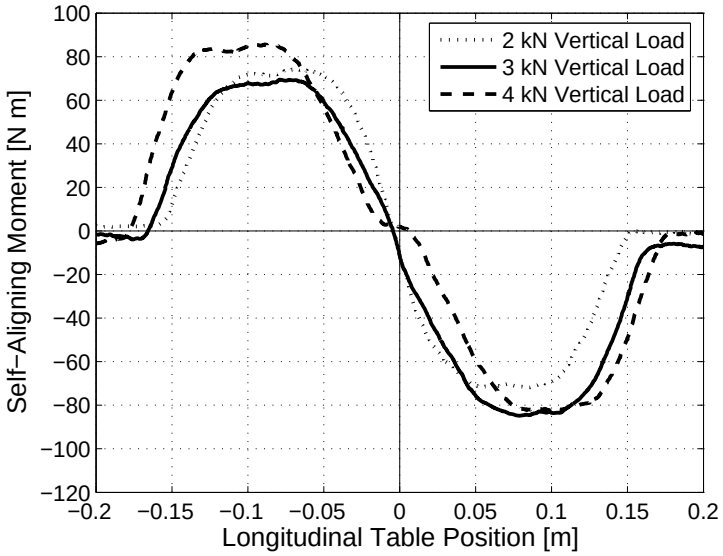

Figure 2.77. The effect of vertical load on self-aligning moment responses for 155/80R13 78 S traversing a rectangular cleat at low speed for 180 kPa rated inflation pressure

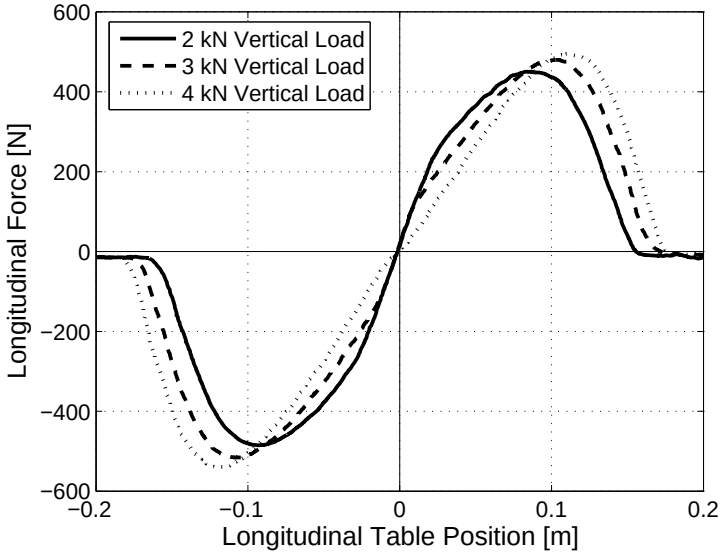

Figure 2.78. The effect of vertical load on longitudinal force responses for 155/80R13 78 S traversing a circular cleat at low speed for 180 kPa rated inflation pressure

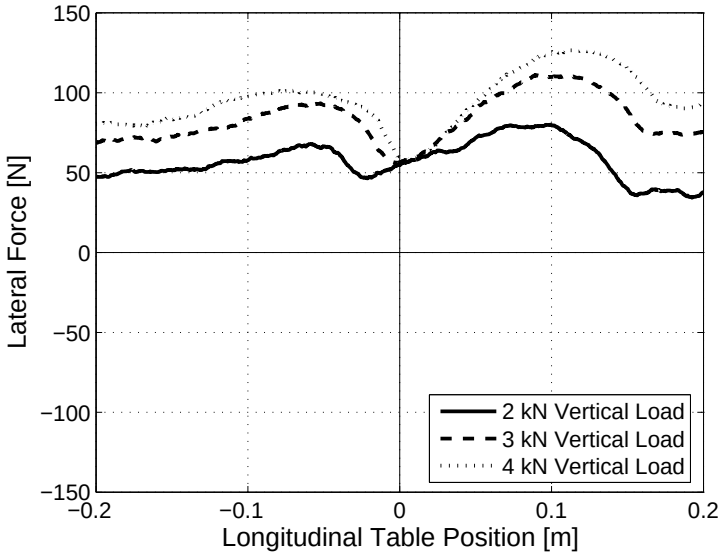

Figure 2.79. The effect of vertical load on lateral force responses for 155/80R13 78 S traversing a circular cleat at low speed for 180 kPa rated inflation pressure

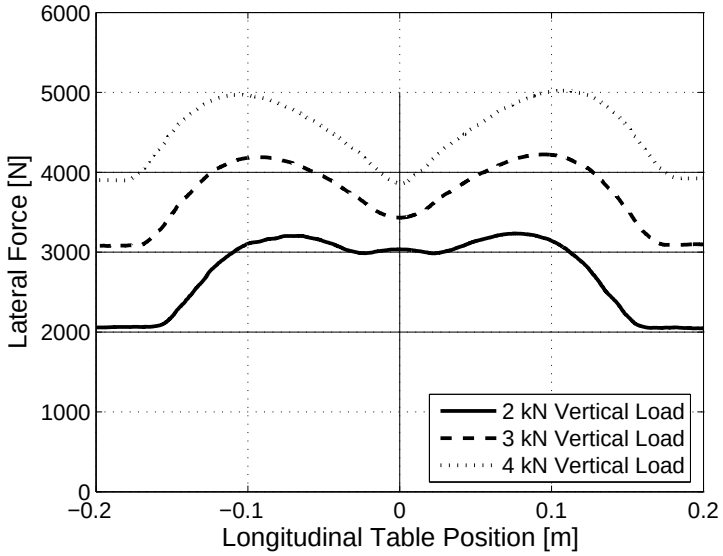

Figure 2.80. The effect of vertical load on vertical force responses for 155/80R13 78 S traversing a circular cleat at low speed for 180 kPa rated inflation pressure

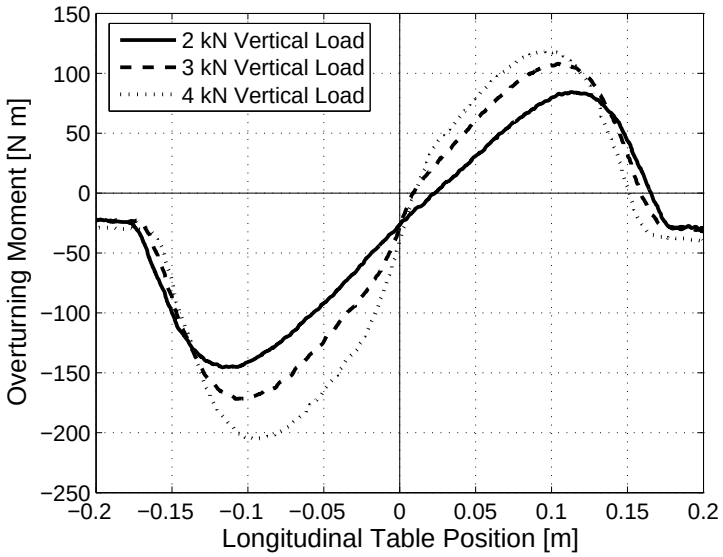

Figure 2.81. The effect of vertical load on overturning moment responses for 155/80R13 78 S traversing a circular cleat at low speed for 180 kPa rated inflation pressure

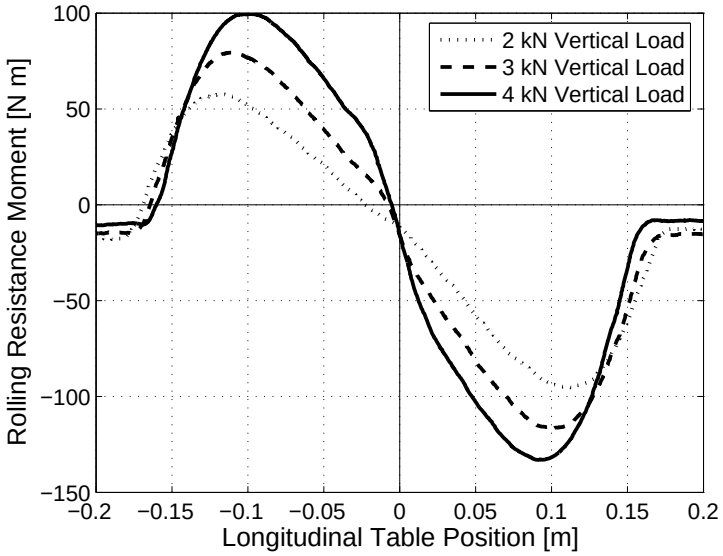

Figure 2.82. The effect of vertical load on rolling resistance moment responses for 155/80R13 78 S traversing a circular cleat at low speed for 180 kPa rated inflation pressure

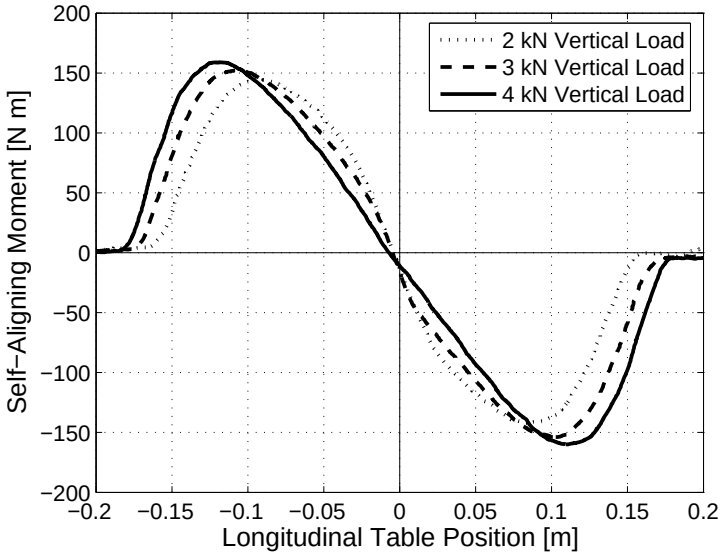

Figure 2.83. The effect of vertical load on self-aligning moment responses for 155/80R13 78 S traversing a circular cleat at low speed for 180 kPa rated inflation pressure

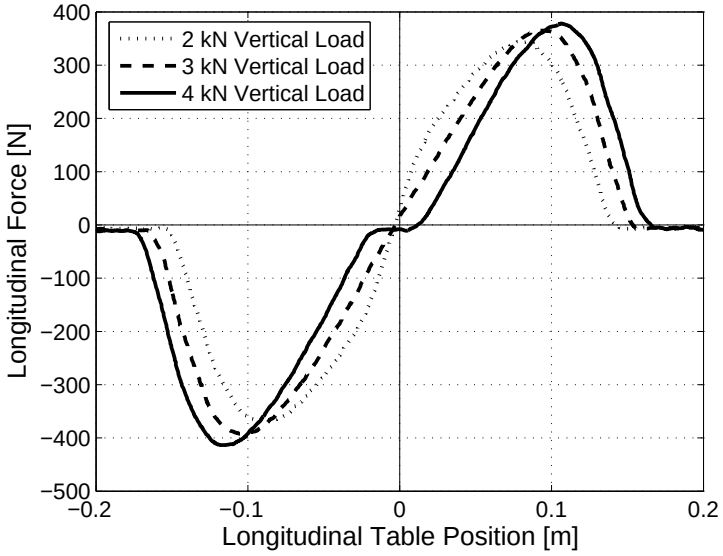

Figure 2.84. The effect of vertical load on longitudinal force responses for 155/80R13 78 S traversing a triangular cleat at low speed for 180 kPa rated inflation pressure

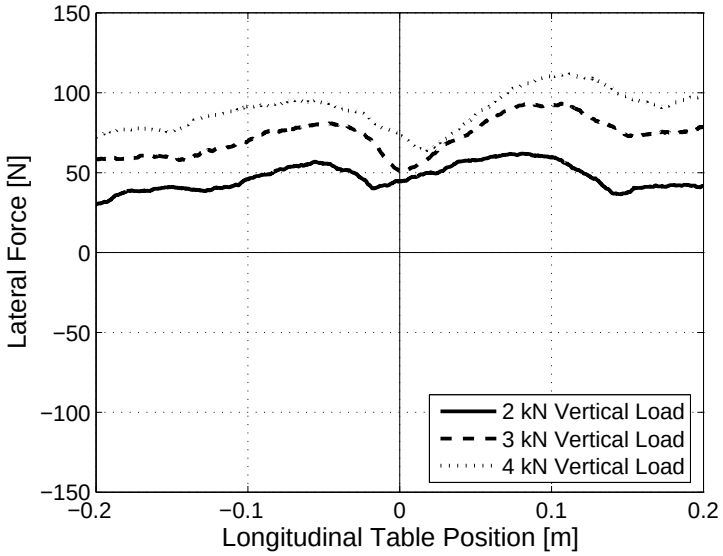

Figure 2.85. The effect of vertical load on lateral force responses for 155/80R13 78 S traversing a triangular cleat at low speed for 180 kPa rated inflation pressure

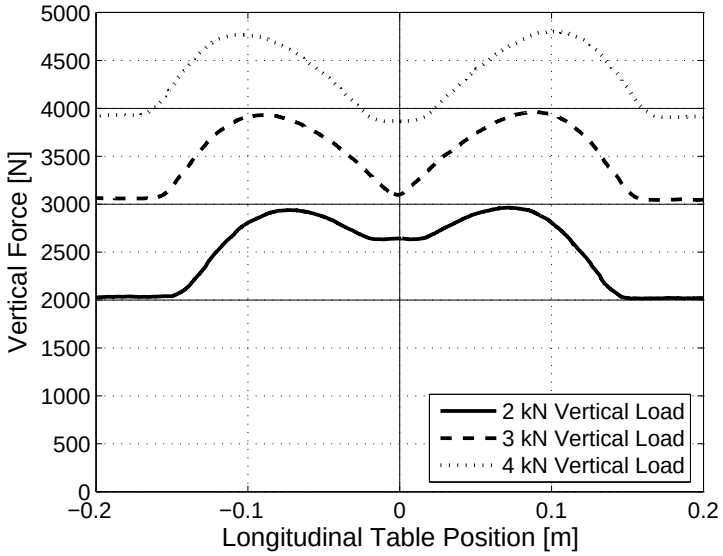

Figure 2.86. The effect of vertical load on vertical force responses for 155/80R13 78 S traversing a triangular cleat at low speed for 180 kPa rated inflation pressure

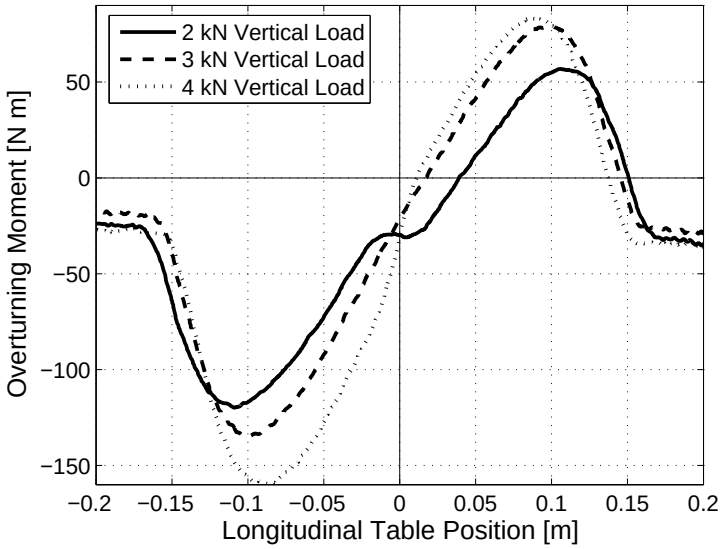

Figure 2.87. The effect of vertical load on overturning moment responses for 155/80R13 78 S traversing a triangular cleat at low speed for 180 kPa rated inflation pressure

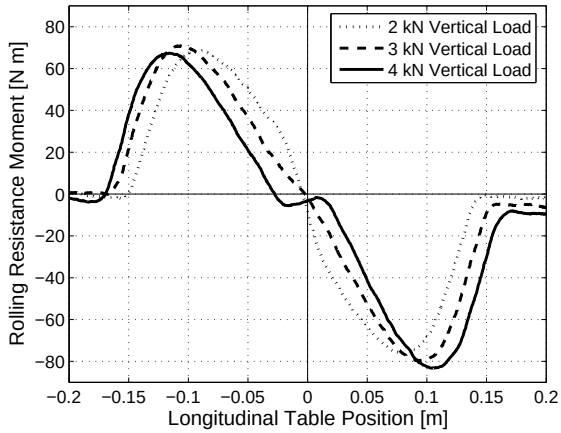

Figure 2.88. The effect of vertical load on rolling resistance moment responses for 155/80R13 78 S traversing a triangular cleat at low speed for 180 kPa rated inflation pressure

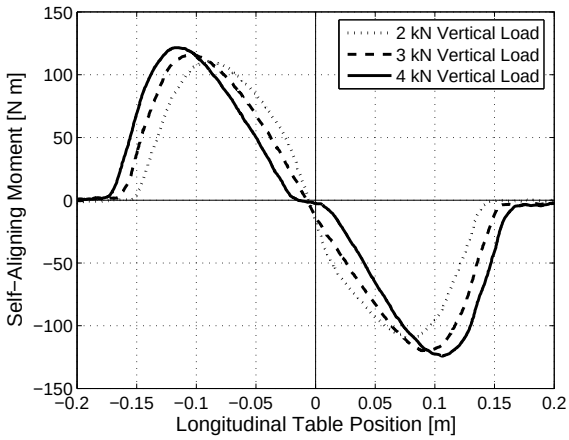

Figure 2.89. The effect of vertical load on self-aligning moment responses for 155/80R13 78 S traversing a triangular cleat at low speed for 180 kPa rated inflation pressure

As mentioned before as a typical enveloping characteristic, the minimum vertical force becomes lower than the force on a flat surface. To illustrate this characteristic , three different cases are considered: 4 kN vertical load and 138 kPa inflation Pressure,3 kN vertical load and 180 kPa inflation pressure and 2 kN vertical load and 220 kPa inflation pressure as shown in Figures 2.90, 2.91 and 2.92, respectively. It can be easily seen from Figures 2.90, 2.91 and 2.92 that these phenomena are more pronounced especially for higher vertical load and lower inflation pressure conditions. In terms of cleats types, there is an exception for the rectangular cross sectioned cleat. However,

when the vertical load is increased, minimum force seems to be lower than the force on a flat surface as mentioned in [49].

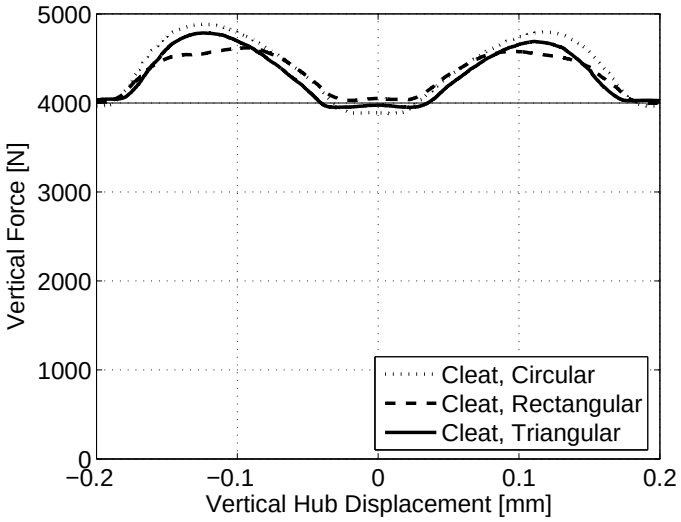

Figure 2.90. For 4 kN vertical load and 138 kPa inflation pressure, the effect of cleat types on vertical load response of 155R13

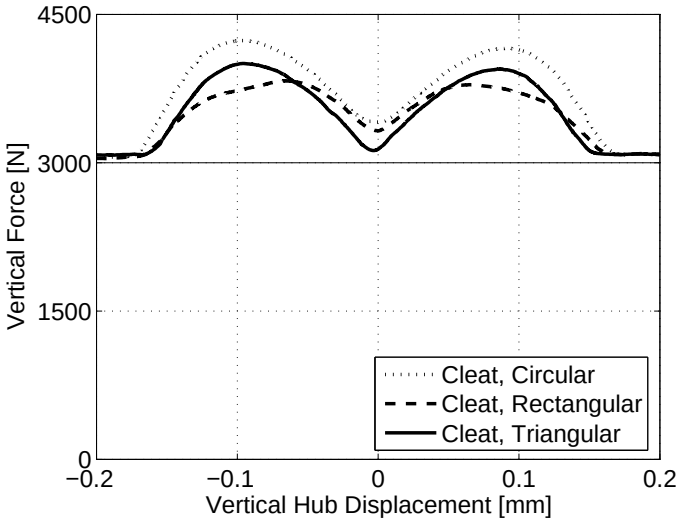

Figure 2.91. For 3 kN rated vertical load and rated 180 kPa inflation pressure, the effect of cleat types on vertical load response of 155R13

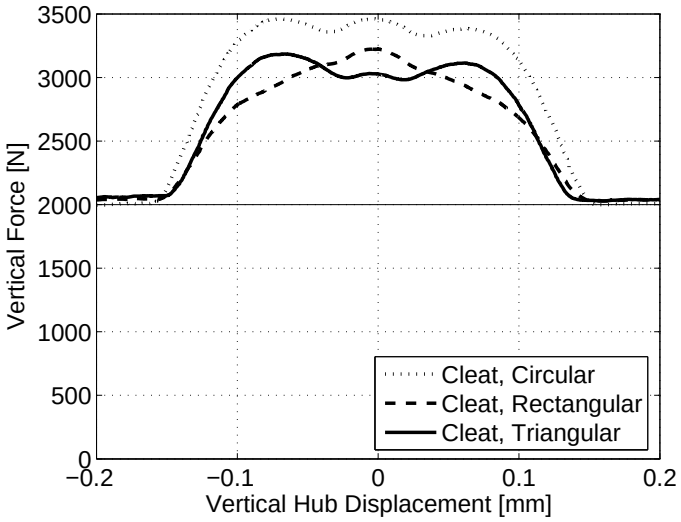

Figure 2.92. For 2 kN vertical load and 220 kPa inflation pressure, the effect of cleat types on vertical load response of 155R13

3. STATIC FINITE ELEMENT ANALYSIS OF THE TIRE

Static tire analysis is an important stage of tire modeling. The pressure distribution over the cross section and the vertical stiffness of the tire are obtained in static analysis. Static analysis is also an indicator for tire modeling before carrying out dynamic analysis which is more complex than the static one. In order to solve the dynamic problem within a meaningful time period, some assumptions are needed to be made. Material modeling, mesh density and solution technique, etc., can be adjusted by comparing results of the static analysis with experimental results or other available results in literature.

In this section, steps of static tire analysis are given in detail. The tire is first modeled using linear elements and then quadratic elements. All procedures are the same for both tire models. However, there are some differences between them and they are mentioned in this section. Axisymmetric tire analysis which is the first step of the static tire modeling is constructed and then ground contact analysis is carried out. The pressure distribution over the cross-section and vertical stiffness of the tire are presented.

3.1. Tire Modeling

A small sized automobile tire, 155/80R13 78S, is modeled. Tire properties are obtained from [24].

The tire has one textile body ply and two steel tread plies. Properties of the tire are given in Table 3.1. There are four types of rubber materials in the tire. The material properties for Mooney-Rivlin material model used in the model are given in Table 3.2. Also, elastic and geometric properties of the reinforcing materials are given in Table 3.3 and Table 3.4, respectively.

Table 3.1. Properties of 155/R13 78S tire [24]

Recommended rims	4.5 B x 13 or 5 B x 13
Inflated section width	157 mm
Inflated outer diameter	578 mm
Maximum load per tire	4220 N (430 kgf)
Maximum inflation pressure	220 kPa (32 psi)

Table 3.2. Mooney-Rivlin material constants of rubber [24]

Rubber material	C_{10}	C_{01}
Bead Filler	14.14 MPa	21.26 MPa
Sidewall	171.8 kPa	830.3 kPa
Undertread	140.4 kPa	427 kPa
Tread	806.1 kPa	1.805 MPa

Table 3.3. Elastic properties of the reinforcing materials [24]

Carcass material	**Modulus in tension**	**Modulus in compression**
Textile Body Ply	3.97 GPa	198.5 MPa
Steel Breaker Plies	200 GPa	100 GPa

Table 3.4. Geometric properties of the reinforcing materials [24]

Reinforcing type	**Ply angle** $[^0]$	**Cord diameter** $[mm]$	**End per decimeter**	**Equivalent thickness** $[mm]$
Bead Bundle	0	1	Not applicable	Not applicable
Body Ply	90	0.68	79	0.120
Breaker (Steel)	± 20	0.25	330	0.162
Breaker (Textile)	± 20	1	112	0.878
Breaker(Zero)	0	0.68	100	0.363

The tire with a smooth tread is analyzed. The static analysis includes two steps: axisymmetric analysis and ground contact analysis. In the first step, the tire is mounted on the wheel by applying predefined displacements to nodes near the bead bundle region or to the special nodes controlling the rim motion to adjust recommended rim width. The specials nodes will be discussed later. Then, the tire is inflated up to the predefined pressures (138, 180, 220 kPa). The second step of the analysis is ground contact analysis. After completed axisymmetric analysis, 3-D tire model is constructed. Then, vertical stiffness of the tire is calculated. For different vertical tire loads, contact patch shapes are also shown.

3.1.1. Axisymmetric Tire Modeling

During the first step of the static tire analysis, the deformation is axisymmetric and an axsymmetric analysis is performed by using MSC. Marc. Main tire geometric dimensions are shown in Figure 3.1.

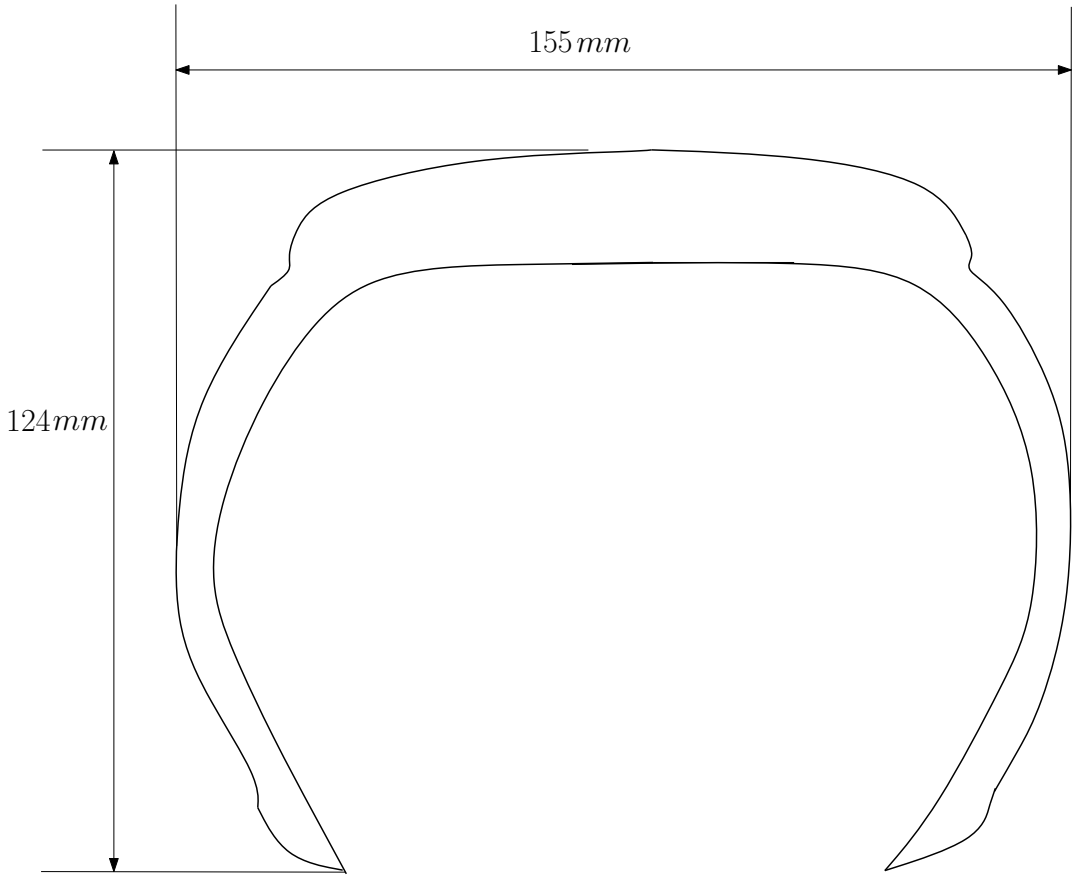

Figure 3.1. Main Tire Geometric Dimensions

The nodes are located in such a way that finite elements are created based on the material distributions over the tire cross section. Finite element mesh of the tire is shown in Figure 3.2. There are 161 nodes and 174 elements in the axisymmetric tire model using linear element types. There are 2 additional special nodes which control the rigid rim movements and are explained in the following sections. Two element types are used in the model. There are 120 elements (namely, Element 10) being four-node, isoparametric, arbitrary quadrilateral written for incompressible axisymmetric applications which are modeling the rubber matrix and 54 elements (namely, Element 144) being a hollow, isoparametric four-node quadrilateral which are modeling reinforcing cords (called as rebar) [87]. Element types are shown in Figure 3.3.

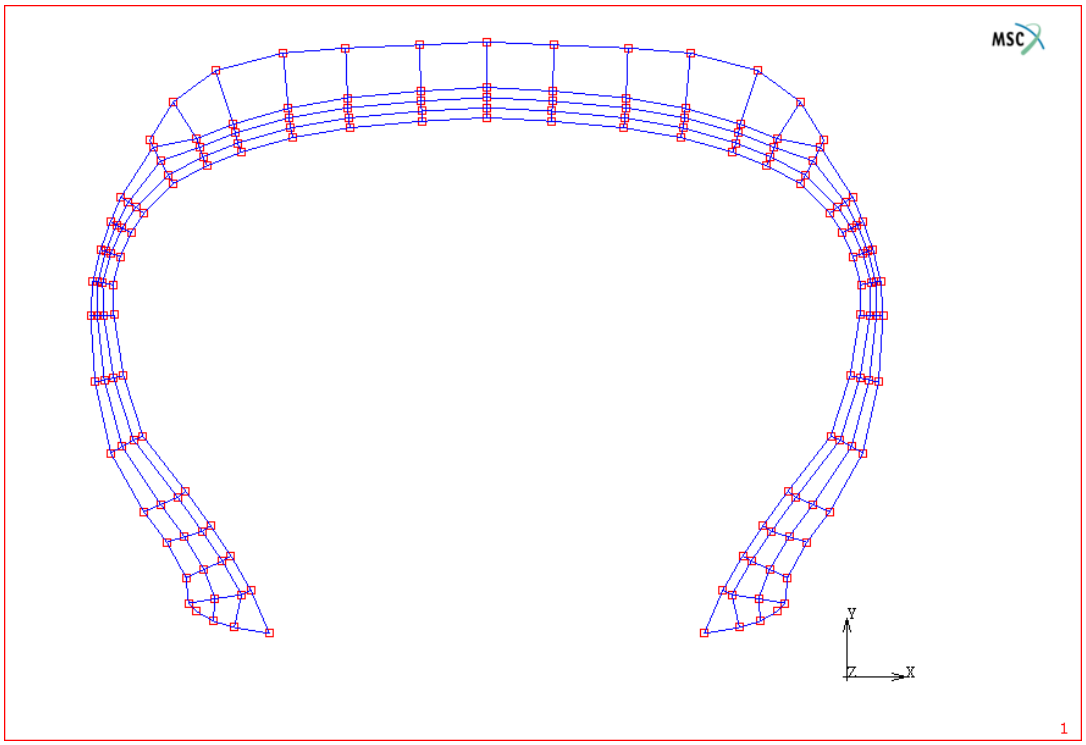

Figure 3.2. Axisymmetric finite element mesh of the tire

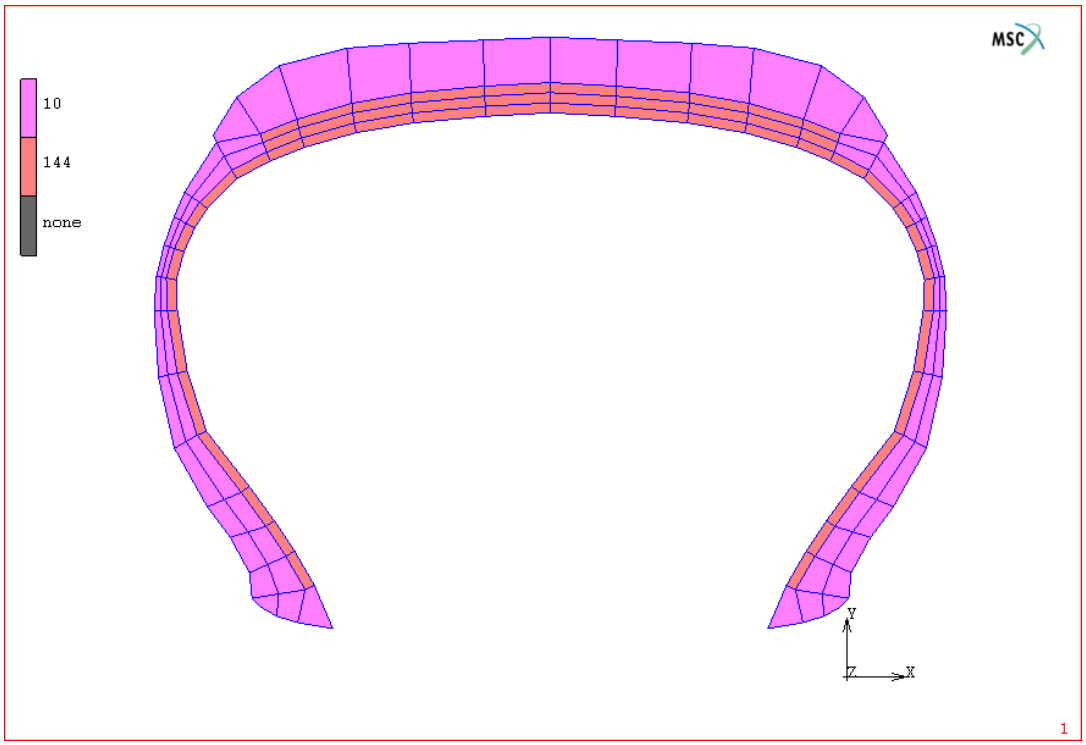

Figure 3.3. Element types used in the model

In MSC. Marc, "Rebar Elements" are the special elements and shown in Figure 3.4. These elements are embedded elements placed in the matrix elements. To model these elements, five inputs are needed. These are rebar orientation, rebar area, relative layer position, number of rebars per unit length and material properties. Rebar orientation and relative layer position concepts are given in Figure 3.5.

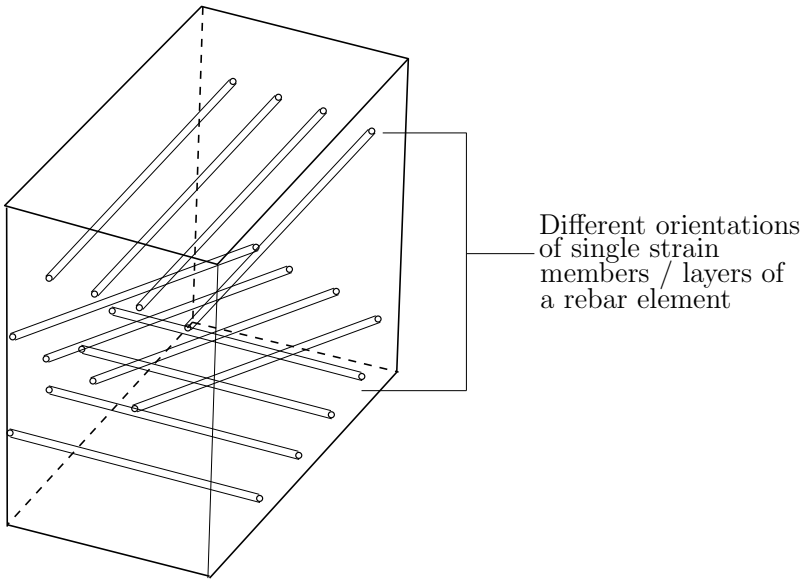

Figure 3.4. Rebar concept in MSC. Marc [87]

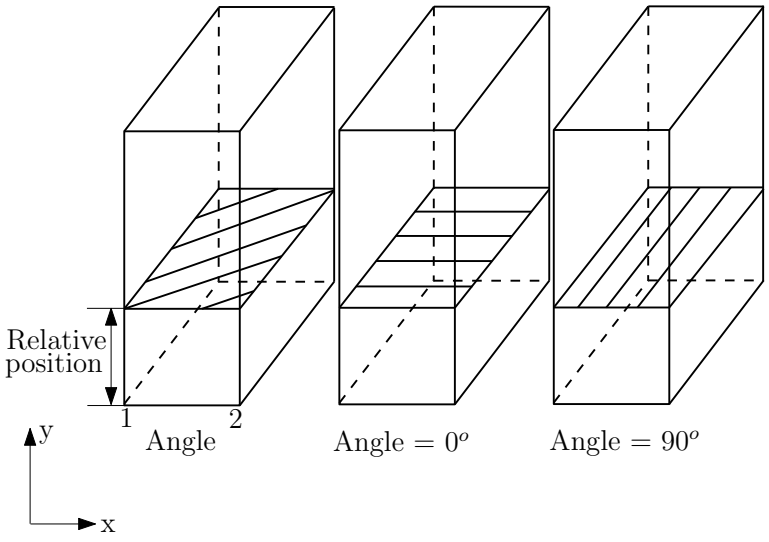

Figure 3.5. Rebar orientation and relative layer position definition in MSC. Marc [87]

Contact bodies are shown in Figure 3.6. In the initial studies, to model rim with 4.5 *in* and 5 *in* width, curves are positioned in such a way that they adjust recom-

mended rim width and then, held fixed in all directions. Then, predefined horizontal displacements (1.84 mm horizontal displacement for 4.5 in rim width and 4.51 mm for 5 in rim width) are applied to the nodes around the bead bundle region of the tire to model sitting the tire on the rim. Then, the second alternative tire-rim interaction is constructed to reduce CPU time. In this case, the curves are positioned as shown in Figure 3.6 and the curve representing the rim is glued to the tire. Both tire model results are compared and there is a little differences between them. So, in the following ground contact and dynamic analysis, the second tire-rim modeling type is used and presented here. There are two boundary conditions applied to the tire, which are fixed displacements and pressure. The predefined internal pressures are applied to the inner edge of the tire. The fixed boundary conditions applied to the node controlling the rigid body movements represent the sitting tire on the wheel. Controlling rigid body motions in MSC. Marc will be mentioned in the following sections. Boundary conditions are shown in Figure 3.7. In reality, inflation pressure remains perpendicular to the tire inner surface and increases while the tire deforms. In the first case, by using FOLLOWER option of MSC. Marc, the inflation pressure remains perpendicular to tire inner surface. However, the second aspect is omitted. On the other hand, Mooney-Rivlin material formulation is used. Viscoelastic effects of rubber are omitted. Material properties of the tire are given in Figure 3.8.

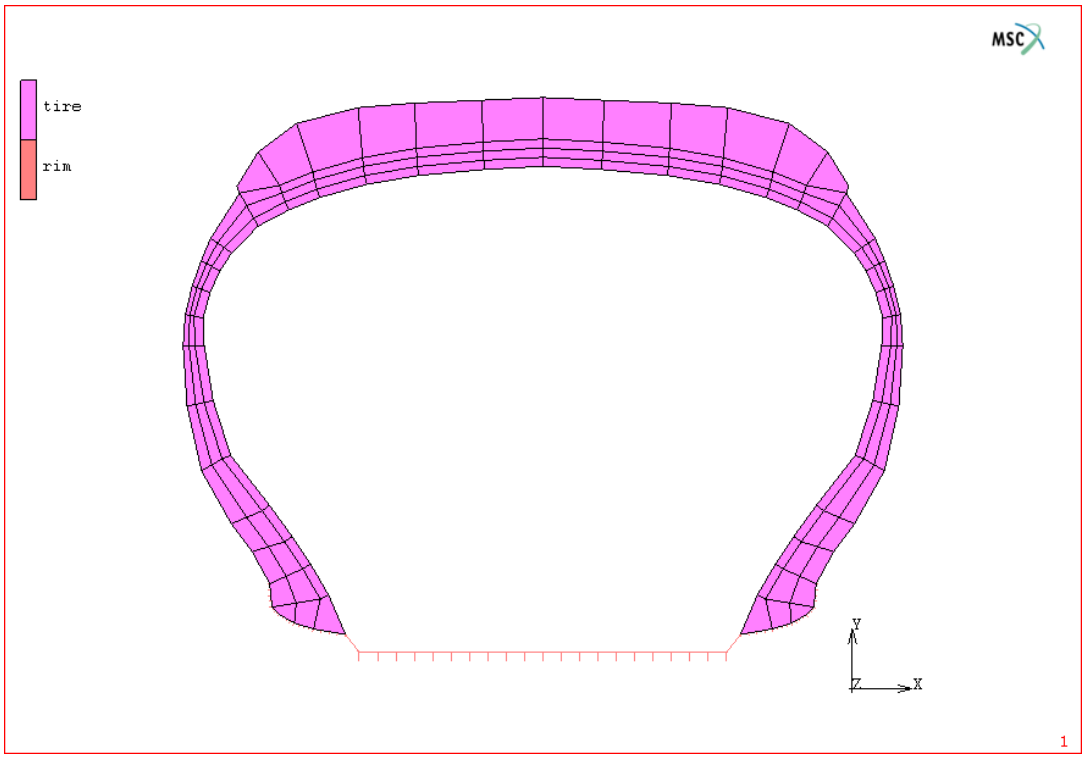

Figure 3.6. Contact bodies in the tire finite element model

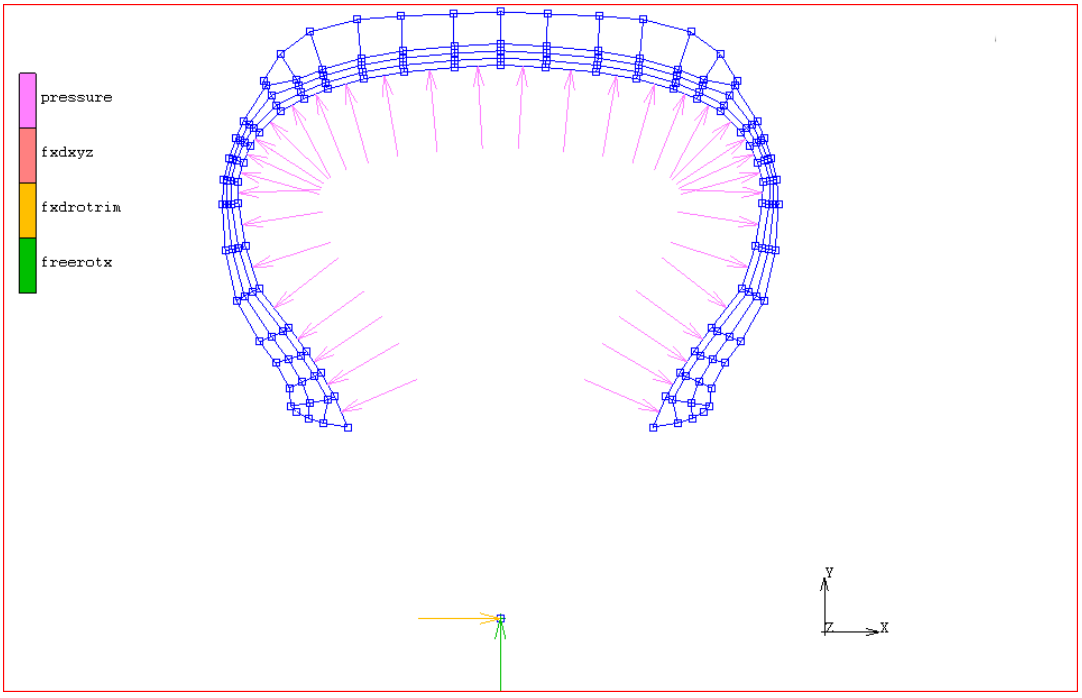

Figure 3.7. Boundary conditions applied to the tire

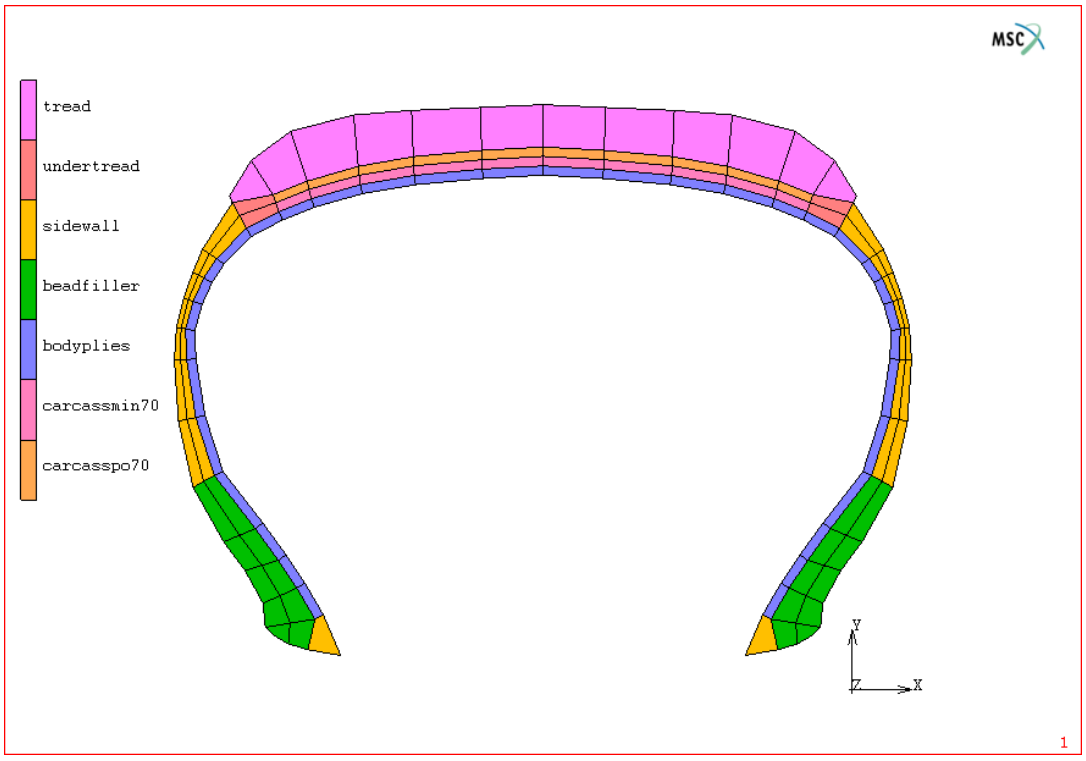

Figure 3.8. Material properties of the tire

The tire has one textile ply and two steel breakers plies reinforcing layers. Rebar layer locations on the cross-section of the tire are shown in Figure 3.9. In MSC. Marc, layer orientation is perpendicular to the symmetry plane. In this figure, bottom layer represents the textile carcass reinforcement and the middle layer represents the reinforcement layer with -20^o belt angle with respect to circumferential axis of the tire. The upper layer, on the other hand, refers to the layer $+20^o$ belt angle with respect to circumferential axis of the tire. In addition, the second tire model using quadratic elements is introduced. Main tire geometry, reinforcements, contact bodies and boundary conditions are the same for both tire models. Finite element mesh and element types for the second tire model are shown in Figures 3.10 and 3.11, respectively. There are 753 nodes and 294 elements in the axisymmetric tire model. 198 elements (namely, Element 33) being eight-node, isoparametric, arbitrary quadrilateral written for incompressible axisymmetric applications modeling the rubber matrix and 98 elements (namely, Element 48) being a hollow, isoparametric eight-node quadrilateral modeling reinforcing cords are used in the model.

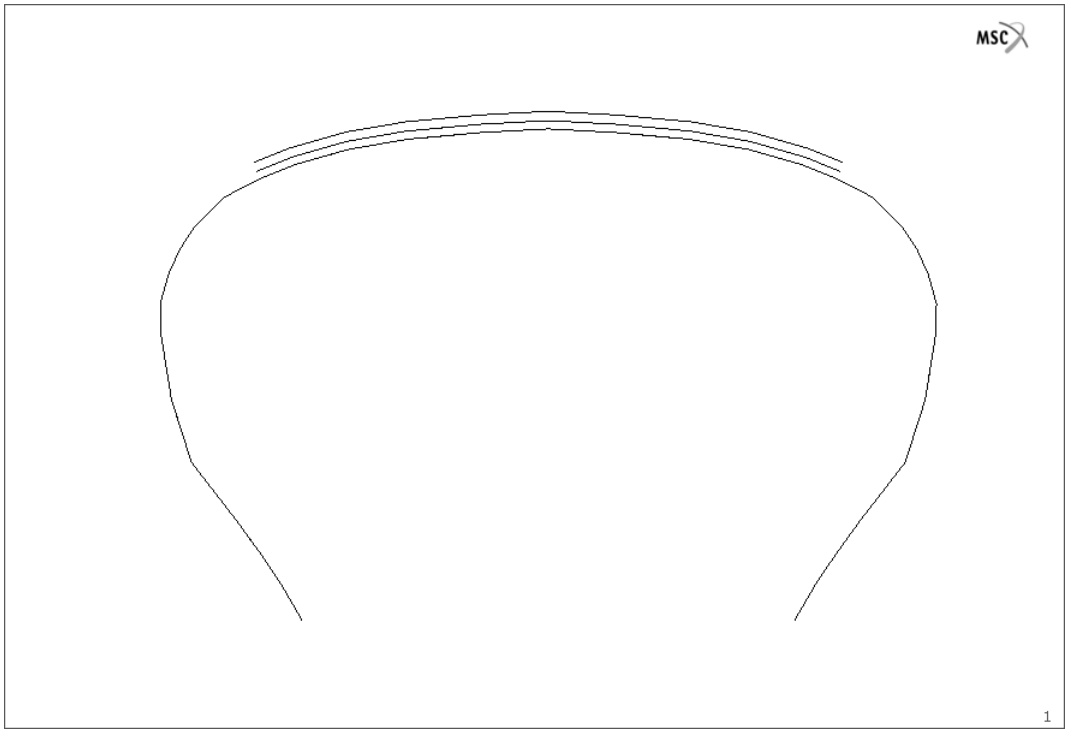

Figure 3.9. Placements of reinforcing layers

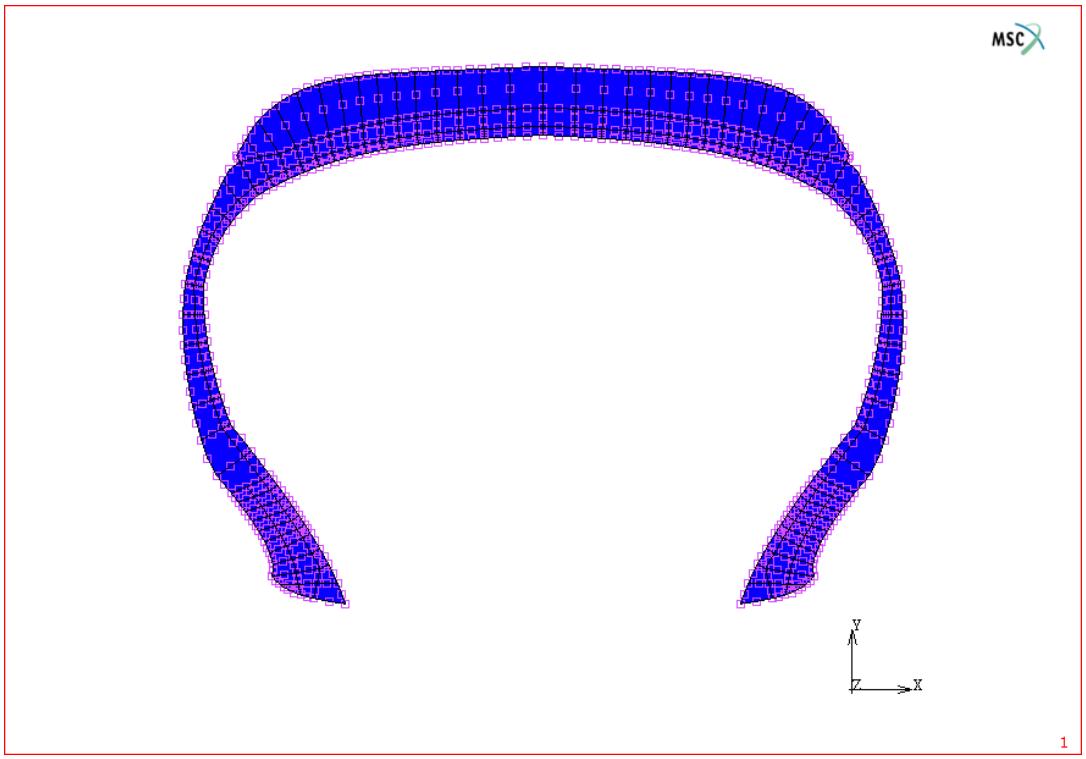

Figure 3.10. Axisymmetric finite element mesh of the tire

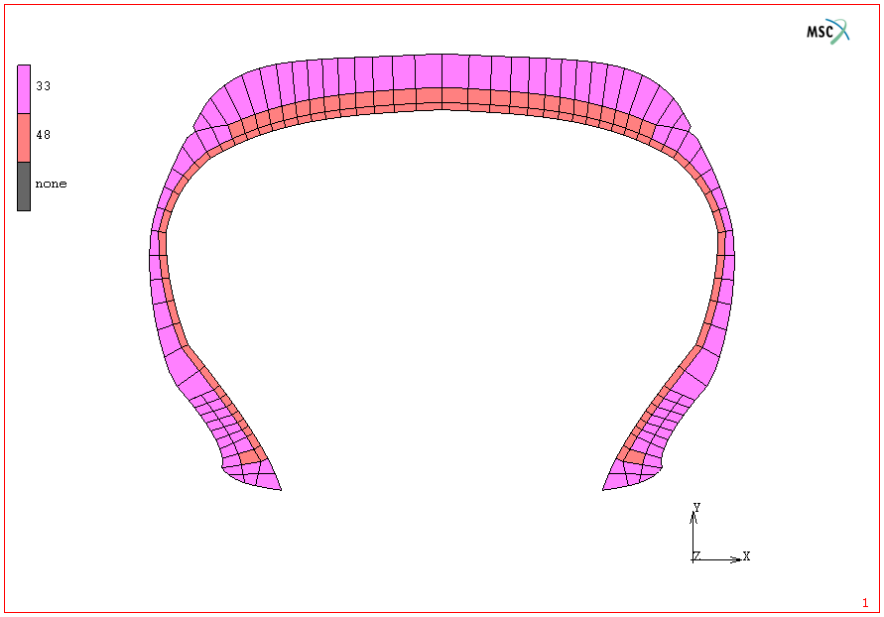

Figure 3.11. Element types used in the model

On the other hand, Mooney-Rivlin material formulation is again used and viscoelastic effects of rubber are omitted. Material properties of the tire are given in Figure 3.12.

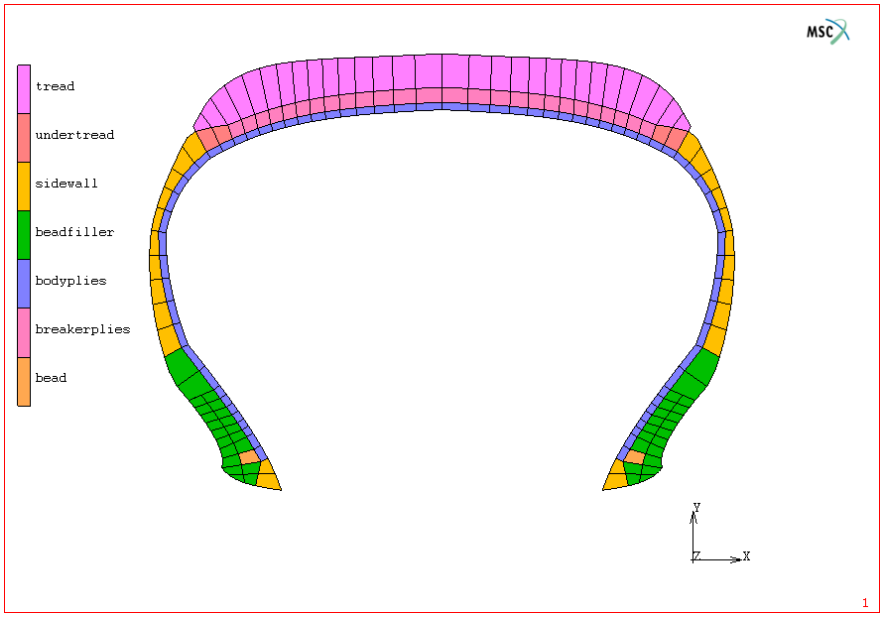

Figure 3.12. Material properties of the tire

3.1.2. Ground Contact Tire Modeling

Ground contact analysis is the last step of the static tire analysis. In this analysis, ground is taken as a rigid flat surface which simulates, to some extent, experimental conditions. The coefficient of friction is taken to be $0,8$. Coulomb friction modeling with 0.01 relative sliding velocities is used.

Ground contact analysis is not axisymmetric and there is a need to construct 3-D tire model. 3-D tire model is constructed by using AXITO3D option of MSC. Marc. In this option, axisymmetric results are taken as the initial conditions for 3D analysis. So, CPU time can be saved by this way. In the first tire model using linear elements, equal spaced mesh expansion (10 degree spacing) is used and final finite element model is shown in Figure 3.13. There are 10440 elements and 9648 nodes in the model. In the second model, non-equal spaced mesh expansion are used and fine mesh is only in the contact region and its vicinity. In the contact region, the tire is meshed with 6 degree spacing and the remaining parts are meshed with 30 degree spacing. The final finite element model is shown in Figure 3.14. There are 5880 elements and 20620 nodes in the model. To some extent, coarse mesh density is used in the static analysis of the tire. As a property of AXITO3D option of MSC. Marc, element types, material properties, reinforcement layers (that is, rebar) and boundary conditions are automatically constructed and expanded. Material and element types of the 3-D tire model using linear elements are shown in Figures 3.15 and 3.16, respectively. Element type 7 is a 8-node, isoparametric, arbitrary hexahedral written for incompressible applications and element type 146 is an isoparametric, 3-D, 8-node empty brick where one can place single strain member such as rods or cords (i.e., rebar) [87]. Material and element types of the 3-D tire model using quadratic elements are also shown in Figures 3.17 and 3.18, respectively. Element type 35 is a 20-node, isoparametric, arbitrary hexahedral written for incompressible applications and element type 23 is an isoparametric, 3-D, 20-node empty brick where one can place single strain member such as rods or cords (i.e., rebar) [87].

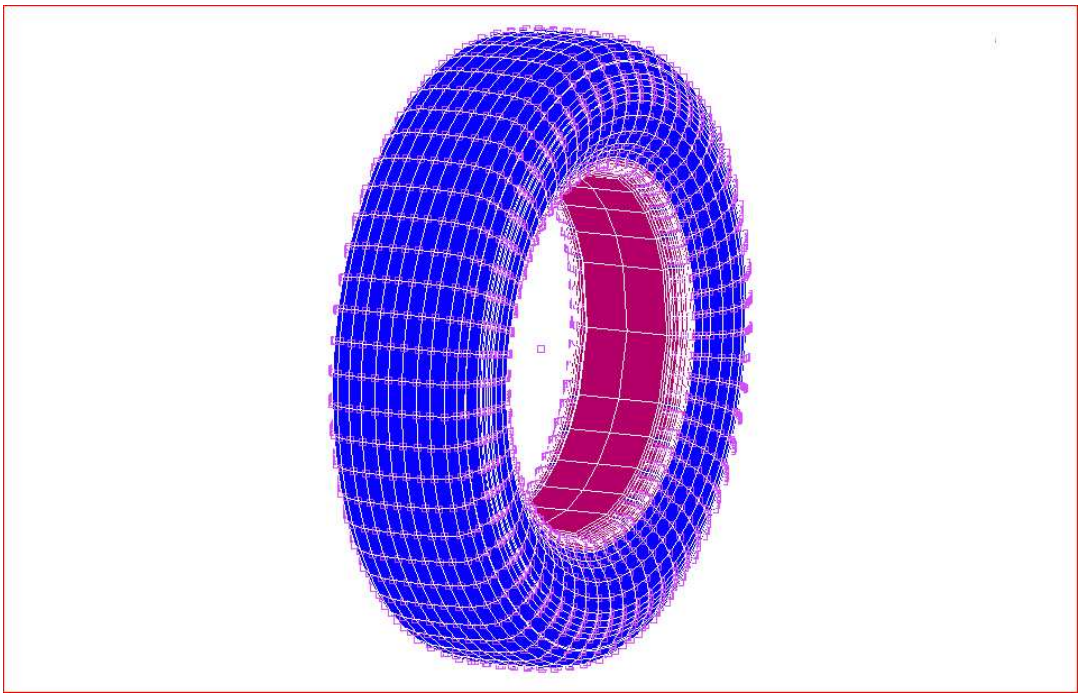

Figure 3.13. 3D finite element mesh of the tire (The tire model using linear elements)

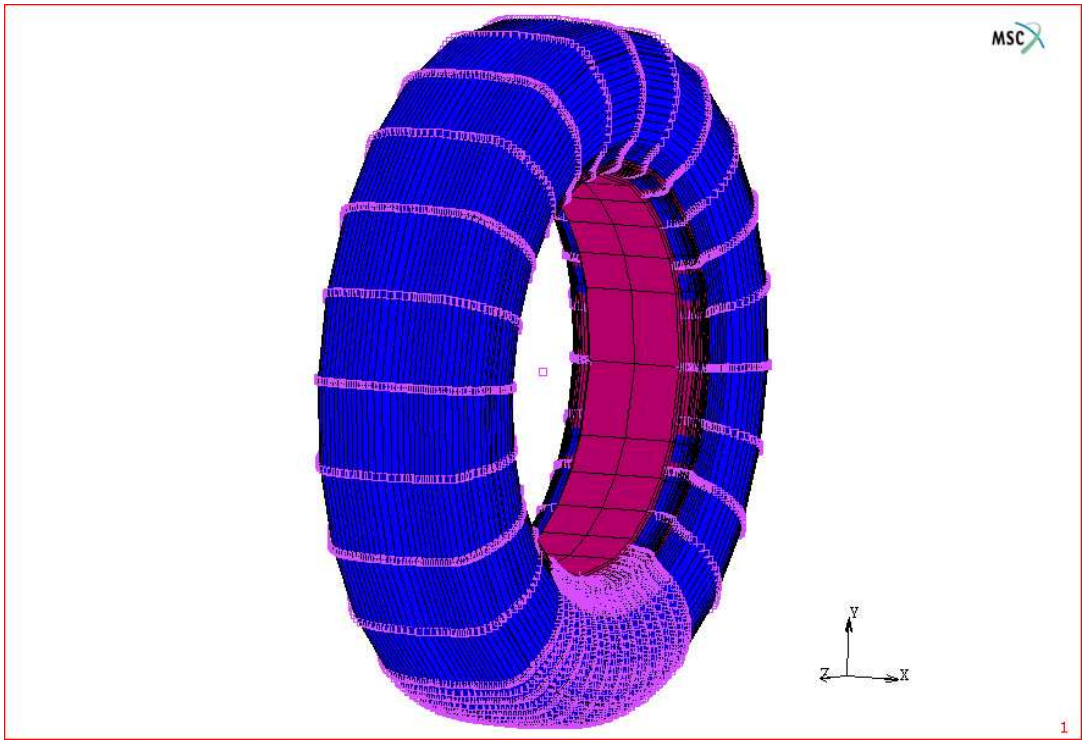

Figure 3.14. 3D finite element mesh of the tire (The tire model using quadratic elements)

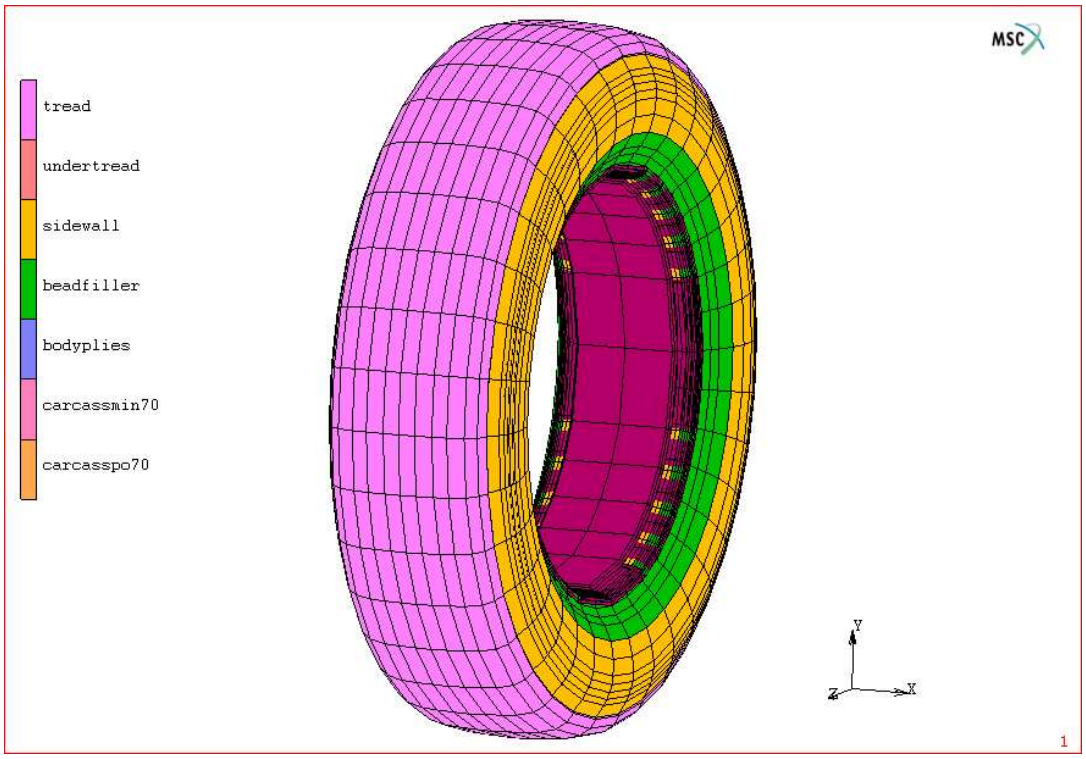

Figure 3.15. Material properties of the 3-D tire model using linear elements

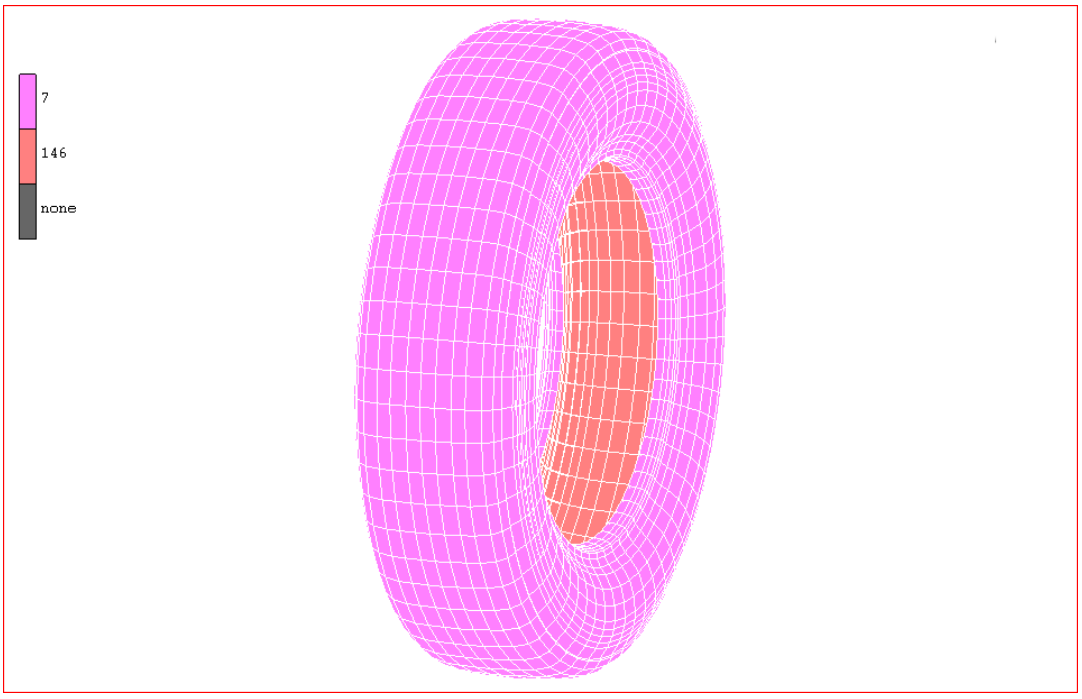

Figure 3.16. Element types used in 3-D tire model using linear elements

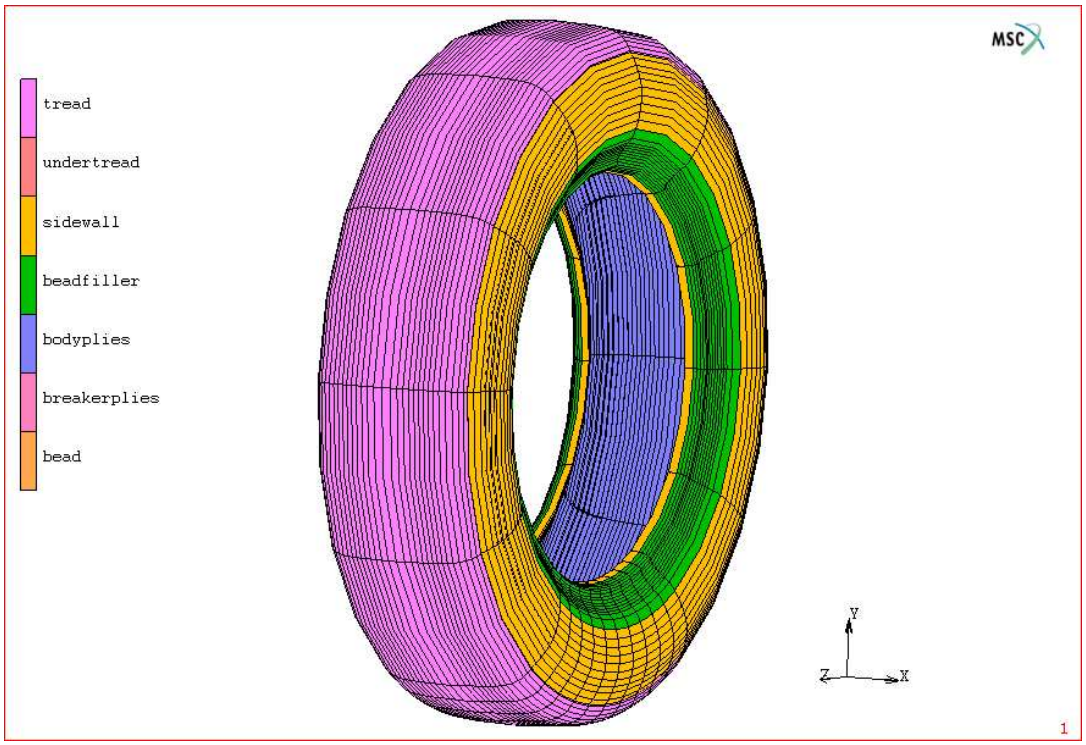

Figure 3.17. Material properties of the 3-D tire model using quadratic elements

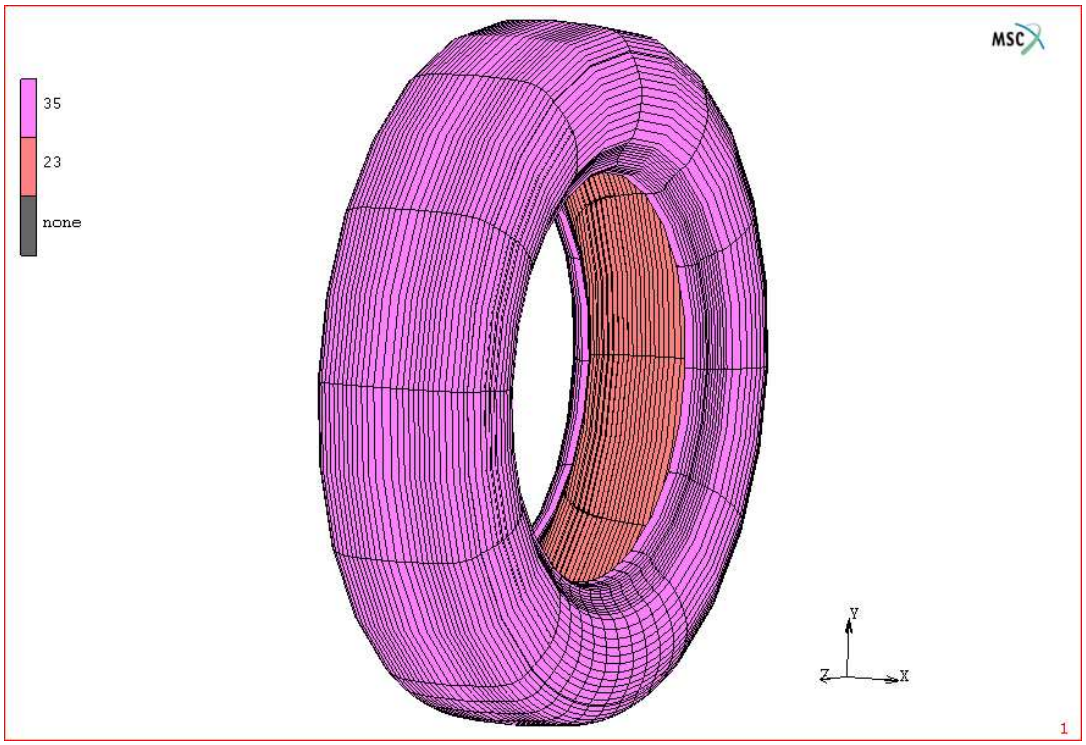

Figure 3.18. Element types used in 3-D tire model using quadratic elements

Ground contact analysis of the tire is carried out on a flat surface as made in experimental studies. The tire-road assembly is shown in the Figure 3.19. Road representing the ground and rim are modeled as a rigid body with analytical surface, which in turn reduce computational time and leads accurate results. The rim is glued to the tire and bead bundle component of the tire is omitted as made in [48]. The glue option is the special type of friction model and there is no relative tangential motion. When the glue type friction model is activated, the constraint equations are automatically written between the two meshes. In this option, nodes in contact can be allowed to separate by specifying the threshold value. Otherwise, nodes are not allowed to separate. So, by using this option, two dissimilar meshes can be joined.

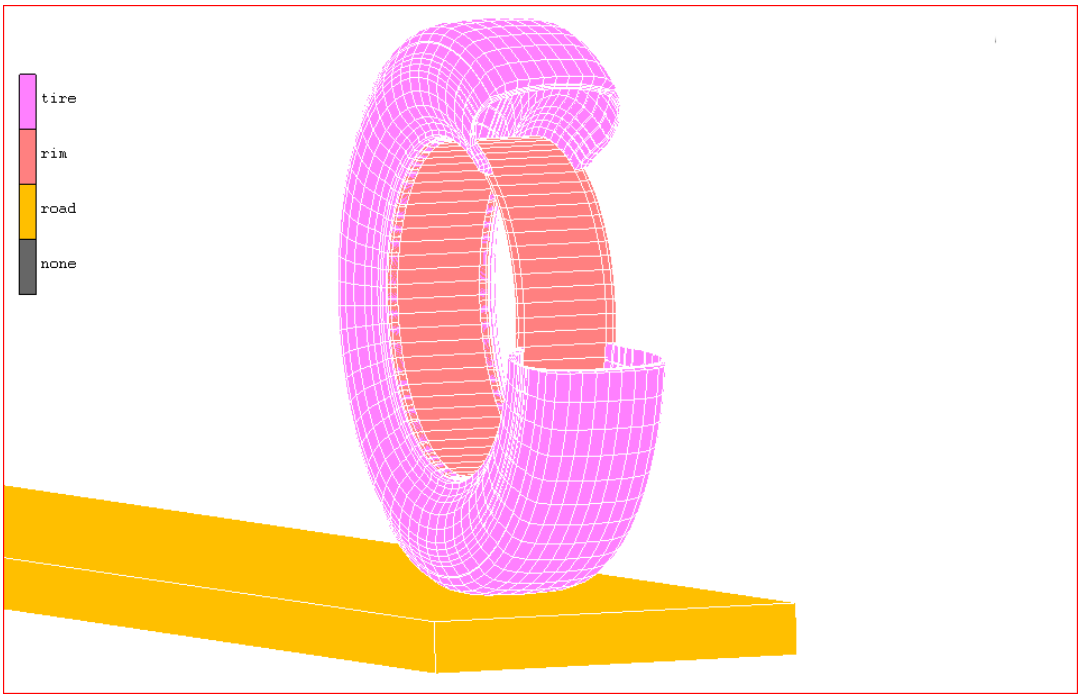

Figure 3.19. The Tire-road Assembly

Location and orientation of reinforcements used in 3-D model are shown in Figure 3.20. The reinforcement layers with an angle of $\pm 20^o$ are shown in this figure.

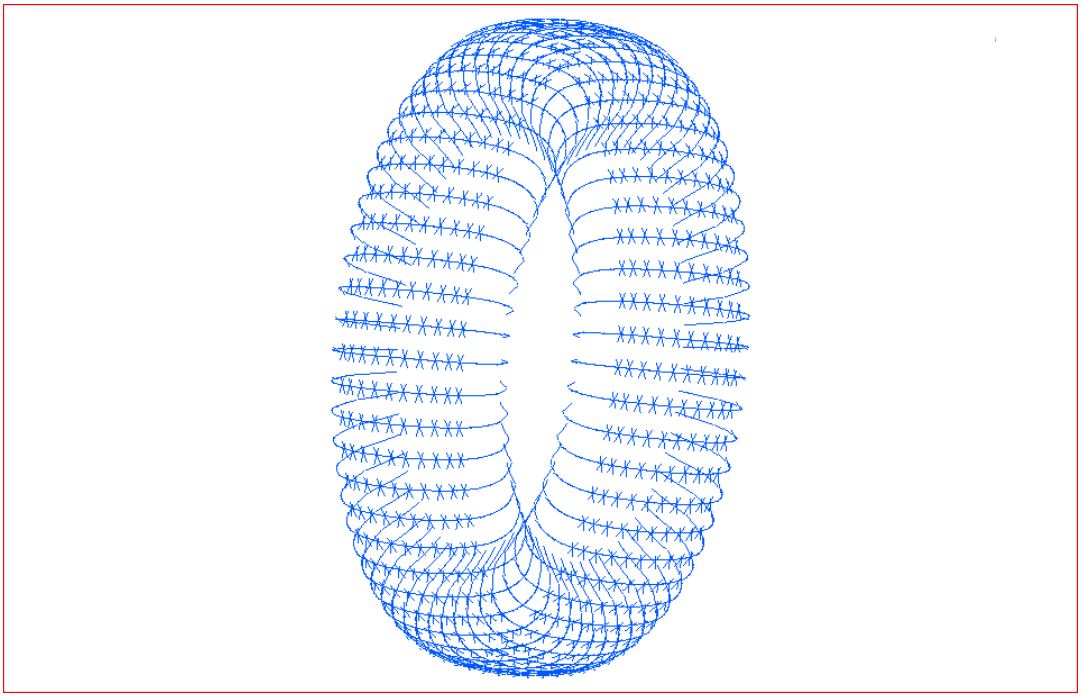

Figure 3.20. General View of Location and Orientation of Reinforcements Used in 3-D Model

As mentioned before, there are two special nodes in MSC. Marc: control node and auxiliary node. By using these two special nodes, rigid body motion is mainly controlled by three ways. These are prescribing load, velocity and position shown in Figures 3.21a and 3.21b. In the following static analysis, load-controlled rigid body will be used. In order to control the load-controlled rigid body motion, there is a need to construct these two nodes different from model and assign them to the rigid body. In 2-D, the control node has two translational degrees of freedom and the auxiliary node has one rotational degree of freedom (corresponding to the global z-direction). In 3-D, the former has three translational degrees of freedom (corresponding to global x-, y-, and z-direction) and the latter has three rotational degrees of freedom (corresponding to the global x-, y-, and z- direction) [87]. In the ground contact analysis, there are two additional boundary conditions. One of them is the fixed displacements in lateral and longitudinal direction applied to the control node and shown in Figure 3.32. Also,

rotational degrees of freedom in all directions are held fixed applied to the auxiliary node and shown in Figure 3.23. Another boundary condition is the displacement in vertical direction. So, vertical load applied to the tire can be adjusted by applying predefined displacements to the road. Vertical displacement boundary condition is shown in Figure 3.24.

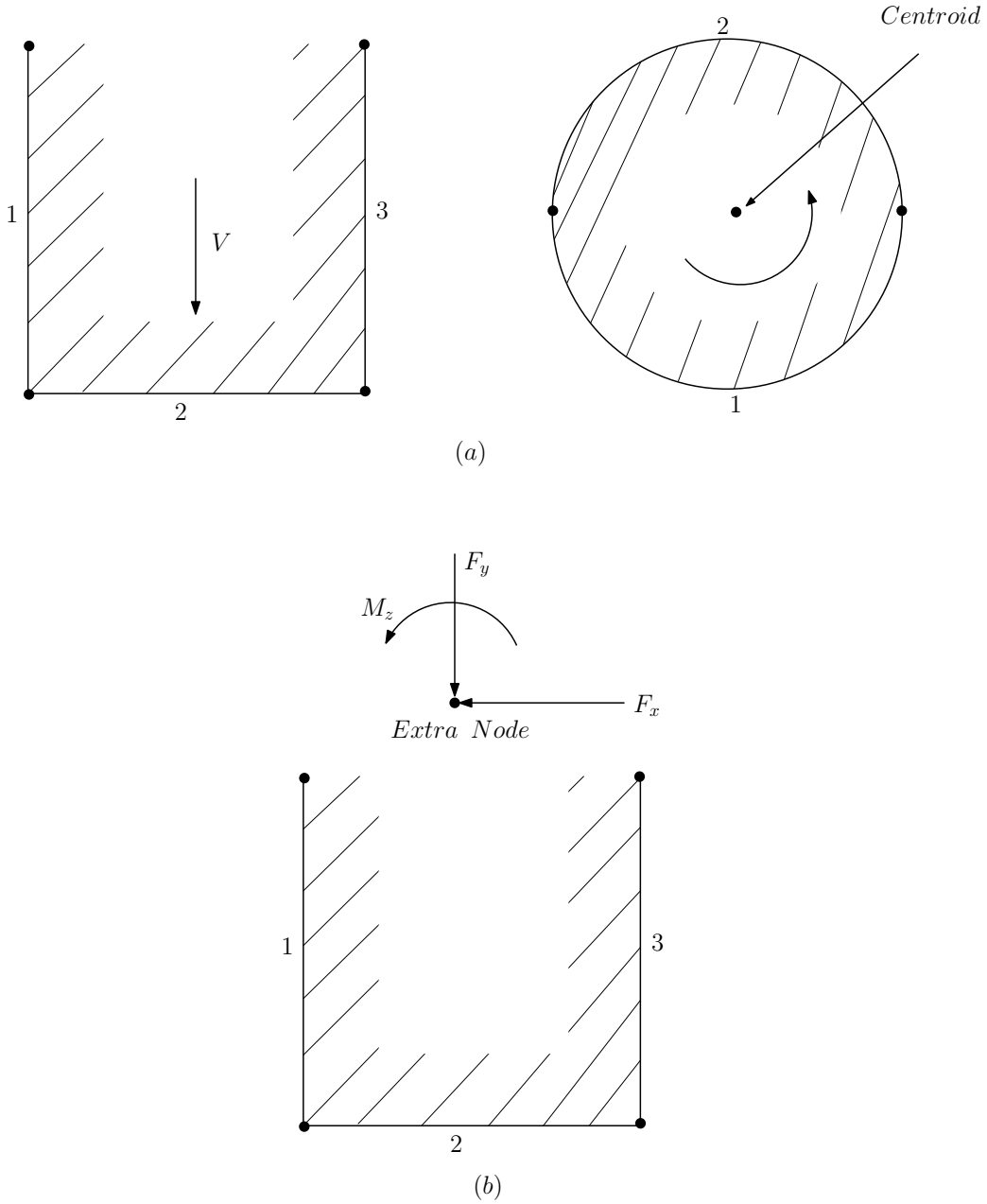

Figure 3.21. Controlling rigid body movement in MSC. Marc (a) Velocity controlled rigid body (b) Load controlled rigid body [87]

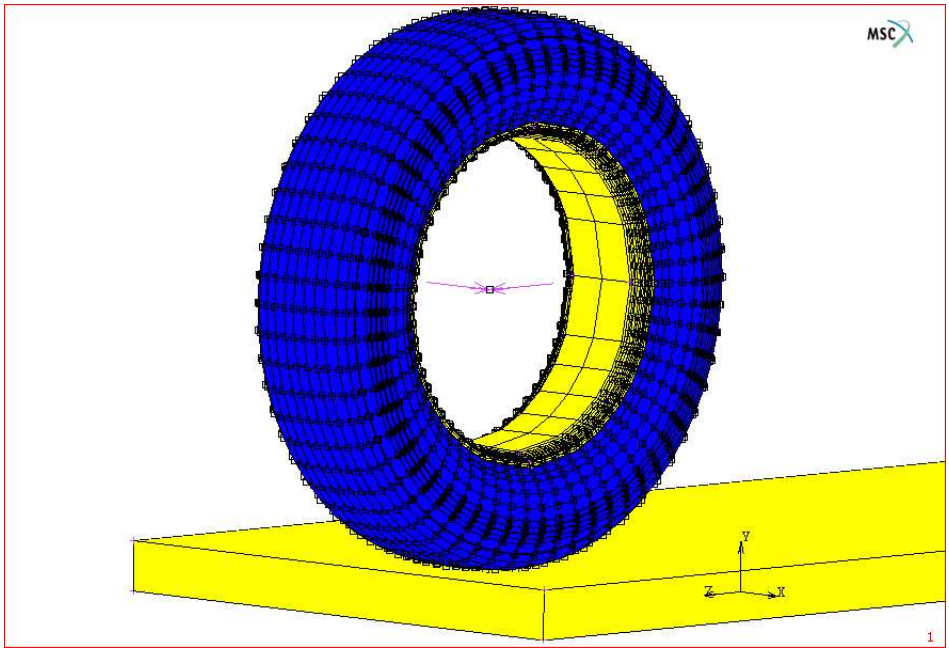

Figure 3.22. Fixed displacement boundary conditions in lateral and longitudinal directions applied to the control node

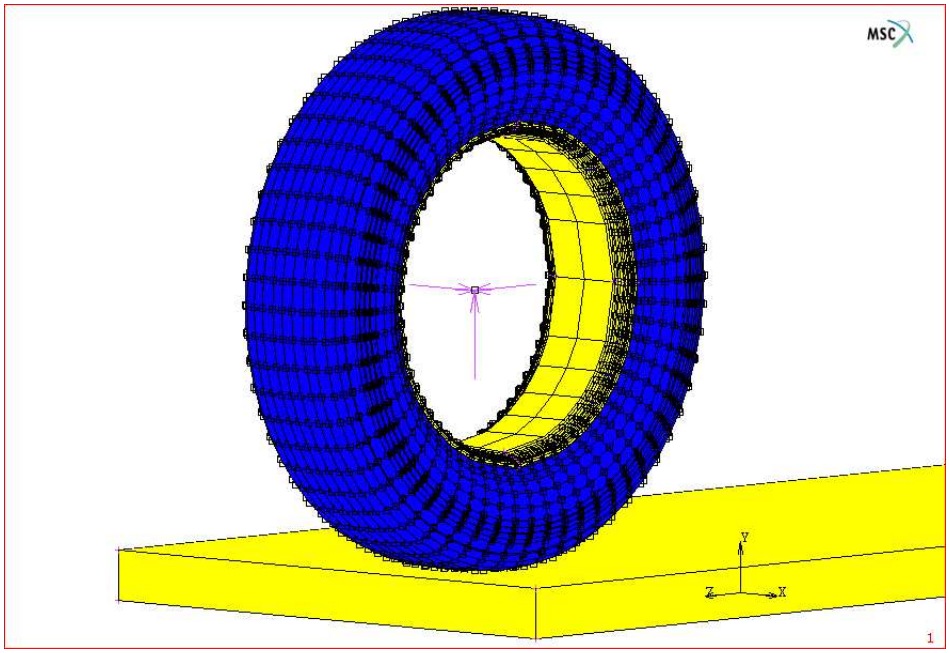

Figure 3.23. Fixed rotation boundary conditions in all directions applied to the auxiliary node

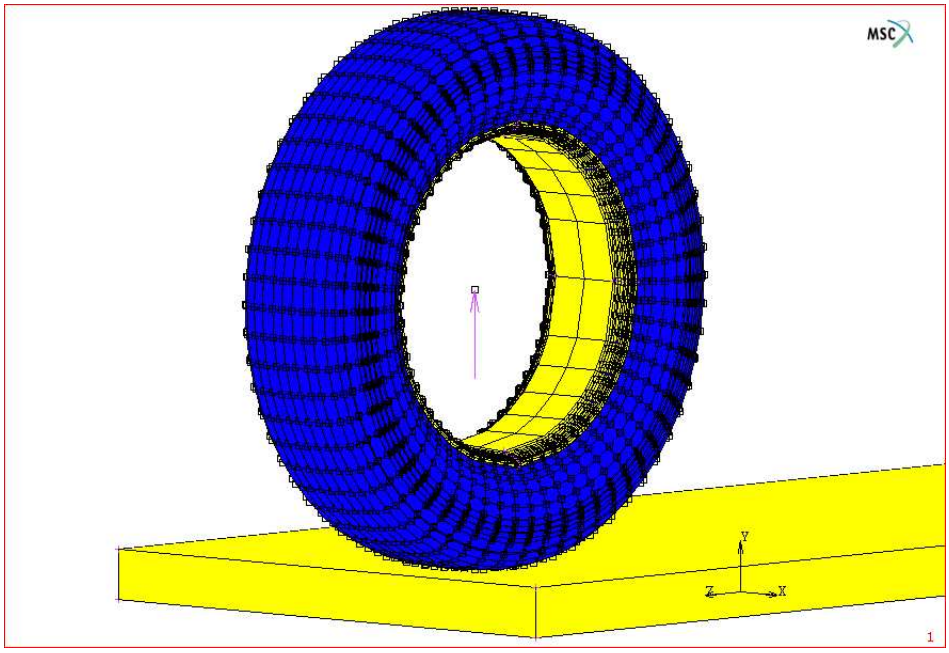

Figure 3.24. Vertical displacement boundary condition applied to the control node

In the deformation process, as a node tends to slide over the deformable/rigid body, it passes a node or edge at a sharp corner. One of the examples of this situation is the tire traversing an obstacle as mentioned in the following sections. This leads to a contact loss and results in deterioration of the solution, especially during the rolling process. To solve this problem, the DELAY SLIDE OFF option in MSC. Marc can be used. This option causes the program to tangentially extend the contacted edge or face. In addition, 2-D and 3-D limit angles are other important parameters to eliminate contact loss. In the 2-D case, these angles are used to adjust the angle at which a node separates from corner or becomes stuck in a concave corner. For the 3-D case, these corner conditions are more complex. A node on the body slides freely up to the intersection of the segments. In the case of a concave corner, the node first tries to slide along the line of intersection before passing to another segment. These conditions are shown in Figures 3.25 and 3.26 [87].

3.2. Static Finite Element Results

In this section, under the above considerations, tire static analysis is conducted and the results are presented for both tire models. Firstly, axisymmetric analysis

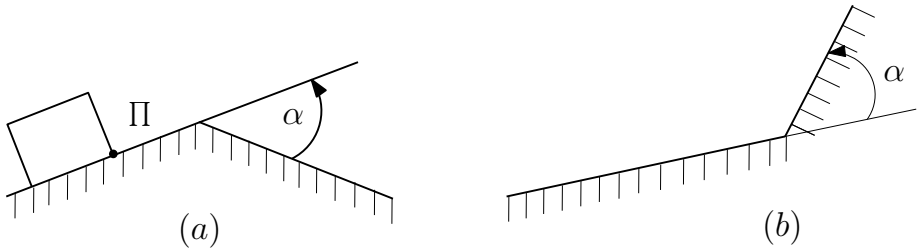

Figure 3.25. Corner conditions (2-D) (a) Convex corner (b) Concave corner [87]

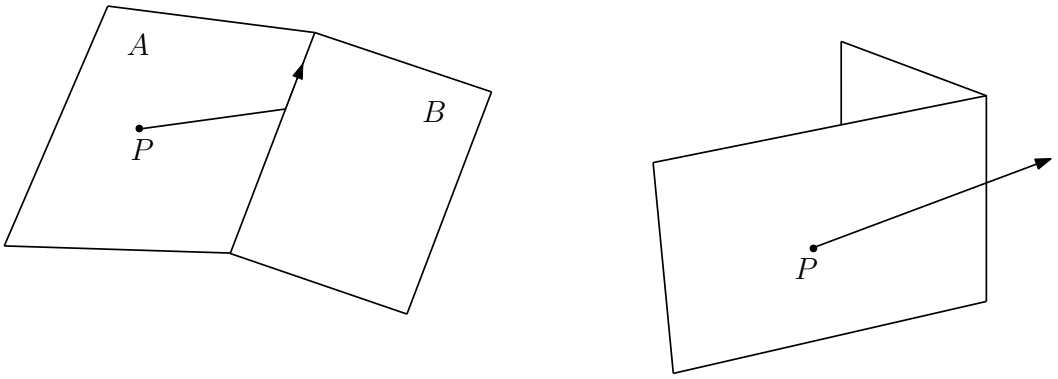

Figure 3.26. Corner conditions (3-D) [87]

results are given. Stress distribution over the cross section and tire profiles are shown. Then, ground contact analysis results are given. Deflected tire on road is shown. Load-deflection diagrams are plotted. That is to say, vertical stiffness of the 155R13 tire is calculated on a surface with and without cleats. Finally, proposed tire models results are compared with those of experiments and validity range of the models is determined and some conclusions are drawn.

3.2.1. Axisymmetric Analysis Results

The stress distributions over the cross section and tire profiles for three different inflation pressures 138, 180 and 220 kPa are shown in the following figures. The stress values (Principal Stress maximum value) are in MPa units. As expected, maximum stress values are seen around the breaker plies region and bead core region. The maximum value was found to be 72 MPa in [24] for 180 kPa pressure value. It can be also noted that the maximum stress value increases with the increase in inflation pressure values.

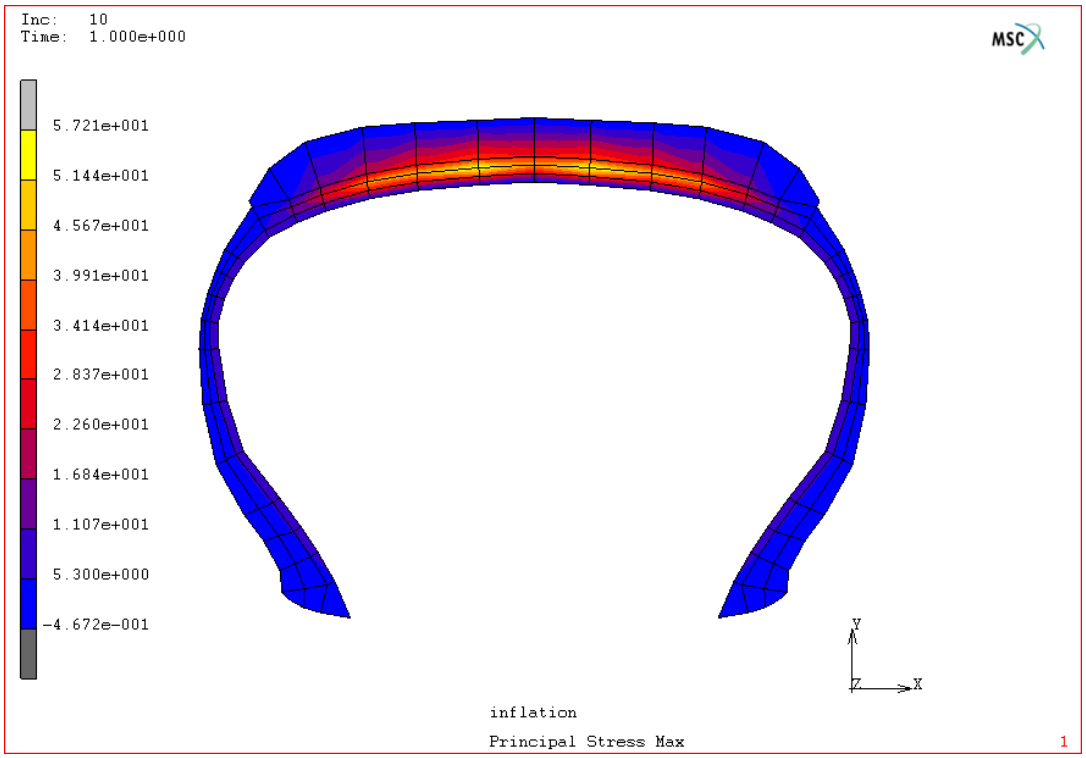

Figure 3.27. 155R13 tire profile and stress distributions over the cross section for 138 kPa inflation pressure

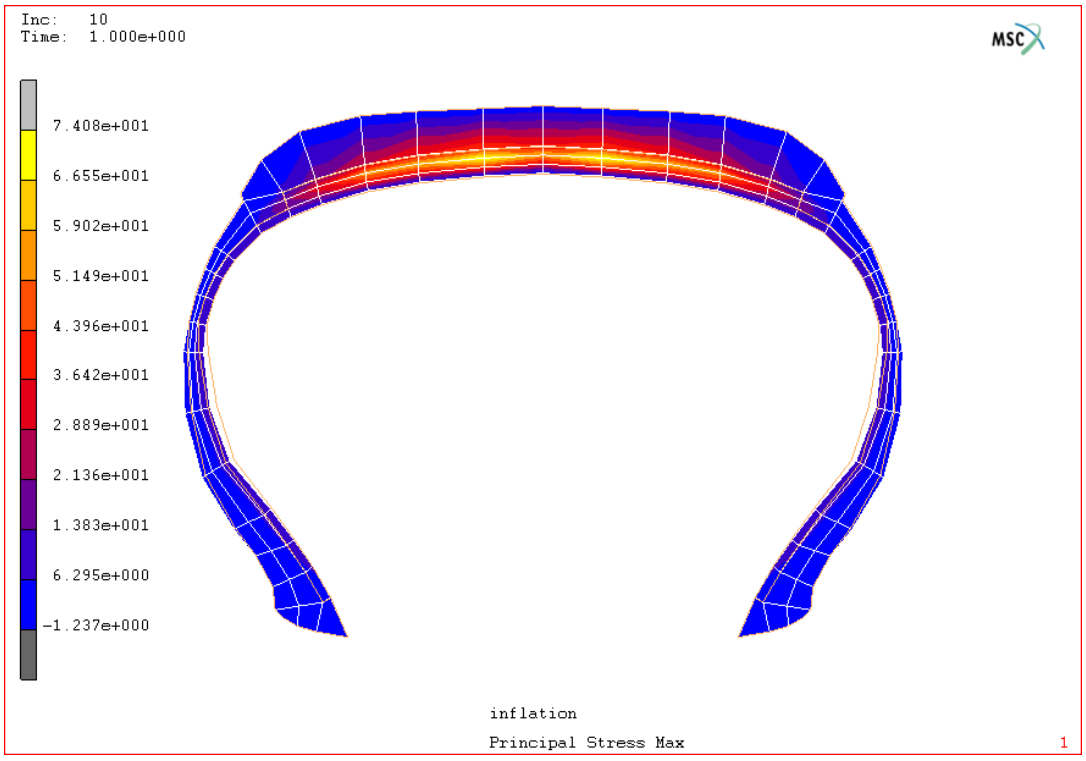

Figure 3.28. 155R13 tire profile and stress distributions over the cross section for 180 kPa inflation pressure

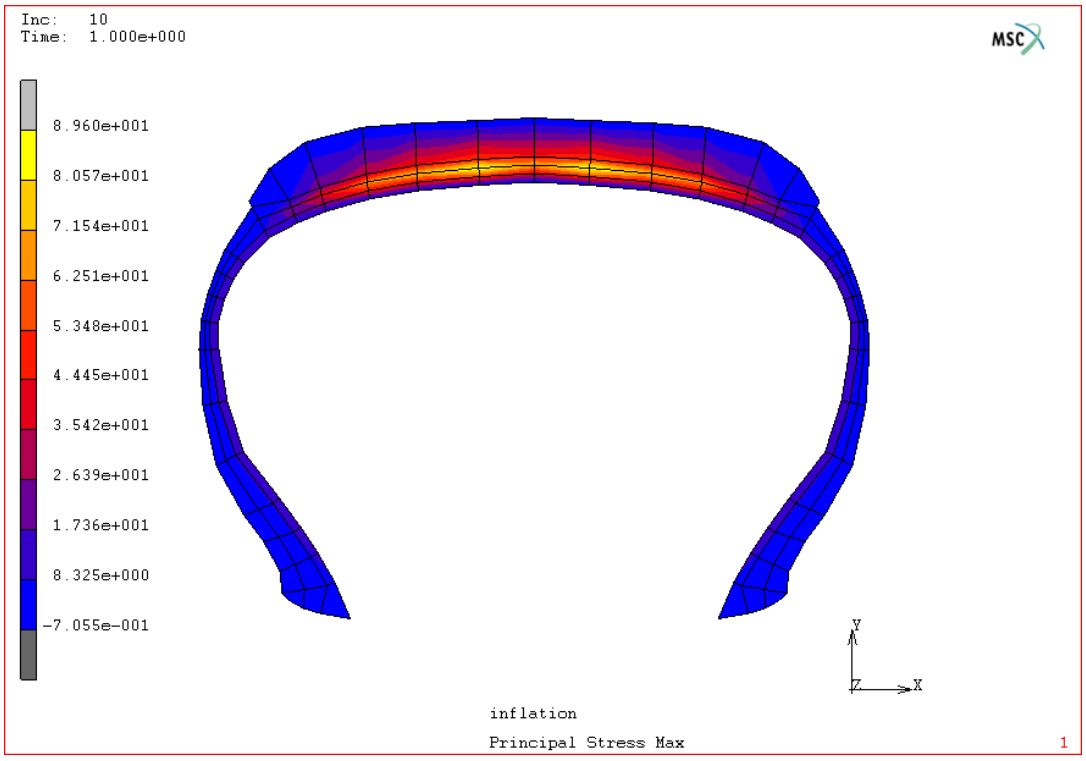

Figure 3.29. 155R13 tire profile and stress distributions over the cross section for 220 kPa inflation pressure

In the following figures, the stress distributions over the cross section and tire profiles for three different inflation pressures 138, 180 and 220 kPa are shown for the second tire model. When comparing the results, it can be seen that both models yield similar results. In [24] maximum stress value for 180 kPa pressure value is found 72 MPa, whereas first model yields 74.08 MPa and the second is 73.12 MPa for 180 kPa pressure value.

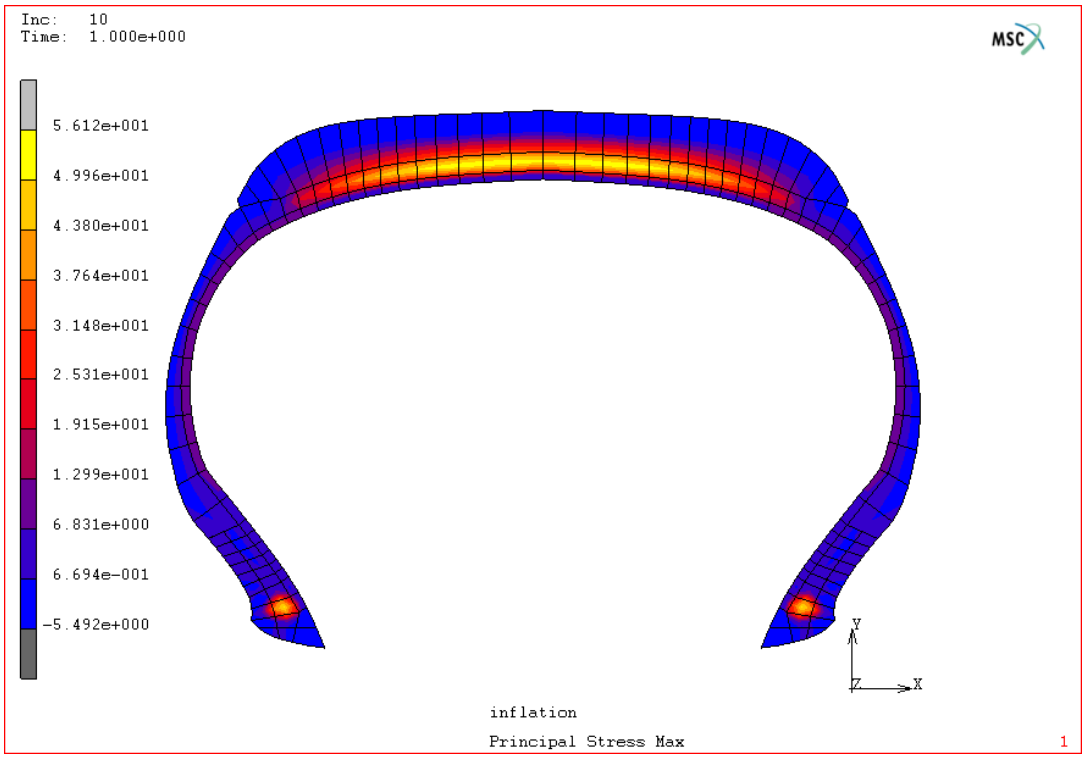

Figure 3.30. 155R13 tire profile and stress distributions over the cross section for 138 kPa inflation pressure

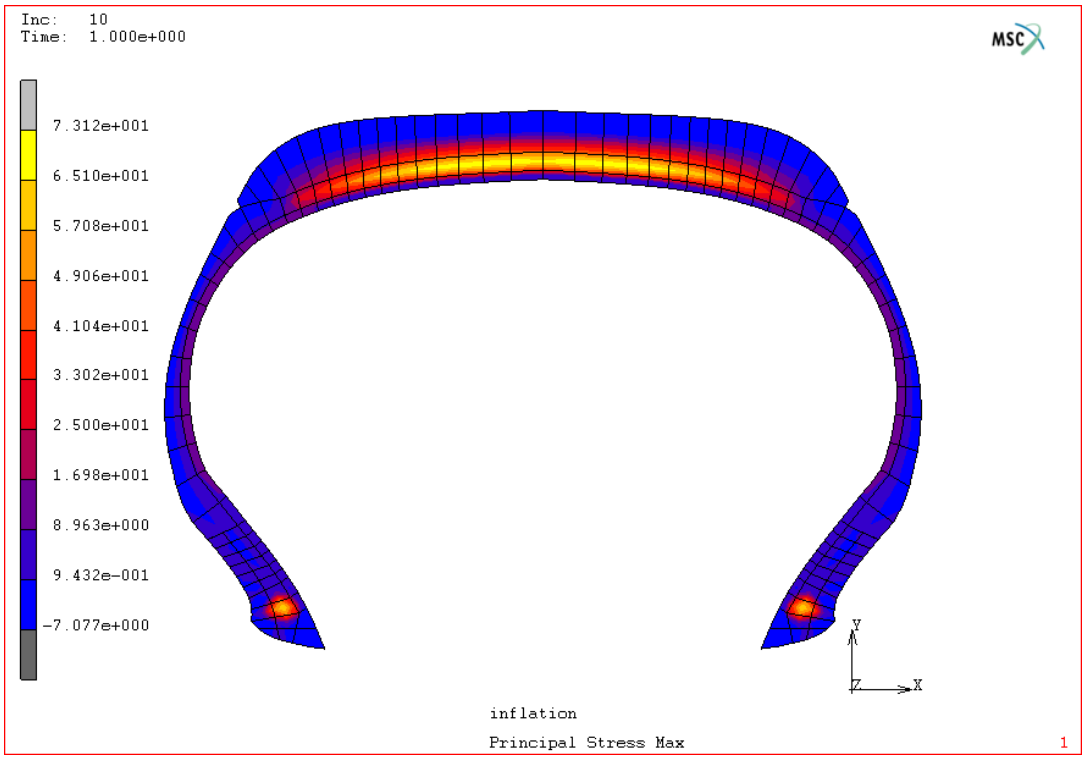

Figure 3.31. 155R13 tire profile and stress distributions over the cross section for 180 kPa inflation pressure

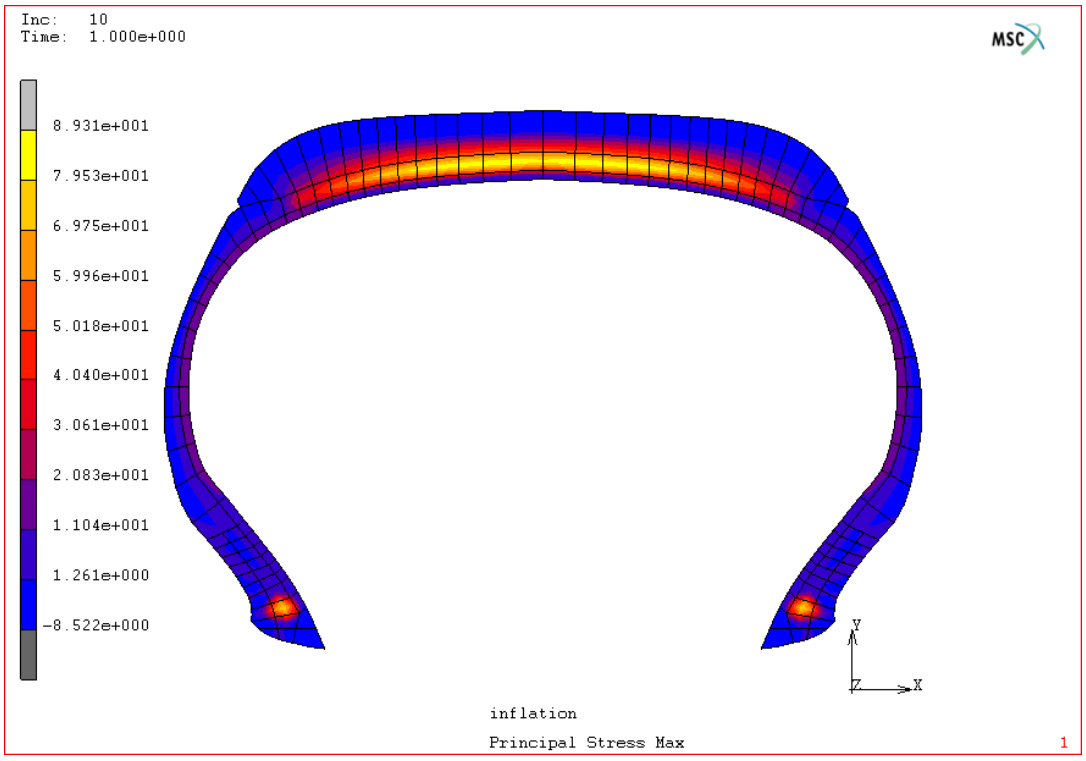

Figure 3.32. 155R13 tire profile and stress distributions over the cross section for 220 kPa inflation pressure

3.2.2. Ground Contact Analysis Results

In this section, first, vertical stiffness of 155R13 tire is calculated using both tire models and their results are compared. Then, vertical stiffness of 155R13 tire is calculated on a surface with cleats. Cleat dimensions were given in the experimental section of this study. As mentioned before, in all experimental results there are hysteresis loops. However, this is not seen in finite element model results because the model does not include a material loss model.

In the following table, it can be easily seen that there is a good match between the results obtained from models using quadratic and linear elements and experimental results. However, in terms of CPU time, there is a big difference between both tire models. The model using quadratic elements require more CPU time than the other. This is the expectable case. It doesn't matter for static analysis to use quadratic elements in the model. But, this is not the case for dynamic analysis, which is more complex and requires more CPU time than the static analysis. Therefore, in the

dynamic analysis, the model using linear elements will be used and in the following sections, only the model using linear elements is considered.

Table 3.5. Comparison of the vertical stiffness of the tire for 180 kPa inflation pressure

	Experimental results	Tire model results obtained using linear elements			Tire model results obtained using quadratic elements		
Vertical disp. (mm)	Vertical force (N)	Vertical force (N)	Error (%)	CPU time (s)	Vertical force (N)	Error (%)	CPU time (s)
5	269	160	-68.125	142.58	320	15.938	1617.95
10	605	550	-10	176.31	655	7.634	1947.86
15	1103	1050	-5.048	199.97	1170	5.726	2258.72
20	1728	1650	-4.727	262.00	1805	4.266	2806.64
25	2393	2330	-2.704	287.56	2420	1.116	3112.94
30	3145	3140	-0.160	360.62	3190	1.411	3781.44
35	3981	3975	-0,151	442.78	4010	0.723	4375.76

In Figures 3.33- 3.35,vertical stiffness of 155R13 tire on a flat surface is numerically predicted and compared with those of experiments. The results show that there is a good match between experimental and numerical results up to a certain displacement value depending on inflation pressure, after which numerical results diverge. This can be due to the fact that a coarse mesh is used and material damping is not included in the analysis. In addition, in Figure 3.36,the effect of inflation pressure values on the vertical stiffness of the tire on a flat surface is investigated and it is seen that as expected, higher inflation pressure values make the tire stiff.

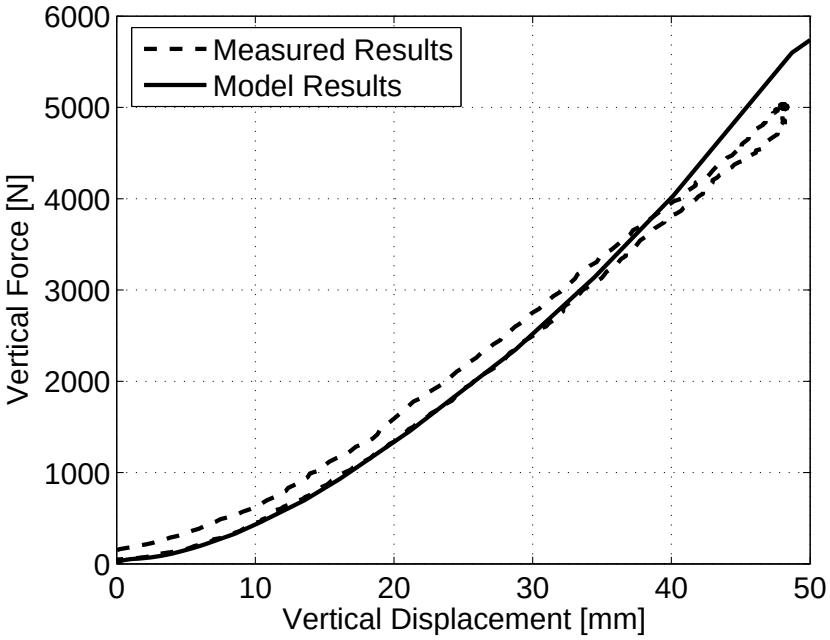

Figure 3.33. Vertical stiffness of 155R13 tire on a flat surface for 138 kPa inflation pressure

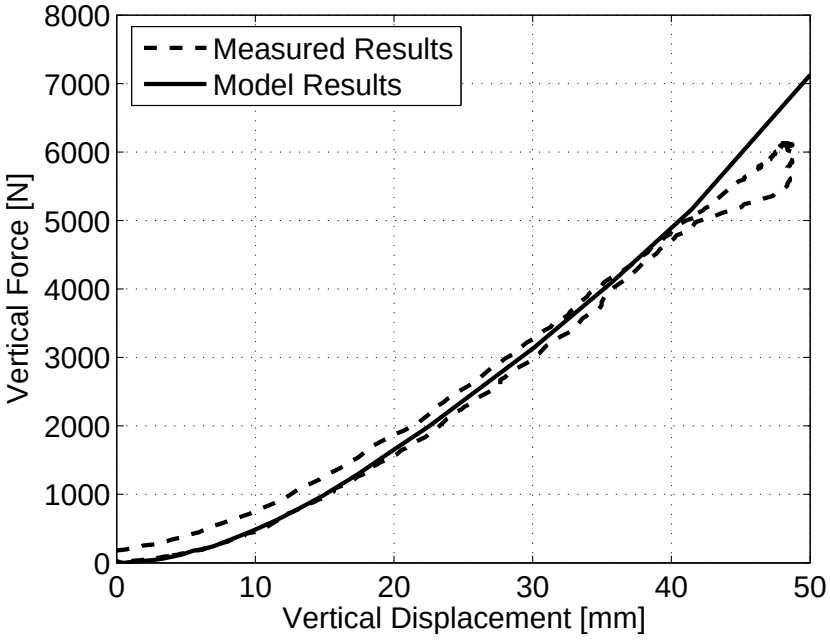

Figure 3.34. Vertical stiffness of 155R13 tire on a flat surface for 180 kPa inflation pressure

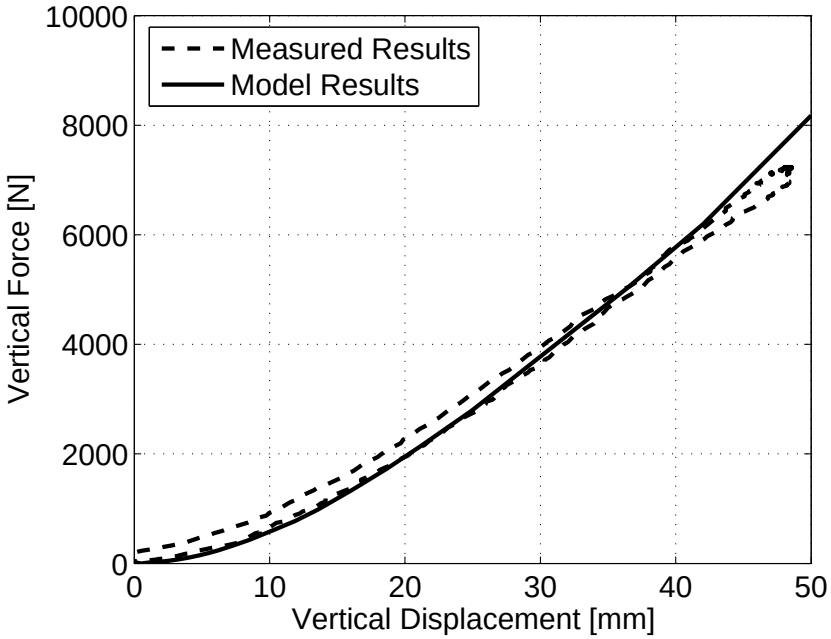

Figure 3.35. Vertical stiffness of 155R13 tire on a flat surface for 220 kPa inflation pressure

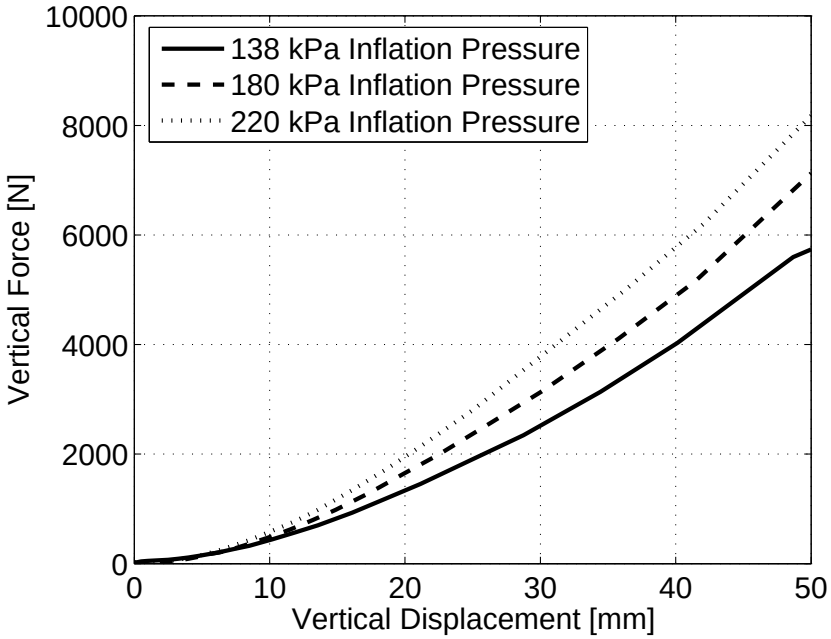

Figure 3.36. Inflation pressure effect on the vertical stiffness of 155R13 tire on a flat surface

In Figures 3.37- 3.39,vertical stiffness of 155R13 tire on a surface with cleats is numerically calculated for rated 180 kPa inflation pressure and the results are compared with those of experiments. As seen in the flat surface cases, up to a certain displacement value, the model showed better agreement with the experiments. It is mentioned in the previous sections that as a static enveloping property of the tire, all curves intersect after a certain displacement depending on the inflation pressure of the tire. This property is numerically confirmed and shown in Figure 3.40. There is a little difference between numerical and measured results. This can be attributed to the both coarse mesh and lack of the material damping parameters. Especially, including material damping constants of tread and sidewall to be exposed to the large displacements are expected to improve the model results. Nevertheless, it can be said that the model yielded satisfactory results when comparing the measured results.

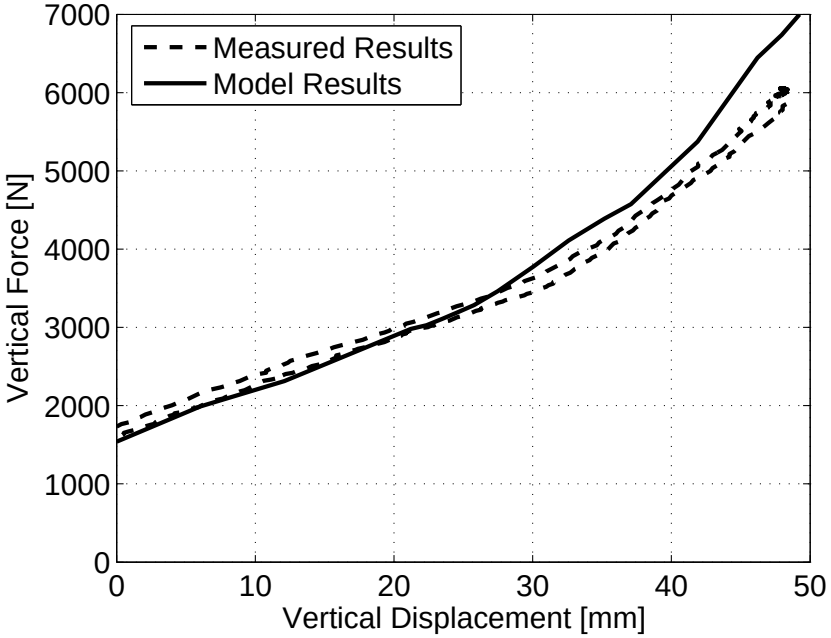

Figure 3.37. Vertical stiffness of 155R13 tire on a surface with circular sectioned cleat for 180 kPa inflation pressure

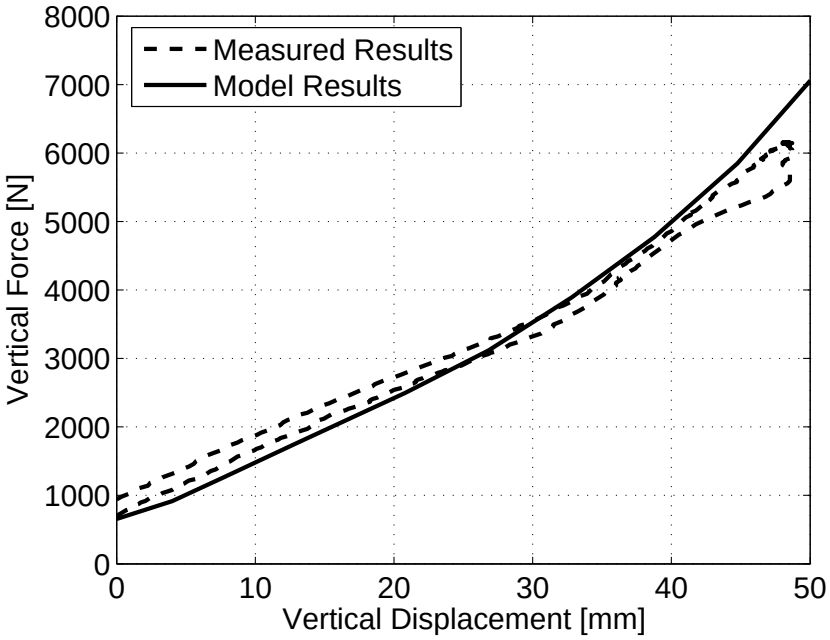

Figure 3.38. Vertical stiffness of 155R13 tire on a surface with rectangular sectioned cleat for 180 kPa inflation pressure

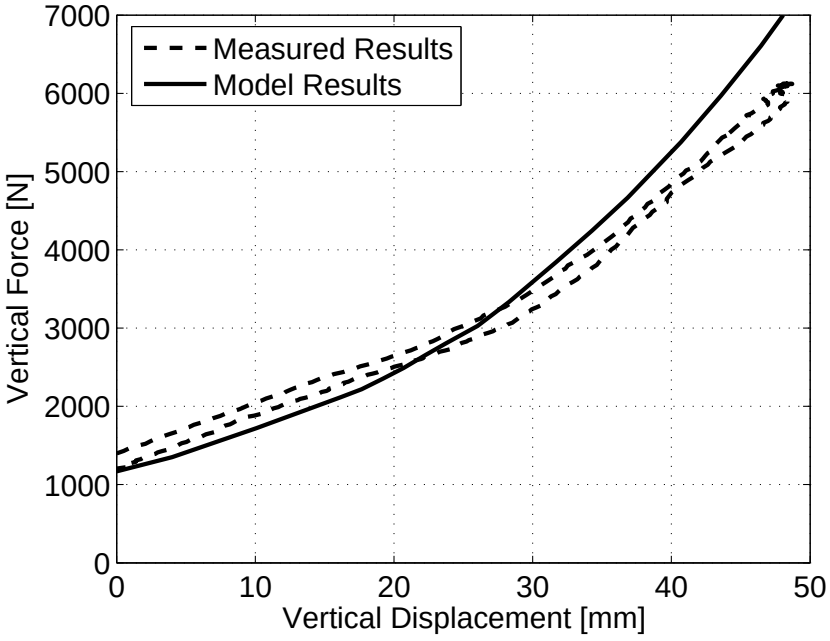

Figure 3.39. Vertical stiffness of 155R13 tire on a surface with triangular sectioned cleat for 180 kPa inflation pressure

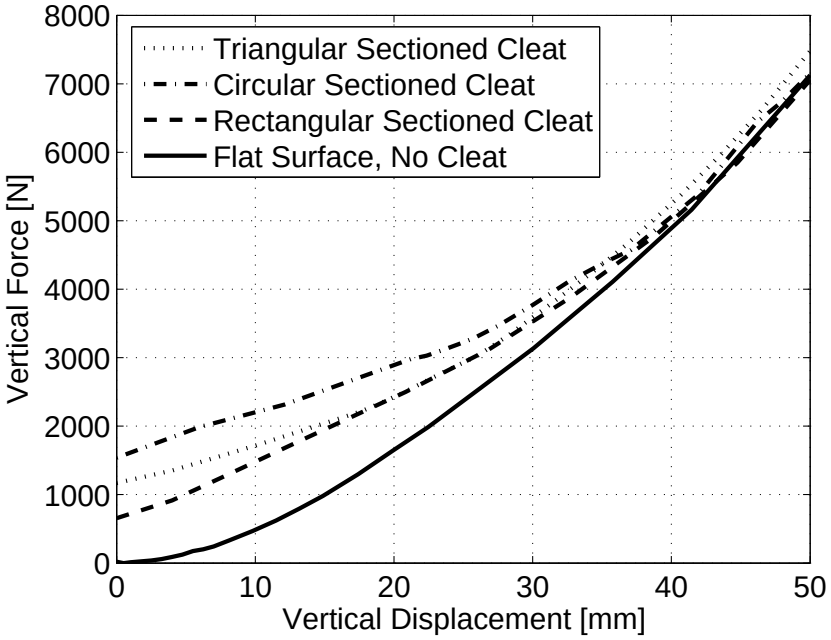

Figure 3.40. Vertical stiffness of 155R13 tire on a surface with triangular sectioned cleat for 180 kPa inflation pressure

One of the typical characteristics of the radial tire constructions different from bias-ply types is that contact patch does not expand laterally after some level vertical load values applied to the tire. Steel belts under the tread prevent tread movement laterally, which in turn, providing longer tread life and lower rolling resistance and hence lower fuel consumptions. Contact patch shapes of the tire pressed against the flat surface are shown in the following figures from their initial position to the 5 mm (3981 N) deflected position.

Figure 3.41. Initial position of the tire on a flat surface

Figure 3.42. 15 mm (1103 N) deflected tire on a flat surface

Figure 3.43. 25 mm (2393 N) deflected tire on a flat surface

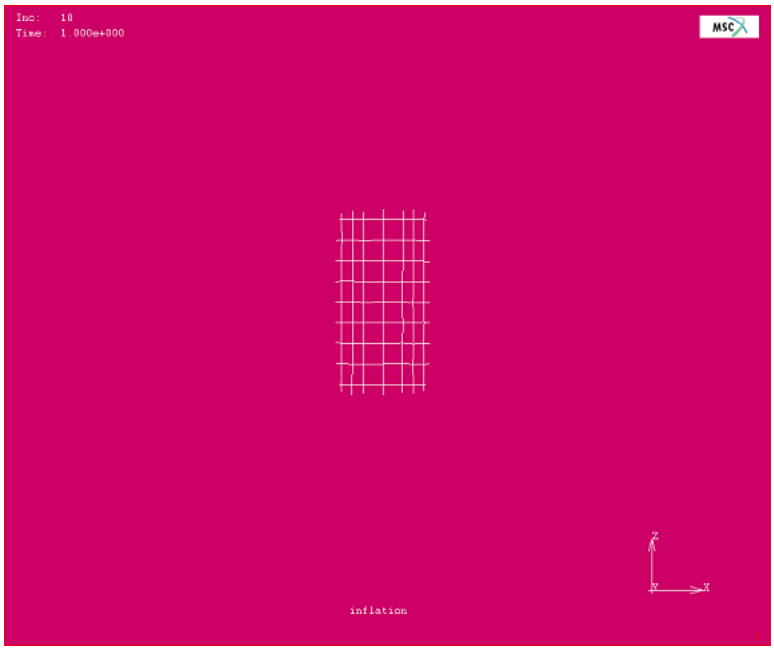

Figure 3.44. 35 mm (3981 N) deflected tire on a flat surface

4. DYNAMIC FINITE ELEMENT ANALYSIS OF THE TIRE

Dynamic tire analysis is the last step of tire modeling. In the dynamic stages, steady-state conditions are considered. Due to the low speed, centrifugal effects are not considered. In this section, tire cornering force characteristics are numerically predicted using MSC. Marc. Cornering force, self-aligning moment, overturning moment and rolling resistance moment versus slip angle plots are given for different vertical force values. Then, tire enveloping characteristics at low speed are investigated. Model results are compared with those of experiments. Error tables are also tabulated.

4.1. Lateral and Vertical Force Characteristics of the Tire

When a tire rolls in such a way that there is no force perpendicular to the wheel plane, it moves along the wheel plane. However, if a side force (F_S) is applied to the tire by i.e., steering the wheel, the tire moves along the OA direction which makes an angle α with the wheel plane as shown in Figure 4.1 and as a result a lateral force is developed at the tire-ground contact area [88]. This force is called as cornering force, $F_{Y\alpha}$, in the case of zero camber angle. In addition, the distribution of lateral forces on the contact patch is not symmetric in general. The resultant lateral force does not pass through the contact patch geometric center. The contact patch center is defined as the intersection of the wheel plane and road plane, which are defined at the previous sections. The distance between resultant lateral force and contact patch geometric center is called as pneumatic trail. The coupling of them produces a moment about the vertical axis, namely, self-aligning moment (or self-aligning torque). It is an important parameter for all tires and especially for steering system of the vehicles.

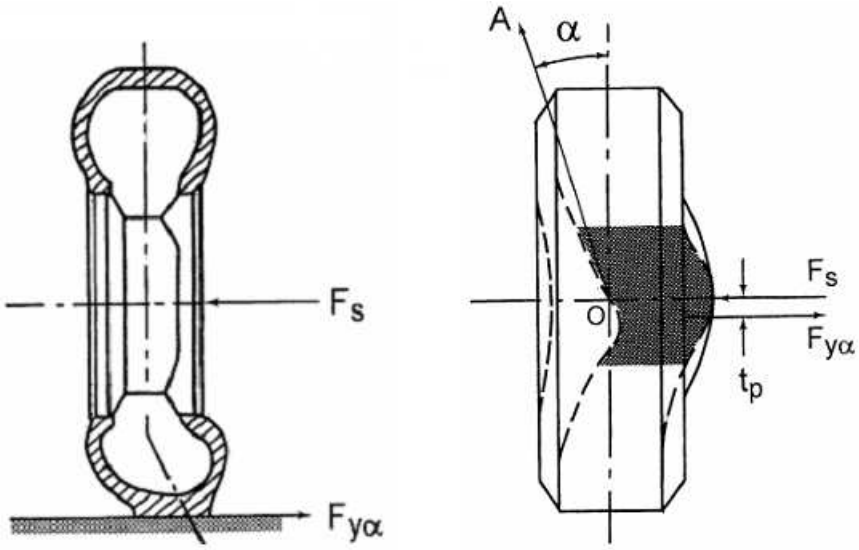

Figure 4.1. Representation of the cornering force and corresponding self-aligning torque [88]

After briefly explaining cornering force phenomenon, finite element model procedures for investigation of the cornering force characteristics of the tire are given in detail. In the cornering force analysis of the tire, all procedures followed are the same as static analysis. In addition to these, slip angle is given to the tire by applying road velocity in longitudinal and lateral directions, the road moves and the tire is fixed. Schematic slip angle representation of a tire is shown in Figure 4.2. Slip angle is calculated using Equation 4.1. During the pressing operation, all rotation degrees of freedom of the rim are fixed. After completing the pressing operation, rotation about the tire axis, at the same time rim rotation center, is set free. Friction force between the tire and road rotates the wheel assembly. Figure 4.3 shows the cornering force versus solution increment. Up to the 10 increment, pressing operation is completed and then the tire starts to rotate. After a certain increment, the cornering force gets steady state value.

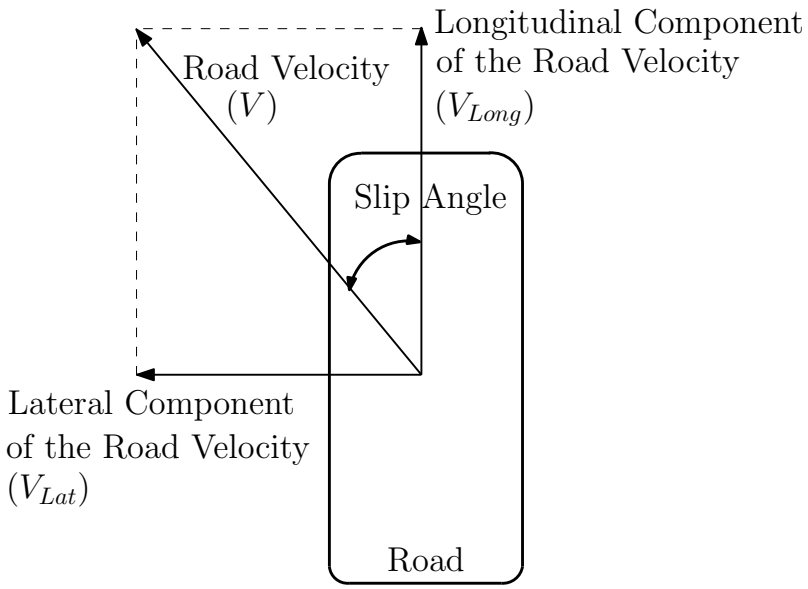

Figure 4.2. Schematic slip angle representation of a tire

$$\text{Slip Angle} = \alpha = tan^{-1}\frac{V_{Lat}}{V_{Long}} \tag{4.1}$$

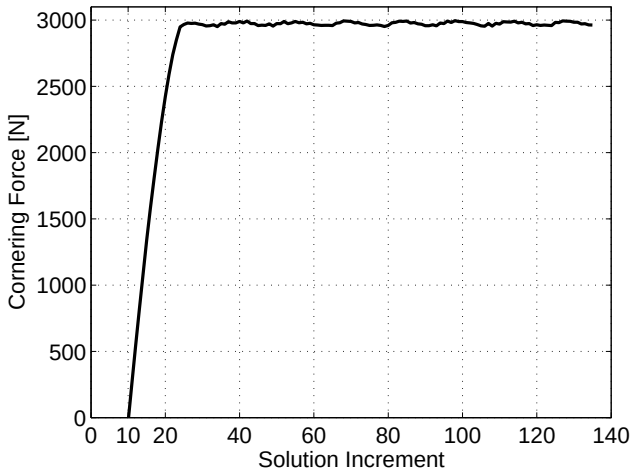

Figure 4.3. Cornering force versus solution increments for 4 kN vertical load and 8 degree slip angle

Contact patch shape of deformed and undeformed tire under 8^o slip angle and 4 kN normal load conditions are shown in Figure 4.4. Red lines correspond to the undeformed state of the contact patch and black lines refer to the deformed state. Also, tire cornering on road for 8 degree slip angle, 4 kN vertical load and 180 kPa inflation pressure on both deformed and undeformed states are shown in Figure 4.5.

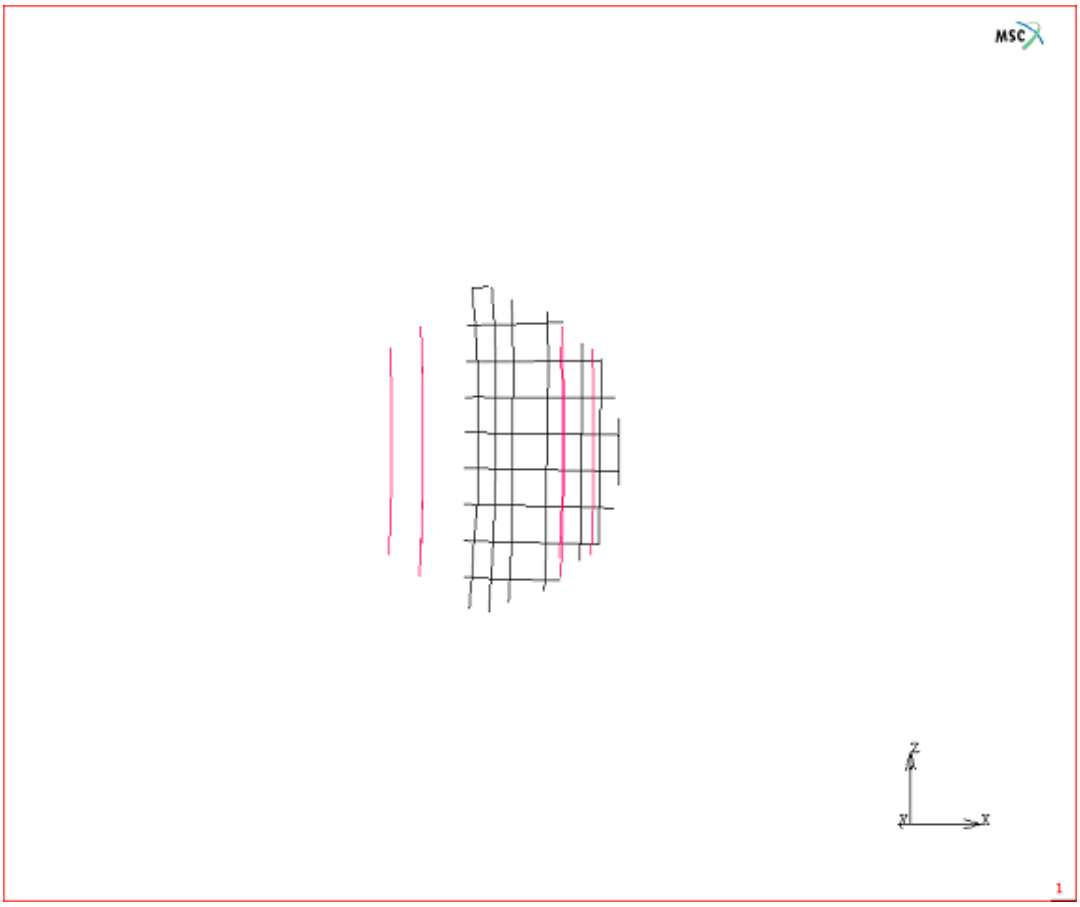

Figure 4.4. Contact patch shape of the deformed and undeformed tire for 8^o slip angle and 4 kN vertical load

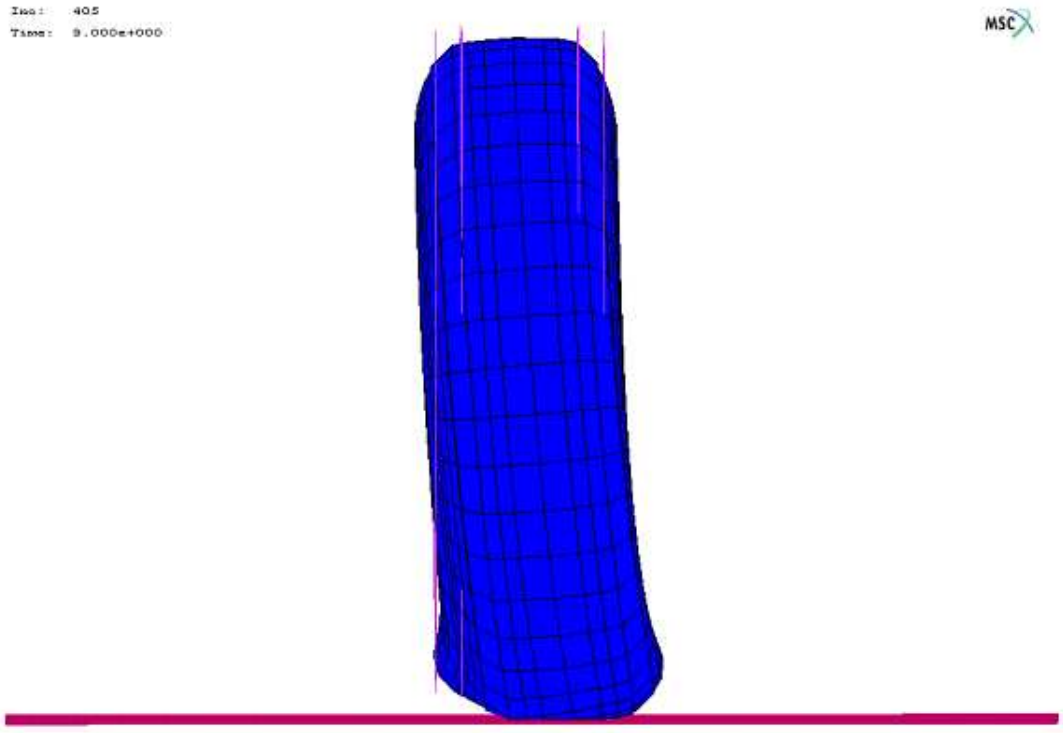

Figure 4.5. Tire cornering on road for 8 degree slip angle, 4 kN vertical load and 180 kPa inflation pressure (Front view)

In Figure 4.6 and Figure 4.7, cornering force and self-aligning moment versus slip angle plots, respectively are given for different vertical loads and compared with those of experiments. There is a satisfactory match between both results. It is noted that there are five experimental points in the force and moment plots for five slip angles. Between them, curve fit procedure is applied. The curve fit curves are created in such a way that all curves pass through the experimental points.

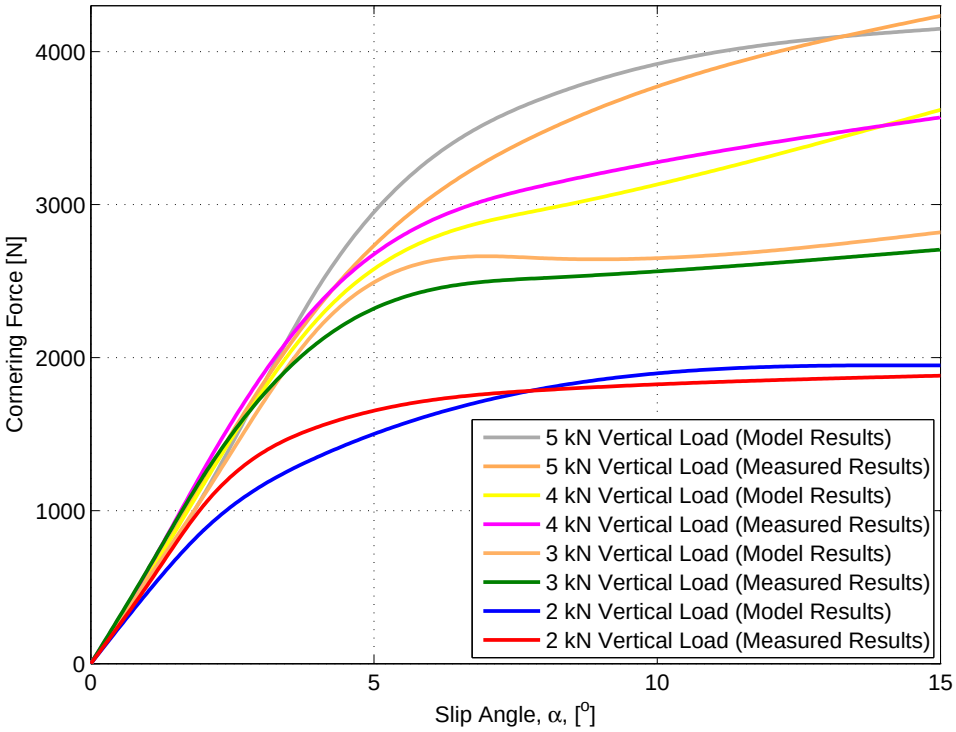

Figure 4.6. Comparison of cornering force vs. slip angle plots of 155R13 for 180 kPa rated inflation pressure and different vertical loads

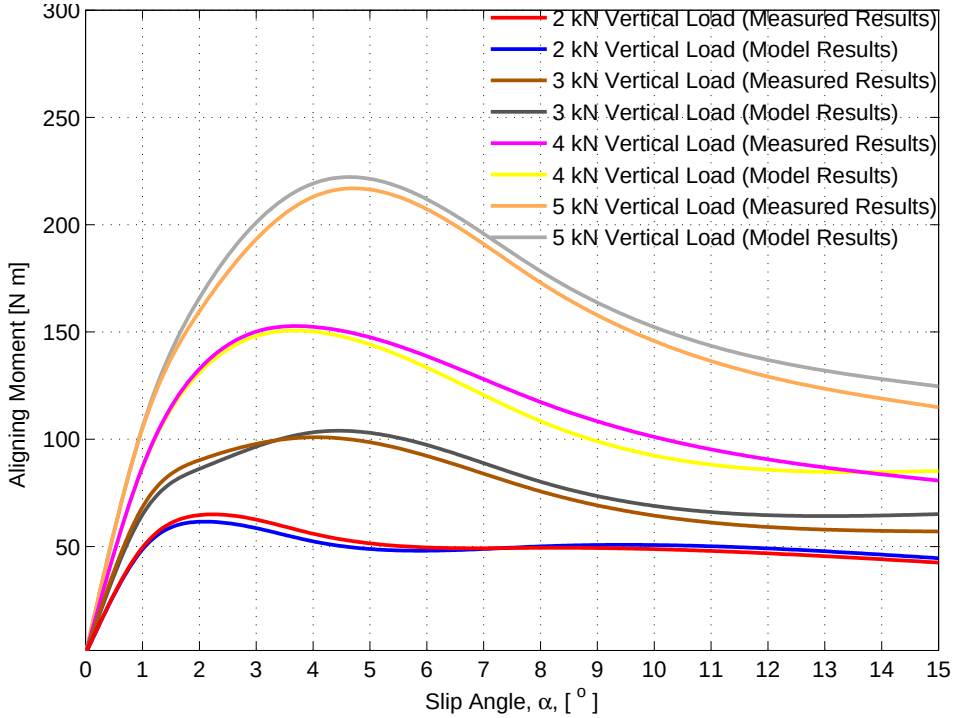

Figure 4.7. Comparison of self-aligning moment vs. slip angle plots of 155R13 for 180 kPa rated inflation pressure and different vertical loads

In addition to the lateral force, deformation of the tire carcass and tread affects the distribution of vertical tire contact forces. There is an offset between contact patch center and resultant vertical tire contact forces during cornering, which is called as pneumatic scrub in [30]. This results in a moment about longitudinal axis, namely, overturning moment and shown in Figure 4.8.

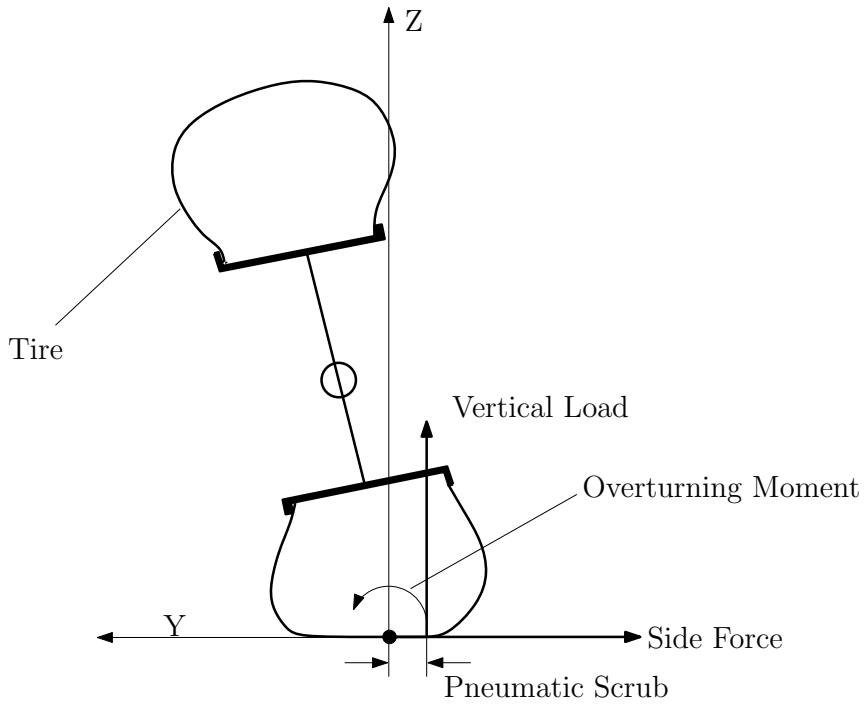

Figure 4.8. Schematic sketch of overturning moment (OTM) generation [30]

Also, rolling resistance moment results from the carcass deflection. The normal pressure in the leading half of the contact patch is higher than that in the trailing half. The rolling resistance of a free rolling tire is mainly caused by the internal friction in the rubber and cord, while the slip in the contact zone and the windage losses at moderate speeds are of less importance. Another factor influencing the rolling resistance are bad road conditions, involving large tire deflections, the presence of snow or the deformation of soft soil. At a constant speed, a free rolling wheel requires a horizontal force F_r in the wheel center to overcome the rolling resistance. The balance of moments around the wheel center is shown in Figure 4.9 [41] called as rolling resistance moment.

$$F_r \times h = F_N \times f_r \tag{4.2}$$

where F_N is the load carried by the wheel and h is the axle height above the ground. The rolling resistance force F_r is the resultant of the longitudinal tangential stresses in the contact patch, while the resultant F_N of the normal force distribution has an offset, ahead of the contact center as shown in Figure 4.9.

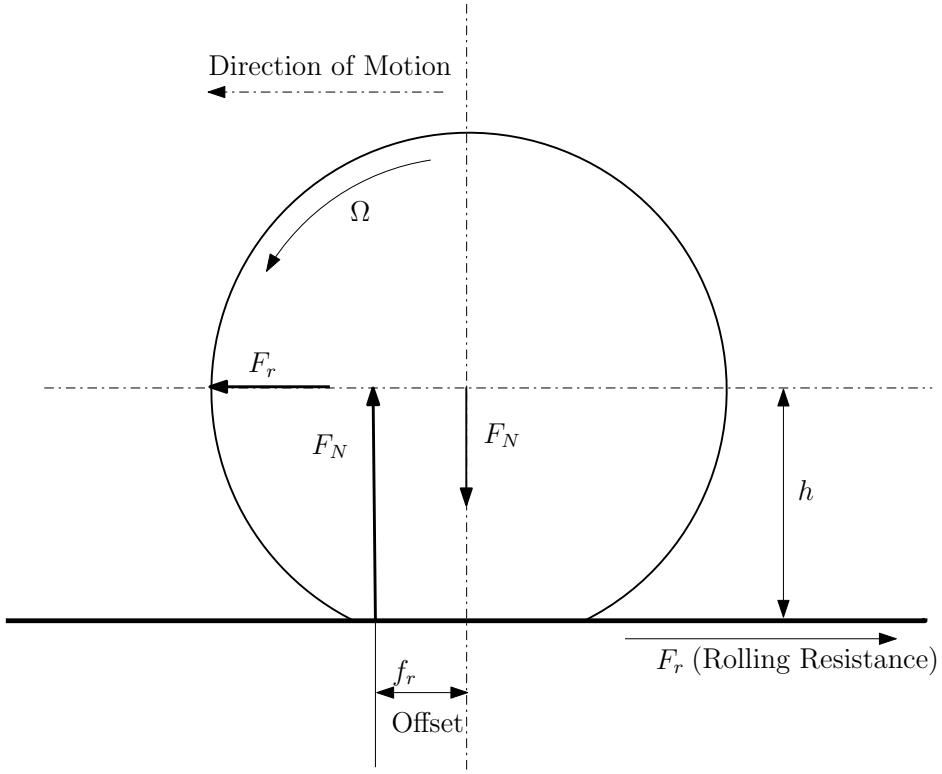

Figure 4.9. Rolling resistance of a free rolling tire [41]

In Figure 4.10 and Figure 4.11, overturning and rolling resistance moment versus slip angle plots, respectively are given for different vertical loads and compared with those of experiments. Again, satisfactory match between both results are obtained.

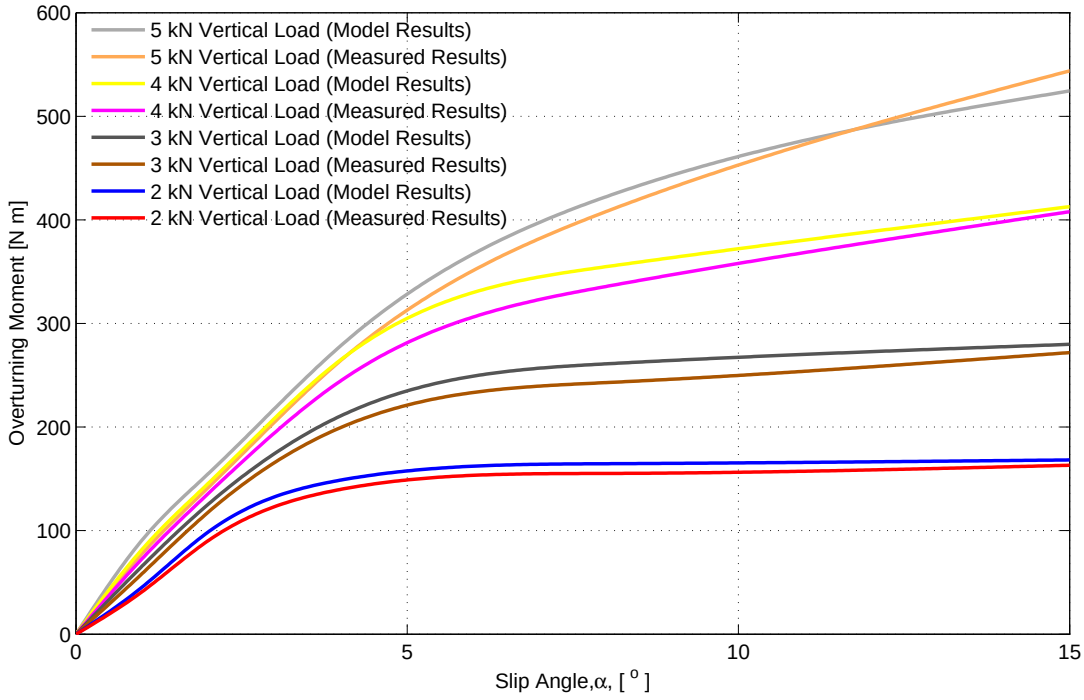

Figure 4.10. Comparison of overturning moment vs. slip angle plots of 155R13 for 180 kPa rated inflation pressure and different vertical loads

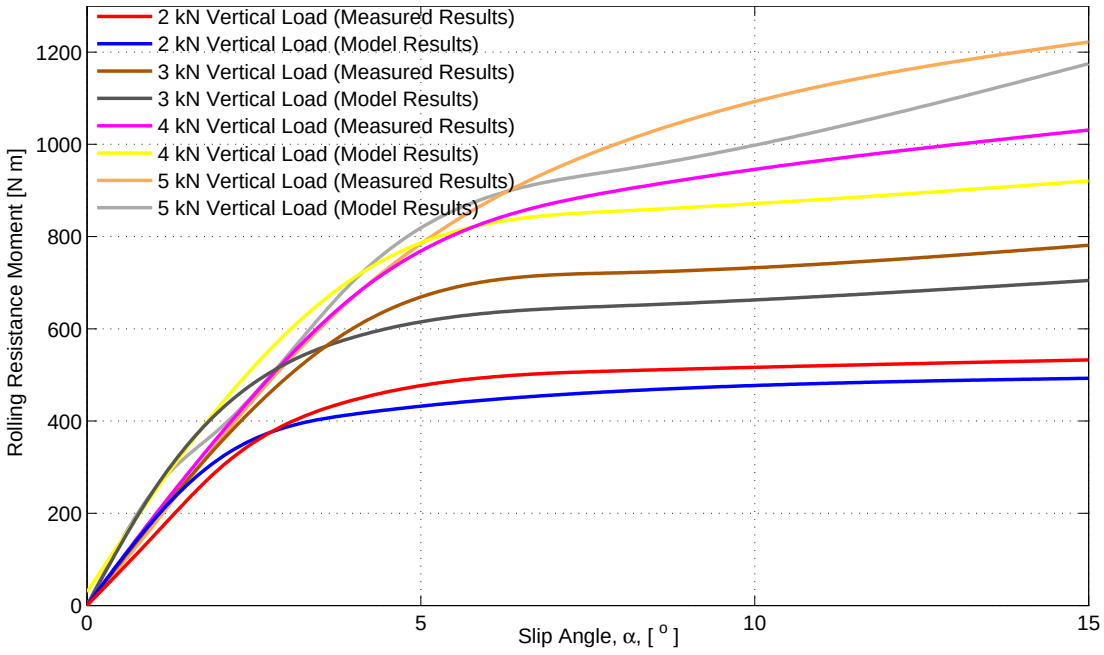

Figure 4.11. Comparison of rolling resistance moment vs. slip angle plots of 155R13 for 180 kPa rated inflation pressure and different vertical loads

Error tables are tabulated as given below. To some extent, proposed model yields satisfactory results when comparing with measurements. Model results can be improved by including some parameters to the model such as actual tread modeling, viscoelastic effect of the rubber material and coefficient of friction depending on some factors such as slip angle, sliding velocity and road texture.

Table 4.1. Comparison of cornering force value of 155R13 tire for rated 180 kPa inflation pressure

		Cornering force (N)		
Vertical load (kN)	Slip angle (^{o})	Model results	Measured results	Error (%)
2	1	475	512	-7.789
	2	875	1039	-18.743
	4	1350	1546	-14.519
	8	1800	1789	0.612
	15	1950	1883	3.436
3	1	550	612	-11.273
	2	1100	1234	-12.182
	4	2185	2096	4.073
	8	2650	2521	4.868
	15	2820	2708	3.972
4	1	567	608	-6.743
	2	1198	1272	-5.818
	4	2250	2343	-3.970
	8	2970	3127	-5.286
	15	3750	3572	4.983
5	1	525	569	-7.733
	2	1200	1203	-0.249
	4	2450	2325	5.376
	8	3698	3476	6.387
	15	4150	4234	-1.984

Table 4.2. Comparison of self-aligning moment value of 155R13 tire for rated 180 kPa inflation pressure

		Self-aligning moment (N m)		
Vertical load (kN)	Slip angle (^{o})	Model results	Measured results	Error (%)
2	1	48.65	49.58	-1.912
	2	61.56	64.67	-5.052
	4	52.43	55.98	-6.771
	8	50.06	49.40	1.318
	15	44.56	42.52	4.579
3	1	64.85	68.37	-5.428
	2	86.21	90.26	-4.698
	4	103.24	100.96	2.208
	8	80.25	75.74	5.620
	15	65.08	56.98	12.446
4	1	86.7	87.08	-0.439
	2	130.98	132.73	-1.336
	4	150.25	152.41	-1.438
	8	108.45	117.38	-8.234
	15	85.15	80.71	5.214
5	1	105.65	104.97	0.644
	2	165.78	159.6	3.728
	4	219.21	213.01	2.829
	8	178.39	173.07	2.982
	15	124.66	114.91	7.821

Table 4.3. Comparison of overturning moment value of 155R13 tire for rated 180 kPa inflation pressure

		Overturning moment (N m)		
Vertical load (kN)	Slip angle (^{o})	Model results	Measured results	Error (%)
2	1	45.56	41.05	9.900
	2	98.87	90.46	8.506
	4	148.85	139.88	6.026
	8	164.65	155.26	5.703
	15	168.32	163.2	3.042
3	1	65.82	58.6	10.970
	2	125.67	118.01	6.095
	4	210.88	199.63	5.335
	8	261.09	242.98	6.936
	15	280.01	272,00	2.861
4	1	82.07	73.00	11.052
	2	145.78	136.00	6.709
	4	265.09	244.8	7.654
	8	354.88	335.76	5.388
	15	412.90	408.00	1.187
5	1	91.00	77.96	14.330
	2	155.15	141.79	8.611
	4	278.66	264.38	5.125
	8	422.35	408.00	3.398
	15	524.65	544.00	-3.688

Table 4.4. Comparison of rolling resistance moment value of 155R13 tire for rated 180 kPa inflation pressure

		Rolling resistance moment (N m)		
Vertical load (kN)	Slip angle (^{o})	Model results	Measured results	Error (%)
2	1	186.01	151.07	18.784
	2	320.23	298.85	6.676
	4	415.98	446.02	-7.222
	8	465.11	509.12	-9.462
	15	493.9	532.82	-7.880
3	1	250.12	184.52	26.227
	2	424.56	353.41	16.759
	4	582.89	602.47	-3.360
	8	650.77	721.7	-10.900
	15	705.46	781.38	-10.762
4	1	265.78	192.7	27.496
	2	435.01	371.95	14.496
	4	730.54	671.71	8.053
	8	843.88	901.05	-6.775
	15	921.19	1031.34	-11.957
5	1	250.88	174.91	30.281
	2	385.62	360.15	6.605
	4	705.35	670.67	4.917
	8	945.93	1004.6	-6.202
	15	1175.12	1222.13	-4.001

4.2. Tire Enveloping Characteristics at Low Speeds

In this section, tire enveloping characteristics at low speed are investigated numerically. Numerical results are given and compared with those of experiments. So, validity range of the model is determined. Three different cleats are considered. For rated 180 kPa and 3 kN vertical load, longitudinal and vertical force, and overturning, aligning and rolling resistance moment variations during the 155R13 tire traversing the obstacles are examined.

In the finite element modeling of tire-cleat interaction, a finer mesh results in a more accurate solution. However, as a mesh is made finer, the computation time increases. To get a mesh that satisfactorily balances accuracy and computing time, mesh convergence study is again performed and presented here only. As seen in Figure 4.12, after 10440 element number, overturning moment value does not change. Below 10440 element number, penetration of a node happens in a certain time leading to more recycles and increases the computational costs.

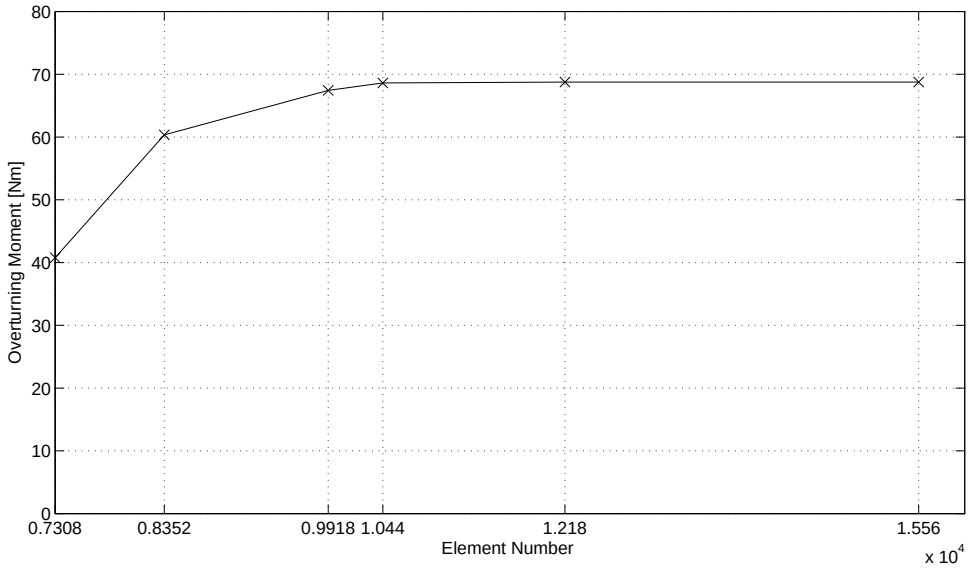

Figure 4.12. Overturning moment versus element number of the tire model

In the tire-impact process, vertical and horizontal force variation are the most important parameters determining the tire enveloping characteristics. While tire traverses the cleat, P_V and P_H vertical and horizontal contact patch forces respectively are transferred to the tread as radial $q(\phi, t)$ and tangential $s(\phi, t)$ force components as shown in Figure 4.13. ϕ is angular measure in tire plane and t refers to time. As mentioned in the experimental section of the thesis, tire slip angle is zero, so the lateral force value takes very small value and there is no general tire lateral force response to be mentioned when comparing nonzero slip angle conditions and oblique cleat conditions. Therefore, here only, vertical force, longitudinal force and three moments predicted are presented and compared with those obtained from experiments.

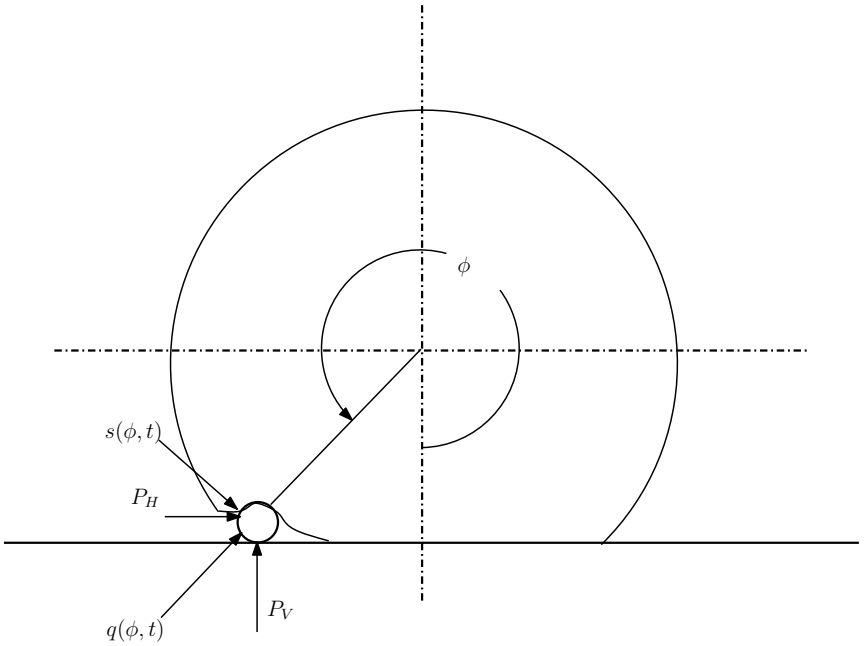

Figure 4.13. Transformation of vertical and horizontal cleat forces to radial and tangential components [55]

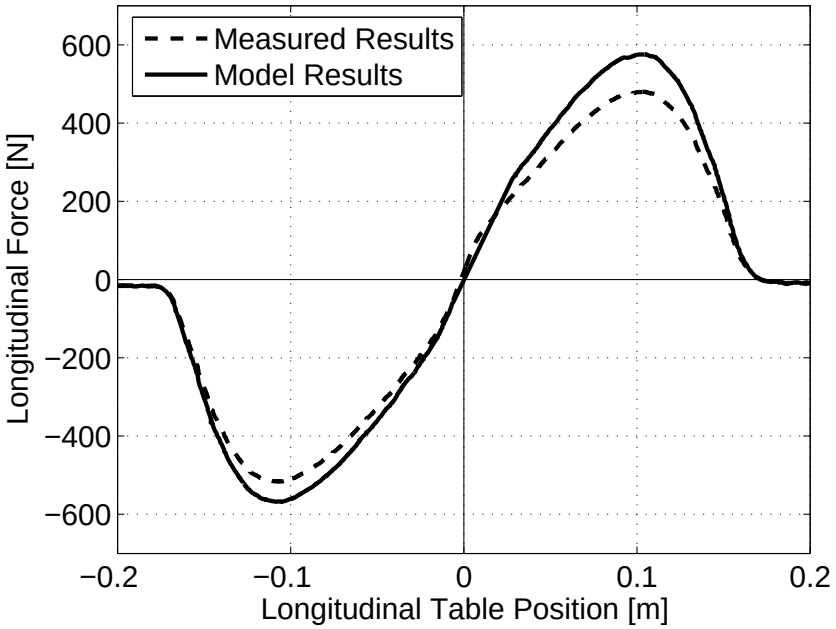

Figure 4.14. Longitudinal force vs. longitudinal position of the table for 155R13 traversing a circular cleat

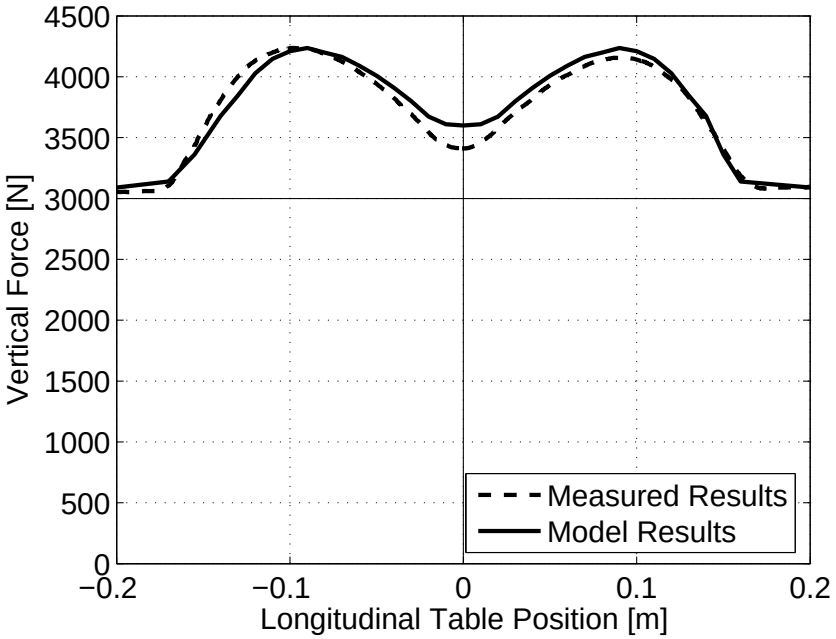

Figure 4.15. Vertical force vs. longitudinal position of the table for 155R13 traversing a circular cleat

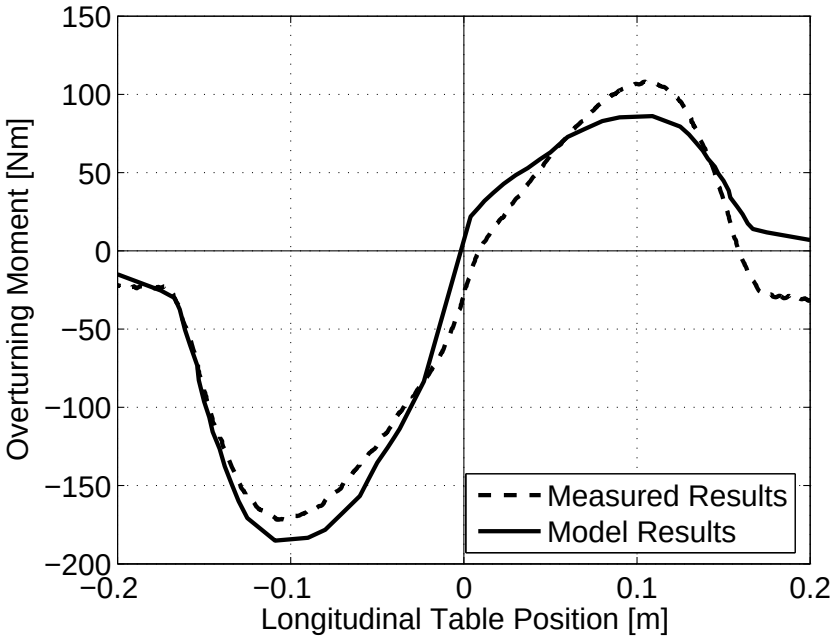

Figure 4.16. Overturning moment vs. longitudinal position of the table for 155R13 traversing a circular cleat

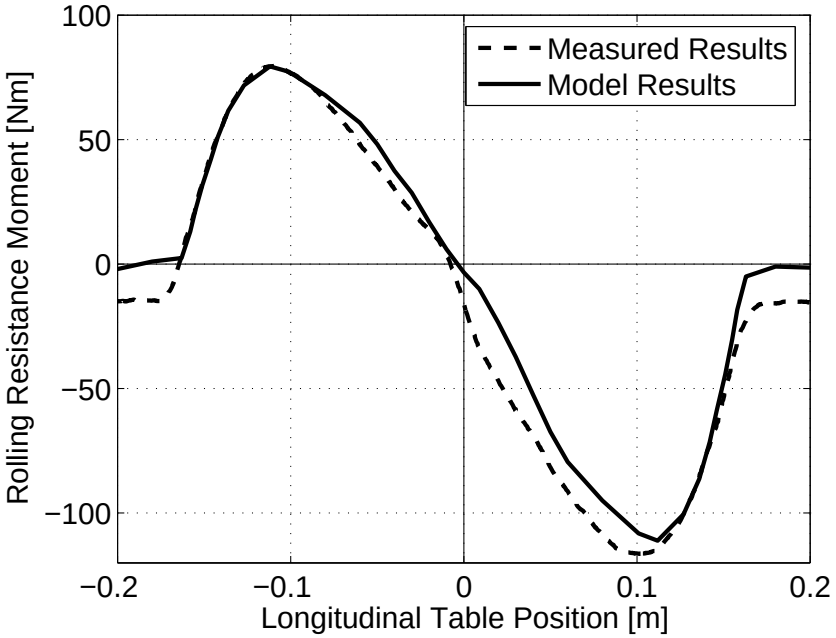

Figure 4.17. Rolling Resistance moment vs. longitudinal position of the table for 155R13 traversing a circular cleat

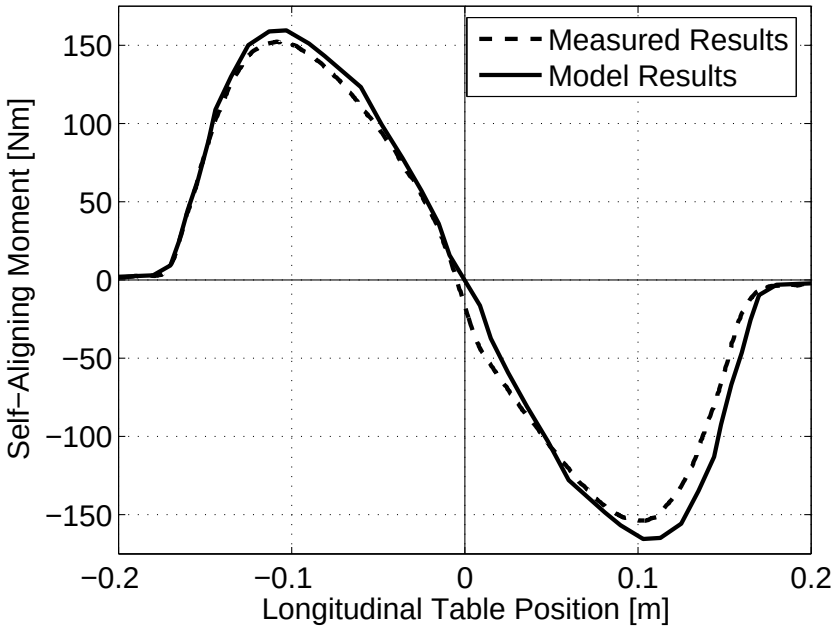

Figure 4.18. Self-Aligning moment vs. longitudinal position of the table for 155R13 traversing a circular cleat

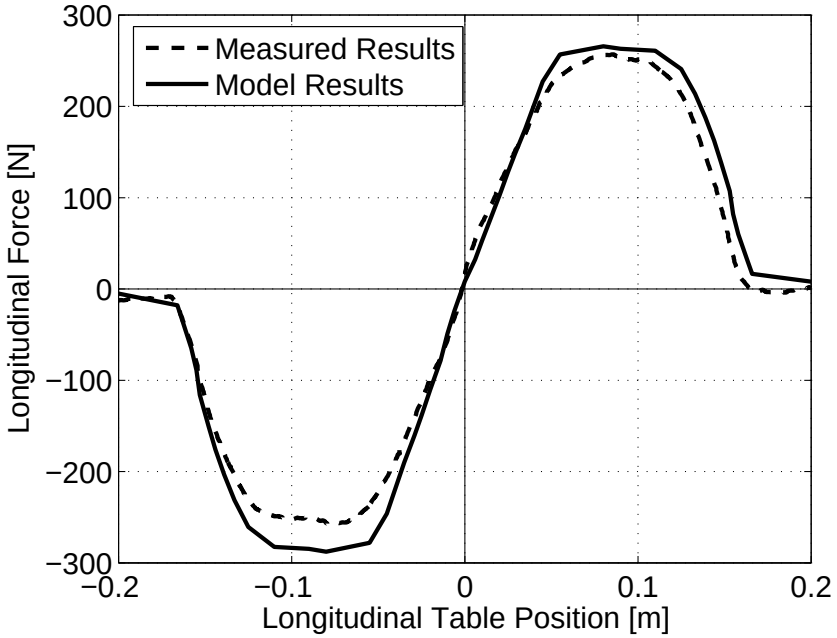

Figure 4.19. Longitudinal force vs. longitudinal position of the table for 155R13 traversing a rectangular cleat

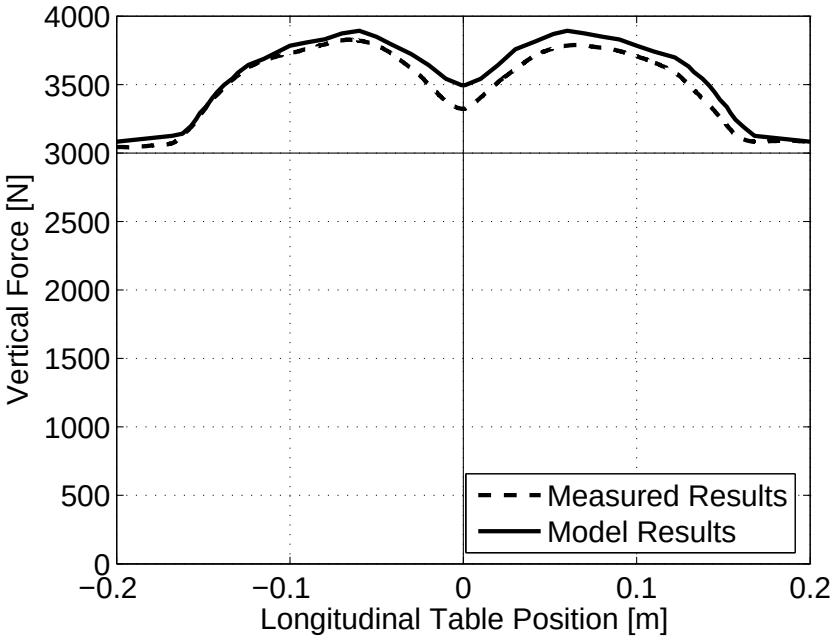

Figure 4.20. Vertical force vs. longitudinal position of the table for 155R13 traversing a rectangular cleat

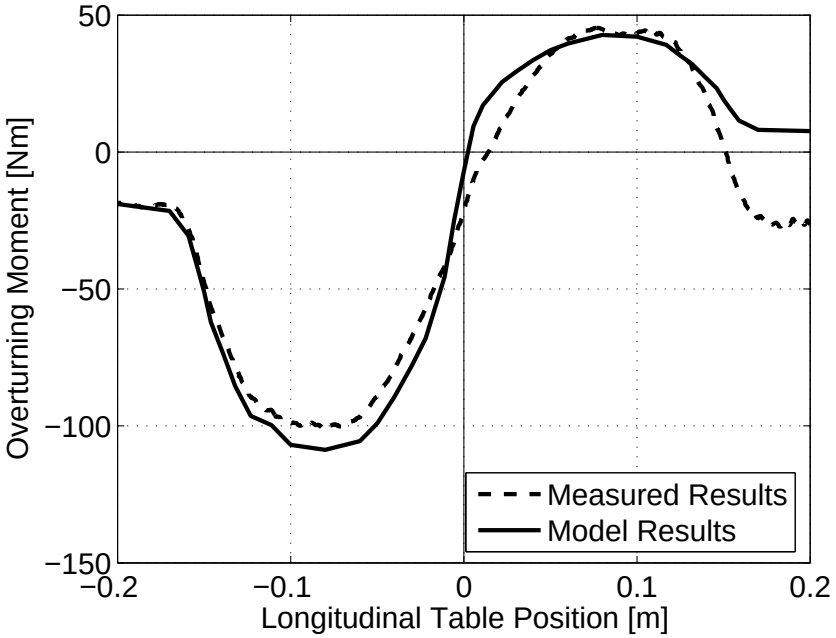

Figure 4.21. Overturning moment vs. longitudinal position of the table for 155R13 traversing a rectangular cleat

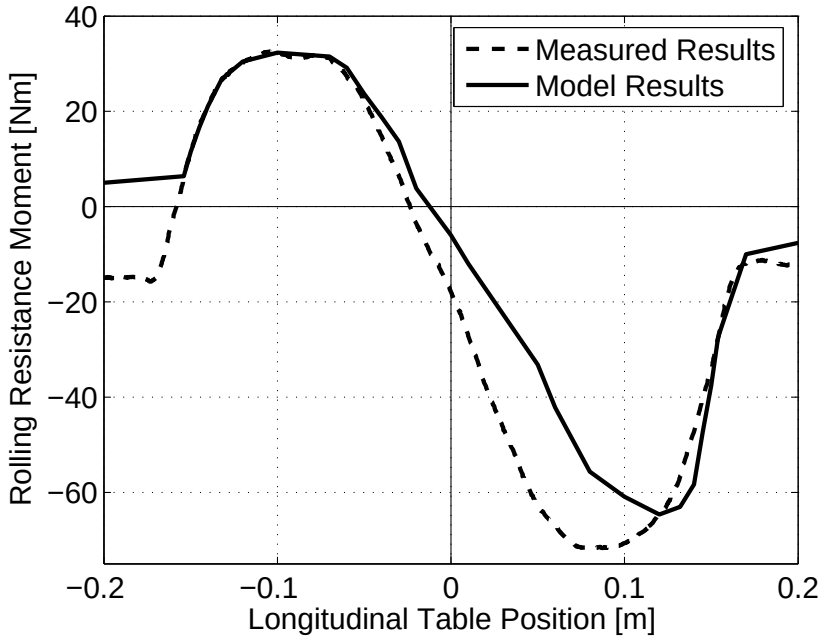

Figure 4.22. Rolling resistance moment vs. longitudinal position of the table for 155R13 traversing a rectangular cleat

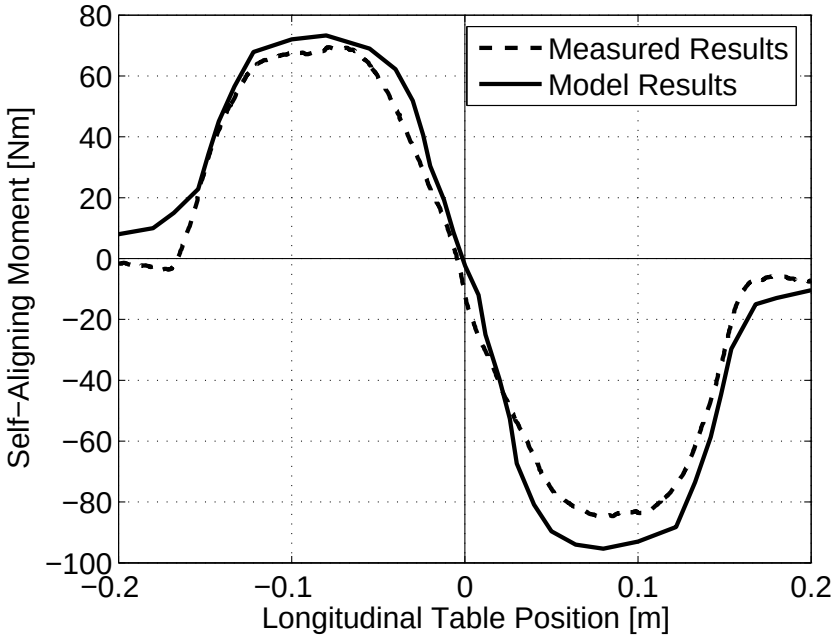

Figure 4.23. Self-Aligning moment vs. longitudinal position of the table for 155R13 traversing a rectangular cleat

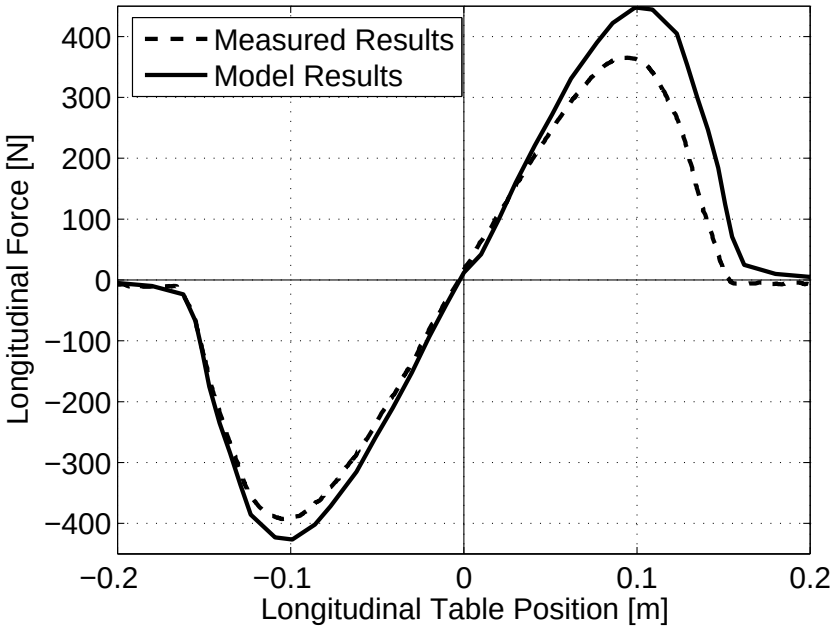

Figure 4.24. Longitudinal force vs. longitudinal position of the table for 155R13 traversing a triangular cleat

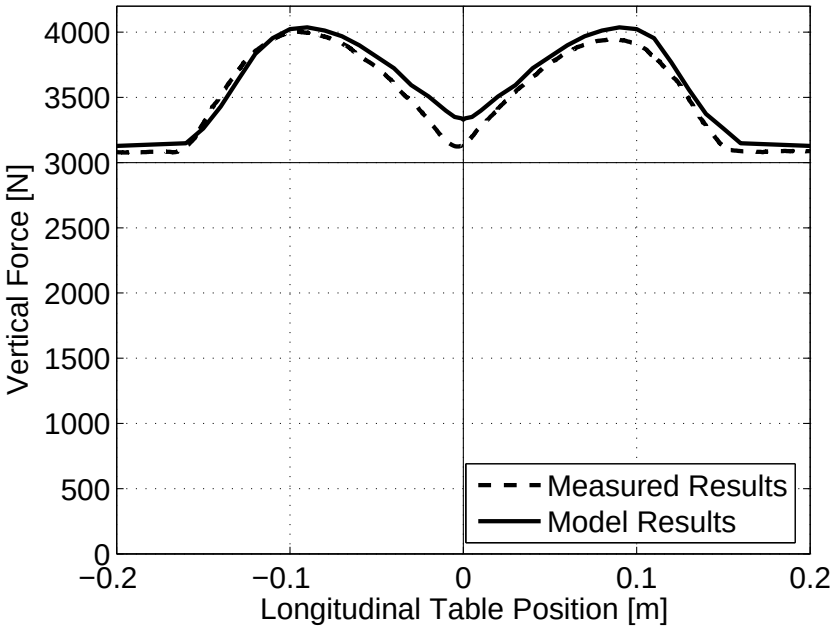

Figure 4.25. Vertical force vs. longitudinal position of the table for 155R13 traversing a triangular cleat

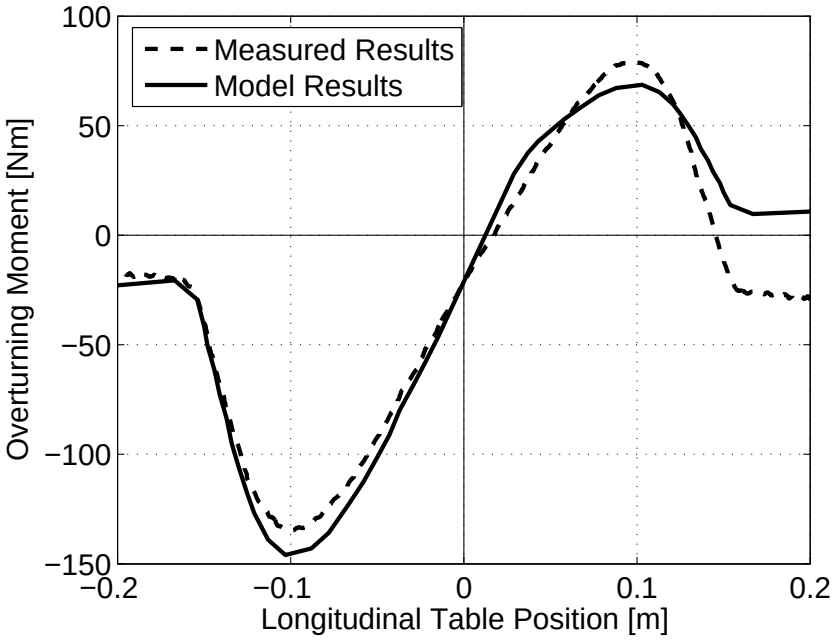

Figure 4.26. Overturning moment vs. longitudinal position of the table for 155R13 traversing a triangular cleat

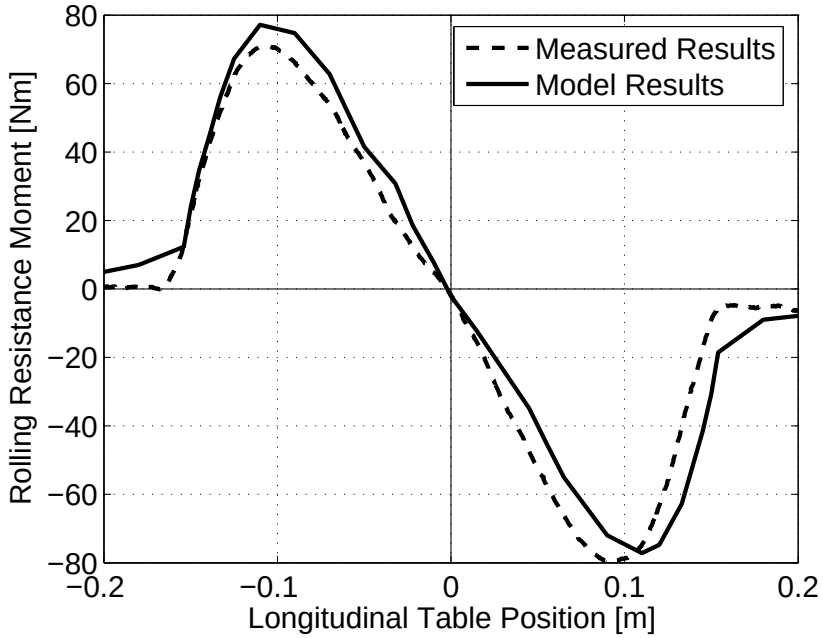

Figure 4.27. Rolling resistance moment vs. longitudinal position of the table for 155R13 traversing a triangular cleat

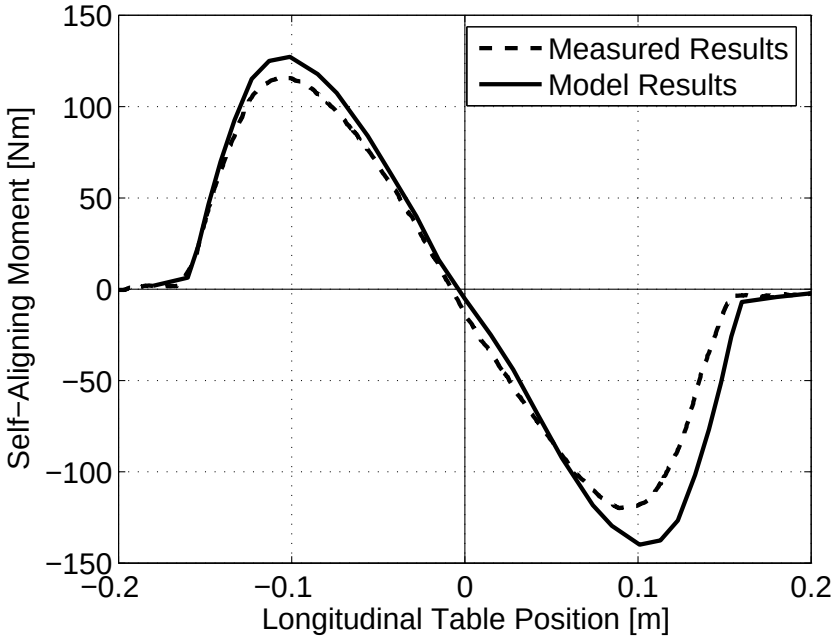

Figure 4.28. Self-Aligning moment vs. longitudinal position of the table for 155R13 traversing a triangular cleat

Error tables are tabulated as follows. To some extent, there is a satisfactory match between the proposed model and experiments. However, there is a need to consider some factors to improve the model results. In addition to parameters mentioned above, including material damping constants to the model can improve the results. Especially, including material damping constants of tread and sidewall to be exposed to the large displacements improves the model results. Inflation pressure is fixed and the pressure increases while tire rolls. This effect should also be considered to improve the model results. In addition, thermal loads arise due to the manufacturing and operational conditions and should be introduced to the model. However, including each parameter to the model results in high CPU.

Table 4.5. Comparison of the absolute maximum longitudinal force value of 155R13 tire while traversing different types of obstacles for rated 180 kPa inflation pressure and 3 kN vertical load

	Maximum longitudinal force at entry (N) (Third quadrant)			Maximum longitudinal force while leaving the cleat (N) (First quadrant)		
Cleat type	Model results	Measured results	Error (%)	Model results	Measured results	Error (%)
Circular sectioned	567.913	516.285	9.091	575.925	479.937	16.667
Rectangular sectioned	287.764	257.440	10.538	265.839	252.142	5.152
Triangular sectioned	426.356	392.977	7.829	447.673	365.825	18.283

Table 4.6. Comparison of the vertical force value of 155R13 tire while traversing different types of obstacles for rated 180 kPa inflation pressure and 3 kN vertical load

	Maximum vertical force (N)			Minimum vertical force (N)		
Cleat type	Model results	Measured results	Error (%)	Model results	Measured results	Error (%)
Circular sectioned	4235.015	4236.685	-0.040	3600.566	3388.632	5.886
Rectangular sectioned	3857.616	3830	0.716	3465	3191	7.908
Triangular sectioned	4001	4004.433	-0.086	3300	3121.871	5.398

Table 4.7. Comparison of the absolute maximum overturning moment value of 155R13 tire while traversing different types of obstacles for rated 180 kPa inflation pressure and 3 kN vertical load

	Maximum overturning moment at entry (N m) (Third quadrant)			Maximum overturning moment while leaving the cleat (N m) (First quadrant)		
Cleat type	Model results	Measured results	Error (%)	Model results	Measured results	Error (%)
Circular sectioned	86.094	108.125	-25.589	185.147	171.814	7.201
Rectangular sectioned	42.784	45.38	-6.068	105.56	100.699	4.605
Triangular sectioned	68.61	78.978	-15.111	145.973	134.74	7.695

Table 4.8. Comparison of the absolute maximum rolling resistance moment value of 155R13 tire while traversing different types of obstacles for rated 180 kPa inflation pressure and 3 kN vertical load

	Maximum rolling resistance moment at entry (N m) (Second quadrant)			Maximum rolling resistance moment while leaving the cleat (N m) (Fourth quadrant)		
Cleat type	Model results	Measured results	Error (%)	Model results	Measured results	Error (%)
Circular sectioned	79.37	79.69	-0.403	111.118	116.437	-4.787
Rectangular sectioned	32.32	32.55	-0.712	64.64	71.92	-11.262
Triangular sectioned	77.072	70.877	8.038	78.072	79.717	-2.107

Table 4.9. Comparison of the absolute maximum self-aligning moment value of 155R13 tire while traversing different types of obstacles for rated 180 kPa inflation pressure and 3 kN vertical load

	Maximum self-aligning moment at entry (N m) (Second quadrant)			Maximum self-aligning moment while leaving the cleat (N m) (Fourth quadrant)		
Cleat type	Model results	Measured results	Error (%)	Model results	Measured results	Error (%)
Circular sectioned	159.443	152.337	4.457	165.517	153.889	7.025
Rectangular sectioned	95.336	84.89	10.957	73.335	69.49	5.243
Triangular sectioned	127.237	115.992	8.838	139.97	119.940	14.310

5. SUMMARY AND CONCLUSIONS

Tire is one of the most important components of a vehicle since it is the only interface with roads. All forces and moments acting on a vehicle except aerodynamic and gravitational forces take place on a small area between the tire and the road. To construct an accurate and reliable vehicle model, tire forces and corresponding moments should be well understood and modeled. In this thesis, tire is modeled using experimental and numerical techniques. Experimental studies are conducted to validate proposed model results and to see its validate range. To do so, flat-bed tire tester constructed at the University of Michigan Transportation Research Institute (UMTRI) is used. In the tire finite element model, MSC. Marc is used. The rubber parts are modeled using solid elements and the reinforcements are modeled using rebar elements available in the software. The tire-ground contact is also modeled. Rim and road are modeled using rigid elements.

In the experimental part of the study, tire lateral, vertical and enveloping characteristics are investigated. Four different types of tires are tested and the effects of inflation pressures, vertical loads and types of obstacles are considered. In-plane and out-of plane forces and moments are calculated. In the vertical stiffness studies, it is observed that after a certain vertical displacement, all curves in force-deflection diagrams plotted for with and without cleat intersect regardless of cleat and tire types depending on the inflation pressure of the tire. After this displacement value, the tire swallows the cleat completely, and the tire behaves as if it were rolling on a flat surface. This tire property is not mentioned in literature. In the lateral and vertical tire force characteristics studies, for different slip angles and vertical loads, cornering force, aligning moment, overturning moment and rolling resistance moment versus slip angle plots are given. All force and moment magnitudes increases parallel to increase in vertical load value. Maximum aligning moment are obtained between $2-5$ degree slip angle values as seen in literature. When viewing in literature, different tires are examined and in general, self-aligning moment takes negative value for a certain slip angle range within the this study limits. However, this not the case for 155R13 tire.

This can be attributed the typical characteristics of the 155R13 tire. In the aspect of tire enveloping characteristics, all force and moment responses of all tires are studied and only small differences are found in tires' general behavior and as expected their magnitudes are different from each other. As a result, only the effects of the inflation pressure and vertical load on force and moment responses of 155R13 while passing over obstacles are presented in this study. A considerable influence of the normal load on vertical and lateral force responses of a tire is determined. On the other hand, it is found that the inflation pressure does not have considerable effect on force and moment responses of the tire. While the tire traverses obstacles, minimum vertical force value between two maxima in the vertical force versus longitudinal table position plots becomes lower than the initial force under large deflection cases as mentioned in literature; the rectangular obstacle being an exception. This phenomenon is less pronounced for the rectangular cross sectioned cleat. In literature, there is a limited study about moment variation during a tire traverses an obstacle. In general, tire longitudinal, lateral and vertical force variations have been considered.

In the numerical part of the study, to solve the problem within the meaningful time, some assumptions are made. It is seen that there is a satisfactory match between the model and experimental results. However, model results can be improved by including some parameters and the model errors can be eliminated. The errors can be attributed to the following factors:

- Friction model: Friction between a tire and road surface plays a more important role in the tire force and moment characteristics and it is very complex problem. The friction force governs tire force and moment formations. In this study, constant static coefficient of friction is taken and it is assumed that the lateral and longitudinal coefficient of frictions are the same (Isotropic coefficient of friction). In fact, it takes different values in both directions (Anisotropic coefficient of friction). In addition, as mentioned in the analytical section, coefficient of friction depends on many factors. Slip angle, sliding velocity, road texture and surface, vertical loads and tire tread pattern are the some of the most important parameters which are not considered.

- Tire material and geometrical properties: There are four different rubber materials over the cross section of the tire. It is well known that rubber shows viscoelastic properties. In this study, viscoelastic effects are not considered. In addition, damping effects are not considered. However, it is expected that including material damping constants to the model can improve the results. Especially, including material damping constants of tread and sidewall to be exposed to the large displacements improves the model results. Another important parameter is the reinforcement. In reality, in addition to the tread and sidewall deformation, another factor leading to the tire deformation is the carcass deformation. The steel belts have bending stiffness. In this study, textile and steel reinforcements are modeled by unidirectional reinforcing model (rebar element formulation). Rebar elements do not carry bending and carcass deformation effects are not included to the model. In addition, the reinforcement locations are specified to some extent accurately. As mentioned in [34], it is possible to determine the geometric details from digitally scanned images. On the other hand, as seen in Table 3.3, the reinforcements show different elastic modulus for tension and compression. In order to implement these properties to the model, there is a need to write a subroutine to control the stress state of the element after each solution increment and the elastic constant can be assigned to the elements according to the stress state.
- Actual tire tread modeling: In this study, the tire with smooth tread is modeled. In the experimental stages, to some extent, worn tire is used. The slight difference between the results can be attributed to this fact. In this study, dry road conditions are considered. In the case of wet or icy road condition cases, the errors will be increased and to overcome this problem, actual tread configuration should be introduced to the model.
- Contact algorithm: The tire is modeled using solid elements which have no rotation degree of freedom. The rim is modeled as rigid body and it is glued to the tire. So, the tire-rim are considered as a body and there is no need to model bead. The road is also modeled with rigid body. The tire-rim and road interaction are modeled with touching type contact modeling with constant coefficient of friction. Especially, for harsh cornering cases and stress distribution, tire-rim

interaction should be modeled as touching type contact modeling and bead effect should be included to the model.

- Tire loads: An accurate determination of the magnitude and distribution of the loads on a tire are some of the most difficult aspects of tire analysis. Inflation pressure is fixed and the pressure increases while tire rolls. This effect should also be considered to improve the model results. In addition, thermal loads arise due to the manufacturing and operational conditions and should be introduced to the model.

5.1. Future Work

In the preceding section, some parameters improving the model results are mentioned. These parameters should be considered. However, including each parameter to the model results in a high CPU time. For industrial applications, high speed cases should also be considered.

In addition to considerations above, it can also be noted that the tire should be modeled as a component of a vehicle. In other word, a full vehicle model should be modeled and the tire behavior should be examined.

REFERENCES

1. Noor, A. K. and J. A. Tanner, "Tire modeling and contact problems: Advances and trends in the developments of computational models for tires", *Computers and Structures*, Vol. 20, No. 1-3, pp. 517–533, 1985.

2. http://www.discounttyre.com/dtcs/infoTyreConstruction.dos.

3. Mark, J. E., B. Erman, and F. R. Eirich, *Science and Technology of Rubbers*, Academic Press, SanDiego, USA, c 1994.

4. Gillespie, T. D., *Fundemantals of Vehicle Dynamics*, Warrendale, PA:Society of Automotive Engineers, New York, NY, c 1992.

5. www.tireguides.com e-mail addresses, Tire Guides, Inc.

6. Fiala, E., "Seitenkrafte am rollenden luftreifen", *Zeitschrift*, Vol. 96, No. 29, pp. 973–979, 1954.

7. Bergman, W., "Theoretical prediction of the effect of traction on cornering force", *Society of Automotive Engineering (SAE)*, Vol. 69, No. paper 186-A, pp. 614–640, 1961.

8. Livingston, D. I. and J. E. Brown, "Physics of the slipping wheel. i. force and torque calculations for various pressure distributions", *Rubber Chemistry and Technology*, Vol. 42, pp. 1014–1027, 1969.

9. Dugoff, H., P. S. Fancher, and L. Segel, "Tire performance characteristics affecting vehicle response to steering and braking control inputs", *Final report for period May 1968-August 1969 prepared for Tire System Section Office of Vehicle System Research NATIONAL BUREAU OF STANDARDS Washington, D. C. 20234*, 1969.

10. Bernard, J. E., L. Segel, and R. Wild, "Tire shear force generation during combined steering and braking maneuvers", *Society of Automotive Engineers (SAE)*, 770852.

11. Sakai, H., "Theoretical and experimentalstudies on the dynamic properties of tyres-3. calculation of the six component of force and moment of a tyre", *International Journal of Vehicle Design*, Vol. 2, No. 3, pp. 335–373, 1961.

12. Singh, D. V., V. K. Goel, and A. Kumar, "A mathematical model for steady state tyre forces", *Inst. Mech. Enngrs. (INDIA)*, Vol. 63, pp. 224–231, 1983.

13. Gim, G. and P. E. Nikravesh, "An analytical model of pneumatic tyres for vehicle dynamic simulations. part 1: Pure slips", *International Journal of Vehicle Design*, Vol. 11, No. 6, pp. 589–618, 1990.

14. Sjahdanulirwan, M., "An analytical model for the prediction of tyre-road friction under braking and cornering", *International Journal of Vehicle Design*, Vol. 14, No. 1, pp. 78–99, 1993.

15. Sjahdanulirwan, M. and Y. Q, "Prediction of tyre-road friction with an inverted-boat shaped pressure distribution", *Vehicle System Dynamics*, Vol. 24, 1995.

16. Gupta, M. K. and V. K. Goel, "An analytical model of small size pneumatic tyres for tyre traction properties: Pure slip", *Proceedings of International Conference on Advances in Mechanical & Industrial Engineering*, 1997.

17. Ramji, K., V. K. Goel, and V. H. Saran, "Stiffness properties of small-sized pneumatic tyres", *Proceeding of the Institution of Mechanical Engineers*, Vol. 216, 2002.

18. Shifrin, B. M., "An analytical model of a rolling pneumatic tire", *International Applied Mechanics*, Vol. 42, No. 4, pp. 479–485, 2006.

19. Zegelaar, P. W., *The Dynamic Response of Tyres to Brake Torque Variations and Road Unevennesses*, Ph.D. thesis, Delft University of Technology, 1998.

20. Gim, G. and P. E. Nikravesh, "An analytical model of pneumatic tyres for vehicle dynamic simulations. part 2: Comprehensive slips", *International Journal of Vehicle Design*, Vol. 12, No. 1, pp. 19–39, 1991.

21. Gim, G. and P. E. Nikravesh, "An analytical model of pneumatic tyres for vehicle dynamic simulations. part 3: Validation against experimental data", *International Journal of Vehicle Design*, Vol. 12, No. 2, pp. 217–228, 1991.

22. Pacejka, H. B., *Tyre and Vehicle Dynamics*, Delft University of Technology Consultant TNO Automotive Delft, The Netherlands, 2006.

23. Tonuk, E. and Y. S. Unlusoy, "Prediction of automobile tire cornering force characteristics by finite element modeling and analysis", *Computers and Structures*, Vol. 79, pp. 1219–1232, 2001.

24. Tonuk, E., *Computer Simulation of Dynamic Behavior of Pneumatic Tires*, Ph.D. thesis, Mechanical Engineering Department, Middle East Technical University, 1998.

25. Burke, A. M. and O. A. Olatunbosun, "Static tyre / road interaction modelling", *Meccanica*, Vol. 32, 1997.

26. Yap, P., "Measurements of radial truck tire dry cornering characteristic", *Society of Automotive Engineers (SAE)*, 912677.

27. Holloway, D. C., T. J. Drach, and B. Mohanty, "An experimental investigation of passenger car tire properties at high slip and camber angles", *Society of Automotive Engineers (SAE)*, 910233.

28. Bakker, E., L. Nyborg, and H. B. Pacejka, "Tyre modeling for use in vehicle dynamics studies", *Society of Automotive Engineers (SAE)*, 870421.

29. Maalej, A. Y., D. A. Guenther, and J. R. Ellis, "Experimental development of tyre force and moment models", *International Journal of Vehicle Design*, Vol. 10,

No. 1, pp. 34–51, 1989.

30. Takahashi, T. and M. Hada, "Modeling of tire overturning moment characteristics and the analysis of their influence on vehicle rollever behavior", *R & D Review of Toyota CRDL*, Vol. 38, No. 4, pp. 10–16, 2003.

31. Kageyama, I. and S. Kuwahara, "A study on tire modeling for camber thrust and camber torque", *JSAE Review*, Vol. 23, No. 3, pp. 325–331, 2002.

32. Fuller, D. L., G. L. Hall, and F. S. Conant, "Effect of testing conditions on rolling resistance of automobile tires", *Society of Automotive Engineers (SAE)*, 840068.

33. Schuring, D. J., *Tire Parameter Determination Volume II-Part1*, The Calspan Corporation, 4455 Genesee Street Buffalo, NewYork 14221, USA, 1975.

34. Danielson, K. T., A. K. Noor, and J. S. Green, "Computational strategies for tire modeling and analysis", *Computers and Structures*, Vol. 61, No. 4, pp. 673–693, 1996.

35. Kabe, K. and M. Koishi, "Tire cornering simulations using finite element analysis", *Journal of Applied Polymer Science*, Vol. 78, No. 8, pp. 1566–1572, 2000.

36. D.E, H. and J. Moreland, "Fundamentals of rolling resistance", *Rubber Chemistry and Technology*, Vol. 74, No. 3, pp. 525–539, 2001.

37. Pelc, J., "Static three-dimensional modeling of pneumatic tyres using the technique of element overlaying", *Proceeding of the Institution of Mechanical Engineers Part D - Journal of Automobile Engineering*, Vol. 216, No. D9, pp. 709–716, 2002.

38. Huh, H. and Y. K. Kwak, "Finite element stress analysis of the reinforced tire contact problem", *Computers and Structures*, Vol. 36, No. 5, pp. 871–881, 1990.

39. Yan, X., "Non-linear three-dimensional finite element modeling of radial tires", *Mathematics and Computers in Simulation*, Vol. 58, No. 1, pp. 51–70, 2001.

40. Wu, B., *Nonlinear Three-Dimensional Finite Element Formulation of Radial Tires*, Ph.D. thesis, Harbin Institute of Technology (in Chinese), 1993.

41. Clark, S. K., *Mechanics of Pneumatic Tires*, US Department of Transportation, Dot HS 805952, Washington, DC, 1981.

42. Patel, H. P. and R. H. Kennedy, "Nonlinear finite element analysis for composite structures of axisymmetric geometry and loading", *Computers and Structures*, Vol. 15, No. 1, pp. 79–84, 1982.

43. Wallerstein, D. V. and G. A. Dilley, "Finite element analysis and the modeling of tires", *MSC. Nastran Users' Conf. Proc., Paper no. 14*, 1984.

44. Watanabe, Y. and M. J. Kaldjian, "Modeling and analysis of bias-ply motorcycle tires", *Computers and Structures*, Vol. 17, No. 5–6, pp. 653–658, 1983.

45. Cho, J. R., K. W. Kim, W. S. Yoo, and S. I. Hong, "Mesh generation considering detailed tread blocks for reliable 3d tire analysis", *Advances in Engineering Software*, Vol. 35, No. 2, pp. 105–113, 2004.

46. Helnwein, P., C. H. Liu, G. Meschke, and H. A. Mang, "A new 3-d finite element model for cord-reinforced rubber composites- application to analysis of automobile tires", *Finite Elements in Analysis and Design*, Vol. 14, pp. 1–16, 1993.

47. Liu, C., G. Meschke, P. Helnwein, and H. A. Mang, "Tying algorithm for linking of finite element meshes with different degrees of refinement. application to finite element analyses of tires", *Computer assisted Mechanics and Engineering Sciences*, Vol. 2, pp. 289–305, 1995.

48. Ersahin, M. A., *Finite Element Analysis of Cornering Characteristics of Rotating Tires*, Ph.D. thesis, Mechanical Engineering Department, Middle East Technical University, 2003.

49. Dihua, G. and F. Chengjian, "Tire modelling for vertical properties including en-

veloping properties using experimental modal parameters", *Vehicle System Dynamics*, Vol. 40, No. 6, pp. 419–433, 2003.

50. Julien, M. and J. Paulsen, "Experimental method for measuring and defining the absorbing capacity of a pneumatic tyre", *S.I.A.J, translated from French by Robinson M.S.*, Vol. 26, No. 1, pp. 33–40, 1953.

51. Gough, V., *Tyres and Air Suspension*, Reprinted from Tidbury: Advances in Automobile Engineering, Pergamon Press, Oxford, London, New York and Paris, 1963.

52. Chiesa, A., L. Oberto, and L. Tamburini, "Transmission of tyre vibrations", *Automobile Engineer*, pp. 520–530, 1964.

53. Mills, B. and J. Dunn, "The mechanical mobility of rolling tyres", *Institution of Mechanical Engineers, Report No: C104/71*, 1971.

54. Bohm, F., *Mechanics of the Belted Tire*, Translated by Eugen Funero Project Director: Clark S.K., The University of Michigan, 1967.

55. Majcher, S., *Simulation of Radial Ply Tires for Ride Tuning of Automobile Suspensions*, Ph.D. thesis, University of Detroit, 1973.

56. Gough, V., C. W. Barson, J. Hutchinson, and D. James, "Tyre and vehicle vibration", *Automobile Division of the Institution of Mechanical Engineers*, 1964/5.

57. Takayama, M. and K. Yamagishi, "Simulation model of tire vibration", *Tire Science and Technology*, Vol. 11, No. 1–4, pp. 38–49, 1984.

58. Lippmann, S. and J. Nanny, "A quantitative analysis of the enveloping forces of passenger tires", *Society of Automotive Engineers (Automotive Engineers Congress, Detroit Michigan,January 9-13,1967)*, 670174.

59. Bandel, P. and C. Monguzzi, "Simulation model of the dynamic behavior of a tire running over an obstacle", *Tire Science and Technology*, Vol. 16, No. 2, pp. 62–77,

1988.

60. Nakajima, Y. and J. Padovan, "Numerical simulation of tire sliding events involving impacts with holes and bumps", *Tire Science and Technology*, Vol. 14, No. 2, pp. 125–136, 1986.

61. Nakajima, Y. and J. Padovan, "Finite element analysis of steady and transiently moving/rolling nonlinear viscoelastic structure-iii. impact/contact simulations", *Tire Science and Technology*, Vol. 27, No. 2, pp. 275–286, 1987.

62. Beres, W., "Linear models of tyre enveloping properties", *International Journal of Vehicle Design*, Vol. 8, No. 4/5/6, pp. 485–503, 1987.

63. Wei, Y., L. Nasdala, and H. Rothert, "Analysis of tire rolling contact response by ref model", *Tire Science and Technology*, Vol. 32, No. 4, pp. 214–235, 2004.

64. Dihua, G., F. Chengjian, and X. Xie, "A dynamic tire model of vertical performance rolling over cleats", *Vehicle System Dynamics Supplement*, Vol. 43, pp. 209–222, 2005.

65. Chengjian, F. and G. Dihua, "The quantitative analysis and experimental verification of the tire static enveloping model using experimental model parameters", *Vehicle System Dynamics*, Vol. 44, No. 9, pp. 675–688, 2006.

66. Kamoulakos, A. and B. G. Kao, "Transient dynamics of a tire rolling over small obstacles-a finite element approach with pam-shock", *Tire Science and Technology*, Vol. 26, No. 2, pp. 84–108, 1998.

67. Chang, Y. P. and M. El-Gindy, "Virtual prediction of a radial-ply tire's in-plane free vibration modes transmissibility", *International Journal of Automotive Technology*, Vol. 6, No. 2, pp. 149–159, 2005.

68. Zegelear, P. and H. Pacejka, "The in-plane dynamics of tyres on uneven roads", *Vehicle System Dynamics Supplement*, Vol. 25, pp. 714–730, 1996.

69. Zegelear, P., *The Dynamic response of Tyres to Brake Torque Variations and Road Unevennesses*, Ph.D. thesis, Delft University of Technology, 1998.

70. Mousseau, C. and S. Clark, "An analytical and experimental study of a tire rolling over a stepped obstacle at low velocity", *Tire Science and Technology*, Vol. 22, No. 3, pp. 162–181, 1994.

71. Mousseau, C. and G. Hulbert, "An efficient tire model for the analysis of spindle forces produced by a tire impacting large obstacles", *Comput. Methods Appl. Mech. Engrg.*, Vol. 135, No. 1-2, pp. 15–34, 1996.

72. Mousseau, C. W. and G. M. Hulbert, "The dynamic response of spindle forces produced by a tire impacting large obstacles in a plane", *Journal of Sound and Vibration*, Vol. 95, 1996.

73. Mousseau, C., *A Numerical and Experimental Investigation into the Force Response of a Tire Impacting a Large Obstacle*, Ph.D. thesis, Mechanical Engineering, the University of Michigan, 1994.

74. Darnell, I., G. M. Hulbert, and C. Mousseau, "An efficient three-dimensional tire model for vehicle dynamics simulations", *Mech. Struct and Mach.*, Vol. 25, No. 1, pp. 1–19, 1997.

75. Mousseau, C., T. A. Laursen, M. Lidberg, and R. L. Taylor, "Vehicle dynamics simulations with coupled multibody and finite element models", *Finite Elements in Analysis and Design*, Vol. 31, pp. 295–315, 1999.

76. Schmeitz, A. J. C., S. T. H. Jansen, H. B. Pacejka, J. C. Davis, N. N. Kota, C. G. Liang, and G. Lodewijks, "Application of a semi-empirical dynamic tire model for rolling over arbitrary road profiles", *International Journal of Vehicle Design*, Vol. 36, No. 2/3, pp. 194–215, 2004.

77. Day, D. T., "Simulation of tire interaction with curbs and irregular terrain", *En-*

gineering Dynamics Corporation, WP-2005-6, 2005.

78. Mousseau, C. and M. Sayers, "The effect of the tyre and suspension dynamics on wheel spindle forces", *Heavy Vehicle Systems, Int. J. of Vehicle Design*, Vol. 6, No. 1/4, pp. 46–65, 1999.

79. Lugner, P., H. B. Pacejka, and M. Plochl, "The quantitative analysis and experimental verification of the tire static enveloping model using experimental model parameters", *Vehicle System Dynamics*, Vol. 43, No. 6-7, pp. 413–436, 2005.

80. Zoeppritz, H. P., "Problemes dans les essais sur pneus automobiles: Problems in testing motor vehicle tyres", *Materialprufung*, Vol. 10, No. 4, pp. 122–125, 1968.

81. Cho, J. R., K. W. Kim, D. H. Jeon, and W. S. Yoo, "Transient dynamic response analysis of 3-d patterned tire rolling over cleat", *European Journal of Mechanics A/Solids*, Vol. 24, 2005.

82. Hanley, R., D. Crolla, and M. Hauke, "Tire modeling for misuse situations", *Society of Automotive Engineers (SAE)*, 2001-01-0748.

83. Howard, D. and B. J. Brown, "Measurement of tire shear forces", *Society of Automotive Engineers (Automotive Engineers Congress, Detroit Michigan,1970)*, 700092.

84. James, L. and R. L. Marlowe, "Road contact forces of truck tires as measured in the laboratory", *Society of Automotive Engineers (Mid-Year Meeting Chicago, Illinois, 1967)*, 670493.

85. van Eldik Thime, H. C. A. and H. Pacejka, "Analysis of tire properties", *In: S.K. Clark, Editor, Mechanics of Pneumatic Tires, NBS Monograph 122 Washington, D.C.*, 1971.

86. Bruce, E. L., "Tire conicity and ply steer effects on vehicle performance", *Society of Automotive Engineers (SAE)*, 740074.

87. MSC. Marc Mentat Documentation, Volume A.

88. Wong, J. Y., *Theory of Ground Vehicles*, John Willey & Sons, Inc.,, 2001.